Mass Spectrometric Analysis of Organic Aerosol Composition: Laboratory and Ambient

Thesis by

ManNin Chan

In Partial Fulfillment of the Requirements

for the Degree of

Doctor of Philosophy

California Institute of Technology

Pasadena, California

2012

(Defended December 1, 2011)

© 2012

ManNin Chan

Dedicated to my family and my wife

Acknowledgements

My graduate years at Caltech and this thesis have had support from many friends and colleagues. I would like to express my sincere gratitude to …

… John Seinfeld, my thesis advisor, for his continuous and competent support of my graduate study, for good discussions and suggestions about research ideas and directions, and for his trust in my work. John has also enlightened me through his passion for science about where the research should go and what is necessary to get there. The advice, guidance, and support of his have been invaluable on both an academic and a personal level, for which I am greatly grateful and appreciative.

… Rick Flagan, Michael Hoffmann, and Paul Wennberg for being willingly in my thesis committee and for their valuable time, encouragement, and insightful comments. I am very grateful to Rick for always being willing to discuss research ideas that I had or he had and to share his profound knowledge and ideas about aerosol measurement techniques.

… Chak Chan, my research advisor at the Hong Kong University of Science and Technology, who has introduced me to scientific research, and has encouraged me to pursue my graduate study in atmospheric science.

…. Jason Surratt and Arthur Chan for their advice and support in my graduate study. I am deeply indebted to Jason for sharing his thoughtful knowledge about mass spectrometry and atmospheric science, for the days and nights we were working together in the labs and

… my parents and brother for their support in my pursuit of higher education and personal interests. They never once complain about how infrequently I visit them, and deserve far more credit than I can ever give them.

… Susanna Wong for her support, encouragement, and companionship over the years. Her love and support has turned my journey through graduate school and my life into a pleasure. For all that, she has my everlasting love.

Abstract

Organic compounds contribute a significant mass fraction of ambient aerosol and play a role in determining the physiochemical properties of ambient aerosol. A significant fraction of organic aerosol is secondary organic aerosol (SOA), which is produced when the volatile organic compounds (VOCs) originating from various anthropogenic and biogenic sources react with atmospheric oxidants such as ozone, hydroxyl radicals, and nitrate radicals to form lower volatility organic compounds, which subsequently partition into the particle phase. Understanding the composition of ambient aerosol is crucial for identifying its sources and formation mechanisms, and predicting its properties and effects on various ambient processes. This thesis focuses on investigating the composition of laboratory–generated SOA formed from the oxidation of biogenic VOCs of atmospheric importance (isoprene and β–caryophyllene) and ambient aerosol collected in field campaigns using advanced mass spectrometric techniques. By comparing the mass spectrometric data collected for the both laboratory–generated SOA and ambient aerosol, we propose reaction pathways and new chemical tracers for these biogenic VOCs, which enhance our knowledge of the composition, sources, and formation pathways of SOA in the atmosphere. With a better knowledge of the SOA composition, a product–specific model is proposed to predict the composition and aerosol mass yields (mass of SOA formed per mass of hydrocarbon reacted) of laboratory–generated α–pinene SOA.

Table of Contents

List of Tables

List of Figures

List of Schemes

Chapter 1

Introduction

Organic compounds are an important component of ambient aerosol and contribute significantly (20–90%) to ambient aerosol mass. Organic aerosol are emitted directly from anthropogenic and natural sources (primary organic aerosol, or POA). A significant fraction of organic compounds form from the oxidation of biogenic and anthropogenic VOCs, followed by gas/particle partitioning of semi–volatile organic compounds (secondary organic aerosol, or SOA). Knowing the sources of organic compounds in ambient aerosol requires the knowledge of the composition of ambient aerosol.

The molecular composition of organic compounds in ambient aerosol is remarkably complex. POA are known to have a high degree of chemical heterogeneity. A single VOC can give rise to thousands of different organic compounds because of complex gas–phase and particle–phase oxidation pathways. The aerosol composition continues to change as a result of the gas/particle partitioning of semi–volatile compounds, photochemical processes, and chemical reactions in the particle phase. All these processes can significantly change the aerosol composition before the ambient aerosol are removed from the atmosphere.

Most analytical approaches and aerosol mass spectrometers to date, use ''hard'' ionization methods, such as electron impact ionization, and observe the fragmentation pattern of the ions in order to assign the molecular structure of the compounds. More recently, electrospray ionization (ESI), which is a ''soft'' ionization technique, can convert the molecules into positive or negative ions without significant fragmentation. ESI coupled

with high-resolution mass spectrometers has been shown to be a powerful tool for the identification of organic compounds in both laboratory–generated SOA and ambient aerosol. This thesis demonstrates how the chemical characterization of laboratory–generated SOA and ambient aerosol using mass spectrometric techniques helps us to better understand and predict the formation and composition of SOA in chamber studies and in the atmosphere.

Isoprene is, with the possible exception of methane, the largest source of reduced carbon emitted into the atmosphere (Guenther et al., 2006). SOA formation from isoprene oxidation contributes significantly to the ambient organic aerosol budget. Recently, gas–phase isoprene derived epoxydiols (IEPOX) have been shown to be produced in high yields from the OH–initiated oxidation of isoprene under low–NO_x conditions (Paulot et al., 2009). Reactive uptake of gas–phase IEPOX onto acidified sulfate seed aerosol, demonstrated in laboratory chamber studies, revealed that these compounds are likely a key gas–phase intermediate responsible for the formation of isoprene low–NO_x SOA (Surratt et al., 2010). Additionally, acid–catalyzed ring–opening reactions of IEPOX in the particle–phase are kinetically favorable under typical tropospheric conditions, leading to the formation of known isoprene SOA tracers (e.g., 2–methyltetrols and their corresponding organosulfates) (Minerath et al., 2009). Recent results from laboratory and modeling studies have shown that IEPOX is likely an important precursor to the formation of isoprene SOA in the atmosphere. In Chapter 2, we analyze the fine ambient aerosol collected in downtown Atlanta, GA, and rural Yorkville, GA, during the 2008 August

Mini–Intensive Gas and Aerosol Study (AMIGAS) using gas chromatography/quadrupole mass spectrometry and gas chromatography/time–of–flight mass spectrometry (GC/TOFMS) with prior trimethylsilylation, and investigate the presence of IEPOX in ambient aerosol, together with other previously identified isoprene tracers (i.e., 2–methyltetrols, 2–methylglyceric acid, C_5–alkenetriols, and organosulfate derivatives of 2–methyltetrols). The potential significance of IEPOX as the isoprene SOA precursor in the atmosphere is discussed.

Sesquiterpenes (C_{15}) can be a potential source of ambient SOA (Sakulyanontvittaya et al., 2008). β–caryophyllene is one of the most abundant and reactive sesquiterpenes, with two double bonds (one endocyclic and one exocyclic), and has reactivity towards O_3 and OH (Shu and Atkinson, 1994, 1995). β–caryophyllene also has a high aerosol formation potential (O_3: 5–46%; OH: 17–68%) (Ng et al., 2006; Winterhalter et al., 2009; Li et al., 2010). Using the tracer–to–SOA mass fractions obtained in chamber experiments, β–caryophyllene SOA is estimated to contribute about 1–10% of the atmospheric aerosol organic mass in the southeastern and midwestern United States (Kleindienst et al., 2007). A recent laboratory study has shown that the SOA yields of β–caryophyllene photooxidation are enhanced by increasing aerosol acidity (Offenberg et al., 2009). In Chapter 3, we first investigate the influence of aerosol acidity on the composition of β–caryophyllene SOA using ultra–performance liquid chromatography/electrospray ionization–time–of–flight mass spectrometry and provide chemical evidences to support the acid–enhanced SOA yields. We also analyze the fine ambient aerosol collected in downtown Atlanta, GA, and

rural Yorkville, GA, during 2008 AMIGAS to investigate the presence of β–caryophyllene SOA in ambient aerosol. Based on the mass spectrometric data collected from chamber and field samples, we suggest new chemical tracers for β–caryophyllene SOA.

To date, the description of SOA formation follows from the assumption that SOA comprises a mixture of semi–volatile compounds that partition between the gas and particle phases (Pankow, 2004). In some systems (e.g., α–pinene/O_3 system), a number of compounds can account for a significant fraction of the total mass of SOA (Yu et al., 1999). These major compounds can serve as the surrogates in a product–specific model to represent other chemically similar compounds, and to give a reasonable approximation of gas/particle partitioning of all other compounds. Additionally, the simulated SOA composition may allow a first approximation of the properties of SOA, such as water uptake and cloud condensation nuclei activity. In Chapter 4, a product–specific model is proposed to represent laboratory data on the ozonolysis of α–pinene under dry and dark conditions in the presence of ammonium sulfate seed particles. Representative compounds are chosen to reflect the current understanding of the particle–phase compounds formed in the ozonolysis of α–pinene. The simulated SOA composition, which can be represented by oxygen–to–carbon and hydrogen–to–carbon ratios, is compared with the experimental results. The aerosol composition changes with organic mass loadings, temperatures, and the amount of hydrocarbon precursors reacted can be tracked. The potential application of the product–specific model in predicting the formation and composition of SOA in chamber studies is discussed.

References

Guenther, A., Karl, T., Harley, P., Wiedinmyer, C., Palmer, P. I., and Geron, C.: Estimates of global terrestrial isoprene emissions using MEGAN (Model of Emissions of Gases and Aerosols from Nature), *Atmos. Chem. Phys.*, 6, 3181–3210, 2006.

Kleindienst, T. E., Jaoui, M., Lewandowski, M., Offenberg, J. H., Lewis, C. W., Bhave, P. V., and Edney, E. O.: Estimates of the contributions of biogenic and anthropogenic hydrocarbons to secondary organic aerosol at a southeastern US location, *Atmos. Environ.*, 41, 8288–8300, 2007.

Li, Y. J., Chen, Q., Guzman, M. I., Chan, C. K., and Martin, S. T.: Second–generation products of β–caryophyllene ozonolysis are the dominant contributors to particle mass concentration, *Atmos. Chem. Phys. Discuss.*, 10, 17699–17726, 2010.

Minerath, E. C., Schultz, M. P., and Elrod, M. J.: Kinetics of the reactions of isoprene–derived epoxides in model tropospheric aerosol solutions, *Environ. Sci. Technol.*, 43, 8133–8139, 2009.

Offenberg, J. H., Lewandowski, M., Edney, E. O., Kleindienst, T. E., and Jaoui, M.: Influence of aerosol acidity on the formation of secondary organic aerosol from biogenic precursor hydrocarbons, *Environ. Sci. Technol.*, 43, 7742–7747, 2009.

Pankow, J. F.: An absorption model of the gas aerosol partitioning involved in the formation of secondary organic aerosol, *Atmos. Environ.*, 28, 189–193, 1994.

Paulot, F., Crounse, J. D., Kjaergaard, H. G., Kürten, A., St Clair, J. M., Seinfeld, J. H., and Wennberg, P. O.: Unexpected epoxide formation in the gas–phase photooxidation of isoprene, *Science*, 325, 730–733, 2009.

Sakulyanontvittaya, T., Duhl, T., Wiedinmyer, C., Helmig, D., Matsunaga, S., Potosnak, M., Milford, J., and Guenther, A. Monoterpene and sesquiterpene emission estimates for the United States, *Environ. Sci. Technol.*, 42, 1623–1629, 2008.

Shu Y., and Atkinson, R.: Rate constants for the gas phase reactions of O_3 with a series of terpenes and OH radical formation from the O_3 reactions with sesquiterpenes at 296 ±2 K, *Int. J. Chem. Kinet.*, 26, 1193–1205, 1994.

Shu, Y., and Atkinson, R.: Atmospheric lifetimes and fates of a series of sesquiterpenes, *J. Geophys. Res.–Atmos.*, 100, 7275–7281,1995.

Surratt, J. D., Chan, A. W. H., Eddingsaas, N. C., Chan, M. N., Loza, C. L., Kwan, A. J., Hersey, S. P., Flagan, R. C., Wennberg, P. O., and Seinfeld, J. H.: Reactive intermediates revealed in secondary organic aerosol formation from isoprene, *Proc. Natl. Acad. Sci. USA*, 107, 6640–6645, 2010.

Winterhalter, R., Herrmann, F., Kanawati, B., Nguyen, T. L., Peeters, J., Vereecken, L., and Moortgat, G. K.: The gas–phase ozonolysis of beta–caryophyllene ($C_{15}H_{24}$), Part 1: an experimental study, *Phys. Chem. Chem. Phys.*, 11, 4152–4172, 2009.

Ng, N.L., Kroll, J.H., Keywood, M.D., Bahreini, R., Varutbangkul, V., Flagan, R.C., Seinfeld, J.H., Lee, A., and Goldstein, A.H.: Contribution of first– versus second–

generation products to secondary organic aerosols formed in the oxidation of biogenic hydrocarbons, *Environ. Sci. Technol.*, 40, 2283–2297, 2006.

Yu, J. Z., Cocker, D. R., Griffin, R. J., Flagan, R. C., and Seinfeld, J. H.: Gas–phase ozone oxidation of monoterpenes: Gaseous and particulate products, *J. Atmos. Chem.*, 34, 207–258, 1999.

Chapter 2

Characterization and Quantification of Isoprene–Derived Epoxydiols in Ambient Aerosol in the Southeastern United States*

2.1 Abstract

Isoprene–derived epoxydiols (IEPOX) are identified in ambient aerosol samples for the first time, together with other previously identified isoprene tracers (i.e., 2–methyltetrols, 2–methylglyceric acid, C_5–alkenetriols, and organosulfate derivatives of 2–methyltetrols). Fine ambient aerosol collected in downtown Atlanta, GA, and rural Yorkville, GA, during the 2008 August Mini–Intensive Gas and Aerosol Study (AMIGAS) was analyzed using both gas chromatography/quadrupole mass spectrometry (GC/MS) and gas chromatography/time–of–flight mass spectrometry (GC/TOFMS) with prior trimethylsilylation. Mass concentrations of IEPOX ranged from ~ 1 to 24 ng m^{-3} in the aerosol collected from the two sites. Detection of particle–phase IEPOX in the AMIGAS samples supports recent laboratory results that gas–phase IEPOX produced from the photooxidation of isoprene under low–NO_x conditions is a key precursor of ambient isoprene secondary organic aerosol (SOA) formation. On average, the sum of the mass concentrations of IEPOX and the measured isoprene SOA tracers accounted for about 3% of the organic carbon, demonstrating the significance of isoprene oxidation to the formation of ambient aerosol in this region.

2.2 Introduction

Isoprene (2–methyl–1,3–butadiene, C_5H_8) is the most abundant non–methane hydrocarbon emitted into Earth's atmosphere, with a global source estimated to be 440–660 TgC yr^{-1} (Guenther et al., 2006). Recent field, experimental, and modeling studies

have shown that SOA formation from isoprene oxidation contributes significantly to the ambient organic aerosol budget, affects regional air quality, and impacts global climate (Carlton et al., 2009, and references therein).

Recently, Paulot et al. (2009) reported that gas–phase IEPOX is produced in high yields from the OH–initiated oxidation of isoprene under low–NO_x conditions. Calculations from a chemical transport model, GEOS–Chem, indicated that the mixing ratios of IEPOX in the planetary boundary layer (PBL) over the southeastern United States could reach values as high as 0.5 ppb during the summer, which is consistent with levels observed in preliminary airborne measurements (Paulot et al., 2009). Reactive uptake of gas–phase IEPOX onto acidified sulfate seed aerosol, demonstrated in laboratory chamber studies, revealed that these compounds are likely a key gas–phase intermediate responsible for the formation of isoprene low–NO_x SOA (Surratt et al., 2010). Acid–catalyzed ring–opening reactions of epoxides in the particle phase are kinetically favorable under typical tropospheric conditions (Minerath et al., 2009), leading to the formation of known isoprene SOA tracers (e.g., 2–methyltetrols and their corresponding organosulfates) (Surratt et al., 2010). These compounds have been identified in ambient aerosol (Hallquist et al., 2009 and references therein). Overall, recent results from laboratory and modeling studies have shown that IEPOX is likely an important precursor to the formation of isoprene SOA.

In this chapter, fine ambient aerosol samples were collected in downtown Atlanta, GA, and a rural location in Yorkville, GA, during the 2008 AMIGAS campaign. The AMIGAS campaign was conducted in order to increase understanding of the interactions between biogenic and anthropogenic emissions; specifically, this campaign was designed to address the following questions: (I) How do atmospheric reactions between biogenic and anthropogenic emissions impact the formation of SOA?; (II) What are the mechanisms regulating the chemistry of primary organic aerosol (POA) and SOA, and how do these processes differ between day and night?; (III) Which compounds contribute to the atmospheric nitrogen loading, and how do these ambient nitrogen compounds impact atmospheric chemistry and ensuing air quality? Although the present manuscript does not explicitly address all of the goals (or questions) of the AMIGAS campaign outlined above, especially those related to POA, we chemically characterize and quantify, for the first time, particle–phase IEPOX in ambient aerosol.

In addition to quantifying the aerosol mass concentrations for IEPOX, we also quantify other known isoprene SOA tracers, which include the 2–methyltetrols, C_5–alkenetriols, 2–methylglyceric acid, as well as the organosulfates of the 2–methyltetrols (i.e., hydroxy sulfate esters), to evaluate the correlation between these SOA tracers and gain insight into their potential formation pathways in the atmosphere. It is noted that the detection of particle–phase IEPOX and its known reaction products (i.e., the 2–methyltetrols, organosulfates of the 2–methyltetrols) in ambient aerosol provides direct evidence for the chemical interaction of biogenic emissions and anthropogenic pollutants (i.e., SO_2 or

aerosol acidity) leading to the formation of isoprene SOA. The latter provides direct insights into questions (I) and (II) outlined above for the AMIGAS campaign, especially those related to SOA formation in this region. Additionally, the detection of IEPOX and its known heterogeneous–reaction products is consistent with recent remote sensing data over the southeastern United States that show biogenic volatile organic compounds combine with anthropogenic pollutants to form substantial amounts of SOA (Goldstein et al., 2009).

2.3 Experimental Section

The Southeastern Aerosol Research and Characterization (SEARCH) network served as the operating platform for the 2008 AMIGAS campaign. SEARCH was chosen due to its location in a region experiencing significant biogenic and anthropogenic emissions, and in which an extensive high–quality long–term data set is available (Edgerton et al., 2005, 2006; Hansen et al., 2003). Detailed descriptions of the sampling sites, aerosol sampling, and particle–phase measurements are given by Hansen et al. (2003) and Edgerton et al. (2005, 2006, 2009). Additional instrumentation from numerous research laboratories across the United States were installed for AMIGAS at the urban Atlanta, GA (at Jefferson Street (JST)), and rural Yorkville, GA (YRK), sites, which complemented the ongoing SEARCH measurements at these locations. The AMIGAS campaign was conducted from August 1, 2008, to September 15, 2008. Day (10 AM–6 PM, local time)– and night (10 PM–6 AM, local time)–segregated PM2.5 (particulate matter with an aerodynamic diameter < 2.5 μm) high–volume quartz filter samples (i.e., quartz microfibre, 20.3×25.4 cm, Whatman) were collected daily from both the JST and YRK sites from August 1

through September 10, 2008, which provided significant overlap with other chemical measurements made at each site. A select number of filters (14 from JST and 6 from YRK) were chemically characterized for the present study; these filters were primarily selected based on the high aerosol loadings and carbon–to–sulfur ratio observed during their respective sampling periods. Averaged gas–phase concentrations of O_3, CO, SO_2, and NO_x during the sampling period are given in Table 2.1.

Isoprene SOA was generated from the photooxidation of isoprene under low–NO_x conditions in the presence of acidified sulfate seed aerosol in the Caltech dual indoor 28 m^3 Teflon smog chambers. Details of the experimental protocols have been outlined previously by Surratt et al. (2010). Isoprene SOA was collected onto Teflon filters once the aerosol volume concentration stabilized. Even though organic carbon denuders were not used in the collection of the Teflon filters, our previous chemical ionization mass spectrometry measurements indicate that IEPOX is completely removed from the gas phase in the presence of acidified sulfate seed aerosol before the initiation of filter sampling (Surratt et al., 2010). As a result of the latter, the particle–phase IEPOX measured from the Teflon filters is not a result of the absorption of gas–phase IEPOX to the filters during chamber aerosol sampling. The laboratory–generated isoprene SOA provides the particle–phase IEPOX standard necessary for comparison to the atmospheric samples collected from the AMIGAS campaign.

A 2,3–epoxy–1,4–butanediol (BEPOX) was used as a surrogate standard to quantify the particle–phase IEPOX detected in the atmospheric aerosol. For the BEPOX synthesis, an aqueous solution of 2–butene–1,4–diol (Fluka, purum, ≥ 98.0%) was reacted with H_2O_2 catalyzed by tungstinic acid, followed by removal of water and other impurities (Paulot et al., 2009, Skinner et al., 1958). Nuclear magnetic resonance (i.e., ^{1}H–NMR) study of the final product revealed a purity > 95%. A BEPOX–derived organosulfate was used as a surrogate to quantify the organosulfate derivatives of the 2–methyltetrols. The BEPOX–derived organosulfate was prepared by reacting BEPOX with H_2SO_4 and Na_2SO_4 in aqueous solution. The concentration of the BEPOX–derived organosulfate in the solution was determined by 1H–NMR.

Prior to methanol extraction, the filters were spiked with cis–ketopinic acid as an internal recovery standard; cis–ketopinic acid was chosen since it was not found in the ambient samples and did not overlap with the targeted compounds. The field and laboratory samples were chemically characterized by both GC/TOFMS and GC/MS with prior trimethylsilylation; these techniques were both equipped with an electron ionization (EI) source. A detailed description of the sample preparation protocols and the GC/MS analyses is provided by Surratt et al. (2010). For the GC/TOFMS analyses, the samples were analyzed by an Agilent 6890N gas chromatograph (GC DB–5MS column (30 m × 0.25 mm ID × 0.25 µm thickness)) coupled to a Waters GCT Premier TOF mass spectrometer, allowing for accurate mass measurements (i.e., determination of molecular

formulas) to be obtained for each observed ion. Further operating details of the GC/TOFMS technique can be found in Kautzman et al. (2009).

The GC/TOFMS analysis was conducted to determine the elemental compositions of the fragment ions produced from the trimethylsilylated IEPOX, allowing preparation of a fragmentation scheme for the latter. The GC/MS analysis was conducted to quantify IEPOX, 2–methyltetrols, C_5–alkenetriols, and 2–methylglyceric acid products by using the peak areas derived from the total ion chromatograms (TICs). From the repeated GC/MS measurements of the C4–tetrol and BEPOX standards, the variation in the intensity is about 2–3%. IEPOX has been detected in laboratory–generated isoprene SOA using the GC/MS with prior trimethylsilylation (Surratt et al., 2010). As previously observed by Surratt et al. (2010), the mass spectral fragmentation of BEPOX is quite similar to that of IEPOX, making BEPOX a suitable surrogate standard to quantify particle–phase IEPOX. Although an epoxide could potentially be considered as a labile molecule in the GC/MS analysis, trimethylsilyl derivatives of isoprenoid glycidic ethers containing a 2,3–epoxy–1–ol moiety have been previously observed using GC/MS techniques (Rontani et al., 2001). Additionally, Yu and Jefferies (1997) reported that the epoxy carbonyl products of toluene photooxidation, as well as a commercially available epoxy carbonyl (i.e., 1,2–epoxy–3–cycohexanone) standard, could be successfully derivatized by PFBHA (O–(2,3,4,5,6–pentafluorobenzyl)–hydroxylamine) in an aqueous solution and detected by GC/MS. In combination with the fact that we observe the BEPOX standard, these two prior studies further support the ability of observing epoxides by GC/MS techniques.

During GC/MS analyses, the dehydration of the BEPOX standard to C_4–alkenetriols was not observed in the calibration experiments. The conversion of BEPOX standard to C_4–tetrols was not significant (~ 1% of BEPOX was converted to C_4–tetrols). It is likely that the conversion of IEPOX to 2–methyltetrols and C_5–alkenetriols was not significant in the GC/MS analyses. The laboratory and field blank filters (day and night) were analyzed identically. Isoprene SOA tracers, including IEPOX, were not detected from these blank filters. Organic carbon denuders were not used for the collection of these samples owing to the design of the PM2.5 inlet on the high–volume filter samplers (Tisch Environmental, Cleves, OH), and thus, some fraction of the measured particle–phase IEPOX mass concentration could be partly due to the gas–phase absorption of IEPOX onto the quartz filter media.

Samples were also analyzed by ultra–performance liquid chromatography/electrospray ionization–time–of–flight mass spectrometry (UPLC/ESI–TOFMS) operated in the negative (–) ion mode in order to quantify the organosulfates of the 2–methyltetrols found in the AMIGAS aerosol samples. From the repeated UPLC/ESI–TOFMS measurements of the BEPOX–derived organosulfate standard, the variation in the intensity is about 3%. It should be noted that nitrated organosulfates of isoprene, which are isoprene SOA high–NO_x tracers, and organosulfates of monoterpenes previously characterized by Surratt et al. (2008) were also observed in these samples using the UPLC/(–)ESI–TOFMS technique; however, they will not be discussed in detail.

2.4 Results and Discussion

Quantification and Characterization of IEPOX. Figure 2.1A shows the extracted ion chromatogram (EIC) of *m/z* 262 for two trimethylsilyl derivatives of IEPOX (MW 262) from laboratory–generated isoprene SOA formed under low–NO_x conditions. These two compounds have similar EI mass spectra (Figures 2.1B and 2.1C) as the particle–phase IEPOX recently reported by Surratt et al. (2010). The interpretation of the fragment ions in the EI mass spectra of the trimethylsilylated IEPOX is given in Figure 2.2. The elemental compositions obtained for the fragment ions measured by the GC/TOFMS technique (see Tables 2.2 and 2.3) support the proposed ion structures in the fragmentation scheme. The EI mass spectra obtained for the two chromatographic peaks are very similar, though there are some differences in the relative abundance of *m/z* 147, which is characteristic of the presence of two trimethylsiloxy groups. We thus assign the IEPOX isomers to enantiomeric forms (i.e., threo and erythro) of the same positional isomer, 2,3–epoxy–2–methyl–1,4–butanediol. Furthermore, it is possible to tentatively assign the first– and second–eluting isomers to the threo and erythro forms, respectively, based on the relative abundance of *m/z* 147. The trimethylsilyl derivatives of IEPOX occur as four stereoisomers, i.e., 2R, 3R (threo), 2S,3S (threo), 2S,3R (erythro), and 2R,3S (erythro). The threo and erythro forms have different shapes and will be separated upon GC, while the two stereoisomers of each form will not be separated since they are mirror images. The *m/z* 147 ion points to the presence of two trimethylsiloxy groups in the molecules and can be explained through formation of an ion–neutral complex in which the trimethylsilyl ion (formed by a heterolytic cleavage of an ionized O–Si bond) migrates to a nucleophilic

position in the molecule, i.e., the second trimethylsiloxy group (Byun et al., 1997). This group is closer in the erythro form than in the threo form (Figure 2.3), resulting in an *m/z* 147 ion with the highest relative abundance in the former enantiomeric form. In the case of the threo form, the inner epoxy group acts as a shuttle for the migration of the trimethylsilyl group to the other side of the molecule.

A second structurally informative ion is *m/z* 218, which can be explained by loss of oxirane (C_2H_4O; 44 u) through a rearrangement of a trimethylsilyl group, a fragmentation similar to that reported for trimethylsilyl derivatives of isoprenoid glycidic ethers containing a 2,3–epoxy–1–ol moiety (Rontani et al., 2001). Figure 1d shows the EIC of *m/z* 262 for two trimethylsilyl derivatives of IEPOX found in ambient aerosol collected during the daytime on August 9, 2008, at JST. The chromatographic and EI mass spectral characteristics of these two compounds (Figures 2.1D–F) correspond to that of the trimethylsilylated IEPOX in the laboratory–generated isoprene SOA (Figures 2.1A–C). Based on this comparison, these two compounds are identified as particle–phase IEPOX in the ambient AMIGAS aerosol. The elemental compositions of the major fragment ions in Figures 2.1E and 2.1F are listed in Tables 2.4 and 2.5, respectively, and correspond to those measured in the laboratory–generated isoprene SOA (Tables 2.2 and 2.3).

IEPOX mass concentration. IEPOX was observed in all ambient samples collected in the AMIGAS campaign, except the nighttime sample on September 6, 2008, at YRK. At JST, the mean mass concentration of IEPOX was 8.6 ng m^{-3} (range: 1.2–21 ng m^{-3}) (Table 2.6).

At YRK, the mean concentration of IEPOX was 16 ng m^{-3} (range: 5.3–32 ng m^{-3}). Even though IEPOX is photochemically produced, no distinctive diurnal variation in the mass concentrations was observed, except on September 6, 2008, at JST. It is possible that the lowering of the PBL at night would increase the IEPOX mass concentrations observed on certain days (i.e., August 9 and September 5 at JST, and August 12 at YRK).

The gas–particle partitioning coefficient, K_p, of IEPOX is estimated to be 4.6×10^{-5} m^3 µg^{-1} at 298 K (effective vapor pressure, $c^* \sim 1/K_p \sim 2.2 \times 10^4$ µg m^{-3}), assuming gas–phase IEPOX partitions into a condensed–organic phase consisting of IEPOX only. The vapor pressure of IEPOX is estimated to be 4.5×10^{-6} atm using the group contribution method developed by Pankow and Asher (2008); the epoxide group is represented by the ether group in using this vapor pressure estimation method. Despite uncertainties in the estimated vapor pressures, the partitioning of gas–phase IEPOX into the condensed–organic phase does not likely explain the presence of IEPOX in ambient aerosol under typical organic mass loadings (1–10 µg m^{-3}). For example, Surratt et al. (2010) observed that the mixing ratio of gas–phase IEPOX did not change in the presence of dry ammonium sulfate seed aerosol with an organic mass loading of 1.7 µg m^{-3} in the chamber study.

IEPOX is highly soluble in H$_2$O (Paulot et al., 2009). The Henry's law constant, H, of IEPOX was estimated using the HenryWin v3.2 (USEPA, EPI Suite v4.0). A 1,4–butanediol was chosen as the base compound, the estimated H value of which at 298K ranges from 1.0×10^5 to 5×10^6 M atm^{-1} using a group contribution method (Saxena et al.,

1996). IEPOX is estimated to have a H value ranging from 1.9×10^7 to 9.6×10^8 M atm^{-1} at 298K. Despite the uncertainties, these estimates suggest that the presence of particle–phase IEPOX may be attributable to the absorption into the aqueous phase of preexisting aerosol.   It is noted that once gas–phase IEPOX partitions into the particle phase, depending on the aerosol composition (e.g., aerosol acidity), IEPOX can be hydrolyzed to form isoprene SOA tracers (e.g., 2–methyltetrols and their corresponding hydroxy sulfate esters). The hydrolysis rate of IEPOX is expected to be similar to that of 1,2–epoxy–3,4–dihydroxybutane (k = 0.0012 M^{-1}s^{-1}, 1 M Na_2SO_4/0.2 M D_2SO_4/D_2O solution), which has a lifetime of 7.7 h at pH = 1.5 and a lifetime of 38 days at pH = 4.0 (Minerath et al., 2009). Thus, incompletely reacted IEPOX in the particle phase might explain the presence of IEPOX in ambient aerosol. In fact, Surratt et al. (2010) previously demonstrated that the reactive uptake of gas–phase BEPOX in the presence of acidified sulfate seed aerosol yielded some fraction of incompletely reacted particle–phase BEPOX, as detected by GC/MS.

The mass concentrations of IEPOX are much lower than those of the 2–methyltetrols and the organosulfate derivatives of the 2–methyltetrols (Table 2.6). This is reasonable since IEPOX is a precursor for the formation of these compounds (Surratt et al., 2010). Since epoxide intermediates react more efficiently with H_2SO_4 to form organosulfates than alcohol intermediates (Minerath et al., 2009, Iinuma et al., 2009), formation of the 2–methyltetrols and the organosulfate derivatives of the 2–methyletrols is likely attributed to the acid–catalyzed ring opening of IEPOX followed by the subsequent nucleophilic

addition of H_2O and inorganic sulfate (Surratt et al., 2010). In addition to previously suggested gas–phase oxidation pathways (Claeys et al., 2004), the 2–methyltetrols can form from the heterogeneous reactions of IEPOX as discussed above. The measured 2–methyltetrol concentrations could be influenced by acid–labile derivatives of the 2–methyltetrols, such as sulfate and nitrate esters, and may not be stable upon trimethylsilylation, and as result, a fraction of these derivatives of the 2–methyltetrols may be measured as 2–methyltetrols by GC/MS techniques (Sato, 2008; Surratt et al., 2010).

Daytime and nighttime samples from two sites are combined for correlation analysis, excluding the one sample at YRK (September, 6, 2008, nighttime), in which IEPOX and C_5–alkenetriols were not detected. Despite the limited sample size (N = 15), the correlation between the measured isoprene SOA tracers and IEPOX can be evaluated. As expected, the isoprene SOA tracers are positively correlated with each other, and the degree of correlation between these tracers may give some insight into their formation pathways. IEPOX is well correlated with the 2–methyltetrols ($R^2 = 0.77$), is fairly well correlated with the organosulfates of the 2–methyltetrols ($R^2 = 0.41$), but exhibits a weaker correlation with 2–methylglyceric acid ($R^2 = 0.24$). IEPOX correlates well with the organosulfates of the 2–methyltetrols when considering the two sites separately ($R^2 = 0.85$ at JST and $R^2 = 0.77$ at YRK). Compared to IEPOX, 2–methyglyceric acid shows a weaker correlation with other known isoprene SOA tracers (2–methyltetrols: $R^2 = 0.18$, and organosulfates of 2–methyltetrols: $R^2 = 0.28$). This is likely a result of the fact that IEPOX is a gas–phase precursor for these tracers (Surratt et al., 2010). In addition, 2–methylglyceric acid (and its

corresponding oligoesters) is formed more efficiently from the photooxidation of isoprene under high–NO_x conditions (i.e., high NO_2/NO ratios), while IEPOX is formed more efficiently under low–NO_x conditions (i.e., high HO_2/NO ratios) (Paulot et al, 2009; Surratt et al., 2010). The latter is due to the fact that IEPOX formation occurs only under conditions when RO_2 radicals react primarily with HO_2 rather than with NO (Paulot et al, 2009; Surratt et al., 2010).

Although IEPOX is weakly correlated with C_5–alkenetriols ($R^2 = 0.25$) in the combined dataset, a high correlation between IEPOX and C_5–alkenetriols was observed when considering the two sites separately ($R^2 = 0.98$ at JST and $R^2 = 0.86$ at YRK). During GC/MS analyses, neither the dehydration of the C_4–tetrols into the C_4–alkenetriols nor the dehydration of the BEPOX to the C_4–alkenetriols was detected in the calibration experiments. Consequently, the formation of the C_5–alkenetriols from the dehydration of 2–methyltetrols and IEPOX in the GC/MS analysis is likely not significant. Also, a lower correlation between C_5–alkenetriols and 2–methyltetrols ($R^2 = 0.63$ at JST and $R^2 = 0.80$ at YRK) was observed. It is likely that the C_5–alkenetriols are not artifacts of the GC/MS analysis with trimethylsilylation. Although the formation mechanism of the C_5–alkenetriols is not certain and the sample size is limited, a high correlation between the C_5–alkenetriols and IEPOX in ambient samples suggests that the dehydration of IEPOX in acidic aerosol, as proposed by Wang et al. (2005), is a potential formation pathways of C_5–alkenetriols.

IEPOX is known to be rapidly removed from the gas phase by pre–existing acidified sulfate seed aerosol to form low–NO_x SOA and is likely dissolved into the aqueous phase of the particles. The IEPOX will continuously react in the particle phase once it dissolves into the aqueous phase. Since the filter samples were collected over 8 hr integrated time periods, it does not allow us to correlate the measured particle–phase IEPOX mass concentrations (and its known reaction products) with an estimate of liquid water content of the aerosol or aerosol acidity. Higher–time resolution data would provide more useful insights.

2.5 Conclusions and Atmospheric Implications

Table 2.6 shows the measured mass concentrations of isoprene SOA tracers at two sites. The mean mass concentration of the 2–methyltetrols is 80 ng m^{-3} at JST (range: 24–181 ng m^{-3}) and 141 ng m^{-3} at YRK (range: 17–285 ng m^{-3}). By comparison, Ding et al. (2008) reported that the mass concentration of the 2–methyltetrols, on average, was 55.1 ng m^{-3} with a maximum mass concentration of 467 ng m^{-3} in their 24 hr integrated filter samples of fine ambient aerosol collected at the JST site from May 2004 to April 2005. Isoprene–derived organosulfates have been detected in both laboratory–generated SOA and ambient aerosol collected from the southeastern U. S. (Surratt et al., 2008). Among the isoprene–derived organosulfates, the organosulfates of the 2–methyltetrols usually exhibit the largest UPLC chromatographic peak in daytime samples; however, individual organosulfates have not been quantified owing to the lack of appropriate standards. Using the synthesized BEPOX–derived organosulfate standard, the mass concentration of the organosulfate

derivatives of the 2–methyletrols ranged from 9.6–92 ng m^{-3} at JST and 8.2–61 ng m^{-3} at YRK, levels at which these ambient tracers for isoprene SOA formation are significant components of fine ambient aerosol formed in the southeastern United States. As observed in the laboratory chamber experiments, the oxidation of SO_2 forms sulfuric acid, which provides the hydrogen ions and sulfate ions necessary for the formation of organosulfates in the atmosphere. We detected 2–methylglyceric acid, as well as nitrated organosulfates of isoprene, which are formed from the photooxidation of isoprene in the presence of NOx (Surratt et al., 2007, 2008) and are known as isoprene SOA high–NO_x tracers. This suggests the isoprene SOA is formed via both the low– and high–NO_x pathways. On average, the sum of the mass concentrations of IEPOX and the measured isoprene SOA tracers (2–methyltetrols, C_5–alkenetriols, and 2–methylglyceric acid) were found to account for about 3% and 4% of the organic carbon at JST and YRK, respectively. It is also noted that acid–labile derivatives of the 2–methyltetrols such as sulfate and nitrate esters may not be stable upon trimethylsilylation and may be measured with the GC/TOFMS and GC/MS techniques as 2–methyltetrols (Sato, 2008).

The secondary organic carbon (SOC) contributions from isoprene oxidation can be estimated using the tracer method developed by Kleindienst et al. (2007). Using the tracer concentrations (i.e., 2–methyltetrols and 2–methylglyceric acid) and the laboratory–derived tracer mass fraction (0.155), the mean SOC contributions from isoprene oxidation were estimated to be 0.6 μgC m^{-3} (range: 0.2–1.2 μgC m^{-3}) at JST and 1.0 μgC m^{-3} (range: 0.1–1.9 μgC m^{-3}) at YRK. These values are comparable to those observed by Kleindienst et al.

(2007) from Research Triangle Park, North Carolina, U.S., during August and September, 2003 (mean: 0.7 µgC m^{-3}; range: 0.2 – 1.5 µgC m^{-3}), and are higher than those observed by Kourtchev et al. (2009) from K–puszta, Hungary (mean: 0.28 µgC m^{-3}), and by Hu et al. (2008) from Hong Kong, China, during the summer period (mean: 0.2 µgC m^{-3}; range: 0.01 – 0.81 µgC m^{-3}). Overall, these results suggest that isoprene oxidation is important to the formation of fine ambient aerosol in this region.

2.6 Acknowledgements

2.7 References

Byun, J., Gross, M., George, M., Parees, D. M., Kamzelski, A. Z., Swijter, D. F. H., and Willcox, D. A.: Investigation of group migration in the fragmentation of bis(trimethylsilyl) ethers of diols separated by rigid groups, *J. Mass Spectrom.*, 32, 71–80, 1997.

Carlton, A. G., Wiedinmyer, C., and Kroll, J. H.: A review of Secondary Organic Aerosol (SOA) formation from isoprene, *Atmos. Chem. Phys.*, 9, 4987–5005, 2009.

Claeys, M., et al.: Formation of secondary organic aerosols through photooxidation of isoprene, *Science*, 303, 1173–1176, 2004.

Ding, X., Zheng, M., Yu, L., Zhang, X., Weber, R. J., Yam, B., Russell, A. G., Edgerton, E. S., and Wang, X.: Spatial and seasonal trends in biogenic secondary organic aerosol tracers and water–soluble organic carbon in the Southern United States, *Environ. Sci. Technol.*, 42, 5171–5176, 2008.

Edgerton, E. S., Hartsell, B. E., Saylor, R. D., Jansen, J. J., Hansen, D. A., and Hidy, G. M.: The Southeastern Aerosol Research and Characterization Study: Part 2. Filter–based measurements of fine and coarse particulate matter mass and composition, *J. Air & Waste Manage. Assoc.*, 55, 1527–1542, 2005.

Edgerton, E. S., Hartsell, B. E., Saylor, R. D., Jansen, J. J., Hansen, D. A., and Hidy, G. M.: The Southeastern Aerosol Research and Characterization Study, Part 3: Continuous measurements of fine particulate matter mass and composition, *J. Air & Waste Manage. Assoc.*, 56, 1325–1341, 2006.

Edgerton, E. S., Casuccio, G. S., Saylor, R. D., Lersch, T. L., Hartsell, B. E., Jansen, J. J., and Hansen, D. A.: Measurements of OC and EC in coarse particulate matter in the southeastern United States, *J. Air & Waste Manage. Assoc.*, 59, 78–90, 2009.

Goldstein, A. H., Koven, C. D., Heald, C. L., and Fung, I. Y.: Biogenic carbon and anthropogenic pollutants combine to form a cooling haze over the southeastern United States, *Proc. Natl. Acad. Sci. USA*, 106, 8835–8840, 2009.

Guenther, A., Karl, T., Harley, P., Wiedinmyer, C., Palmer, P. I., and Geron, C.: Estimates of global terrestrial isoprene emissions using MEGAN (Model of Emissions of Gases and Aerosols from Nature), *Atmos. Chem. Phys.*, 6, 3181–3210, 2006.

Hansen, D. A., Edgerton, E. S., Hartsell, B. E., Jansen, J. J., Kandasamy, N., Hidy, G. M., and Blanchard, C. L.: The Southeastern Aerosol Research and Characterization Study: Part 1 – Overview, *J. Air & Waste Manage. Assoc.*, 53, 1460–1471, 2003.

Hallquist, M., Wenger, J. C., Baltensperger, U., Rudich, Y., Simpson, D., Claeys, M., Dommen, J., Donahue, N. M., George, C., Goldstein, A. H., Hamilton, J. F., Herrmann, H., Hoffmann, T., Iinuma, Y., Jang, M., Jenkin, M. E., Jimenez, J. L., Kiendler–Scharr, A., Maenhaut, W., McFiggans, G., Mentel, Th. F., Monod, A., Prevot, A. S. H., Seinfeld, J. H., Surratt, J. D., Szmigielski, R., and Wildt, J.: The formation, properties and impact of secondary organic aerosol: Current and emerging issues, *Atmos. Chem. Phys.*, 9, 5155–5235, 2009.

Hu, D., Bian, Q., Li, T. W. Y., Lau, A. K. H., and Yu, J. Z.: Contributions of isoprene, monoterpenes, β–caryophyllene, and toluene to secondary organic aerosol in Hong Kong during the summer of 2006, *J. Geophys. Res.*, 113, D22206, 2008, doi: 10.1029/2008JD010437.

Iinuma, Y., Böge, O., Kahnt, A., and Herrmann, H.: Laboratory chamber studies on the formation of organosulfates from reactive uptake of monoterpene oxides, *Phys. Chem. Chem. Phys.*, 11, 7985–7997, 2009.

Kautzman, K. E., Surratt, J. D., Chan, M. N., Chan, A. W. H., Hersey, S. P., Chhabra, P. S., Dalleska, N. F., Wennberg, P. O., Flagan, R. C., and Seinfeld, J. H.: Chemical composition of gas– and aerosol–phase products from the photooxidation of naphthalene, *J. Phys. Chem. A*, 114, 913–934, 2009.

Kleindienst, T. E., Jaoui, M., Lewandowski, M., Offenberg, J. H., Lewis, C. W., Bhave, P. V., and Edney, E. O.: Estimates of the contributions of biogenic and anthropogenic hydrocarbons to secondary organic aerosol at a southeastern US location, *Atmos. Environ.*, 41, 8288–8300, 2007.

Kourtchev, I., Copolovici, L., Claeys, M., and Maenhaut, W.: Characterization of atmospheric aerosols at a forested site in Central Europe, *Environ. Sci. Technol.*, 43, 4665–4671, 2009.

Minerath, E. C., Schultz, M. P., and Elrod, M. J.: Kinetics of the reactions of isoprene–derived epoxides in model tropospheric aerosol solutions, *Environ. Sci. Technol.*, 43, 8133–8139, 2009.

Pankow, J. F., and Asher, W. E.: SIMPOL.1: a simple group contribution method for predicting vapor pressures and enthalpies of vaporization of multifunctional organic compounds, *Atmos. Chem. Phys.*, 8, 2773–2796, 2008.

Paulot, F., Crounse, J. D., Kjaergaard, H. G., Kürten, A., St Clair, J. M., Seinfeld, J. H., and Wennberg, P. O.: Unexpected epoxide formation in the gas–phase photooxidation of isoprene, *Science*, 325, 730–733, 2009.

Rontani, J.–F., Rabourdin, A., and Aubert, C.: Electron ionization mass spectral fragmentation of some isoprenoid glycidic ethers, *Rapid Commun. Mass Spectrom.*, 15, 2091–2095, 2001.

Sato, K.: Detection of nitrooxypolyols in secondary organic aerosol formed from the photooxidation of conjugated dienes under high–NO_x conditions, *Atmos. Environ.*, 42, 6851–6861, 2008.

Saxena, P., and Hildemann, L. M.: Water–soluble organics in atmospheric particles: A critical review of the literature and application of thermodynamics to identify candidate compounds, *J. Atmos. Chem.*, 24, 57–109, 1996.

Skinner, J. R., Wilcoxen, C. H., and Carlson, G. J.: *Production of epoxides*. United States Patent Office, 1958, no. 2,833,788.

Surratt, J. D., et al.: Evidence for organosulfates in secondary organic aerosol, *Environ. Sci. Technol.*, 41, 517–527, 2007.

Surratt, J. D., et al.: Organosulfate formation in biogenic secondary organic aerosol, *J. Phys. Chem. A*, 112, 8345–8378, 2008.

Surratt, J. D., Chan, A. W. H., Eddingsaas, N. C., Chan, M. N., Loza, C. L., Kwan, A. J., Hersey, S. P., Flagan, R. C., Wennberg, P. O., and Seinfeld, J. H.: Reactive intermediates revealed in secondary organic aerosol formation from isoprene, *Proc. Natl. Acad. Sci. USA*, 107, 6640–6645, 2010.

U.S. Environmental Protection Agency, *EPI Suite v4.0.* Available at http://www.epa.gov/opptintr/exposure/pubs/episuitedl.htm.

Wang, W., Kourtchev, I., Graham, B., Cafmeyer, J., Maenhaut, W., and Claeys, M.: Characterization of oxygenated derivatives of isoprene related to 2–methyltetrols in Amazonian aerosols using trimethylsilylation and gas chromatography/ion trap mass spectrometry, *Rapid Commun. Mass Spec.*, 19, 1343–1351, 2005.

Yu, J. Z., and Jefferies, H. E.: Atmospheric photooxidation of alkylbenzenes – II. Evidence of formation of epoxide intermediates, *Atmos. Environ.*, 31, 2281–2287, 1997.

Table 2.1: Averaged gas–phase concentrations in downtown Atlanta, GA (JST) and a rural location in Yorkville, GA (YRK) during the 2008 AMIGAS campaign [a]

	JST									
Sampling date	August 9, 2008		August 24, 2008 to August 26, 2008 (Rain period)[b]		September 3, 2008		September 5, 2008		September 6, 2008	
	Day	Night	Day	Night	Day	Night	Day	Night	Day	Night
O_3	76	16	22	12	60	7.8	56	0.2	45	10
CO	191	392	164	131	187	549	161	668	165	216
SO_2	2.4	3.2	1.0	1.0	1.4	2.3	0.6	3.0	16	0.3
NO	0.7	2.0	4.5	3.6	2.6	35	1.1	43	0.5	0.7
NO_2	3.6	28	9.4	7.7	9.2	30	5.0	36	4.0	12

	YRK					
Sampling date	August 12, 2008		August 13, 2008		September 6, 2008	
	Day	Night	Day	Night	Day	Night
O_3	51	34	60.2	21	39	13
CO	188	235	186	185	146	155
SO_2	3.5	1.3	7.2	0.5	1.0	0.1
NO	0.6	0.0	0.2	0.2	0.2	0.1
NO_2	3.5	4.4	0.8	1.9	0.6	1.6

[a] Averaged gas–phase concentrations are reported in ppb. [b] For the rain period, averaged gas–phase concentrations are reported from August 24, 2008, to August 26, 2008.

Table 2.2: The major fragment ions observed in the EI mass spectrum of trimethylsilylated IEPOX formed from the photooxidation of isoprene in the presence of acidified sulfate seed aerosol under low–NO_x conditions at retention time (RT) = 23.23 min (Figure 2.1B)

Measured mass	Calculated mass	Formula	mDa
262.1418	262.1421	$C_{11}H_{26}O_3Si_2$	–0.3
218.1147	218.1158	$C_9H_{22}O_2Si_2$	–1.1
147.0663	147.0661	$C_5H_{15}OSi_2$	0.2
131.0896	131.0892	$C_6H_{15}OSi$	0.4
130.0808	130.0814	$C_6H_{14}OSi$	–0.6
117.0722	117.0736	$C_5H_{13}OSi$	–1.4
116.0656	116.0657	$C_5H_{12}OSi$	–0.1
101.0427	101.0423	C_4H_9OSi	0.4

Table 2.3: The major fragment ions observed in the EI mass spectrum of trimethylsilylated IEPOX formed from the photooxidation of isoprene in the presence of acidified sulfate seed aerosol under low–NO_x conditions at RT = 23.73 min (Figure 2.1C)

Measured mass	Calculated mass	Formula	mDa
262.1414	262.1421	$C_{11}H_{26}O_3Si_2$	–0.7
248.1145	218.1158	$C_9H_{22}O_2Si_2$	–1.3
147.0655	147.0661	$C_5H_{15}OSi_2$	–0.6
131.0873	131.0892	$C_6H_{15}OSi$	–1.9
130.0811	130.0814	$C_6H_{14}OSi$	–0.3
117.0733	117.0736	$C_5H_{13}OSi$	–0.3
116.0659	116.0657	$C_5H_{12}OSi$	0.2
101.0426	101.0423	C_4H_9OSi	0.3

Table 2.4: The major fragment ions observed in the EI mass spectrum of trimethylsilylated IEPOX in fine atmospheric aerosol collected during the daytime on August 9, 2008 at JST at RT = 23.35 min (Figure 2.1E)

Measured mass	Calculated mass	Formula	mDa
262.1408	262.1421	$C_{11}H_{26}O_3Si_2$	–1.3
218.1133	218.1158	$C_9H_{22}O_2Si_2$	–2.5
147.0676	147.0661	$C_5H_{15}OSi_2$	1.5
131.0923	131.0892	$C_6H_{15}OSi$	3.1
130.0810	130.0814	$C_6H_{14}OSi$	–0.4
117.0725	117.0736	$C_5H_{13}OSi$	–1.1
116.0657	116.0657	$C_5H_{12}OSi$	0
101.0424	101.0423	C_4H_9OSi	0.1

Table 2.5: The major fragment ions observed in the EI mass spectrum of trimethylsilylated IEPOX in fine atmospheric aerosol collected during the daytime on August 9, 2008 at JST at RT = 23.86 min (Figure 2.1F)

Measured mass	Calculated mass	Formula	mDa
262.1436	262.1421	$C_{11}H_{26}O_3Si_2$	1.5
218.1127	218.1158	$C_9H_{22}O_2Si_2$	−3.1
147.0663	147.0661	$C_5H_{15}OSi_2$	0.2
131.0921	131.0892	$C_6H_{15}OSi$	2.9
130.0830	130.0814	$C_6H_{14}OSi$	1.6
117.0722	117.0736	$C_5H_{13}OSi$	−1.4
116.0652	116.0657	$C_5H_{12}OSi$	−0.5
101.0422	101.0423	C_4H_9OSi	−0.1

Table 2.6: Ambient aerosol mass concentrations of IEPOX and of isoprene SOA tracers in fine atmospheric aerosol collected in downtown Atlanta, GA (JST) and a rural location in Yorkville, GA (YRK) during the 2008 AMIGAS campaign [a]

	JST									
Sampling date	August 9, 2008		August 24, 2008 to August 26, 2008 (Rain period)[b]		September 3, 2008		September 5, 2008		September 6, 2008	
	Day	Night	Day	Night	Day	Night	Day	Night	Day	Night
IEPOX[c]	13	21	1.6	1.2	14	13	3.2	4.9	12	1.5
2–methyltetrols[d,f]	95	136	43	32	144	88	24	27	181	29
C_5–alkenetriols[e,f]	135	206	17	14	153	152	32	46	109	23
2–methylglyceric acid[f]	15	10	3.4	1.9	18	6.3	8.9	5.1	12	4.1
Organosulfates of 2–methyltetrols[g]	91	86	13	9.6	79	92	33	41	68	29
Organic Carbon (OC)[h]	7.0	9.4	2.7	1.6	6.5	7.8	5.0	8.1	6.6	4.6
$PM_{2.5}$ [h]	14.8	23.0	5.4	3.2	13.7	15.0	8.3	14.1	21.9	6.9
∑Tracers/OC[i]	3.7	4.0	2.4	3.1	5.1	3.3	1.4	1.0	4.8	1.3
SOC[j]	0.7	0.9	0.3	0.2	1.1	0.6	0.2	0.2	1.2	0.2

	YRK					
Sampling date	August 12, 2008		August 13, 2008		September 6, 2008	
	Day	Night	Day	Night	Day	Night
IEPOX[c]	10	18	32	16	5.3	n.d.
2–methyltetrols[d,f]	70	144	285	233	97	17
C_5–alkenetriols[e,f]	22	47	59	45	20	n.d.
2–methylglyceric acid[f]	12	18	7.9	10	7.1	3.4
Organosulfates of 2–methyltetrols[g]	30	42	61	56	25	8.2
Organic Carbon (OC)[h]	5.9	5.0	6.5	4.4	4.9	1.5
$PM_{2.5}$ [h]	13.8	20.5	33.4	26.3	13.2	5.1
∑Tracers/OC[i]	1.9	4.5	5.9	6.9	2.6	1.3
SOC[j]	0.5	1.0	1.9	1.6	0.7	0.1

[a] The aerosol mass concentrations are reported in ng m^{-3}, n.d.: not detected. [b] For the rain period, the samples from August 24, 2008, to August 26, 2008, were combined for the analysis. [c] The concentration of IEPOX is the sum of the concentrations of the two enantiomeric forms (threo and erythro) of of IEPOX (2,3–epoxy–2–methyl–1,4–butanediol) and was determined by using the response factor of BEPOX. [d] The concentration of the 2–methyltetrols is the sum of the concentrations of 2–methylthreitol and 2–methylerythritol. [e] The concentration of the C_5–alkenetriols is the sum of the concentrations of three isomers of C_5–alkenetriols. [f] The concentration of the 2–methyltetrols, C_5–alkenetriols and 2–methylglyceric acid were determined using the response factor of meso–erythritol. [g] The concentration of the organosulfates of the 2–methyltetrols was determined by using the response factor of the BEPOX–derived organosulfate standard. [h] The concentration of organic carbon and $PM_{2.5}$ is reported in μg m^{-3}. Averaged organic carbon and $PM_{2.5}$ concentrations are reported for the rain period. [i] Percentage of the sum of the mass concentrations of IEPOX, 2–methyltetrols, C_5–alkenetriols, and 2–methylglyceric acid to the organic carbon. [j] The concentration of SOC is reported in μgC m^{-3}. The SOC contributions from isoprene oxidation were estimated using the tracer method developed by Kleindienst et al. (2007).
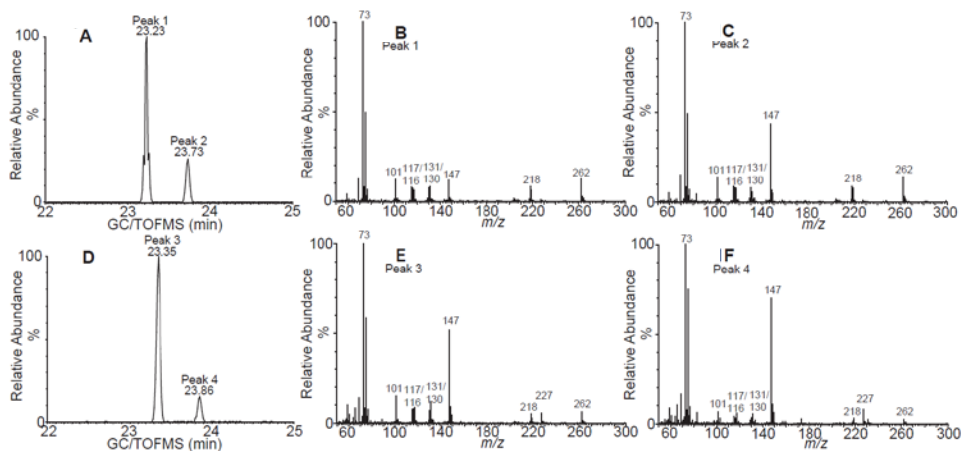
Figure 2.1: GC/TOFMS data for trimethylsilylated IEPOX (MW 262): (A) EIC of *m/z* 262 for particle–phase IEPOX formed from the photooxidation of isoprene under low–NO$_x$ conditions in the presence of acidified sulfate seed aerosol, (B) EI mass spectrum for the chromatographic peak at retention time (RT) = 23.23 min, (C) EI mass spectrum for the chromatographic peak at RT = 23.73 min, (D) EIC of *m/z* 262 for IEPOX detected during the daytime on August 9, 2008 at the JST site, (E) EI mass spectrum for the chromatographic peak at RT = 23.35 min, (F) EI mass spectrum for the chromatographic peak at RT = 23.86 min. The ion at *m/z* 227 in the mass spectra obtained for the ambient sample (E and F) is most likely due to coelution from an interfering compound.
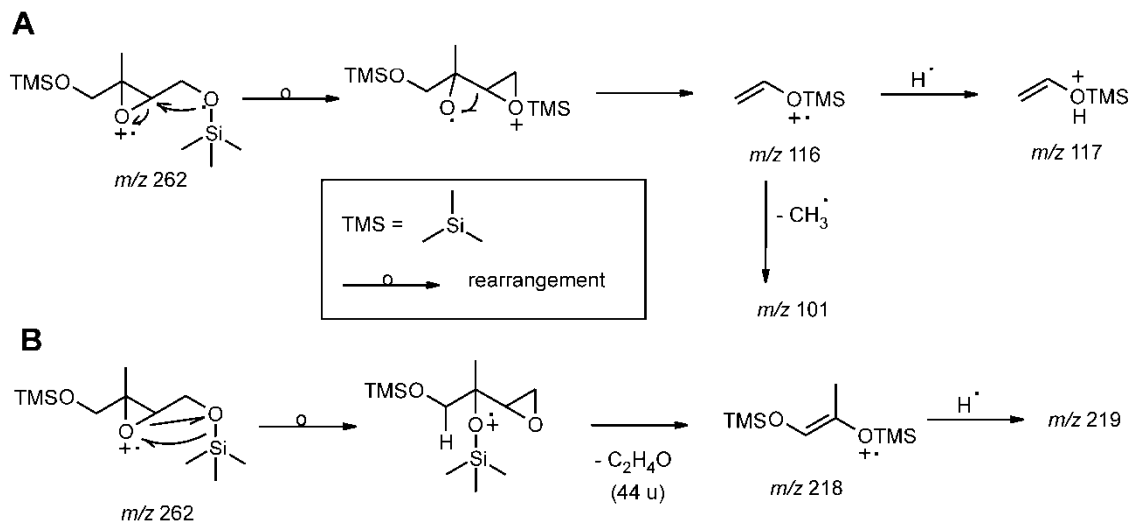
Figure 2.2: Proposed fragmentation pathways of trimethylsilylated 2,3–epoxy–2–methyl–1,4–butanediol (threo and erythro forms) upon electron ionization–mass spectrometry. The same reactions at the other side of the molecular ion lead to the *m/z* 131, 130, and 115 ions in the case of pathway (A) and to the very minor *m/z* 204 ion in the case of pathway (B).
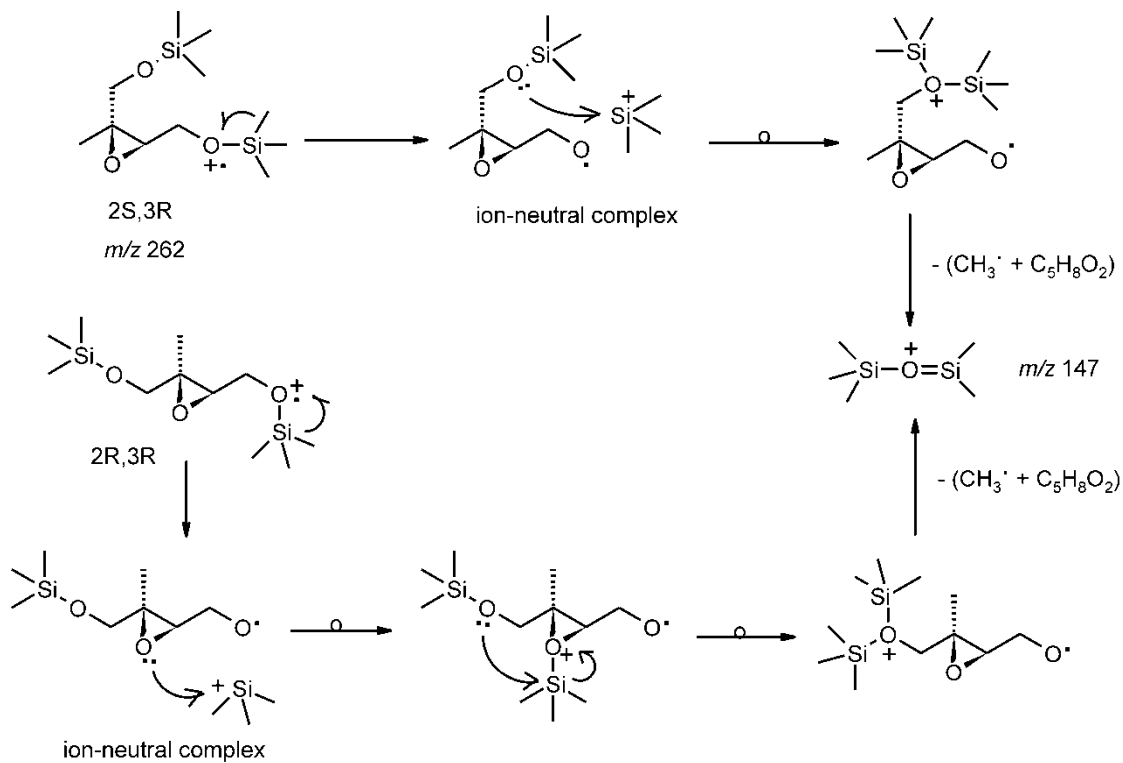
Figure 2.3: Proposed formation of the *m/z* 147 ion in the EI mass spectra of the trimethylsilyl derivatives of the erythro and threo forms of 2,3–epoxy–2–methyl–1,4–butanediol

Chapter 3

Influence of Aerosol Acidity on the Chemical Composition of Secondary Organic Aerosol from β–caryophyllene*

3.1 Abstract

The secondary organic aerosol (SOA) yield of β–caryophyllene photooxidation is enhanced by aerosol acidity. In the present study, the influence of aerosol acidity on the chemical composition of β–caryophyllene SOA is investigated using ultra–performance liquid chromatography/electrospray ionization–time–of–flight mass spectrometry (UPLC/ESI–TOFMS). A number of first– , second–, and higher–generation gas–phase products having carbonyl and carboxylic acid functional groups are detected in the particle phase. Particle–phase reaction products formed via hydration and organosulfate formation processes are also detected. Increased acidity leads to different effects on the abundance of individual products; significantly, abundances of organosulfates are correlated with aerosol acidity. To our knowledge, this is the first detection of organosulfates and nitrated organosulfates derived from a sesquiterpene. The increase of certain particle–phase reaction products with increased acidity provides chemical evidence to support the acid–enhanced SOA yields. Based on the agreement between the chromatographic retention times and accurate mass measurements of chamber and field samples, three β–caryophyllene oxidation products (i.e., β–nocaryophyllon aldehyde, β–hydroxynocaryophyllon aldehyde, and β–dihydroxynocaryophyllon aldehyde) are suggested as chemical tracers for β–caryophyllene SOA. These compounds are detected in both day and night ambient samples collected in downtown Atlanta, GA, and rural Yorkville, GA, during the 2008 August Mini–Intensive Gas and Aerosol Study (AMIGAS).

3.2 Introduction

Secondary organic aerosol (SOA) formation from the oxidation of biogenic precursors, such as isoprene (C_5H_8), monoterpenes ($C_{10}H_{16}$), sesquiterpenes ($C_{15}H_{24}$), and oxygenated terpenes, contributes significantly to atmospheric aerosol mass (Hallquist et al., 2009 and references therein). β–caryophyllene ($C_{15}H_{24}$) is one of the most reactive sesquiterpenes, with two double bonds (one endocyclic and one exocyclic), and has reactivity toward ozone (O_3), hydroxyl radicals (OH), and nitrate radicals (NO_3). Shu and Atkinson (1994, 1995) estimated that under typical tropospheric conditions the lifetime of β–caryophyllene with respect to O_3 and OH reaction is 2 min and 53 min, respectively. β–caryophyllene also has a high aerosol formation potential (Griffin et al., 1999; Jaoui et al., 2003; Lee et al., 2006ab; Ng et al., 2006; Winterhalter et al., 2009; Li et al., 2010). A range of aerosol yields (mass of SOA formed per mass of hydrocarbon reacted) has been reported (O_3: 5–46%; OH: 17–68%), depending on the aerosol organic mass and experimental conditions.

Particle–phase products of β–caryophyllene ozonolysis have been extensively studied in the presence or absence of ammonium sulfate ((NH_4)$_2SO_4$) seed particles. A number of first–generation ozonolysis products, such as aldehydes (e.g., β–caryophyllon aldehyde and β–hydroxycaryophyllon aldehyde) and acids (e.g., β–caryophyllonic acid and β–caryophyllinic acid), have been identified (Calogirou et al. 1997; Jaoui et al. 2003; Kanawati et al., 2008; Winterhalter et al. 2009; Li et al. 2010). Ng et al. (2006) observed continued aerosol growth after all β–caryophyllene was consumed in ozonolysis and photooxidation experiments, demonstrating the importance of second– or higher–

generation reactions. More recently, Li et al. (2010) showed that first–generation ozonolysis products, which still contain a double bond, can be oxidized to second–generation ozonolysis products (e.g., β–nocaryophyllon aldehyde and β–hydroxynocaryophyllon aldehyde), which represent a larger contribution to the SOA mass than first–generation ozonolysis products. β–caryophyllinic acid has been detected in both chamber and ambient aerosol samples and has been suggested as a tracer for β–caryophyllene SOA (Jaoui et al., 2007). Using the tracer–to–SOA mass fractions obtained in laboratory chamber experiments, β–caryophyllene SOA is estimated to contribute about 1–10% of the atmospheric aerosol organic mass in the southeastern and midwestern United States (Kleindienst et al., 2007).

Chamber studies have shown that increasing aerosol acidity enhances SOA formation from the oxidation of certain biogenic hydrocarbons such as isoprene, α–pinene, and β–pinene (Kroll and Seinfeld, 2008, and references therein). Acid–catalyzed reactions (e.g., hydration, esterification, hemiacetal/acetal formation, aldol condensation) leading to the formation of higher molecular–weight compounds have been proposed to explain the enhanced SOA yields (Jang et al., 2002). When the acidity is provided by sulfuric acid (H_2SO_4), sulfate esters (or organosulfates) can form (Liggio and Li, 2006; Surratt et al., 2007ab, 2008; Iinuma et al., 2009). By comparing mass spectrometric measurements for both laboratory–generated and ambient aerosol, Iinuma et al. (2007) and Surratt et al. (2007ab, 2008) have reported the presence of organosulfates derived from isoprene, α–pinene, β–pinene, and limonene–like monoterpenes (e.g., myrcene) in ambient aerosol.

SOA yields are enhanced by aerosol acidity in the photooxidation of mixtures of β–caryophyllene/NO_X (Offenberg et al. 2009). In this chapter, the influence of aerosol acidity on the chemical composition of β–caryophyllene SOA from β–caryophyllene photooxidation is investigated using ultra–performance liquid chromatography/electrospray ionization–time–of–flight mass spectrometry (UPLC/ESI–TOFMS). Certain β–caryophyllene reaction products are shown to serve as tracers for the identification of β–caryophyllene SOA in ambient aerosol collected in downtown Atlanta (at Jefferson Street (JST)), GA and rural Yorkville (YRK), GA during the 2008 August Mini–Intensive Gas and Aerosol Study (AMIGAS).

3.3 Experimental Section

β–caryophyllene/NO_X irradiation experiments in the presence of seed aerosol of varying acidity were carried out in a 14.5 m^3 fixed volume Teflon–coated reaction chamber at 297 K and 30% RH. Details of the experiments have been given in Offenberg et al. (2009). Initial aerosol acidity was controlled by nebulizing dilute aqueous $(NH_4)_2SO_4$ /H_2SO_4 solutions. To change the acidity of the seed aerosol, the ratio of the two liquids was changed to produce a constant aerosol sulfate concentration of 30 µg m^{-3} across the range of resulting acidities. The reaction chamber was operated as a continuous stirred tank reactor, having a residence time of 6 h, to produce a constant, steady–state aerosol distribution. For the aerosol acidity measurement, filters were extracted by sonication for 30 min using 10 mL of distilled, deionized water in a 50 mL polypropylene vial. Once the extract cooled to room temperature, the pH of each extract was measured with a Mettler–

Toledo MP220 pH meter using an InLab 413 pH electrode. Aerosol acidity is expressed as the hydrogen ion air concentrations ($[H^+]_{air}$), which were calculated by dividing the measured aqueous concentration of the hydrogen ion by the volume of air collected. Table 3.1 summarizes the steady–state concentrations of gas–phase species, aerosol acidity, and secondary organic carbon (SOC) for the experiments.

For the chemical analysis, aerosol was collected on Teflon impregnated glass fiber filters (Pall Gelman Laboratory, 47 mm diameter, Teflon impregnated). To collect sufficient aerosol mass for the analysis, about 0.7–1.0 mg was collected on each filter and the sampling air volume was about 15.4–16.3 m^3. One–half of each filter was extracted with methanol (LC–MS CHROMASOLV–grade, Sigma–Aldrich) under ultrasonication for 45 min. The extract was dried under ultra–pure nitrogen gas, and the residue was reconstituted with a 50:50 (v/v) solvent mixture of methanol with 0.1% acetic acid (LC–MS CHROMASOLV–grade, Sigma–Aldrich) and water with 0.1% acetic acid (LC–MS CHROMASOLV–grade, Sigma–Aldrich). Day (10 AM–6 PM, local time)– and night (10 PM–6 AM, local time)–segregated PM$_{2.5}$ (particulate matter with an aerodynamic diameter < 2.5 μm) high–volume quartz filter samples (i.e., quartz microfibre, 20.3 × 25.4 cm, Whatman) were collected from JST and YRK sites during the 2008 AMIGAS campaign and were analyzed for the presence of β–caryophyllene SOA constituents. Details of the 2008 AMIGAS campaign, filter collection, and sample preparation procedures are given by Chan et al. (2010). Both chamber and field sample extracts were analyzed by UPLC/ESI–TOFMS operated in both positive and negative ion modes. Details of the UPLC/ESI–

TOFMS analysis have been given in Surratt et al. (2008). All accurate mass measurements were within +/–5 mDa of the theoretical mass associated with the proposed chemical formula for each observed ion. Owing to the lack of authentic standards or suitable surrogates, concentrations are reported as the sum of the UPLC chromatographic peak area of the ions normalized by the volume of air collected. From repeated UPLC/ESI–TOFMS measurements, the variations in the chromatographic peak areas are about 5%. The concentrations are not corrected for extraction efficiencies.

3.4 Results and Discussion

Gas– and particle–phase reactions. In the series of β–caryophyllene photooxidation experiments, β–caryophyllene and its gas–phase products react with O_3 and OH in the presence of NO_x. Rate constants (296 K) for the reaction of β–caryophyllene with O_3 (k_{O3} = 1.16×10^{-14} cm^3 $molecule^{-1}s^{-1}$) and OH (k_{OH} = 1.97×10^{-10} cm^3 $molecule^{-1}s^{-1}$) have been reported by Shu and Atkinson (1994, 1995). At steady state in the reaction chamber, the O_3 level was 24–29 ppb (5.93×10^{11} – 7.16×10^{11} molecules cm^{-3}) (Table 3.1). The OH concentration in the chamber was not directly measured. At an assumed OH level of 10^6 molecules cm^{-3}, the ratio of the rates of β–caryophyllene reaction with O_3 to OH at the O_3 levels in the reaction chamber is about 36. β–caryophyllene ozonolysis is therefore likely the dominant reaction pathway in the first oxidization step. The two double bonds of β–caryophyllene have different reactivity with respect to O_3. Nguyen et al. (2009) predicted that the rate coefficient for O_3 attack on the exocyclic double bond is less than 5% of that for O_3 attack on the endocyclic double bond. Thus, addition of O_3 to the

endocyclic double bond is likely the dominant reaction of β–caryophyllene with O_3. Since O_3 and OH are in excess relative to β–caryophyllene in the reaction chamber, the remaining double bond (either exocyclic or endocyclic) of the first–generation products undergoes a second ozonolysis or reacts with OH, leading to second– or higher–generation products. Based on an average rate coefficient for the ozonolysis of the first–generation products ($k_{O3} = 1.1 \times 10^{-16}$ cm^3 molecule^{-1}s^{-1}) reported by Winterhalter at al. (2009) at 295 K, the average lifetime of the first–generation products with respect to ozonolysis is about 3.5 to 4.2 h. Rate coefficients for the photooxidation of the first–generation products have not been reported. If the rate coefficient for the photooxidation of β–caryophyllene is used ($k_{OH} = 1.97 \times 10^{-10}$ cm^3 molecule^{-1}s^{-1}), as an approximation, the average lifetime of the first–generation products with respect to photooxidation is about 1.4 h at an OH level of 10^6 molecules cm^{-3}. Thus, the first–generation products can be further oxidized in the gas phase at the residence time in the reaction chamber.

The gas–phase chemistry of β–caryophyllene in our system involves OH, O_3, and NO_x. For clarity and simplicity, we focus on the reactions of the first–generation products of β–caryophyllene in the gas and particle phases, leading to particle–phase products detected by UPLC/ESI–TOFMS (Scheme 3.1). Formation mechanisms of β–caryophyllon aldehyde, β–hydroxycaryophyllon aldehyde, β–oxocaryophyllon aldehyde, and β–norcaryophyllon aldehyde from the photooxidation and ozonolysis of β–caryophyllene have been proposed (Jaoui et al., 2003; Lee et al., 2006ab; Winterhalter et al., 2009; Li et al., 2010). Additionally, ring–retaining compounds can form (Jaoui et al., 2003; Lee et al., 2006b). For

example, β–caryophyllene oxide can form from the reaction of β–caryophyllene with O_3 similar to α–pinene oxide formation (Iinuma et al., 2009) and has been detected in both gas– and particle phases in the ozonolysis of β–caryophyllene (Jaoui et al. 2003). β–caryophylla ketone can form from β–caryophyllene reaction with O_3 or OH at its exocyclic double bond (Jaoui et al., 2003; Lee et al., 2006b). The first–generation ring–retaining compounds, which contain an unreacted double bond, can be further oxidized before partitioning to the particle phase.

Schemes 3.2 – 3.5 show the further oxidation of the first–generation products, leading to compounds detected by ESI in the particle phase. In the presence of excess O_3 and OH, it can be assumed that the remaining double bond (exocyclic double bond) of the gas–phase products will be rapidly oxidized. Reaction of gas–phase products with O_3 generally proceeds via four channels: stabilized Criegee intermediates (CIs), isomerization, hydroperoxide, and ester channels. Detailed reaction mechanisms for these channels have been given by Jaoui et al. (2003), Winterhalter et al. (2009), and Li et al. (2010). Stabilized CIs and hydroperoxide channels are considered to explain the formation of detected compounds. The stabilized CIs can react with H_2O, NO_2, and carbonyls. The stabilized CIs channel (SCI) here refers to the reaction between the stabilized CIs and H_2O or NO_2 to form carbonyls. For example, β–caryophyllon aldehyde and β–caryophyllonic acid undergo oxidation by O_3 on their exocyclic double bond, forming β–nocaryophyllon aldehyde and β–nocaryophyllonic acid (Scheme 3.2). The stabilized CIs can react with carbonyls to form secondary ozonides (SOZ). Winterhalter et al. (2009) have detected the presence of SOZ in

the particle phase using Fourier transform infrared spectroscopy in their β–caryophyllene ozonolysis experiments. SOZ were not detected in the particle phase in the present study. It is possible that SOZ may decompose to form organic acids in the particle phase under acidic conditions (or during the analytical procedure) (Winterhalter et al. 2009). For the hydroperoxide channel, the CIs can rearrange via a 1,4–hydrogen shift to a vinyl hydroperoxide, which can subsequently form hydroxyl carbonyls and dicarbonyls (Winterhalter et al., 2009). The hydroperoxide channel refers to the formation of hydroxyl carbonyls. For example, β–caryophyllon aldehyde undergoes oxidation by O_3 on the exocyclic double bond forming β–hydroxynocaryophyllon aldehyde (Scheme 3.2).

The OH reaction with the exocyclic double bond of the gas–phase products forms alkyl radicals, followed by rapid addition of O_2 to yield peroxy radicals. In the presence of NO_x, peroxy radicals react with NO to form either alkoxy radicals plus NO_2 or organic nitrates. Alkoxy radicals can also form from the reactions between peroxy radicals. Alkoxy radicals can decompose, isomerize or react with O_2. Here, alkoxy radicals are considered to undergo decomposition to produce a carbonyl and an alkyl radical ($CH_2OH\cdot$). For example, β–nocaryophyllon aldehyde can form from the reaction of β–caryophyllon aldehyde with OH at its exocyclic double bond (Scheme 3.2). Many gas–phase products have an aldehyde group. An aldehydic hydrogen atom can be abstracted by OH to produce an acyl radical, which rapidly adds O_2 to yield an acyl peroxy radical. The reaction of acyl peroxy radicals with HO_2 forms carboxylic acid (Winterhalter et al., 2009). The acyl peroxy radicals can also react with NO and subsequently undergo decomposition or can

react with NO_2 in the presence of NO_X to form peroxyacyl nitrates. The reaction of acyl peroxy radicals with HO_2 to form carboxylic acid may explain the formation of acids detected in the particle phase. For example, acyl peroxy radicals formed from the aldehydic hydrogen abstraction of β–caryophyllon aldehyde can react with HO_2 to form β–caryophyllonic acid (Scheme 3.2). However, it cannot be ruled out that the acids can form via other reaction pathways in the gas and particle phases. The OH abstraction of secondary or tertiary hydrogen may also occur (Jaoui et al., 2003) but is not considered here. Once the gas–phase products partition into the particle phase, they may undergo further chemical reactions. Reaction products formed via hydration and organosulfate formation have been detected in the particle phase, as discussed below.

Particle–phase β–caryophyllene products. Tables 3.2 – 3.5 summarize the compounds detected by UPLC/ESI–TOFMS in both positive and negative ion modes in the series of β–caryophyllene/NO_X irradiation experiments. Proposed chemical structures are derived from accurate mass measurements, proposed reaction pathways, and previously identified chemical structures reported in the literature (Jaoui et al. 2003; Kanawati et al., 2008; Winterhalter et al. 2009; Li et al. 2010). Table 3.2 shows the compounds detected by ESI in the positive ion mode. Products having carbonyl groups can be ionized via proton attachment to form $[M+H]^+$ ions and are detected in the positive ion mode (Kanawati et al., 2008). Adducts with sodium $[M+Na]^+$ and with methanol + sodium $[M+CH_3OH+Na]^+$ are used for redundant determination of the chemical formulas of the products (Li et al., 2010). Recently, Parshintsev et al. (2008) have synthesized β–caryophyllene aldehyde and β–

nocaryophyllone aldehyde. They reported that sodium adduct ions were the most abundant ions in their accurate mass measurements using ESI–TOF and could be used for identification and quantification of these two compounds in the aerosol samples by liquid chromatography–mass spectrometry. First–generation products (e.g., β–hydroxycaryophyllon aldehyde) and second–generation products (e.g., β–nocaryophyllon aldehyde, β–hydroxynocaryophyllon aldehyde, and β–dihydroxynocaryophyllon aldehyde) are detected in the particle phase.

Table 3.3 shows the compounds detected by ESI in negative ion mode. Products having a carboxylic acid group can be ionized via deprotonation and are detected in the negative ion mode as [M–H]$^-$ ions. Several acids detected such as β–caryophyllonic acid, β–caryophyllinic acid, β–nocaryophyllonic acid, β–hydroxycaryophyllonic acid, β–hydroxynocaryophyllonic acid, and β–oxocaryophyllonic acid have been reported (Jaoui et al., 2003, Winterhalter et al., 2009, Li et al., 2010). Based on the accurate mass measurements and proposed reaction pathways, three new acids (β–dihydroxycaryophyllonic acid, β–hydroxynornocaryophyllonic acid, and β–oxonocaryophyllonic acid) are tentatively identified in this study. β–caryophyllinic acid and β–nocaryophyllonic acid have the same chemical formula ($C_{14}H_{22}O_4$) and cannot be differentiated in the accurate mass measurements, especially since our study lacked authentic standards as well as tandem MS data.

β–caryophyllonic acid and β–caryophyllinic acid have traditionally been detected as first–generation products in the ozonolysis of β–caryophyllene. In the presence of OH and NO_x, β–caryophyllonic acid can form from the oxidation of β–caryophyllon aldehyde, which can form in the ozonolysis and photooxidation of β–caryophyllene (Scheme 3.2). β–caryophyllonic acid thus can be considered as either a first– or second–generation product. A number of other acids have been detected in this study. As shown in Schemes 3.2 – 3.5, many first– or higher–generation gas–phase products formed from the reaction of β–caryophyllene with O_3 and OH have an aldehyde group. In the presence of OH, the aldehydic hydrogen can be abstracted by OH, leading to an acyl peroxy radical, which reacts with HO_2 to give a carboxylic acid. This pathway could explain the formation of most of the organic acids observed in this study. However, it cannot be ruled out that the acids can form via other reaction pathways in the gas and particle phases. As shown in Tables 3.2 and 3.4, nitrogen–containing compounds have been detected by ESI in both positive and negative ion modes. The formation of nitrogen–containing compounds may attribute to the gas–phase reactions of peroxy radicals with NO; however, heterogeneous reaction processes in the particle phase (e.g., reactions between ammonia/ammonium ions with condensed gas–phase products containing carbonyl groups) cannot be completely ruled out (Nozière et al., 2009; Bones et al. 2010) and warrants future investigation.

Particle–phase reaction products formed via hydration and organosulfate formation of gas–phase products have been detected. Condensed gas–phase products can undergo hydrolysis in the particle phase. For example, a carbonyl group of β–hydroxycaryophyllonic acid

could be hydrated into a diol (Scheme 3.3). The hydrated gas–phase products tend to have low volatility and are preferentially present in the particle phase. Compounds having molecular weights larger than 300 Da have been detected. It is likely that these compounds are esters, which can be detected by ESI due to their stability and ionization efficiency (Camredon et al., 2010). Several organosulfates, as well as two nitrated organosulfates, have been detected (Table 3.5). As shown in Schemes 3.1 – 3.5, many gas–phase products contain hydroxyl groups, carbonyl groups, epoxide groups, or a combination of these groups. Organosulfates can possibly form from the particle–phase esterification of sulfate ions with gas–phase products containing one or more hydroxyl groups; however, this reaction process has been shown to be kinetically infeasible for smaller alcohols at atmospherically relevant pH conditions (Minerath et al., 2008, 2009). Additionally, organosulfates can form from gas–phase products containing an aldehyde or a keto group. The reaction involves the electron pair of the carbonyl oxygen accepting a proton, producing the oxonium ion, and becoming susceptible to nucleophilic attack from a lone pair of electrons on one of the oxygen atoms of the sulfate ions (Surratt et al., 2007a, 2008). β–caryophyllene oxide can form in the ozonolysis of β–caryophyllene (Jaoui et al. 2003); this compound has been detected in a forested area in central Greece (Pio et al., 2001). Recent work has shown that organosulfates can form from the reactive uptake of epoxide intermediates (Minerath et al., 2009), such as those derived from isoprene (Cole–Filipiak et al., 2010; Eddingsaas et al., 2010; Surratt et al., 2010) or from α– and β–pinene (Iinuma et al., 2009). Reactive uptake of simple epoxides leading to organosulfates has been estimated to be kinetically feasible under atmospherically relevant pH conditions (Minerath

et al., 2009; Cole–Filipiak et al., 2010, Eddingsaas et al., 2010). Similar to isoprene–derived epoxydiols and α– and β–pinene oxides, the sulfate ester of *m/z* 317 (Table 3.5) likely arises from the acid–catalyzed ring opening of β–caryophyllene oxide in the presence of acidic sulfate (Scheme 3.1). Most recently, organosulfates have also been shown to form from the irradiation of the aqueous–aerosol phase that contains sulfate (Galloway et al., 2009; Rudzinski et al., 2009; Nozière, et al., 2010; Perri et al., 2010). The formation of organosulfates via sulfate radical reaction mechanisms may warrant further investigation. It is noted that isobaric organosulfates cannot be differentiated by the accurate mass measurements; however, further tandem MS studies, as well as synthesis of authentic standards, could elucidate these isobaric structures. Depending on the β–caryophyllene oxidation product (e.g., carbonyls or epoxides) formed, a number of chemical pathways may be leading to the formation of the organosulfates we observe.

Bonn and Moortgat (2003) and Li et al. (2010) have suggested that new particle formation can be initiated by very low volatile gas–phase products produced from β–caryophyllene ozonolysis. In the present study, some particle–phase products (first– or higher–generation products) form dimers in the mass spectra collected in the negative ion mode of ESI (e.g., for β–caryophyllonic acid (MW 252, $C_{15}H_{24}O_3$) $[2M - H]^-$ at *m/z* 503 ($C_{30}H_{27}O_6^-$) was detected). No dimer formation was observed for organosulfates despite relatively high signal intensity of these compounds. Although dimer formation could be potential artifacts of the ESI, the importance of dimer formation of β–caryophyllene gas–phase products to new particle formation can be noted and certainly warrants further investigation.

Influence of aerosol acidity on the β–caryophyllene SOA composition. In the series of β–caryophyllene/NO_x irradiation experiments, the aerosol acidity ranged from 112 to 1150 nmol H^+ m^{-3} and SOA concentrations ranged from 9.97 to 34.0 μg C m^{-3}. Higher SOA concentrations were measured in the presence of increased aerosol acidity. For comparison, field measurements of aerosol acidity as $[H^+]_{air}$ have been reported (e.g., Liu et al., 1996; Pathak et al. 2003, 2004; Surratt et al., 2007b). The $[H^+]_{air}$ generally ranged from about 20 to 130 nmol H^+ m^{-3}. Aerosol acidities have been observed to exceed 300 nmol of H^+ m^{-3} during episodes of high photochemical activity in the eastern U.S. For example, Liu et al. (1996) observed an aerosol acidity of up to 400 nmol of H^+ m^{-3} in particles collected from Uniontown, PA. Since changes in the aerosol acidity in the present study had no significant direct effect on the gas–phase chemistry in these series of experiments (Offenberg et al., 2009), changes in the composition of β–caryophyllene SOA at different acidities is likely attributed to the particle–phase reactions. Figures 3.1 – 3.5 show the concentrations of compounds detected by ESI in both positive and negative ion modes in the series of β–caryophyllene/NO_x irradiation experiments. Different effects of acidity on the abundance of individual compounds have been observed. For gas–phase products (Figures 3.1 – 3.3) and nitrogen–containing compounds (Figure 3.4) detected, some compounds (β–hydroxynocaryophyllon aldehyde, β–dihydroxynocaryophyllon aldehyde, β–oxonocaryophyllonic acid, and β–hydroxynocaryophyllonic acid) show an increase with increasing aerosol acidity, while other compounds (β–nocaryophyllon aldehyde, β–hydroxycaryophyllon aldehyde, β–caryophyllonic acid, and β–hydroxycaryophyllonic acid) exhibit a decrease at higher aerosol acidity. It is also seen that acidity has no significant

effect on the concentration of some compounds (β–hydroxynornocaryophyllonic acid and β–dihydroxynocaryophyllonic acid).

For particle–phase reaction products, many hydrated compounds are detected at low aerosol acidity, while a few hydrated compounds (e.g., hydrated β–caryophyllonic acid and hydrated β–norcaryophyllonic acid) are detected only at higher aerosol acidity. The concentrations of many, but not all, hydrated compounds are found to increase with increasing aerosol acidity. By contrast, hydrated β–nocaryophyllonic acid has a lower concentration at higher aerosol acidity. Different effects of aerosol acidity on the concentration of high molecular weight compounds (MW > 300 Da) are observed. Figure 3.5 shows that the concentration of organosulfates and nitrated organosulfates generally increases with increasing aerosol acidity, except *m/z* 349 and 363. The concentrations of some organosulfates increase substantially with the aerosol acidity. For example, the signal intensities for *m/z* 317 and 347 increase by a factor of ~ 8 at the highest aerosol acidity, as compared to the lowest aerosol acidity. Also, a larger array of organosulfates is detected under higher acidic conditions. The aerosol acidity and sulfate content determine not only the concentration of organosulfates but also the kinds of organosulfates formed. To our knowledge, this is the first detection of organosulfates and nitrated organosulfates derived from a sesquiterpene.

Although the mechanisms by which acidity affects the concentrations of individual compounds are not well understood, some observations can be made. It is found that not all

particle–phase concentrations of gas–phase products increase with increasing aerosol acidity. Although gas/particle equilibrium shifts further toward the particle phase due to enhanced particle–phase reactions, the condensed gas–phase products can, as a result, react in the particle phase to form other products (e.g., hydrated compounds and sulfate esters) at an accelerated rate under acidic conditions. Because such reactions serve to convert the specific partitioning species to another compound, the enhanced gas/particle equilibrium does necessarily lead to an increase in the particle–phase concentration of gas–phase products. Although an increase in gas/particle partitioning coefficients of gas–phase products may help to capture the acid–enhanced SOA formation in a model (Kroll and Seinfeld, 2005), increased acidity does not always lead to an increase in the particle–phase concentration of gas–phase products.

The concentrations of particle–phase reaction products formed via acid–catalyzed reactions are expected to increase with increasing aerosol acidity. However, a few hydrated gas–phase products and some higher molecular weight compounds have a lower concentration at higher aerosol acidity. It is possible that other chemical reactions (e.g., organosulfate formation processes) may become kinetically more favorable and competitive at higher aerosol acidity. Due to the complexity of chemical reactions that can potentially occur among the compounds in the particle phase, it may not be surprising to see that the acidity exhibits different effects on the concentration of particle–phase reaction products at different acidities and not all classes of particle–phase reaction products have a higher concentration at higher acidity.

Overall, increased acidity exhibits different effects on the abundance of individual compounds and does not always enhance the concentration of gas–phase and particle–phase reaction products. Varying acidity also changes the product distribution. Although qualitative data are obtained for the concentrations, the relative increase in concentration of many gas–phase and particle–phase reaction products provides chemical evidence for the acid–enhanced SOA formation from β–caryophyllene/NO$_x$ irradiation experiments.

3.5 Conclusions and Atmospheric Implications

Chemical characterization of particle–phase products in the chamber samples can suggest possible chemical tracers for SOA formation from β–caryophyllene in ambient aerosol. Fine ambient aerosol collected in downtown Atlanta, GA (JST), and rural Yorkville, GA (YRK), during the AMIGAS campaign was analyzed for the presence of β–caryophyllene SOA constituents characterized from the laboratory studies. As shown in Table 3.6, the retention time and accurate mass measurements match very well for four ions detected in both ambient and chamber samples by ESI in the positive ion mode. Three of these compounds have been tentatively identified in the present study and are β–nocaryophyllon aldehyde, β–hydroxynocaryophyllon aldehyde, and β–dihydroxynocaryophyllon aldehyde. Each of these three compounds is a second–generation ozonolysis product previously identified in β–caryophyllene ozonolysis (Li et al., 2010). As shown in Schemes 3.2 – 3.4, these compounds can also be produced from the reaction of β–caryophyllene with a combination of O$_3$ and OH. The chemical structure of the compound (C$_{15}$H$_{24}$O$_4$) is not known yet. Although the emission of β–caryophyllene drops sharply at night

(Sakulyanontvittaya et al., 2008), all these compounds have been detected in most day and night samples at both sites. As shown in Table 3.6, based on the limited sample sizes, β–nocaryophyllon aldehyde showed a higher concentration in the nighttime samples at both JST and YRK sites. No strong diurnal variation in the concentrations was observed for the other compounds. Recently, Parshintsev et al. (2008) reported that β–nocaryophyllon aldehyde was present in ambient aerosol collected during spring 2003 at Hyytiälä, Finland. β–caryophyllon aldehyde was not detected in their ambient samples.

Gas/particle partitioning coefficients of the three aldehydes, K_p ($m^3\ \mu g^{-1}$), are estimated at 297 K (Pankow, 1994). As a first approximation, the activity coefficients of the products in the particle phase are assumed to be unity and the molecular weight of the products is used as mean molecular weight in the absorbing phase. Vapor pressures are estimated at 297 K using the model developed by Pankow and Asher (2008). Saturation vapor pressure, c* is inversely proportional to K_p (c* ~ 1/ K_p). The fraction F of a semivolatile compound in the particle phase can be expressed in term of K_p as $F = MK_p/(1+MK_p)$, where M is the amount of absorbing material ($\mu g\ m^{-3}$). Based on estimated gas/particle partitioning coefficients of β–nocaryophyllon aldehyde ($K_p = 2.5 \times 10^{-3}\ m^3\ \mu g^{-1}$; c* = 400 $\mu g\ m^{-3}$), β–hydroxynocaryophyllon aldehyde ($K_p = 0.37\ m^3\ \mu g^{-1}$; c* = 2.7 $\mu g\ m^{-3}$), and β–dihydroxynocaryophyllon aldehyde ($K_p = 54\ m^3\ \mu g^{-1}$; c* = 0.018 $\mu g\ m^{-3}$), a significant fraction of β–hydroxynocaryophyllon aldehyde ($F = 0.787$) and β–dihydroxynocaryophyllon aldehyde ($F = 0.998$) is present in the particle phase under typical organic mass loading (M ~ 10 $\mu g\ m^{-3}$). A small portion of β–nocaryophyllon

aldehyde ($F = 0.024$) can partition into the particle phase. The estimated saturated vapor pressures of these compounds in the present work are lower by a factor of about 2–40 than those estimated by Li et al. (2010) using a different vapor pressure estimation model.

Organosulfates detected in the laboratory–generated β–caryophyllene SOA were not observed in the ambient samples collected from the AMIGAS campaign. It is possible that the acidity of ambient aerosol is not strong enough for the formation of β–caryophyllene–derived organosulfates. As shown in Figure 3.5, most organosulfates detected in the chamber samples require high aerosol acidity (467–1150 nmol H^+ m^{-3}). It is worth noting that isoprene–derived organosulfates (e.g., organosulfates of 2–methyltetrols) have been detected in these AMIGAS ambient samples (Chan et al., 2010), which were also detected in laboratory–generated isoprene SOA that employed a lower $[H^+]_{air}$ that was between 275 and 517 nmol m^{-3} (Surratt et al., 2007b). Although accurate mass measurements obtained in the negative ion mode show that similar molecular ions were detected in both the AMIGAS and chamber samples for some β–caryophyllene–derived acids, the chromatographic peaks of these ions in the AMIGAS samples elute at different retention times (RT)(ΔRT > 0.2 min) and may not correspond to those of the chamber samples, especially since our study lacked authentic standards and tandem MS data. The detection of β–caryophyllinic acid in ambient samples is also complicated by β–nocaryophyllonic acid. β–caryophyllinic acid and β–nocaryophyllonic acid have the same chemical formula ($C_{14}H_{22}O_4$) and cannot be differentiated in the accurate mass measurements.

Overall, the presence of β–caryophyllene products in ambient aerosol has been confirmed based on the agreement of chromatographic retention times and accurate mass measurements between chamber and field samples. These results suggest that the presence of β–caryophyllene products in biogenic SOA can be used as an indication of its contribution to SOA. β–nocaryophyllon aldehyde, β–hydroxynocaryophyllon aldehyde, and β–dihydroxynocaryophyllon aldehyde may be good candidates for β–caryophyllene SOA tracers.

3.6 Acknowledgements

3.7 References

Bones, D. L., Henricksen, D. K., Mang, S. A., Gonsior, M., Bateman, A. P., Nguyen, T. B., Cooper, W. J. and Sergey Nizkorodov, S. A.: Appearance of strong absorbers and fluorophores in limonene–O_3 secondary organic aerosol due to NH_4^+–mediated chemical

aging over long time scales, *J. Geophys. Res.*, 115, D05203, 2010, doi:10.1029/ 2009JD012864.

Bonn, B., and Moortgat, G. K.: Sesquiterpene ozonolysis: Origin of atmospheric new particle formation from biogenic hydrocarbons, *Geophys. Res. Lett.*, 30, 1585, 2003, doi:10.1029/2003GL017000.

Calogirou, A., Kotzias, D., and Kettrup, A.: Product analysis of the gas–phase reaction of beta–caryophyllene with ozone, *Atmos. Environ.*, 31, 283–285, 1997.

Camredon, M., Hamilton, J. F., Alam, M. S., Wyche, K. P., Carr, T., White, I. R., Monks, P. S., Rickard, A. R., and Bloss, W. J.: Distribution of gaseous and particulate organic composition during dark α–pinene ozonolysis, *Atmos. Chem. Phys.*, 10, 2893–2917, 2010.

Chan, M. N., Surratt, J. D., Claeys, M., Edgerton, E. S., Tanner, R. L., Shaw, S. L., Zheng, M., Knipping, E. M., Eddingsaas, N. C., Wennberg, P. O., and Seinfeld, J. H.: Characterization and quantification of isoprene–derived epoxydiols in ambient aerosol in the southeastern United States, *Environ. Sci. Technol.*, 44, 4590–4596, 2010.

Cole–Filipiak, N. C., O, Connor, A. E., and Elrod, M. J.: Kinetics of the hydrolysis of atmospherically relevant isoprene–derived hydroxy epoxides, *Environ. Sci. Technol.*, 44, 6718–6723, 2010.

Eddingsaas, N. C., VanderVelde, D. G., and Wennberg, P. O.: Kinetics and products of the acid–catalyzed ring–opening of atmospherically relevant butyl epoxy alcohols, *J. Phys. Chem. A*, 114, 8106–8113, 2010.

Galloway, M. M., Chhabra, P. S., Chan, A. W. H., Surratt, J. D., Flagan, R. C., Seinfeld, J. H., and Keutsch, F. N.: Glyoxal uptake on ammonium sulphate seed aerosol: reaction products and reversibility of uptake under dark and irradiated conditions, *Atmos. Chem. Phys.*, 9, 3331–3345, 2009.

Griffin, R. J., Cocker, D. R., Flagan, R. C., and Seinfeld, J. H.: Organic aerosol formation from the oxidation of the biogenic hydrocarbons, *J. Geophys. Res.*, 104, 3555–3567, 1999.

Hallquist, M., Wenger, J. C., Baltensperger, U., Rudich, Y., Simpson, D., Claeys, M., Dommen, J., Donahue, N. M., George, C., Goldstein, A. H., Hamilton, J. F., Herrmann, H., Hoffmann, T., Iinuma, Y., Jang, M., Jenkin, M. E., Jimenez, J. L., Kiendler–Scharr, A., Maenhaut, W., McFiggans, G., Mentel, Th. F., Monod, A., Prevot, A. S. H., Seinfeld, J. H., Surratt, J. D., Szmigielski, R., and Wildt, J.: The formation, properties and impact of secondary organic aerosol: Current and emerging issues, *Atmos. Chem. Phys.*, 9, 5155–5235, 2009.

Iinuma, Y., Müller, C., Berndt, T., Böge, O., Claeys, M., and Herrmann, H.: Evidence for the existence of organosulfates from beta–pinene ozonolysis in ambient secondary organic aerosol, *Environ. Sci. Technol.*, 41, 6678–6683, 2007.

Iinuma, Y., Böge, O., Kahnt, A., and Herrmann, H.: Laboratory chamber studies on the formation of organosulfates from reactive uptake of monoterpene oxides, *Phys. Chem. Chem. Phys.*, 11, 7985–7997, 2009.

Jang, M., Czoschke, N. M., Lee, S., and Kamens, R. M.: Heterogeneous atmospheric aerosol production by acid–catalyzed particle phase reactions, *Science*, 298, 814–817, 2002.

Jaoui, M., Leungsakul, S., and Kamens, R. M.: Gas and particle products distribution from the reaction of beta–caryophyllene with ozone, *J. Atmos. Chem.*, 45, 261–287, 2003.

Jaoui, M., Lewandowski, M., Kleindienst, T. E., Offenberg, J. H., and Edney, E. O.: Beta–caryophyllinic acid: An atmospheric tracer for beta–caryophyllene secondary organic aerosol, *Geophys. Res. Lett.*, 34, L05816, 2007, doi:10.1029/2006GL028827.

Kanawati, B., Herrmann, F., Joniec, S., Winterhalter, R., and Moortgat, G. K.: Mass spectrometric characterization of b–caryophyllene ozonolysis products in the aerosol studied using an electrospray triple quadrupole and time–of–flight analyzer hybrid system and density functional theory, *Rapid Com. Mass Spectrom.*, 22, 165–186, 2008.

Kleindienst, T. E., Jaoui, M., Lewandowski, M., Offenberg, J. H., Lewis, C. W., Bhave, P. V., and Edney, E. O.: Estimates of the contributions of biogenic and anthropogenic hydrocarbons to secondary organic aerosol at a southeastern US location, *Atmos. Environ.*, 41, 8288–8300, 2007.

Kroll, J. H., and Seinfeld, J. H.: Representation of secondary organic aerosol laboratory chamber data for the interpretation of mechanisms of particle growth, *Environ. Sci. Technol.*, 39, 4159–4165, 2005.

Kroll, J. H., and Seinfeld, J. H.: Chemistry of secondary organic aerosol: Formation and evolution of low–volatility organics in atmosphere, *Atmos. Environ.*, 42, 3593–3624, 2008.

Larsen, B. R., Lahaniati, M., Calogirou, A., and Kotzias, D.: Atmospheric oxidation products of terpenes: a new nomenclature, *Chemosphere*, 37, 1207–1220, 1998.

Lee, A., Goldstein, A. H., Keywood, M. D., Gao, S., Varutbangkul, V., Bahreini, R., Ng, N. L., Flagan, R. C., and Seinfeld, J. H.: Gas–phase products and secondary aerosol yields from the ozonolysis of ten different terpenes, *J. Geophys. Res.*, 111, D7, D07302, 2006a.

Lee, A., Goldstein, A.H., Kroll, J.H., Ng, N.L., Varutbangkul, V., Flagan, R.C., and Seinfeld, J.H: Gas–phase products and secondary aerosol yields from the photooxidation of 16 different terpenes, *J. Geophys. Res.*, 111, D17, D17305, 2006b.

Li, Y. J., Chen, Q., Guzman, M. I., Chan, C. K., and Martin, S. T.: Second–generation products of β–caryophyllene ozonolysis are the dominant contributors to particle mass concentration, *Atmos. Chem. Phys. Discuss.*, 10, 17699–17726, 2010.

Liggio, J., and Li, S.M.: Organosulfate formation during the uptake of pinonaldehyde on acidic sulfate aerosols, *Geophys. Res. Lett.*, 33, 13, L13808. 2006.

Liu, L.–J. S., Burton, R., Wilson, W. E., and Koutrakis, P.: Comparison of aerosol acidity in urban and semirural environments, *Atmos. Environ.*, 30, 1237–1245, 1996.

Minerath, E.C., Casale, M.T., and Elrod, M.J.: Kinetics feasibility study of alcohol sulfate esterification reactions in tropospheric aerosols, *Environ. Sci. Technol.*, 42, 4410–4415, 2008.

Minerath, E. C., Schultz, M. P., and Elrdo, M. J.: Kinetics of the reactions of isoprene–derived epoxides in model tropospheric aerosol solutions, *Environ. Sci. Technol.*, 43, 8133–8139, 2009.

Ng, N.L., Kroll, J.H., Keywood, M.D., Bahreini, R., Varutbangkul, V., Flagan, R.C., Seinfeld, J.H., Lee, A., and Goldstein, A.H.: Contribution of first– versus second–generation products to secondary organic aerosols formed in the oxidation of biogenic hydrocarbons, *Environ. Sci. Technol.*, 40, 2283–2297, 2006.

Nguyen, T. L., Winterhalter, R., Moortgat, G., Kanawati, B., Peeters, J., and Vereecken, L.: The gas–phase ozonolysis of beta–caryophyllene ($C_{15}H_{24}$), Part 2: A theoretical study, *Phys. Chem. Chem. Phys.*, 11, 4173–4183, 2009.

Nozière, B., Ekstrom, S., Alsberg, T., and Holmstrom, S.: Radical–initiated formation of organosulfates and surfactants in atmospheric aerosols, *Geophys. Res. Lett.*, 37, L05806, 2010.

Nozière, B., Dziedzic, P., and Córdova, A.: Products and kinetics of the liquid–phase reaction of glyoxal catalyzed by ammonium ions (NH_4^+), *J. Phys. Chem. A*, 113, 231–237, 2009.

Offenberg, J. H., Lewandowski, M., Edney, E. O., Kleindienst, T. E., and Jaoui, M.: Influence of aerosol acidity on the formation of secondary organic aerosol from biogenic precursor hydrocarbons, *Environ. Sci. Technol.*, 43, 7742–7747, 2009.

Pankow, J. F.: An absorption model of the gas aerosol partitioning involved in the formation of secondary organic aerosol, *Atmos. Environ.*, 28, 189–193, 1994.

Pankow, J. F., and Asher, W. E.: SIMPOL.1: a simple group contribution method for predicting vapor pressures and enthalpies of vaporization of multifunctional organic compounds, *Atmos. Chem. Phys.*, 8, 2773–2796, 2008.

Parshintsev, J., Nurmi, J., Kilpelainen, I., Hartonen, K., Kulmala, M., and Riekkola, M. L.: Preparation of beta–caryophyllene oxidation products and their determination in ambient aerosol samples, *Anal. Bioanal. Chem.*, 390, 913–919, 2008.

Pathak, R. K., Yao, X. H., Lau, A. K. H., and Chan, C. K.: Acidity and concentrations of ionic species of PM2.5 in Hong Kong, *Atmos. Environ.*, 37, 1113–1124, 2003.

Pathak, R. K., Louie, P. K. K., and Chan, C. K.: Characteristics of aerosol acidity in Hong Kong, *Atmos. Environ.*, 38, 2965–2974, 2004.

Perri, M. J., Lim, Y. B., Seitzinger, S. P., and Turpin, B. J.: Organosulfates from glycolaldehyde in aqueous aerosols and clouds: Laboratory studies, *Atmos. Environ.*, 44, 2658–2664, 2010.

Pio, C., Alves, C., and Duarte, A.: Organic components of aerosols in a forested area of central Greece, *Atmos. Environ.*, 35, 389–401, 2001.

Rudzinski, K. J., Gmachowski, L., and Kuznietsova, I.: Reactions of isoprene and sulphoxy radical–anions– a possible source of atmospheric organosulphites and organosulphates, *Atmos. Chem. Phys.*, 2129–2140, 2009.

Sakulyanontvittaya, T., Duhl, T., Wiedinmyer, C., Helmig, D., Matsunaga, S., Potosnak, M., Milford, J., and Guenther, A. Monoterpene and sesquiterpene emission estimates for the United States, *Environ. Sci. Technol.*, 42, 1623–1629, 2008.

Shu Y., and Atkinson, R.: Rate constants for the gas phase reactions of O_3 with a series of terpenes and OH radical formation from the O_3 reactions with sesquiterpenes at $296 \pm 2K$, *Int. J. Chem. Kinet.*, 26, 1193–1205, 1994.

Shu, Y., and Atkinson, R.: Atmospheric lifetimes and fates of a series of sesquiterpenes, *J. Geophys. Res.– Atmos.*, 100, 7275–7281, 1995.

Surratt, J. D., Kroll, J. H., Kleindienst, T. E., Edney, E. O., Claeys, M., Sorooshian, A., Ng, N. L., Offenberg, J. H., Lewandowski, M., Jaoui, M., Flagan, R. C., and Seinfeld, J. H.: Evidence for organosulfates in secondary organic aerosol, *Environ. Sci. Technol.,* 41, 517–527, 2007a.

Surratt, J. D., Lewandowski, M., Offenberg, J. H., Jaoui, M., Kleindienst, T. E., Edney, E. O., and Seinfeld, J. H.: Effect of acidity on secondary organic aerosol formation from isoprene, *Environ. Sci. Technol*., 41, 5363–5369, 2007b.

Surratt, J. D., Gómez–González, Y., Chan, A. W. H., Vermeylen, R., Shahgholi, M., Kleindienst, T. E., Edney, E. O., Offenberg, J. H., Lewandowski, M., Jaoui, M., Maenhaut, W., Claeys, M., Flagan, R. C., and Seinfeld, J. H.: Organosulfate formation in biogenic secondary organic aerosol, *J. Phys. Chem. A*, 112, 8345–8378, 2008.

Surratt, J. D., Chan, A. W. H., Eddingsaas, N. C., Chan, M. N., Loza, C. L., Kwan, A. J., Hersey, S. P., Flagan, R. C., Wennberg, P. O., and Seinfeld, J. H.: Reactive intermediates revealed in secondary organic aerosol formation from isoprene, *Proc. Natl. Acad. Sci. USA*, 107, 6640–6645, 2010.

Winterhalter, R., Herrmann, F., Kanawati, B., Nguyen, T. L., Peeters, J., Vereecken, L., and Moortgat, G. K.: The gas–phase ozonolysis of beta–caryophyllene ($C_{15}H_{24}$), Part 1: an experimental study, *Phys. Chem. Chem. Phys.*, 11, 4152–4172, 2009.

Table 3.1: Steady state concentrations of gas–phase species, aerosol acidity, and secondary organic carbon (SOC) for β–caryophyllene/NO$_X$ irradiation experiments, reproduced from Offenberg et al. (2009)

Experiment	Δ[HC] (ppmC)	[NO] (ppbV)	[NO$_x$ – NO] (ppbV)	O$_3$ (ppbV)	[H$^+$]$_{air}$ (nmol m^{-3})	SOC (μgC m^{-3})
1	0.58	60	51	25	112	9.97
2	0.58	61	51	24	204	14.7
3	0.58	63	54	29	467	21.3
4	0.58	65	53	24	1150	34.0

Table 3.2: Compounds detected by ESI in the positive ion mode in the series of β–caryophyllene/NO_X irradiation experiments

ESI(+) compound	Suggested chemical formula	[M+H]+ (Theoretical mass)	[M+Na]+ (Theoretical mass)	[M+CH₃OH+Na]+ (Theoretical mass)	Suggested compound [a] (Scheme)	Proposed chemical structure [b]
184(+)	$C_{10}H_{26}O_3$	$C_{10}H_{27}O_3^+$ (185.1178)	$C_{10}H_{16}O_3Na^+$ (207.0997)			
238(+)	$C_{14}H_{22}O_3$	$C_{14}H_{23}O_3^+$ (239.1647)	$C_{14}H_{22}O_3Na^+$ (261.1467)	$C_{15}H_{26}O_4Na^+$ (293.1729)	β –nocaryophyllon aldehyde [c, d, e] (2)	
250(+)	$C_{15}H_{22}O_3$	$C_{15}H_{23}O_3^+$ (251.1647)	$C_{15}H_{22}O_3Na^+$ (273.1467)		β –oxocaryophyllon aldehyde [d] (4)	
252a(+)	$C_{14}H_{20}O_4$	$C_{14}H_{21}O_4^+$ (253.1440)	$C_{14}H_{20}O_4Na^+$ (275.1259)	$C_{15}H_{24}O_5Na^+$ (307.1521)	β –oxonocaryophyllon aldehyde (4)	
252b(+)	$C_{15}H_{24}O_3$	$C_{15}H_{25}O_3^+$ (253.1804)		$C_{16}H_{28}O_4Na^+$ (307.1885)	β –hydroxycaryophyllon aldehyde [c, d, e] (3)	
N253(+)	$C_{14}H_{23}NO_3$	$C_{14}H_{24}NO_3^+$ (254.1756)	$C_{14}H_{23}NO_3Na^+$ (276.1576)			
254a(+)	$C_{14}H_{22}O_4$	$C_{14}H_{23}O_4^+$ (255.1596)	$C_{14}H_{22}O_4Na^+$ (277.1416)	$C_{15}H_{26}O_5Na^+$ (309.1678)	β –hydroxynocaryophyllon aldehyde [c, e] (2, 3)	
254b(+)	$C_{15}H_{26}O_3$		$C_{15}H_{26}O_3Na^+$ (277.1780)			
N267(+)	$C_{15}H_{25}NO_3$	$C_{15}H_{26}NO_3^+$ (268.1913)	$C_{15}H_{25}NO_3Na^+$ (290.1732)			
268(+)	$C_{15}H_{24}O_4$	$C_{15}H_{25}O_4^+$ (269.1753)	$C_{15}H_{24}O_4Na^+$ (291.1572)			
270(+)	$C_{14}H_{22}O_5$	$C_{14}H_{23}O_5^+$ (271.1545)	$C_{14}H_{22}O_5Na^+$ (293.1365)	$C_{14}H_{26}O_6Na^+$ (325.1627)	β –dihydroxynocaryophyllon aldehyde [c] (3)	
298(+)	$C_{15}H_{22}O_6$	$C_{15}H_{23}O_6^+$ (299.1495)	$C_{15}H_{22}O_6Na^+$ (321.1314)			

Labels (+): Compound detected by ESI in positive ion mode; (–): Compound detected by ESI in negative ion mode; N: Nitrogen–containing compound; S: Sulfate esters or nitrooxy sulfate esters. Number represents the molecular weight of the compound. M is the compound. [a] Terpene nomenclature (Larsen et al., 1998); [b] Only one possible isomer is shown for simplicity; [c] Compound has been reported by Li et al. (2010); [d] Compound has been reported by Winterhalter et al. (2009); [e] Compound has been reported by Jaoui et al. (2003); 309(+) has been detected by the ESI in positive ion mode in this study, however, no reasonable chemical formula can be assigned.

Table 3.3: Compounds detected by ESI in the negative ion mode in the series of β–caryophyllene/NO$_X$ irradiation experiments
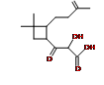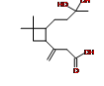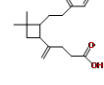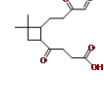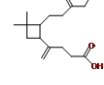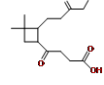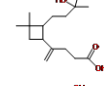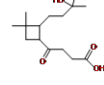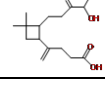
ESI(–) compound	[M–H]$^-$	Suggested chemical formula	Theoretical mass	Suggested compound [a] (Scheme)	Proposed chemical structure [b]	Detection of dimer in ESI negative ion mode
186(–)	185	C$_9$H$_{13}$O$_4^-$	185.0814			
216(–)	215	C$_{10}$H$_{15}$O$_5^-$	215.0919			
252a(–)	251	C$_{14}$H$_{19}$O$_4^-$	251.1283	[c]		
252b(–)	251	C$_{15}$H$_{23}$O$_3^-$	251.1647	β–caryophyllonic acid (2) [c, d, e]		C$_{30}$H$_{47}$O$_6^-$
254(–)	253	C$_{14}$H$_{21}$O$_4^-$	253.1440	β–nocaryophyllonic acid (2) [e] β–caryophyllinic acid [c, d, e]		C$_{28}$H$_{43}$O$_8^-$
256a(–)	255	C$_{13}$H$_{19}$O$_5^-$	255.1232	β–hydroxynornocaryophyllonic acid (5)		C$_{26}$H$_{39}$O$_{10}^-$
256b(–)	255	C$_{14}$H$_{23}$O$_4^-$	255.1596	Hydrated β–norcaryophyllonic acid (5)		
266(–)	265	C$_{15}$H$_{21}$O$_4^-$	265.1440	β–oxocaryophyllonic acid (4) [e]		
268a(–)	267	C$_{14}$H$_{19}$O$_5^-$	267.1232	β–oxonocaryophyllonic acid (4)		
268b(–)	267	C$_{15}$H$_{23}$O$_4^-$	267.1596	β–hydroxycaryophyllonic acid (3) [e]		
70a(–)	269	C$_{14}$H$_{21}$O$_5^-$	269.1389	β–hydroxynocaryophyllonic acid (2, 3) [e]		C$_{28}$H$_{43}$O$_{10}^-$
270b(–)	269	C$_{15}$H$_{25}$O$_4^-$	269.1753	Hydrated β–caryophyllonic acid (2)		
272(–)	271	C$_{14}$H$_{23}$O$_5^-$	271.1545	Hydrated β–nocaryophyllonic acid (2)		C$_{28}$H$_{47}$O$_{10}^-$
284(–)	283	C$_{15}$H$_{23}$O$_5^-$	283.1545	Hydrated β–oxocaryophyllonic acid (4)		C$_{30}$H$_{47}$O$_{10}^-$

Table 3.3: Continued

ESI(–) compound	[M–H]⁻	Suggested chemical formula	Theoretical mass	Suggested compound [a] (Scheme)	Proposed chemical structure [b]	Detection of dimer in ESI negative ion mode
286a(–)	285	$C_{14}H_{21}O_6^-$	285.1338	β–dihydroxynocaryophyllonic acid (3, 4)		$C_{28}H_{43}O_{12}^-$
286b(–)	285	$C_{15}H_{25}O_5^-$	285.1702	Hydrated β–hydroxycaryophyllonic acid (3)		$C_{30}H_{51}O_{10}^-$
294(–)	293	$C_{17}H_{25}O_4^-$	293.1753			$C_{34}H_{51}O_8^-$
312(–)	311	$C_{13}H_{27}O_8^-$	311.1706			
314a(–)	313	$C_{15}H_{21}O_7^-$	313.1287			
314b(–)	313	$C_{16}H_{25}O_6^-$	313.1651			
320(–)	319	$C_{14}H_{23}O_8^-$	319.1393			
328(–)	327	$C_{17}H_{27}O_6^-$	327.1808			
330a(–)	329	$C_{16}H_{25}O_7^-$	329.1600			
330b(–)	329	$C_{17}H_{29}O_6^-$	329.1964			

[a] Terpene nomenclature (Larsen et al., 1998); [b] Only one possible isomer is shown for simplicity; [c] Compound has been reported by Li et al. (2010); [d] Compound has been reported by Winterhalter et al. (2009); [e] Compound has been reported by Jaoui et al. (2003)

Table 3.4: Compounds detected by ESI in the negative ion mode in the series of β–caryophyllene/NO$_X$ irradiation experiments (Nitrogen–containing compounds)

ESI(–) compound	[M–H]$^-$	Suggested chemical formula	Theoretical mass	Suggested compound (Scheme)	Proposed chemical structure [a]	Detection of dimer in ESI negative ion mode
N195(–)	194	C$_{10}$H$_{12}$NO$_3$$^-$	194.0817			C$_{20}$H$_{25}$N$_2$O$_6$$^-$
N345(–)	344	C$_{16}$H$_{26}$NO$_7$$^-$	344.1709			
N347(–)	346	C$_{15}$H$_{24}$NO$_8$$^-$	346.1502	(3)		C$_{30}$H$_{49}$N$_2$O$_{16}$$^-$
N349a(–)	348	C$_{14}$H$_{22}$NO$_9$$^-$	348.1295			C$_{28}$H$_{45}$N$_2$O$_{18}$$^-$
N349b(–)	348	C$_{15}$H$_{26}$NO$_8$$^-$	348.1658	(2)		
N350(–)	349	C$_{13}$H$_{21}$N$_2$O$_9$$^-$	349.1247			
N363a(–)	362	C$_{15}$H$_{24}$NO$_9$$^-$	362.1451	(4)		C$_{30}$H$_{49}$N$_2$O$_{18}$$^-$
N363b(–)	362	C$_{16}$H$_{28}$NO$_8$$^-$	362.1815			
N375(–)	374	C$_{17}$H$_{28}$NO$_8$$^-$	374.1815			
N546(–)	545	C$_{24}$H$_{37}$N$_2$O$_{12}$$^-$	545.2347			C$_{12}$H$_{18}$NO$_6$$^-$ (Monomer)

[a] Only one possible isomer is shown for simplicity

Table 3.5: Compounds detected by ESI in the negative ion mode in the series of β–caryophyllene/NO$_X$ irradiation experiments (Organosulfates)
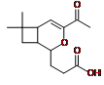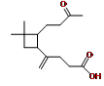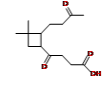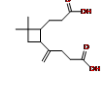
ESI(–) compound	[M–H]$^-$	Suggested chemical formula	Theoretical mass	Suggested compound (Scheme)	Proposed chemical structure [a]
S252(–)	251	C$_9$H$_{15}$O$_6$S$^-$	251.0589		
S304(–)	303	C$_{14}$H$_{23}$O$_5$S$^-$	303.1266	(1)	
S318(–)	317	C$_{15}$H$_{25}$O$_5$S$^-$	317.1423	(1)	
S320(–)	319	C$_{14}$H$_{23}$O$_6$S$^-$	319.1215	(1), (5)	
S334a(–)	333	C$_{14}$H$_{21}$O$_7$S$^-$	333.1008	(2), (3)	
S334b(–)	333	C$_{15}$H$_{25}$O$_6$S$^-$	333.1372	(2)	
S348(–)	347	C$_{15}$H$_{23}$O$_7$S$^-$	347.1165	(3), (4)	

Table 3.5: Continued

ESI(−) compound	[M–H]⁻	Suggested chemical formula	Theoretical mass	Suggested compound (Scheme)	Proposed chemical structure [a]
S350a(−)	349	$C_{14}H_{21}O_8S^-$	349.0957	(2),(3),(4)	
S350b(−)	349	$C_{15}H_{25}O_7S^-$	349.1321	(2),(3)	
S352(−)	351	$C_{14}H_{23}O_8S^-$	351.1114	(2),(3)	
S364a(−)	363	$C_{15}H_{23}O_8S^-$	363.1114	(4)	
S364b(−)	363	$C_{16}H_{27}O_7S^-$	363.1478		
S380(−)	379	$C_{16}H_{27}O_8S^-$	379.1427		
Nitrated Organosulfates					
S363(−)	362	$C_{15}H_{24}NO_7S^-$	362.1273	(1)	
S383(−)	382	$C_{14}H_{24}NO_9S^-$	382.1172	(1)	

[a] Only one possible isomer is shown for simplicity

Table 3.6: β–caryophyllene products observed both in the series of β–caryophyllene/NO$_X$ irradiation experiments and in fine ambient aerosol collected in downtown Atlanta, GA (JST) and a rural location in Yorkville, GA (YRK) during the 2008 AMIGAS Campaign [a]

Compound	Sample	RT[b] (min)	[M+H]$^+$ Formula	Measured mass	Theoretical mass	mDa
β–nocaryophyllon aldehyde	Experiment 4	9.94	C$_{14}$H$_{23}$O$_3^+$	239.1632	239.1647	–1.5
(C$_{14}$H$_{22}$O$_3$)	JST 080908D	9.91		239.1658	239.1647	1.1
238(+)	JST 080908N	9.90		239.1654	239.1647	0.7
	JST 090608D	9.91		239.1656	239.1647	0.9
	JST 090608N	9.93		239.1642	239.1647	–0.5
	YRK 081208D	n.d.				
	YRK 081208N	n.d.				
	YRK 090608D	9.97		239.1670	239.1647	2.3
	YRK 090608N	9.96		239.1674	239.1647	2.7
β–hydroxynocaryophyllon aldehyde	Experiment 4	9.78	C$_{14}$H$_{23}$O$_4^+$	255.1593	255.1596	–0.3
(C$_{14}$H$_{22}$O$_4$)	JST 080908D	9.75		255.1613	255.1596	1.7
254a(+)	JST 080908N	9.76		255.1624	255.1596	2.8
	JST 090608D	9.74		255.1619	255.1596	2.3
	JST 090608N	9.78		255.1603	255.1596	0.7
	YRK 081208D	9.76		255.1609	255.1596	1.3
	YRK 081208N	9.80		255.1637	255.1596	4.1
	YRK 090608D	9.80		255.1604	255.1596	0.8
	YRK 090608N	9.79		255.1609	255.1596	1.3
C$_{15}$H$_{24}$O$_4$	Experiment 4	9.44	C$_{15}$H$_{25}$O$_4^+$	269.1739	269.1753	–1.4
268(+)		9.60		269.1746	269.1753	–0.7
	JST 080908D	9.41		269.1721	269.1753	–3.2
		9.57		269.1739	269.1753	–1.4
	JST 080908N	9.40		269.1706	269.1753	–4.7
		9.56		269.1717	269.1753	–3.6
	JST 090608D	9.40		269.1725	269.1753	–2.8
		9.56		269.1741	269.1753	–1.2
	JST 090608N	9.42		269.1750	269.1753	–0.3
		9.59		269.1727	269.1753	–2.6
	YRK 081208D	9.42		269.1737	269.1753	–1.6
		9.59		269.1740	269.1753	–1.3
	YRK 081208N	9.46		269.1749	269.1753	–0.4
		9.61		269.1769	269.1753	1.6
	YRK 090608D	9.45		269.1751	269.1753	–0.2
		9.61		269.1738	269.1753	–1.5
	YRK 090608N	9.45		269.1747	269.1753	–0.6
		9.61		269.1755	269.1753	0.2
β–dihydroxynocaryophyllon aldehyde	Experiment 4	9.23	C$_{14}$H$_{23}$O$_5^+$	271.1501	271.1545	–4.4
(C$_{14}$H$_{22}$O$_5$)[c]	JST 080908D	9.20		271.1549	271.1545	0.4
270(+)	JST 080908N	n.d.				
	JST 090608D	9.21		271.1561	271.1545	1.6
	JST 090608N	n.d.				
	YRK 081208D	9.22		271.1570	271.1545	2.5
	YRK 081208N	9.26		271.1571	271.1545	2.6
	YRK 090608D	9.25		271.1548	271.1545	0.3
	YRK 090608N	n.d.				

Table 3.6: Continued

Compound	Sample	RT[b] (min)	[M+Na]+ Formula	Measured mass	Theoretical mass	mDa
β–nocaryophyllon aldehyde	Experiment 4	9.94	$C_{14}H_{22}O_3Na^+$	261.1465	261.1467	–0.2
($C_{14}H_{22}O_3$)	JST 080908D	9.91		261.1490	261.1467	2.3
238(+)	JST 080908N	9.90		261.1496	261.1467	2.9
	JST 090608D	9.91		261.1495	261.1467	2.8
	JST 090608N	9.93		261.1478	261.1467	1.1
	YRK 081208D	n.d.				
	YRK 081208N	n.d.				
	YRK 090608D	9.97		261.1476	261.1467	0.9
	YRK 090608N	9.96		261.1432	261.1467	–3.5
β–hydroxynocaryophyllon aldehyde	Experiment 4	9.78	$C_{14}H_{22}O_4Na^+$	277.1374	277.1416	–4.2
($C_{14}H_{22}O_4$)	JST 080908D	9.75		277.1424	277.1416	0.8
254a(+)	JST 080908N	9.76		277.1424	277.1416	0.8
	JST 090608D	9.74		277.1422	277.1416	0.6
	JST 090608N	9.78		277.1431	277.1416	1.5
	YRK 081208D	9.76		277.1422	277.1416	0.6
	YRK 081208N	9.80		277.1435	277.1416	1.9
	YRK 090608D	9.80		277.1430	277.1416	1.4
	YRK 090608N	9.79		277.1426	277.1416	1.0
$C_{15}H_{24}O_4$	Experiment 4	9.44	$C_{15}H_{24}O_4Na^+$	291.1525	291.1572	–4.7
268(+)		9.60		291.1528	291.1572	–4.4
	JST 080908D	9.41		291.1577	291.1572	0.5
		9.57		291.1578	291.1572	0.6
	JST 080908N	9.40		291.1565	291.1572	–0.7
		9.56		291.1578	291.1572	0.6
	JST 090608D	9.40		291.1578	291.1572	0.6
		9.56		291.1561	291.1572	–1.1
	JST 090608N	9.42		291.1581	291.1572	0.9
		9.59		291.1575	291.1572	0.3
	YRK 081208D	9.42		291.1548	291.1572	–2.4
		9.59		291.1578	291.1572	0.6
	YRK 081208N	9.46		291.1591	291.1572	1.9
		9.61		291.1577	291.1572	0.5
	YRK 090608D	9.45		291.1577	291.1572	0.5
		9.61		291.1569	291.1572	–0.3
	YRK 090608N	9.45		291.1578	291.1572	0.6
		9.61		291.1567	291.1572	–0.5
β–dihydroxynocaryophyllon aldehyde	Experiment 4	9.23	$C_{14}H_{22}O_5Na^+$	293.1348	293.1365	–1.7
($C_{14}H_{22}O_5$)[c]	JST 080908D	9.20		293.1395	293.1365	3
270(+)	JST 080908N	n.d.				
	JST 090608D	9.21		293.1406	293.1365	4.1
	JST 090608N	n.d.				
	YRK 081208D	9.22		293.1408	293.1365	4.3
	YRK 081208N	9.26		293.1415	293.1365	5.0
	YRK 090608D	9.25		293.1408	293.1365	4.3
	YRK 090608N	n.d.				

Table 3.6: Continued

Compound	Sample	RT[b] (min)	[M+CH₃OH+Na]⁺ Formula	Measured mass	Theoretical mass	mDa	Concentration [d]
β–nocaryophyllon aldehyde	Experiment 4	9.94	$C_{15}H_{26}O_4Na^+$	293.1719	293.1729	−1.0	
($C_{14}H_{22}O_3$)	JST 080908D	9.91		293.1734	293.1729	0.5	3.7
238(+)	JST 080908N	9.90		293.1752	293.1729	2.3	5.3
	JST 090608D	9.91		293.1723	293.1729	−0.6	2.7
	JST 090608N	9.93		293.1727	293.1729	−0.2	14
	YRK 081208D	n.d.					
	YRK 081208N	n.d.					
	YRK 090608D	9.97		293.1734	293.1729	0.5	4.5
	YRK 090608N	9.96		293.1743	293.1729	1.4	20
β–hydroxynocaryophyllon aldehyde	Experiment 4	9.78	$C_{15}H_{26}O_5Na^+$	309.1667	309.1678	−1.1	
($C_{14}H_{22}O_4$)	JST 080908D	9.75		309.1671	309.1678	−0.7	2.5
254a(+)	JST 080908N	9.76		309.1650	309.1678	−2.8	3.7
	JST 090608D	9.74		309.1713	309.1678	3.5	1.9
	JST 090608N	9.78		309.1707	309.1678	2.9	2.9
	YRK 081208D	9.76		309.1718	309.1678	4.0	8.1
	YRK 081208N	9.80		309.1708	309.1678	3.0	1.7
	YRK 090608D	9.80		309.1707	309.1678	2.9	2.9
	YRK 090608N	9.79		309.1699	309.1678	2.1	2.1
$C_{15}H_{24}O_4$	Experiment 4	9.44		n.d.			
268(+)		9.60		n.d.			
	JST 080908D	9.41		n.d.			1.2
		9.57		n.d.			1.2
	JST 080908N	9.40		n.d.			1.4
		9.56		n.d.			1.6
	JST 090608D	9.40		n.d.			1.3
		9.56		n.d.			1.5
	JST 090608N	9.42		n.d.			1.1
		9.59		n.d.			1.5
	YRK 081208D	9.42		n.d.			1.8
		9.59		n.d.			1.3
	YRK 081208N	9.46		n.d.			1.1
		9.61		n.d.			1.2
	YRK 090608D	9.45		n.d.			2.0
		9.61		n.d.			2.0
	YRK 090608N	9.45		n.d.			1.8
		9.61		n.d.			1.6
β–dihydroxynocaryophyllon aldehyde	Experiment 4	9.23	$C_{15}H_{26}O_6Na^+$	325.1674	325.1627	4.7	
($C_{14}H_{22}O_5$)[c]	JST 080908D	9.20		325.1645	325.1627	1.8	0.6
270(+)	JST 080908N	n.d.					
	JST 090608D	9.21		325.1652	325.1627	2.5	0.7
	JST 090608N	n.d.					
	YRK 081208D	9.22		325.1650	325.1627	2.3	1.1
	YRK 081208N	9.26		325.1646	325.1627	1.9	0.6
	YRK 090608D	9.25		325.1655	325.1627	2.8	0.5
	YRK 090608N	n.d.					

n.d. = adduct ions are not detected; [a] Day (10 a.m. to 6 p.m., local time) and night (10 p.m. to 6 a.m., local time); [b] RT = retention time; [c] Weak signal intensity observed for ambient samples; GF 14 sample is chosen as an example; [d] Concentration is expressed in term of the intensity of ion normalized by the sampling air volume (ion intensity/m³) in the AMIGAS samples.

Figure 3.1: Concentration of compounds detected by ESI in positive ion mode in the series of β–caryophyllene/NO$_X$ irradiation experiments. Chemical formulas and proposed chemical structures of these compounds are given in Table 3.2.

Figure 3.2: Concentration of compounds detected by ESI in negative ion mode in the series of β–caryophyllene/NO$_X$ irradiation experiments. Chemical formulas and proposed chemical structures of these compounds are given in Table 3.3.

Figure 3.3: Concentration of compounds detected by ESI in negative ion mode in the series of β–caryophyllene/NO$_X$ irradiation experiments. Chemical formulas and proposed chemical structures of these compounds are given in Table 3.3.

Figure 3.4: Concentration of compounds detected by ESI in negative ion mode in the series of β–caryophyllene/NO$_X$ irradiation experiments (nitrogen–containing compounds). Chemical formulas and proposed chemical structures of these compounds are given in Table 3.4.

Figure 3.5: Concentration of compounds detected by ESI in negative ion mode in the series of β–caryophyllene/NO$_X$ irradiation experiments (organosulfates and nitrated organosulfates). Chemical formulas and proposed chemical structures of these compounds are given in Table 3.5.

Scheme 3.1: Proposed reaction pathways of β–caryophyllene, leading to compounds detected by ESI in the particle phase. Boxes indicate compounds detected by ESI in the particle phase. One possible structural isomer is shown. SCI is the stabilized Criegee intermediates channel.

Scheme 3.2: Proposed reaction pathways of β–caryophyllon aldehyde, leading to compounds detected by ESI in the particle phase. Formation mechanism of β–caryophyllon aldehyde from the photooxidation and ozonolysis of β–caryophyllene (Lee et al., 2006b; Winterhalter et al., 2009). Boxes indicate compounds detected by ESI in the particle phase. One possible structural isomer is shown. SCI is the stabilized Criegee intermediates channel. HP is the hydroperoxide channel.

Scheme 3.3: Proposed reaction pathways of β–hydroxycaryophyllon aldehyde, leading to compounds detected by ESI in the particle phase. Formation mechanism of β–hydroxycaryophyllon aldehyde from the ozonolysis of β–caryophyllene (Winterhalter et al., 2009). β–14–hydroxycaryophyllon aldehyde is chosen as illustration. Boxes indicate compounds detected by ESI in the particle phase. One possible structural isomer is shown. SCI is the stabilized Criegee intermediates channel. HP is the hydroperoxide channel.

Scheme 3.4: Proposed reaction pathways of β–oxocaryophyllon aldehyde, leading to compounds detected by ESI in the particle phase. Formation mechanism of β–oxocaryophyllon aldehyde from the ozonolysis of β–caryophyllene (Winterhalter et al., 2009). β–14–oxocaryophyllon aldehyde is chosen as illustration. Boxes indicate compounds detected by ESI in the particle phase. One possible structural isomer is shown. SCI is the stabilized Criegee intermediates channel.

Scheme 3.5: Proposed reaction pathways of β–norcaryophyllon aldehyde, leading to compounds detected by ESI in the particle phase. Formation mechanism of β–norcaryophyllon aldehyde from the ozonolysis of β–caryophyllene (Winterhalter et al., 2009). Boxes indicate compounds detected by ESI in the particle phase. One possible structural isomer is shown. HP is the hydroperoxide channel.

Chapter 4

Modeling of Secondary Organic Aerosol Yields from Laboratory Chamber Data*

4.1 Abstract

Laboratory chamber data serve as the basis for constraining models of secondary organic aerosol (SOA) formation. Current models fall into three categories: empirical two–product (Odum), product–specific, and volatility basis set. The product–specific and volatility basis set models are applied here to represent laboratory data on the ozonolysis of α–pinene under dry, dark, and low–NO$_x$ conditions in the presence of ammonium sulfate seed aerosol. Using five major identified products, the model is fit to the chamber data. From the optimal fitting, SOA organic–to–carbon (O/C) and hydrogen–to–carbon (H/C) ratios are modeled. The discrepancy between measured H/C ratios and those based on the oxidation products used in the model fitting suggests the potential importance of particle–phase reactions. Data fitting is also carried out using the volatility basis set, wherein oxidation products are parsed into volatility bins. The product–specific model is most likely hindered by lack of explicit inclusion of particle–phase accretion compounds. While prospects for identification of the majority of SOA products for major volatile organic compounds (VOCs) classes remain promising, for the near future empirical product or volatility basis set models remain the approaches of choice.

4.2 Introduction

Laboratory chamber data are needed to determine secondary organic aerosol (SOA) yields from volatile organic compounds (VOCs). The fundamental concept on which all descriptions of SOA formation lie is that SOA comprises a mixture of semi–volatile

organic compounds that partition between the gas and particle phases (Pankow, 1994a, 1994b; Odum et al., 1996; Hallquist et al., 2009). Gas–particle partitioning of each compound is described by an equilibrium partitioning coefficient, K_p,

$$K_p = \frac{P}{GM} \sim \frac{1}{c^*} \quad (4.1)$$

where G is the mass concentration per unit volume of air ($\mu g\ m^{-3}$) of the semivolatile species in the gas phase, P is the mass concentration per unit volume of air ($\mu g\ m^{-3}$) of the semivolatile species in the particle phase, and M is the mass concentration per unit volume of air ($\mu g\ m^{-3}$) of the total absorbing particle phase. The equilibrium partitioning coefficient, K_p ($m^3\ \mu g^{-1}$) is inversely proportional to the saturation vapor concentration, c^* ($\mu g\ m^{-3}$), of the pure semivolatile compound. M refers only to the portion of the particulate matter participating in absorptive partitioning (organic aerosol into which semivolatile organics can partition and the aqueous portion of the particles in the case of water–soluble organics). Note that as long as absorbing mass is present, some fraction of a given semivolatile compound partitions into the particle phase, even if its gas–phase concentration is below its saturation vapor concentration, c^*. Oxidation of a parent VOC leads to a variety of semivolatile products, each with its own saturation vapor concentration. Moreover, the semivolatile oxidation products may be formed from first– or higher–generation gas–phase reactions, and the products themselves may react further in the gas phase to yield compounds of either lower (in the case of addition of more functional groups) or greater (in the case in which the carbon backbone of the molecule is cleaved) volatility.

The fraction F of a semivolatile compound in the particle phase can be expressed in terms of K_p or $c*$ as

$$F = \frac{P}{G+P} = \frac{MK_p}{1+MK_p} = \frac{1}{1+c*/M} \quad (4.2)$$

As the amount of absorbing material (M) increases, compounds of greater volatility (larger $c*$, smaller K_p) will partition increasingly into the particle phase. When $c* = M$, half of the semivolatile mass resides in the particle phase. If $M \gg c*$, essentially all of the semivolatile species is in the particle phase. In the first basic model of SOA formation, Odum et al. (1996) represented the process of SOA formation by n semivolatile products and showed that the SOA yield Y, defined as the mass of aerosol formed per mass of hydrocarbon reacted, can be expressed as the following

$$Y = M \sum_i \frac{\alpha_i K_{p,i}}{1+MK_{p,i}} \quad (4.3)$$

where α_i is the mass–based stoichiometric coefficient for product i (mass of i produced per mass of parent VOC reacted). Note that Y can exceed 1.0 as a result of the increase of molecular mass of oxidation products. (The designation "aerosol mass fraction" is also used for Y). Eqn. (4.3) is an equilibrium model in that it relates the amount of each product formed to the amount of VOC reacted regardless of the number of chemical steps involved. While, in principle, n can be as large as desired, in the application of the Odum model usually $n = 2$. The two products are not necessarily associated with actual products, and the 4 parameters, α_1, α_2, $K_{p,1}$, and $K_{p,2}$, are estimated by optimal fitting of Eqn. (4.3) to the data. OA forms when gas–phase oxidation products of a hydrocarbon precursor partition

between the gas and particle phases. Products with lower vapor pressures partition preferentially to the particle phase; compounds that are more highly functionalized tend to have lower vapor pressures. The degree of partitioning to the particle phase depends also on the quantity of absorbing organic material in that phase into which the compounds can condense; as the mass of absorbing material increases, compounds of higher vapor pressure that tend not to partition to the particle phase under low mass loadings do so at the higher mass loadings. The result is that SOA at low mass loading tends to be enriched in the least volatile (and more oxygenated) products (Bahreini et al., 2005; Shilling et al., 2008). In typical chamber experiments, a range of initial hydrocarbon precursor concentrations is employed in order to determine SOA yields as a function of the mass concentration of organic particles generated. When chamber experiments are conducted over a range of initial VOC concentrations, such experiments afford a view of the full spectrum of oxidation products, thereby facilitating the formulation of chemical mechanisms.

Laboratory chamber studies are limited in duration to about 12 hours or so, as constrained by particle deposition on the chamber walls, whereas the typical atmospheric lifetime of a particle is considerably longer. Chamber studies capture the initial multi–hour VOC oxidation but not that which takes place on a multi–day timescale. The sequence of reactions and associated SOA formation that occur over the duration of a chamber experiment can be termed as the *chamber phase*. (Stainer et al., 2008, have referred to this as the "prompt" phase.) The chamber or prompt phase chemistry begins with oxidant (OH, O_3, NO_3) attack on the VOC, initiating a series of reactions, which can depend critically on

NO$_X$ level, leading to semivolatile products. Experimentally–derived SOA yields reflect the extent of SOA formation over the chamber phase. Reactions that occur on a timescale longer than a chamber experiment can be termed the *aging phase*, during which the following processes may occur: (1) particle–phase accretion reactions that convert semivolatile condensed products to essentially non–volatile compounds; (2) gas–phase oxidation reactions of chamber phase semivolatile products that are too slow to be important during the chamber phase but are capable of producing compounds of even lower volatility over the aging phase; and (3) gas–particle reactions that convert some particulate material to volatile products. Over the typical timescale and spatial grid scale of atmospheric models, SOA formation occurring on the chamber phase timescale can be considered as taking place essentially instantaneously, suggesting that an equilibrium partitioning model for this phase is appropriate. Over the longer aging timescale, the equilibrium partitioning can be considered to be slowly perturbed as chemical aging takes place.

4.3 Form of SOA Model

If a number of products accounting for a significant fraction of the total mass of SOA have been identified, these major products can serve as SOA surrogates in a product–specific model (Pankow et al., 2001; Seinfeld et al., 2001). Upon estimating the vapor pressures, the values of K_p of the major products can be determined. For the product–specific model, major identified particle–phase products are chosen as SOA surrogates to represent other chemically similar compounds, and to give a reasonable approximation of gas/particle

partitioning of all other products (Pankow et al., 2001). The simulated SOA composition may allow a first approximation of the properties of SOA (e.g., water uptake and cloud condensation nuclei activity). The SOA composition changes with organic mass loading, and the amount of hydrocarbon precursors reacted can be tracked. Using the simulated SOA composition, one can also calculate the aerosol oxygen–to–carbon (O/C) and hydrogen–to–carbon (H/C) ratios at different loadings. Simulated ratios for O/C and H/C can be compared with those measured.

An alternative approach is the *volatility basis set,* in which the range of products is specified in terms of volatility bins (Donahue et al., 2006; Stainer et al., 2008). The product volatilities can be segmented into order–of–magnitude volatility bins (expressed as values of $c*$). Since SOA products are grouped into volatility bins, specific information about the chemical composition of SOA is not required. For the volatility basis set, Stainer et al. (2008) present a methodology for selecting the maximum and minimum values of $c*$, and logarithmic spacing between $c*$ values then determines the number of volatility bins.

Either treatment has the potential to reproduce the measured concentrations of major reaction products (both gas–phase and particle–phase), even in the absence of details of major particle–phase reactions. On the other hand, if an equilibrium state is not attained during the chamber phase, the kinetics of gas–phase and particle–phase reactions determine the SOA composition. In such cases, development of kinetic models in which reaction products undergo reactions in both gas–phase and particle–phase is needed to describe the

SOA formation (Chan et al., 2007). The goal of this chapter is to evaluate the product–specific approach to SOA modeling, using a system that has been relatively well characterized in the laboratory: ozonolysis of α–pinene. Because of a general lack of complete product identification for any SOA system, as well as uncertainty about the properties of the products, in practical terms, parameters in the model need to be determined by optimal fitting of the model to chamber data.

4.4 Results and Discussion

Product–specific model. Ozonolysis of α–pinene is, in many respects, an excellent test case for an SOA model. A number of experimental studies exist in the literature, and relatively complete product identification has been carried out. Oxocarboxylic acids, hydroxy oxocarboxylic acids, dicarboxylic acids, oxoaldehydes, and organic peroxides are the major classes of SOA products identified (Yu et al., 1999; Docherty et al., 2005). For the purposes of evaluating the product–specific model it is assumed that there are five major products: pinonic acid, pinic acid, pinonaldehyde, a hydroperoxide, and terpenylic acid (Table 4.1). These compounds are chosen to reflect the current understanding of the gas–phase products formed in the ozonolysis of α–pinene.

The vapor pressure of a product i is estimated by using a group contribution method developed by Pankow and Asher (2008). At a given temperature, the $K_{p,i}$ of the product i is determined by assuming that its activity coefficient, ζ_i , is unity and the molecular

weight of product i is taken as the mean molecular weight of the surrogate mixture, $\overline{MW}$, as a first approximation. These assumptions may be reasonable as the range of molecular weight of products is small ($168 - 200$ g mol^{-1}, see Table 4.1) and the amount of water presented in the particle phase is not significant under dry conditions ($<$ 5–40% RH). Bilde and Pandis (2001) measured the vapor pressure of semivolatile products formed from oxidation of biogenic monoterpenes using a laminar flow reactor with uncertainty of $\pm50\%$. They reported a vapor pressure of 1.989×10^{-10} atm for pinic acid of at 293 K, which is comparable to the estimated value (4.605×10^{-10} atm) using Pankow and Asher (2008) model. At a given temperature, the estimated vapor pressures of the major products using the Pankow and Asher (2008) model are lower than that estimated by Jenkin (2004). Hence, the present estimated K_p values of major products are larger than those reported by Jenkin (2004). For example, Jenkin (2004) estimated a higher vapor pressure of pinic acid of 4.7×10^{-4} torr (or 6.18×10^{-7} atm) at 298 K compared to that reported by Bilde and Pandis (2001) (4.213×10^{-10} atm).

When the vapor pressure estimation is carried out for the α–pinene/ozone system, two sets of two products each are estimated to have very similar K_p values. For example, at 293 K, the estimated value of K_p of hydroxy pinonic acid (K_p = 0.2802) is very close to that of pinic acid (K_p = 0.2822), and the estimated K_p of pinonic acid (K_p = 0.0018) is close to that of hydroxy pinonaldehyde (K_p = 0.0017). In such a case, two products of essentially identical vapor pressures cannot be distinguished, and a single product is chosen to represent the two products. Pinonic acid is chosen to represent the pinonic acid,

norpinonic acid, hydroxy pinonaldehyde, and isomers. Pinic acid is chosen to represent pinic acid, norpinonic acid, hydroxy pinonic acid, and isomers.

The basic chamber data are considered to be in the form of particle mass concentration as a function of VOC reacted. The actual chamber data are in the form of aerosol volume concentration. Aerosol density needed to convert volume to mass concentration is estimated by comparing the aerosol number distribution measured by a differential mobility analyzer with that obtained from the Aerodyne Aerosol Mass Spectrometer (AMS), through the theoretical relationship between mobility diameter and vacuum aerodynamic diameter. Ng et al. (2006) have shown that for the oxidation of a number of hydrocarbons with a single double bond, the growth curve for one experiment over the course of the experiment ("time–dependent growth curve") follows that of final SOA growth over different experiments. This suggests that in this case the time–dependent SOA growth data can also be used for model data fitting.

Data from ozonolysis of α–pinene are obtained from experiments conducted under dry, dark, and low–NO_x conditions in the presence of dry $(NH_4)_2SO_4$ particles (Ng et al. 2006; Pathak et al. 2007; Shilling et al. 2008). The SOA yield data cover a range of organic mass loading (0.5–411 $\mu g\ m^{-3}$) and are used for the parameterization to model the SOA yield relevant to the atmospheric conditions (Presto and Donahue, 2006). An effective SOA density of 1.25 g cm^{-3} is applied for conversion of volume to mass concentration in determination of SOA yield. It is noted that Shilling et al. (2009)

reported a higher effective SOA density (1.73–1.4 g cm^{-3}) at low organic mass loading

(0.5–7 μg m^{-3}). The SOA yield data from Shilling et al. (2008) are adjusted to 293 K,

using a temperature correction factor suggested by Pathak et al. (2007). Generally, time–

dependent SOA yield data reported by Ng et al. (2006) are in good agreement with the

final SOA yield data reported by Pathak et al. (2007) and Shilling et al. (2008) but are

lower than those reported by Shilling et al. (2008) for organic mass loading less than 2 μg

m^{-3}. Measurement uncertainties may explain part of the variability in SOA yield data

reported by Ng et al. (2006) at low organic mass loading.

Data, plotted as SOA yield, Y, versus organic mass loading, *M,* are shown in Figure 4.1.

The SOA yield increases rapidly at low organic mass loading and more slowly at high

organic mass loading. Shown in Figure 4.1 are the optimal fits to the product–specific

and volatility basis set models. In order to evaluate the effect of uncertainty in the K_p

values, results are shown for the estimated values of K_p (termed the $K_p \times 1$ case) and the

estimated values of K_p increased by a factor of 100 (termed the $K_p \times 100$ case). Previous

modeling studies on this system have also shown that an overall increase of K_p of all

products of a factor on the order of 10^2 is needed to explain the partitioning (Jenkin 2004;

Chen and Griffin, 2005). In each case, the α_i values are determined by optimal fitting to

the data. Different sets of α_i values produce essentially the same goodness of fit to the

overall mass yield. The sets can be discriminated between according to how well they fit

the SOA composition as compared to that measured. The α_i values are chosen to give the

best fit to experimental SOA yields and SOA composition. As shown in Figure 4.1, the

predicted SOA yields agree well with the experimental SOA yield data in both $K_p \times 1$ and $K_p \times 100$ cases. The $K_p \times 100$ case gives a better estimation of SOA yields at low organic mass loading than the $K_p \times 1$ case. However, the optimized curves underpredict the SOA yield data reported by Shilling et al. (2008) when the organic mass loading is less than $2~\mu g~m^{-3}$.

For the $K_p \times 1$ case, the predicted SOA yields are lower than the measured ones at low organic mass loading. The data fitting produces the unrealistic result that the mass yield of the pinonaldehyde is unity. The sum of fitted molar yields exceeds 1. One likely explanation is the uncertainty in the estimation of the K_p of major products (vapor pressure and activity coefficient). The estimated vapor pressure of the products using the group contribution method is too high, and the products are estimated to be too volatile. In order to match experimental SOA yields, large mass yields of the products are predicted so that a significant amount of the products is partitioned into the particle phase. This results in unrealistically high mass yields of the products. Another likely explanation is that other products (gas–phase and/or particle–phase) of higher K_p (and lower volatilities) are present. Particle–phase reaction products (e.g., oligomers and esters), which are likely present, tend to have higher molecular weights and lower volatilities (Gao et al., 2004; linuma et al., 2004; Müller et al., 2008), effectively enhancing the K_p values (Kroll et al., 2005). For example, an ester, which is formed between pinic acid and hydroxy pinonic acid, has been detected (Müller et al. 2008). At

293 K, the estimated K_p of the ester is 4.96×10^5, which is much larger than that of hydroxy pinonic acid ($K_p = 0.2802$) and of pinic acid ($K_p = 0.2822$).

Volatility basis set model. The volatility basis set model is also applied to fit the experimental SOA yields. The estimated volatility (or c^*) of products spans from 0.035 to 873 µg m^{-3}. A volatility basis set of six volatility bins is chosen and the volatility bins are separated by an order of magnitude (c^*: 0.01, 0.1, 1, 10, 100, and 1000 µg m^{-3}). The mass of aerosol in bin i is obtained by optimal fitting to the experimental SOA yield data. Figure 4.1 shows that for the volatility basis set, the predicted SOA yields agree well with the experimental SOA yield data, even at low organic mass loading (< 0.5 µg m^{-3}). This suggests that products with volatility as low as $c^* = 0.01$ µg m^{-3} (or $K_p = 100$ µg^{-1} m^3) are present. The quantity of aerosol in the volatility bin i is in good agreement with that of the product i with similar K_p or c^* (Table 4.1) in the $K_p \times 100$ case. Overall, the volatility basis set produces the smallest fitting error of SOA yield prediction over the whole range of the organic mass loading (mean absolute fractional error, *err* = 0.1572) compared to the $K_p \times 1$ case (*err* = 0.1688) and the $K_p \times 100$ case (*err* = 0.1598).

Temperature dependence of SOA yield. We also investigate temperature dependence of SOA yield using the product–specific model (only the $K_p \times 100$ case that gives a better description of SOA yields is shown). The temperature–dependent vapor pressure of the products can be estimated using the group contribution method developed by Pankow and Asher (2008). The temperature dependence of the structural groups ($b(T)$) are assumed to

follow $b(T) = B_1/T + B_2 + B_3T + B_4\ln T$. The B coefficients are obtained by optimal fitting to a number of compounds. In the calculation of the K_p, it is assumed that the activity coefficient is unity and the molecular weight of the product is taken as the mean molecular weight of the surrogate mixture. The α values determined at 293 K are assumed to be constant over the temperature range studied (273–313 K). The enthalpy of vaporization, ΔH_v of the products can also be estimated by the group contribution method. By plotting the estimated vapor pressure of the product against the temperature, the ΔH_v of the product can be estimated from the slope of the line following the Clausius–Clapeyron equation give in the following. Estimated values of ΔH_v of major products are listed in Table 4.1.

Gas/particle partitioning coefficient. The gas/particle partitioning coefficient for compound i to a condensed phase of i only is given by (Pankow, 1994a, b)

$$K_{p,i} = \frac{RT}{10^6 MW_i p^o_{L,i}} \quad (4.4)$$

where $R = 8.2 \times 10^{-5}$ m^3 atm mol^{-1} K^{-1}, MW$_i$ = molecular weight of i (g mol^{-1}), and $p^o_{L,i}$ is the vapor pressure of pure i as a liquid (atm). When multiple condensed–phase compounds exist

$$K_{p,i} = \frac{RTf}{10^6 \overline{MW} \zeta_i p^o_{L,i}} \quad (4.5)$$

where f = weight fraction of the total particulate matter that is the absorbing phase, $\overline{MW}$ is the mean molecular weight of the absorbing organic phase (g mol^{-1}), and ζ_i = mole–

fraction–based activity coefficient. $K_{p,i}$ varies as a function of T, through both its explicit

dependence on T as well as the strong dependence of $p_{L,i}^o$ on T. The value of $K_{p,i}$ is also

influenced by ζ_i and $\overline{MW}$ owing to the types and amounts of condensed–phase

compounds. The vapor pressure of each component obeys Clausius–Clapeyron equation,

$$p_{L,i}^o(T) = p_{L,i}^o(T_o)\exp\left[-\frac{\Delta H_{v,i}}{R}\left(\frac{1}{T}-\frac{1}{T_o}\right)\right] \quad (4.6)$$

For a set of compounds at a given T, $p_{L,i}^o$ tends to decrease with increasing $\Delta H_{v,i}$.

The variation of gas–partitioning coefficient with temperature results from variation of

$p_{L,i}^o$ as well as the explicit dependence on T,

$$\frac{K_{p,i}(T)}{K_{p,i}(T_o)} = \left(\frac{T}{T_o}\right)\frac{p_{L,i}^o(T_o)}{p_{L,i}^o(T)} = \left(\frac{T}{T_o}\right)\exp\left[-\frac{\Delta H_{v,i}}{R}\left(\frac{1}{T}-\frac{1}{T_o}\right)\right] \quad (4.7)$$

Following Pankow and Chang (2008), one may choose $\Delta H_v = 100$ kJ mol^{-1} as a

"reference" value of $\Delta H_{v,i}$, so that any $\Delta H_{v,i}$ can be written as a multiple of the reference

value, $\Delta H_{v,i} = a_i \times 100$ kJ mol^{-1}. For $T_o = 293$K, for $a_i = 1$, a 10 K decrease in T leads to

$$\frac{K_{p,i}(283K)}{K_{p,i}(293K)} = \left(\frac{283}{293}\right)\exp\left[-\frac{100}{R}\left(\frac{1}{283}-\frac{1}{293}\right)\right] = 4.1 \quad (4.8)$$

Thus, for a compound with $\Delta H_v = 100$ kJ mol^{-1}, a 10 K decrease in T leads to a factor of

4 increase in $K_{p,i}$. For a compound with $a_i = 0.5$, the increase of $K_{p,i}$ for a 10 K decrease

in T is about a factor of 2. Note that the factor (T/T_o) exerts only a minor effect compared

to that from the temperature dependence of $p_{L,i}^o$.

As shown in Figure 4.2, the predicted SOA yield increases as the temperature decreases, as lower temperature favors the partitioning of gas–phase reaction products into the particle phase. The model predicts a stronger temperature dependence of SOA yield than that observed by Pathak et al. (2007). The predicted SOA yields agree well with those measured at 293 and 303 K. The mean absolute fractional error between the measured and predicted SOA yields, *err* is 0.1666 and 0.0895 at 293 and 303 K, respectively. On the other hand, the predicted SOA yields are higher than those measured at 288 K (*err* = 0.6728) and 273 K (*err* = 0.6266) but slightly lower than those measured at 313 K (*err* = 0.1968). In the product–specific model, the temperature dependence of the vapor pressure of major products is estimated directly using the group contribution method (Pankow and Asher, 2008). In this approach, uncertainties in the vapor pressure estimation method will lead to uncertainties in data fitting. Uncertainties in the vapor pressure estimation using the group contribution method is likely one factor contributing to a relatively large deviation between measured and predicted values at lower temperatures in present study.

SOA Composition. At a given temperature and organic massing loading, *M* the mass yield of the product *i*, Y_i can be determined as:

$$Y_i = \frac{M_i}{\Delta HC} = \frac{MK_{p,i}}{1 + MK_{p,i}} \alpha_i \qquad (4.9)$$

where the mass–based stoichiometric coefficient of the product *i* , α_i , is obtained from the parameterization of SOA yield data using the product–specific model (Table 4.1). M_i is the concentration of product *i* in the particle phase (μg m^{-3}). The SOA yield, *Y*, is the sum

of the mass yields of all products (SOA yield, $Y = \sum_i Y_i$) at a given organic mass loading.

The ratio of mass yield of product i to total yield (Y_i / Y) is the relative contribution of the product i to the total SOA yield (or total SOA mass).

Figure 4.3 shows the predicted relative contributions of the products to the SOA yield at different organic mass loading for the $K_p \times 100$ case. The predicted SOA composition is compared to the measured concentration of the corresponding classes of compounds at one value of M. Yu et al. (1999) reported the product distribution of ozonolysis of α–pinene at 306 K and organic mass loading of 38.8 μg m^{-3}: hydroxy pinonic acid (17.7%), pinic acid and norpinic acid (22.5%), pinonic acid and norpinonic acid, and isomers (36.5%), hydroxy pinonaldehyde (15.9%), and pinonaldehyde and norpinonaldehyde (7.4%).   It is noted that organic peroxides, particle–phase reaction products (e.g., oligomers and esters), and terpenylic acid were not reported in Yu et al. (1999). Docherty et al. (1995) estimated that organic peroxides contributed ~ 47% of the SOA mass at high organic mass loading. The concentration of terpenylic acid in chamber SOA has not been reported previously (Claeys et al. 2009). A smaller effective density of 1 g cm^{-3} was used to calculate the SOA mass in Yu et al. (1999). This change in density will increase the reported percentage of the products.   In addition, the relative abundance of products reported by Yu et al. (1999) may be overestimated if the organic peroxides, terpenylic acid, or other unidentified products contribute significantly to the SOA mass at the given organic mass loading.

As shown in the bottom panel of Figure 4.3, for the $K_p \times 100$ case, the predicted percentage of pinonic acid is about 51%, which is close to the sum of the percentages of pinonic acid and norpinonic acid and isomers and hydroxy pinonaldehyde (52.4%). The predicted percentage of pinonaldehyde is also close to that of pinonaldehyde and norpinonaldehyde (7.4%). On the other hand, the predicted percentage of pinic acid is about 28%, which is smaller than the sum of the percentages of pinic acid and norpinic acid and hydroxy pinonic acid (40.2%). For organic peroxides, using a hydroperoxide as surrogate gives ~ 7% of SOA yield, which is lower than that reported by Docherty et al. (2005) at high organic mass loading. The percentage of terpenylic acid contributes about 5% of the SOA yield. Overall, the $K_p \times 100$ case may give a good first estimation of the gas/particle partitioning and composition of the SOA products at the given organic mass loading and temperature.

O/C and H/C ratios. The chemical composition of SOA formed from ozonolysis of α–pinene has been recently characterized by an Aerodyne high–resolution time–of–flight aerosol mass spectrometer (HR–ToF–AMS) at 298 K (Shilling et al., 2009). This characterization provides measurement of the O/C and H/C ratios at different organic mass loadings; these data provide additional information about the SOA composition and impose important constraints on the SOA parameterization. As shown in Figures 4.4 and 4.5, the data show that the O/C ratio decreases as the organic mass loading increases, while the H/C ratio increases (Shilling et al., 2009). This observation indicates, as

expected, that the SOA is more oxygenated at low organic mass loading than at high organic mass loading.

O/C and H/C ratios of the SOA can also be determined from the predicted SOA composition. At a given organic mass loading, the number of moles of the product i, m_i can be calculated from its particle–phase mass concentration and molecular weight. The number of carbon atoms, $n_{c,i}$, $(O/C)_i$ and $(H/C)_i$ ratios of the product i are known (Table 4.1). The O/C and H/C ratios of the SOA can be determined as follows:

$$O/C = \frac{\sum_i m_i \cdot n_{c,i} \cdot (O/C)_i}{\sum_i m_i \cdot n_{c,i}} \qquad (4.10)$$

$$H/C = \frac{\sum_i m_i \cdot n_{c,i} \cdot (H/C)_i}{\sum_i m_i \cdot n_{c,i}} \qquad (4.11)$$

At 298 K, for the $K_p \times 1$ case (Figure 4.4, upper panel), the modeled O/C ratios decrease from 0.44 to 0.36 as the organic mass loading increases from 0.5 $\mu g\ m^{-3}$ to 150 $\mu g\ m^{-3}$. The predicted O/C ratios are higher than those in Shilling et al. (2009), except at low organic mass loading ($< 1\ \mu g\ m^{-3}$). The predicted ratios decrease less rapidly as the organic mass loading increases. For the $K_p \times 100$ case (Figure 4.4, lower panel), the predicted O/C ratios agree quite well with those measured; predicted O/C ratios decrease from 0.43 to 0.30 as the organic mass loading increases. On the other hand, in both $K_p \times 1$ and $K_p \times 100$ cases, the predicted H/C ratios exceed those measured at these loadings (Figure 4.5).

The O/C ratios of selected major products range from 0.2 to 0.5, which cover the range of the experimental O/C ratios. On the other hand, the H/C ratios of the selected major products range from 1.5 to 1.6, which exceed the reported H/C ratios (1.38 – 1.51). Using the experimentally identified gas–phase reaction products, the predicted H/C ratios do not match those reported at low organic mass loading. Notably, the H/C ratios of the major SOA products identified in the literature range from 1.5 to 1.6. In addition to uncertainties in determination of the O/C and H/C ratios, the formation of oligomers or organic peroxides will shift the H/C ratio without greatly affecting the O/C ratio (Shilling et al., 2009). Formation of esters can alter the H/C and O/C ratios (Müller et al., 2008). The discrepancy in the H/C ratios based on known gas–phase products and those measured stresses the potential importance of particle–phase reactions on the determination of SOA yield and composition in the ozonolysis of α–pinene under dry, dark, and low–NO$_x$ conditions.

Figures 4.4 and 4.5 also show the temperature dependence of the O/C and H/C ratios in the temperature range (273–313 K). For both the $K_p \times 1$ and $K_p \times 100$ cases (Figure 4.4), the modeled O/C ratio increases when the temperature increases. On the other hand, the modeled H/C ratio decreases when the temperature increases (Figure 4.5). At a higher temperature, the less volatile gas–phase products, which are usually more oxygenated (i.e., usually a higher O/C ratio and a lower H/C ratio), partition preferentially into the particle phase than the more volatile gas–phase products. As shown in Figure 4.3 ($K_p \times$ 100 case), the contribution of the pinic acid, which is the least volatile product and is

more oxygenated, increases when the temperature increases from 293 to 306 K. On the other hand, the relative abundance of pinonaldehyde, which is the most volatile product and is the least oxygenated, decreases with increasing temperature. The effect of particle–phase reactions on O/C and H/C ratios at different temperatures is not considered.

We also report here on an α–pinene ozonolysis experiment conducted in the Caltech laboratory chamber under dry, dark, and low–NO_x conditions in the presence of dry $(NH_4)_2SO_4$ particles to generate a data set comparable to that of Shilling et al. (2008, 2009). The chemical composition of the SOA was continuously monitored using an Aerodyne HR–ToF–AMS. Details of the experiment are given below.

Measurement of O/C and H/C ratios of SOA from α–pinene ozonolysis. To provide an additional set of data on the O/C ratio of SOA generated from α–pinene ozonolysis, an experiment was performed in one of the dual Caltech 28 m^3 Teflon chambers. Details of the facility have been described elsewhere (Cocker et al., 2001; Keywood et al., 2004). Before the experiment, the chamber was flushed continuously with dry, purified air for at least 24 h. Aerosol number concentration, size distribution, and volume concentrations were measured by a differential mobility analyzer (DMA, TSI model 3081) coupled with a condensation nucleus counter (TSI model 3760). Ammonium sulfate seed particles were generated by atomizing an aqueous solution of 0.015 M $(NH_4)_2SO_4$ with a constant–rate atomizer. The volume concentration of the seed particles was 12 $\mu m^3 \, cm^{-3}$.

The parent hydrocarbon, α–pinene, and an OH scavenger, cyclohexane, were then introduced separately by injecting known volumes of the liquid hydrocarbon into a glass bulb, subsequently carried into the chamber by an air stream at 5 L min^{-1}. The mixing ratio of α–pinene was monitored with a gas chromatograph coupled with a flame ionization detector (GC–FID, Agilent model 6890N). The initial mixing ratio of α–pinene was 44 ppb. The estimated mixing ratio of cyclohexane was 37 ppm, which corresponds to a rate of cyclohexane + OH 100 times faster than that of α–pinene + OH.

Ozone was generated with a UV lamp ozone generator (EnMet Corporation, MI), and monitored with a commercial ozone analyzer (Horiba Instruments, CA). Ozone injection was stopped after the ozone concentration reached 180 ppb. The aerosol growth data were corrected for wall deposition of particles. First–order size–dependent wall–loss coefficients were determined from a separate seed–only experiment. The final SOA volume was 46 μm^3 cm^{-3}, as measured by the DMA.

Real–time particle mass spectra were collected continuously by an Aerodyne high resolution time–of–flight aerosol mass spectrometer (HR–ToF–AMS). The HR–ToF–AMS is described in detail elsewhere (Canagaratna et al., 2007, and references therein). The HR–ToF–AMS switched once every minute between the high resolution "W–mode" and the lower resolution, higher sensitivity "V–mode". The "V–mode" data were analyzed using a fragmentation table to separate sulfate, ammonium, and organic spectra, and to time–trace specific mass–to–charge ratios. "W–mode" data were analyzed using a

separate high–resolution spectra tool box known as PIKA to determine the chemical formulas contributing to distinct mass–to–charge ratios (DeCarlo et al., 2006).

To determine elemental ratios, the computational toolbox Analytical Procedure for Elemental Separation (APES) was used. This toolbox applies the analysis procedure described in Aiken et al. (2007) to the high–resolution "W–mode" data. The particle–phase signal of CO^+ and the organic contribution to H_xO^+ ions were estimated as described in Aiken et al. (2008). It is noted that chamber air is cleaned through a series of chemical denuders and filters. Fourier transform infrared spectroscopy measurements show that the concentration of CO_2 in the chamber air is nominally the same as that in the atmosphere. Due to the relatively large SOA loadings generated in this study, the sensitivity of the O/C calculation to the CO_2 concentration input is relatively small.

Figure 4.6 shows the time evolution of α–pinene concentration, organic mass loading, and aerosol O/C and H/C ratios. Once the ozone is injected, α–pinene oxidation commences, and the organic mass loading increases almost immediately. When $α$–pinene is completely reacted, organic aerosol mass loading remains unchanged. These observations are consistent with those reported by Ng et al. (2006). Measured O/C and H/C ratios as a function of organic mass loading are shown in Figure 4.7. The data scatter reflects the inherent uncertainty in measurement of O/C and H/C ratios at low organic mass loading. Generally, the H/C ratio increases as time increases, while the O/C ratio decreases. The trends in O/C and H/C ratios are in good agreement with those reported by

Shilling et al. (2009). The absolute values of the O/C ratios are slightly lower than those reported by Shilling et al. (2009), but well within the experimental uncertainty. When all α–pinene is consumed and the SOA growth has leveled out (~ 58 μg m^{-3}), O/C and H/C ratios and fragment mass spectrum (not shown here) remain unchanged. As discussed by Ng et al. (2006), the first oxidation step in the ozonolysis of α–pinene (a hydrocarbon with a single double bond) is most likely the rate–determining step in SOA formation. Either the condensable products are the initial reaction products of the parent hydrocarbon oxidation (first– or higher–generation products), or subsequent reactions (in either the gas or particle phase) proceed at relatively fast rates. Thus, the instantaneous product spectrum can be considered as that at equilibrium during the chamber phase.

To determine the extent to which an equilibrium state is achieved, the chemical composition of SOA can be measured by the Aerodyne HR–ToF–AMS over the course of the chamber experiments. The change in element–to–carbon ratios (e.g., O/C, H/C ratios) can provide insight about the change in SOA composition. If the ratios or the mass spectra do not vary with time, this may suggest that an equilibrium state is achieved within the timescale of the chamber experiment. In that case, major experimentally identified products (both particle–phase and gas–phase reaction products) can be chosen as SOA surrogates in the product–specific model. In addition, the O/C, H/C, N/C, or S/C ratios can be calculated from the detailed gas–chemistry model coupled with gas/particle partitioning theory. Recently, Dzepina et al. (2009) suggest that the O/C ratio and volatility can be used to compare modeled and measured SOA. The authors calculate O/C

ratios using various models and compare these to the measured O/C ratios of ambient Mexico City aerosol. They find that O/C ratios predicted by different models do not agree and are generally lower than the measured ratios.

4.5 Conclusions

In this chapter, we show that although good agreement in O/C ratio between observations and predictions can exist, a discrepancy in H/C ratio is not removed by data fitting. Hence, in addition to the O/C ratio, other element–to–carbon ratios such as H/C are important for modeling fitting and comparison. S/C and N/C ratios could be used once accurate determinations can be made using the AMS. These element–to–carbon ratios can also be calculated using detailed gas–chemistry models coupled with gas/particle partitioning theory and can be used as additional constraints on the SOA parameterization in chamber experiments and modeling studies.

SOA yields from volatile organic compounds are determined from laboratory chamber data. Gas–particle partitioning of semivolatile oxidation products forms the basis of all current models of SOA formation. As identification of aerosol–phase products has become feasible using advanced mass spectrometric techniques, we investigate the extent to which a product–specific model, certain parameters of which are determined from chamber data, can be used to represent SOA formation. In the present work we address this question using data on SOA formation in the α–pinene/ozone system. While the product–specific model can be fit to available chamber data, fitting of the product–

specific model required increasing estimated equilibrium partitioning coefficients by two orders of magnitude, and the predicted fractional contributions of the selected products to SOA are unreasonable in several respects and no better than a fitting of the data to a volatility basis set representation. The performance of the product–specific model is most likely hindered by lack of explicit inclusion of particle–phase accretion compounds that are almost certainly present but have yet to be identified in this system. Prospects for identification of the majority of SOA products for major VOC classes remain promising. However, for the near future, empirical product Odum–type or volatility basis set models remain the approaches of choice.

4.6 Acknowledgements

4.7 References

Aiken, A. C., DeCarlo, P. F., and Jimenez, J. L.: Elemental analysis of organic species with electron ionization high–resolution mass spectrometry, *Anal. Chem.*, 79, 8350–8358, 2007.

Aiken, A. C., Decarlo, P. F., Kroll, J. H., Worsnop, D. R., Huffman, J. A., Docherty, K. S., Ulbrich, I. M., Mohr, C., Kimmel, J. R., Sueper, D., Sun, Y., Zhang, Q., Trimborn, A., Northway, M., Ziemann, P. J., Canagaratna, M. R., Onasch, T. B., Alfarra, M. R., Prevot, A. S. H., Dommen, J., Duplissy, J., Metzger, A., Baltensperger, U., and Jimenez, J. L.: O/C and OM/OC ratios of primary, secondary, and ambient organic aerosols with high–resolution time–of–flight aerosol mass spectrometry, *Environ. Sci. Technol.*, 42, 4478–4485, 2008.

Bahreini, R., Keywood, M. D., Ng, N. L., Varutbangkul, V., Gao, S., Flagan, R. C., Seinfeld, J. H.,Worsnop, D. R., and Jimenez, J. L.: Measurements of secondary organic aerosol from oxidation of cycloalkenes, terpenes, and m–xylene using an Aerodyne aerosol mass spectrometer, *Environ. Sci. Technol.*, 39, 5674–5688, 2005.

Bilde, M., and Pandis, S. N.: Evaporation rates and vapor pressures of individual aerosol species formed in the atmospheric oxidation of alpha– and beta–pinene, *Environ. Sci. Technol.*, 35, 3344–3349, 2001.

Canagaratna, M. R., Jayne, J. T., Jimenez, J. L., Allan, J. D., Alfarra, M. R., Zhang, Q., Onasch, T. B., Drewnick, F., Coe, H., Middlebrook, A., Delia, A., Williams, L. R., Trimborn, A. M., Northway, M. J., DeCarlo, P. F., Kolb, C. E., Davidovits, P., and Worsnop, D. R.: Chemical and microphysical characterization of ambient aerosols with the aerodyne aerosol mass spectrometer, *Mass. Spectrom. Rev.*, 26, 185–222, 2007.

Chan, A. W. H., Kroll, J. H., Ng, N. L., and Seinfeld, J. H.: Kinetic modeling of secondary organic aerosol formation: effects of particle– and gas–phase reactions of semivolatile products, *Atmos. Chem. Phys.*, 7, 4135–4147, 2007.

Chen, J. J., and Griffin, R. J.: Modeling secondary organic aerosol formation from oxidation of alpha–pinene, beta–pinene, and dlimonene, *Atmos. Environ.*, 39, 7731–7744, 2005.

Claeys, M., Iinuma, Y., Szmigielski, R., Surratt, J. D., Blockhuys, F., Van Alsenoy, C., B¨oge, O., Sierau, B., G´omez–Gonz´alez, Y., Vermeylen, R., Van der Veken, P., Shahgholi, M., Chan, A. W. H., Herrmann, H., Seinfeld, J. H., and Maenhaut, W.: Terpenylic acid and related compounds from the oxidation of α–pinene: Implications for new particle formation and growth above forests, *Environ. Sci. Technol.*, 43, 6976–6982, 2009.

Cocker, D. R., Flagan, R. C., and Seinfeld, J. H.: State–of–the–art chamber facility for studying atmospheric aerosol chemistry, *Environ. Sci. Technol.*, 35, 2594–2601, 2001.

DeCarlo, P. F., Kimmel, J. R., Trimborn, A., Northway, M. J., Jayne, J. T., Aiken, A. C., Gonin, M., Fuhrer, K., Horvath, T., Docherty, K. S., Worsnop, D. R., and Jimenez, J. L.: Field–deployable, high–resolution, time–of–flight aerosol mass spectrometer, *Anal. Chem.*, 78, 8281–8289, 2006.

Docherty, K. S., Wu, W., Lim, Y. B., and Ziemann, P. J.: Contributions of organic peroxides to secondary aerosol formed from reactions of monoterpenes with O–3, *Environ. Sci. Technol.*, 39, 4049–4059, 2005.

Donahue, N. M., Robinson, A. L., Stanier, C. O., and Pandis, S. N.: Coupled partitioning, dilution, and chemical aging of semivolatile organics, *Environ. Sci. Technol.*, 40, 2635–2643, 2006.

Dzepina, K., Volkamer, R. M., Madronich, S., Tulet, P., Ulbrich, I. M., Zhang, Q., Cappa, C. D., Ziemann, P. J., and Jimenez, J. L.: Evaluation of new secondary organic aerosol models for a case study in Mexico City, *Atmos. Chem. Phys. Discuss.*, 9, 4417–4488, 2009.

Gao, S., Keywood, M., Ng, N. L., Surratt, J., Varutbangkul, V., Bahreini, R., Flagan, R. C., and Seinfeld, J. H.: Low–molecular weight and oligomeric components in secondary organic aerosol from the ozonolysis of cycloalkenes and alpha–pinene, *J. Phys. Chem. A*, 108, 10147–10164, 2004.

Hallquist, M., Wenger, J. C., Baltensperger, U., Rudich, Y., Simpson, D., Claeys, M., Dommen, J., Donahue, N. M., George, C., Goldstein, A. H., Hamilton, J. F., Herrmann, H., Hoffmann, T., Iinuma, Y., Jang, M., Jenkin, M. E., Jimenez, J. L., Kiendler–Scharr, A., Maenhaut, W., McFiggans, G., Mentel, Th. F., Monod, A., Prevot, A. S. H., Seinfeld, J. H., Surratt, J. D., Szmigielski, R., and Wildt, J.: The formation, properties and impact of secondary organic aerosol: Current and emerging issues, *Atmos. Chem. Phys.*, 9, 5155–5235, 2009.

Iinuma, Y., Boge, O., Gnauk, T., and Herrmann, H.: Aerosolchamber study of the alpha–pinene/O$_3$ reaction: Influence of particle acidity on aerosol yields and products, *Atmos. Environ.*, 38, 761–773, 2004.

Jenkin, M. E.: Modeling formation and composition of secondary organic aerosol from α– and β–pinene ozonolysis using MCM v3, *Atmos. Chem. Phys.*, 4, 1741–1757, 2004.

Keywood, M. D., Varutbangkul, V., Bahreini, R., Flagan, R. C., and Seinfeld, J. H.: Secondary organic aerosol formation from the ozonolysis of cycloalkenes and related compounds, *Environ. Sci. Technol.*, 38, 4157–4164, 2004.

Kroll, J. H., and Seinfeld, J. H.: Representation of secondary organic aerosol laboratory chamber data for the interpretation of mechanisms of particle growth, *Environ. Sci. Technol.*, 39, 4159–4165, 2005.

Muller, L., Reinnig, M.–C., Warnke, J., and Hoffmann, Th.: Unambiguous identification of esters as oligomers in secondary organic aerosol formed from cyclohexene and cyclohexene/alpha–pinene ozonolysis, *Atmos. Chem. Phys.*, 8, 1423–1433, 2008.

Ng, N. L., Kroll, J. H., Keywood, M. D., Bahreini, R., Varutbangkul, V., Flagan, R. C., Seinfeld, J. H., Lee, A., and Goldstein, A. H.: Contribution of first– versus second–generation products to secondary organic aerosols formed in the oxidation of biogenic hydrocarbons, *Environ. Sci. Technol.*, 40, 2283–2297, 2006.

Odum, J. R., Hoffmann, T., Bowman, F., Collins, D., Flagan, R. C., and Seinfeld, J. H.: Gas/particle partitioning and secondary organic aerosol yields, *Environ. Sci. Technol.*, 30, 2580–2585, 1996.

Pankow, J. F.: An absorption–model of gas–particle partitioning of organic–compounds in the atmosphere, *Atmos. Environ.*, 28, 185–188, 1994a.

Pankow, J. F.: An absorption–model of the gas aerosol partitioning involved in the formation of secondary organic aerosol, *Atmos. Environ.*, 28, 189–193, 1994b.

Pankow, J. F., and Asher, W. E.: SIMPOL.1: a simple group contribution method for predicting vapor pressures and enthalpies of vaporization of multifunctional organic compounds, *Atmos. Chem. Phys.*, 8, 2773–2796, 2008.

Pankow, J. F., and Chang, E. I.: Variation in the sensitivity of predicted levels of atmospheric organic particulate matter (OPM), *Environ. Sci. Technol.*, 42, 7321–7329, 2008.

Pankow, J. F., Seinfeld, J. H., Asher, W. E., and Erdakos, G. B.: Modeling the formation of secondary organic aerosol. 1. Application of theoretical principles to measurements obtained in the alpha–pinene/, beta– pinene/, sabinene/, Delta(3)–carene/, and cyclohexene/ozone systems, *Environ. Sci. Technol.*, 35, 1164–1172, 2001.

Pathak, R. K., Stanier, C. O., Donahue, N. M., and Pandis, S. N.: Ozonolysis of alpha–pinene at atmospherically relevant concentrations: Temperature dependence of aerosol

mass fractions (yields), *J. Geophys. Res.–Atmos.*, 112, D03201, 2007, doi:10.1029/ 2006JD007436.

Presto, A. A. and Donahue, N. M.: Investigation of alpha–pinene plus ozone secondary organic aerosol formation at low total aerosol mass, *Environ. Sci. Technol.*, 40, 3536–3543, 2006.

Seinfeld, J. H., Erdakos, G. B., Asher, W. E., and Pankow, J. F.: Modeling the formation of secondary organic aerosol (SOA). 2.The predicted effects of relative humidity on aerosol formation in the alpha–pinene–, beta–pinene–, sabinene–, Delta(3)–Carene–, and cyclohexene–ozone systems, *Environ. Sci. Technol.*, 35, 1806–1817, 2001.

Shilling, J. E., Chen, Q., King, S. M., Rosenoern, T., Kroll, J. H., Worsnop, D. R., McKinney, K. A., and Martin, S. T.: Particle mass yield in secondary organic aerosol formed by the dark ozonolysis of alpha–pinene, *Atmos. Chem. Phys.*, 8, 2073–2088, 2008.

Shilling, J. E., Chen, Q., King, S. M., Rosenoern, T., Kroll, J. H., Worsnop, D. R., DeCarlo, P. F., Aiken, A. C., Sueper, D., Jimenez, J. L., and Martin, S. T.: Loading–dependent elemental composition of α–pinene SOA particles, *Atmos. Chem. Phys.*, 9, 771–782, 2009.

Stanier, C. O., Donahue, N., and Pandis, S. N.: Parameterization of secondary organic aerosol mass fractions from smog chamber data, *Atmos. Environ.*, 42, 2276–2299, 2008.

Yu, J. Z., Cocker, D. R., Griffin, R. J., Flagan, R. C., and Seinfeld, J. H.: Gas–phase ozone oxidation of monoterpenes: Gaseous and particulate products, *J. Atmos. Chem.*, 34, 207–258, 1999.

Table 4.1: Major products chosen to represent the ozonolysis of α–pinene under dry, dark, and low–NO$_x$ conditions in the presence of dry ammonium sulfate particles

Product	Chemical structure	O/C	H/C	ΔH_v [c]	Product–Specific Model ($K_p \times 1$ case)		($K_p \times 100$ case)		Volatility Basis Set		α from Product–Specific Model ($K_p \times 100$ case)
					K_p [a] (c^*)	α	K_p (c^*)	α	K_p (c^*)	α	
Pinic acid $C_9H_{14}O_4$ (MW: 186)		0.444	1.556	99.89	0.2822 (3.544)	0.2308	28.22 (0.0354)	0.0563	100 (0.01)	0.0707	0.0563 (Pinic acid: $c^* = 0.0354$)
Terpenylic acid [b] $C_8H_{12}O_4$ (MW: 172)		0.5	1.5	76.73	0.0332 (30.12)	0.0172	3.32 (0.3012)	0.0132	10 (0.1)	0.0110	0.0131 (Terpenylic acid: $c^* = 0.3012$)
Hydroperoxide $C_{10}H_{16}O_4$ (MW: 200)		0.4	1.6	83.99	0.0029 (344.8)	0.0181	0.29 (3.448)	0.0173	1 (1)	0.0120	0.0172 (Hydroperoxide: $c^* = 3.448$)
Pinonic acid $C_{10}H_{16}O_3$ (MW: 184)		0.3	1.6	81.72	0.0018 (555.6)	0.6883	0.18 (5.556)	0.1573	0.1 (10)	0.1603	0.1573 (Pinonic acid: $c^* = 5.556$)
									0.01 (100)	0.0210	–
Pinonaldehyde $C_{10}H_{16}O_2$ (MW: 168)		0.2	1.6	69.53	1.14×10^{-5} (87334)	1	1.15×10^{-3} (873.34)	0.9380	0.001 (1000)	0.9554	0.9380 (Pinonaldehyde: $c^* = 873.34$)

[a] Vapor pressure is determined at 293 K using a model developed by Pankow and Asher (2008). K_p is determined at 293 K with the assumption of activity coefficient of the products equal to one and the molecular weight of product i is used as mean molecular weight in organic absorbing phase, as a first approximation; [b] (Claeys et al., 2009); [c] The enthalpy of vaporization, ΔH_v (kJ mol^{-1}) of the product is estimated by plotting the estimated vapor pressure of the product against temperature. The ΔH_v of the product can be estimated from the slope of the line following the Clausius–Clapeyron equation.
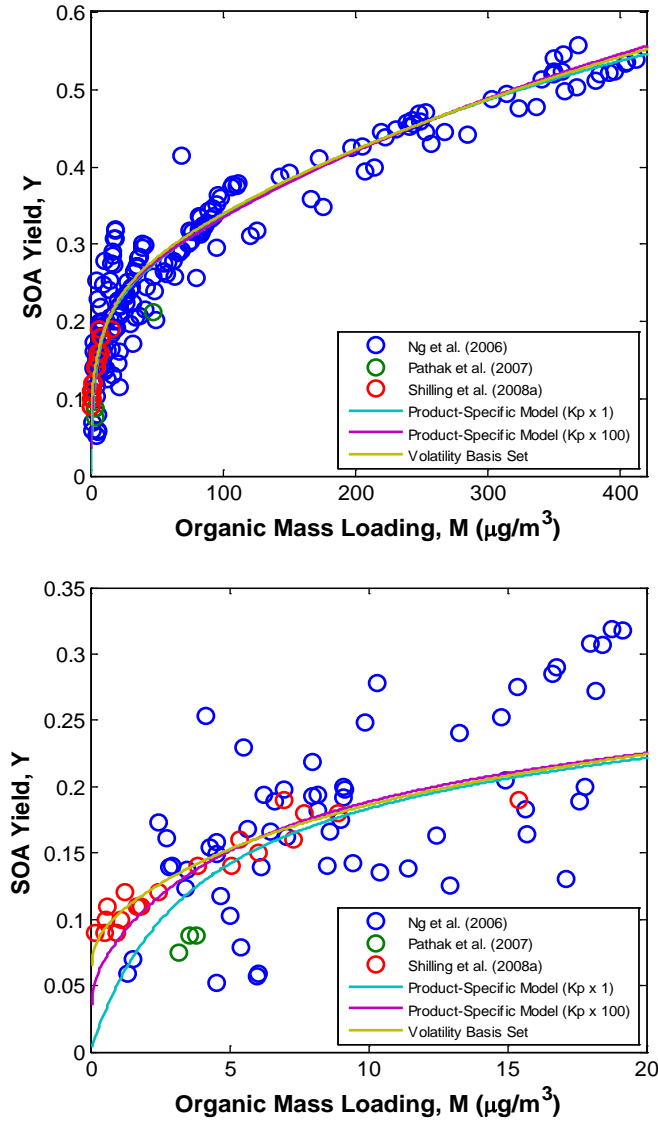
Figure 4.1: SOA yield of ozonolysis of α–pinene at different organic mass loading, *M*. Data of ozonolysis of α–pinene are obtained from experiments conducted under dry, dark, and low–NO$_x$ condition in the presence of dry ammonium sulfate particles (Ng et al., 2006; Pathak et al., 2007; Shilling et al., 2008). **Top panel**: organic mass loading: 0–411μg m^{-3}; **Bottom panel**: organic mass loading: 0–20 μg m^{-3}. SOA yield data are adjusted to 293 K, using a temperature correction factor. Lines show the model fit with the parameters given in Table 4.1.
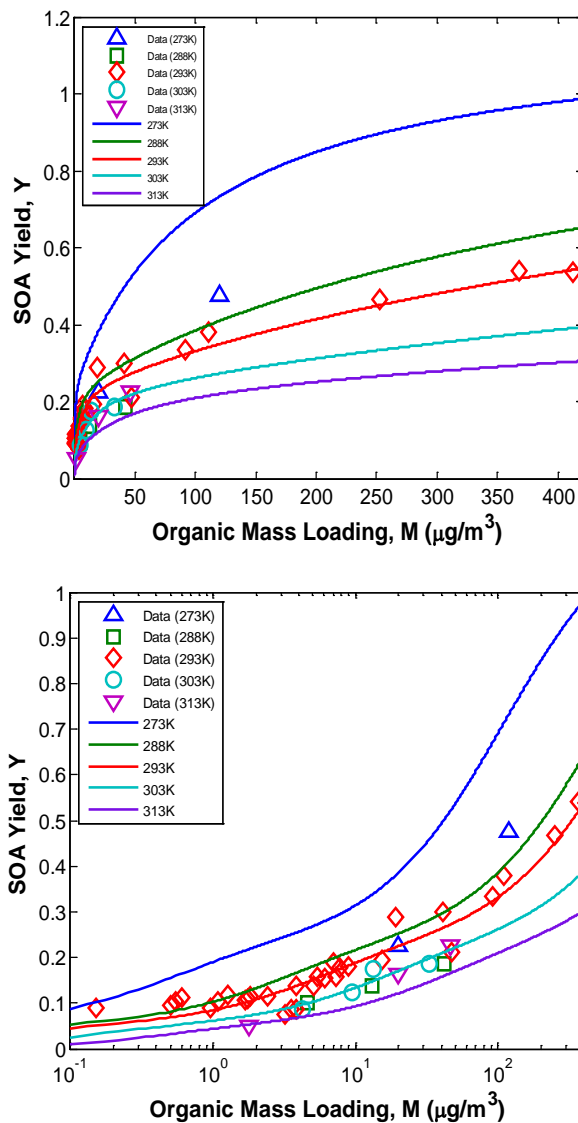
Figure 4.2: Temperature dependence of SOA yield of ozonolysis of α–pinene obtained from experiments conducted under dry, dark, and low–NO$_x$ condition in the presence of dry ammonium sulfate particles. Data (293 K) are the final SOA yields from Ng et al. (2006), Pathak et al. (2007), and Shilling et al. (2008). Data from Shilling et al. (2008) have been adjusted to 293 K. Data at other temperatures are obtained from Pathak et al. (2007). The lines show the model fit at different temperatures for the $K_p \times 100$ case.
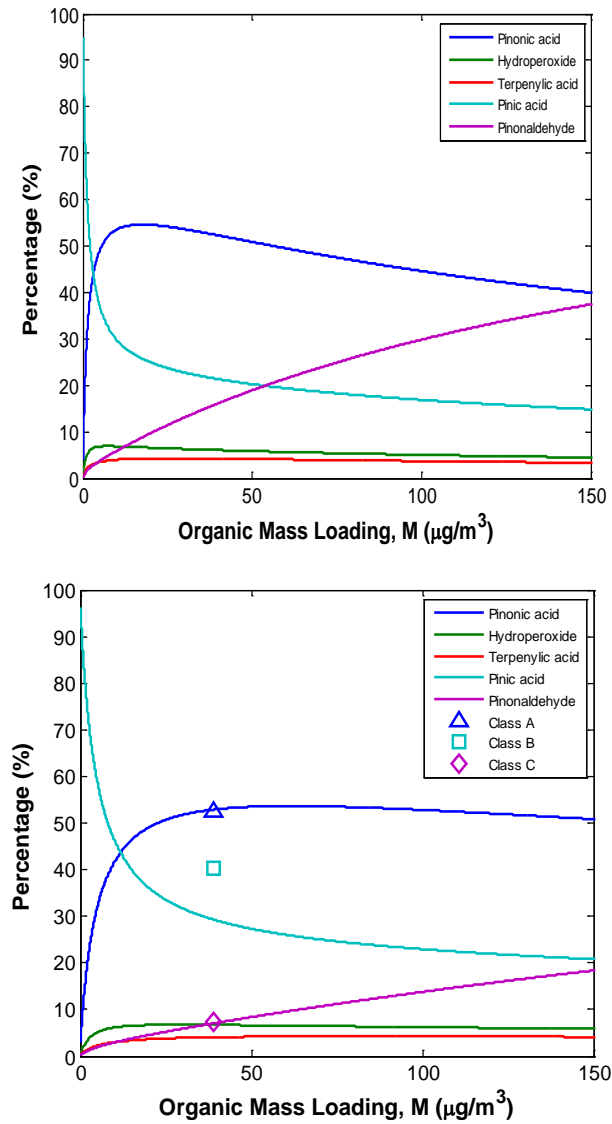
Figure 4.3: Relative contributions of the modeled products to the SOA yield at different organic mass loadings for $K_p \times 100$ case at different temperatures (solid curves). **Top panel**: 293 K; **Bottom panel**: 306 K; Class A data point refers to the sum of the percentage of pinonic acid and norpinonic acid and isomers and hydroxy pinonaldehyde (Yu et al., 1999); Class B data point refers to the sum of the percentage of pinic acid and norpinic acid and hydroxy pinonic acid (Yu et al., 1999); Class C data point refers to the sum of the percentage of pinonaldehyde and norpinonaldehyde (Yu et al., 1999).
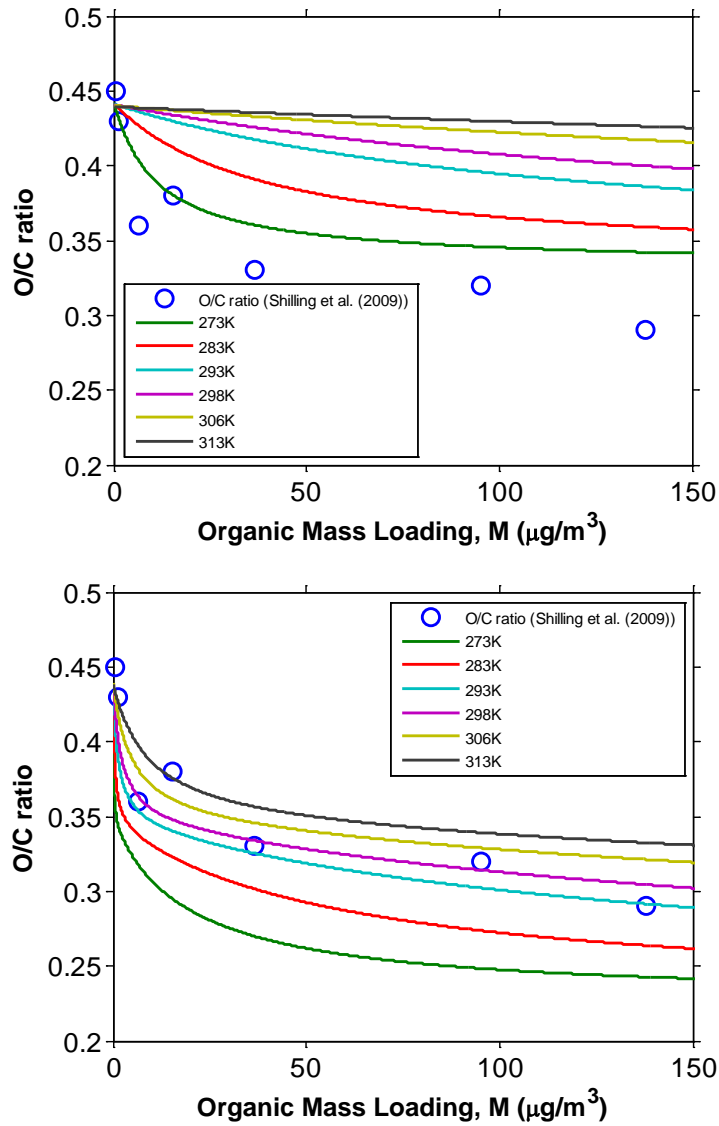
Figure 4.4: O/C ratio of SOA formed from the ozonolysis of α–pinene under dry, dark, and low–NO$_x$ condition in the presence of dry ammonium sulfate particles as function of organic mass loading, *M,* at different temperatures. **Top panel**: $K_p \times 1$ case; **Bottom panel**: $K_p \times 100$ case; Blue open circles are experimental O/C ratios reported by Shilling et al. (2009) at 298 K.

Figure 4.5: H/C ratio of SOA formed from the ozonolysis of α–pinene under dry, dark, and low–NO$_x$ condition in presence of dry ammonium sulfate particles as function of organic mass loading, *M,* at different temperatures. **Top panel**: $K_p \times 1$ case; **Bottom panel**: $K_p \times 100$ case; Blue open circles are experimental H/C ratios reported by Shilling et al. (2009) at 298 K.
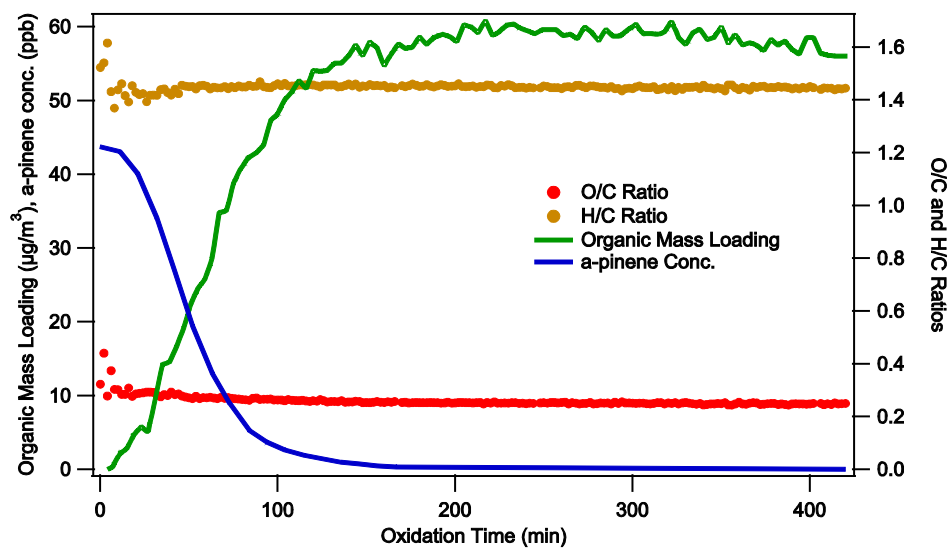
Figure 4.6: Time evolution of α–pinene concentration, organic mass loading, and the O/C and H/C ratios in the ozonolysis of α–pinene under dry, dark, and low–NO$_x$ condition in presence of dry ammonium sulfate particles. Experiment conducted in Caltech laboratory chamber.
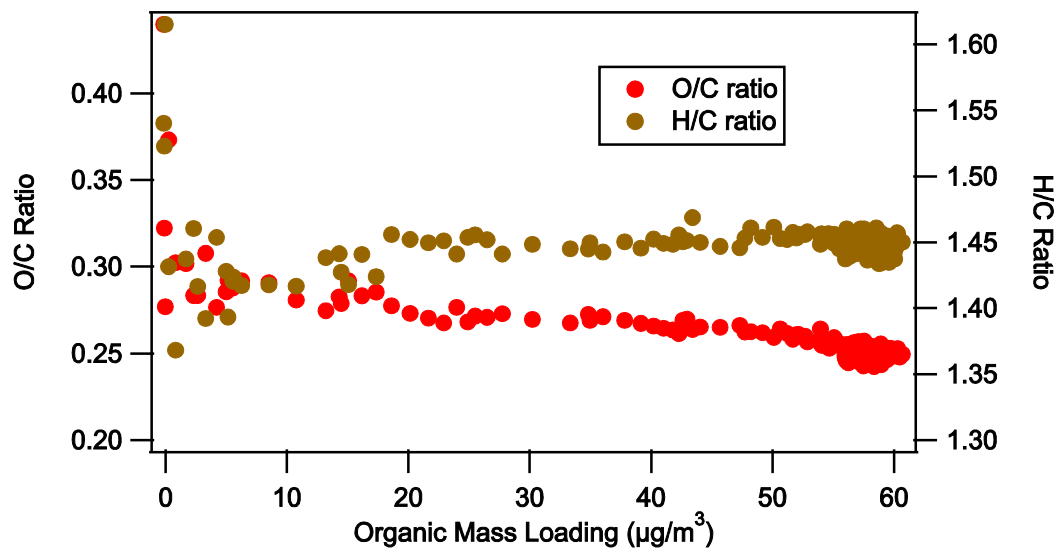
Figure 4.7: O/C and H/C ratio of SOA formed from the ozonolysis of α–pinene under dry, dark, and low–NO_x condition in presence of dry ammonium sulfate particles as function of organic mass loading, *M*. Experiment conducted in Caltech laboratory chamber.

Chapter 5

Conclusions and Future Works

5.1 Conclusions

This thesis demonstrates how the aerosol composition data collected from both laboratory–generated secondary organic aerosol (SOA) and ambient aerosol using advanced mass spectrometric techniques help us to better understand the composition and formation mechanisms of SOA in chamber studies, to identify the sources of organic compounds in ambient aerosol, and to the model the formation and composition of SOA.

Recent laboratory chamber and modeling studies have shown that the oxidation of isoprene is a significant source of SOA in the atmosphere and suggest that isoprene–derived epoxydiols (IEPOX) are an important precursor for isoprene SOA. The role of IEPOX in the SOA formation in the atmosphere, however, is not known. In Chapter 2, we analyze both isoprene SOA generated from the photooxidation of isoprene under low NO_x conditions in the chamber experiments and ambient aerosol collected in downtown Atlanta, GA, and rural Yorkville, GA, during 2008 AMIGAS using gas chromatography/quadrupole mass spectrometry and gas chromatography/time–of–flight mass spectrometry with prior trimethylsilylation. We firstly report the detection of IEPOX in ambient aerosol and the mass concentrations of IEPOX range from ~ 1 to 24 ng m^{-3}. The concentration of IEPOX correlate well with 2–methylterols and organosulfates of 2–methylterols in the ambient samples analyzed. This observation is in good agreement with the laboratory findings that the hydrolysis of IEPOX in the presence of sulfate ions gives these two compounds. The detection of particle–phase IEPOX in the AMIGAS samples supports recent laboratory

results that gas–phase IEPOX produced from the photooxidation of isoprene under low–
NO_x conditions is a key precursor of ambient isoprene SOA formation and demonstrates
the significance of isoprene oxidation to the formation of ambient aerosol in this region.

While β–caryphyllene has been suggested as a source of ambient SOA, the formation
mechanisms and significance of β–caryphyllene SOA in the atmosphere remain unclear.
In Chapter 3, we first investigate the chemical composition of β–caryophyllene SOA using
ultra–performance liquid chromatography/electrospray ionization–time–of–flight mass
spectrometry at different levels of aerosol acidity. We propose gas–phase reaction
mechanisms for the photooxidation of β–caryphyllene based on the compounds detected in
particle phase. Once the gas–phase oxidation compounds condensed into the particle phase,
they may undergo further chemical reactions. Particle–phase compounds such as
organosulfates are detected in the presence of acidic sulfate seed particles. Increased acidity
leads to different effects on the abundance of individual products; significantly, abundances
of organosulfates are correlated with aerosol acidity. The increase of certain particle–phase
reaction products with increased acidity provides chemical evidences to support the
observed acid–enhanced SOA yields. To investigate the significance of β–caryophyllene
SOA in the atmosphere, we analyze the ambient aerosol collected from 2008 AMIGAS.
Based on the agreement between the chromatographic retention times and accurate mass
measurements of chamber and field samples, some compounds detected in laboratory–
generated β–caryophyllene SOA are present in ambient aerosol. We suggest that in
addition to β–caryophyllinic acid, three β–caryphyllene oxidation products (β–

nocaryophyllon aldehyde, β–hydroxynocaryophyllon aldehyde, and β–dihydroxynocaryophyllon aldehyde) can be consideral chemical tracers for β–caryophyllene SOA.

Current equilibrium partitioning models (e.g., empirical two–product (Odum), product–specific, and volatility basis set) have been developed to predict the SOA formation. However, these models cannot predict the composition of SOA, which determines the physiochemical properties of SOA. A product–specific model is proposed here to predict the formation and compos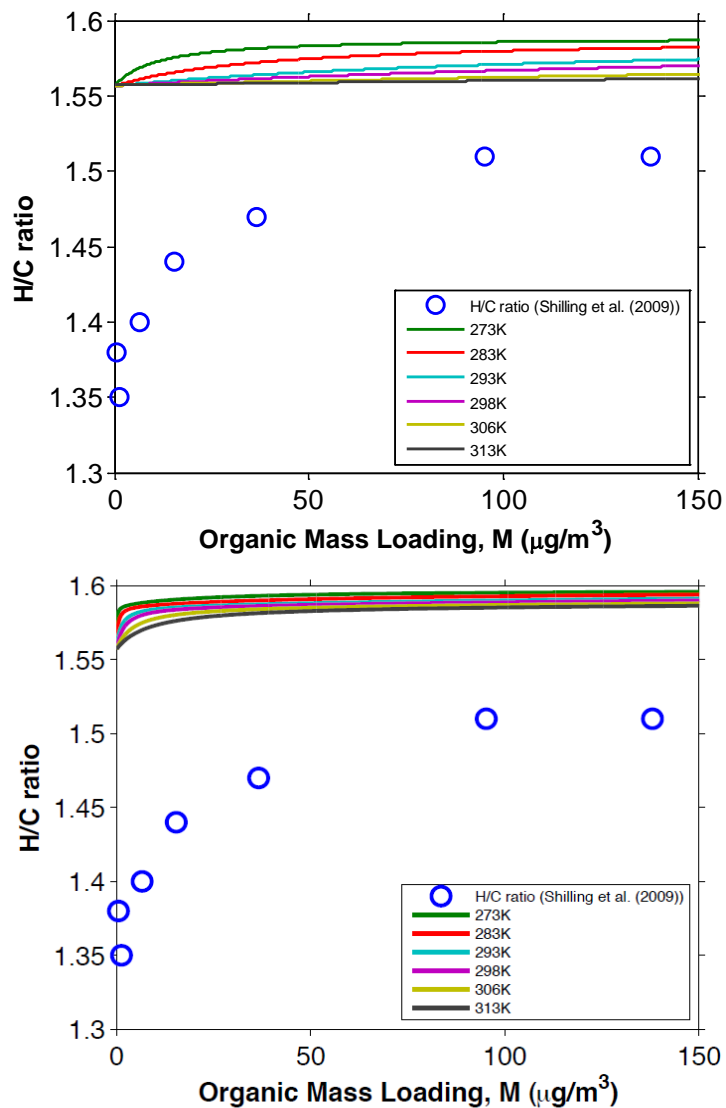ition of SOA formed from the ozonolysis of α–pinene under dry, dark, and low–NO$_x$ conditions in the presence of ammonium sulfate seed aerosol. Using five major identified compounds, the model is fit to the chamber data. From the optimal fitting, the SOA composition (e.g., organic–to–carbon (O/C) and hydrogen–to–carbon (H/C) ratios) are modeled at different temperatures and organic mass loadings. While the model can well capture the measured O/C ratios, the discrepancy between measured H/C ratios and those based on the major gas–phase oxidation compounds used in the model fitting suggests the significance of particle–phase reactions. The product–specific model is likely hindered by lack of explicit inclusion of particle–phase chemistry. To accurately model the composition and formation of SOA in the chamber studies, current thermodynamic equilibrium models should be extended to include gas– and particle–phase reactions. If an equilibrium state is not attained during the chamber phase, the development of kinetic models in which reaction products undergo reactions in both gas–phase and particle–phase is needed to describe the SOA formation and composition. While the

prospects for identification of the majority of SOA compounds for major volatile organic compounds classes remain promising, empirical product– or volatility basis set models remain the approaches of choice in the near future.

5.2 Future Works

Recent studies have shown that the composition of SOA formed from the ozonolysis and photooxidation of biogenic and anthropogenic VOCs depends on the organic mass loadings. The Aerodyne aerosol mass spectrometer (AMS) has been widely used to provide real–time bulk, chemical characterization of organic compounds in laboratory– generated SOA and ambient aerosol. f_{44} and f_{43}, which are the ratios of the organic signal at m/z 44 (mainly $C_2H_3O^+$) and m/z 43(CO_2^+) to the total organic signal, respectively, elemental–to–carbon molar ratios (e.g., O/C and H/C ratios), and whole–particle mass spectra can be used to indicate the oxidation state and chemical characteristics of the SOA. Shilling et al. (2009) have shown that the mass spectra of α–pinene SOA measured by the AMS depend on the organic mass loadings. They found that α–pinene SOA become less oxygenated at higher loadings (the O/C ratio decreases from 0.45 to 0.29 when the organic mass loading increases from ~ 0.5 to ~ 140 μgm^{-3}). Chhabra et al. (2010, 2011) have used the AMS to extensively investigate the variability of the composition of SOA formed in laboratory chamber experiments from various biogenic and anthropogenic precursors. They observed that the O/C ratio decreases when the organic mass loading increases during the course of the experiments. One possible explanation for these observations is that more volatile and less oxidized gas–phase products can condense into the particle–phase as the

organic mass loading increases. A nonlinear behavior of the oxidation state of the SOA formed from the photooxidation of α–pinene, m–xylene, and p–xylene (O/C ratio, f_{44}, and f_{43}) as a function of the organic mass loading can be attributed to the volatilities of gas–phase products that can partition into the particle–phase (Kang et al., 2011). It is noted that organic mass loadings investigated in the laboratory have often been greater than the typical ambient loadings of 10 μg m^{-3} or less. More volatile gas–phase products can partition into the particle–phase than would at lower loadings. While the particle compositions have been studied using the AMS, thermal desorption/vaporization of aerosol particles and electron impact ionization utilized in the AMS cause significant fragmentation. Much of the chemical identity of organic compounds is lost, and this precludes the molecular speciation of organic compounds. An improved understanding of the composition of the SOA, especially at typical ambient loadings, is needed.

In typical chamber and flow tube experiments, the VOCs and gas–phase products are continuously oxidized. The evolution and gas/particle partitioning of gas–phase products occur simultaneously during the SOA growth. It is difficult to determine and identify which gas–phase products are responsible for the SOA growth. For example, at a given loading, gas–phase products, which have low enough volatility, can partition into the particle–phase immediately and will not be detected by the mass spectrometer. It is thus important to understand which gas–phase products condense into the particle–phase at typical ambient loadings. Overall, measurements under typical ambient loadings can provide better insights into the formation and properties of SOA and are important for the accurate prediction by

chemical transport models of SOA formation in the atmosphere. Here, I propose to investigate the gas/particle partitioning of gas–phase products and the SOA composition at typical ambient organic mass loadings (1–10 $\mu g \ m^{-3}$).

Experimental approach. To investigate the formation and composition of the SOA at loadings below 10 $\mu g m^{-3}$, a preset amount of the VOC will first be introduced into the chamber together with the oxidant precursors. As in the traditional chamber experiments, the UV lamps will be turned on to initiate the photooxidation of the VOC without seed particles. Oxidation of the VOC typically produces a number of gas–phase products of different volatilities. Unlike the nucleation experiments, the VOC and gas–phase products will be allowed to undergo oxidization for a period of time without the occurrence of nucleation. The evolution of gas–phase products will be monitored by a chemical ionization mass spectrometer. The particle size (or volume) and particle mass spectra will be monitored by the differential mobility analyzer and AMS, respectively, to ensure that nucleation does not occur. After a certain period of time, the UV lamps will be turned off and seed particles will be introduced into the chamber. Some gas–phase products will partition into the seed particles. The change in concentration of gas–phase products and the size and composition of aerosol particles will be monitored. To avoid a nucleation event during the ageing period and to have final organic mass loadings close to the target values, a priori knowledge of the SOA yield of the VOC may be required. When the organic mass loading becomes stabilized, filter sampling will commence to collect aerosol particles for subsequent chemical analysis. Measurements can thus be made while the loadings are low,

allowing the measurements of the SOA compositions for loadings at atmospherically relevant concentrations. The ageing and chemical evolution of gas–phase products can also be investigated. Gas–phase products, which significantly partition into the particle–phase after the introduction of seed particles, are important for the SOA formation at the given loadings. The SOA composition obtained by this approach can be compared to those of the traditional approach (i.e., complete reaction of a higher concentration of hydrocarbons) at loadings for which the data sets overlapped.

5.3 References

Chhabra, P. S., Flagan, R. C., and Seinfeld, J. H.: Elemental analysis of chamber organic aerosol using an aerodyne high–resolution aerosol mass spectrometer, *Atmos. Chem. Phys.*, 10, 4111–4131, 2010

Chhabra, P. S., Ng, N. L., Canagaratna, M. R., Corrigan, A. L., Russell, L. M., Worsnop, D. R., Flagan, R. C., and Seinfeld, J. H.: Elemental composition and oxidation of chamber organic aerosol, *Atmos. Chem. Phys. Discuss.*, 11, 10305–10342, 2011.

Kang, E., Toohey, D. W., and Brune, W. H.: Dependence of SOA oxidation on organic aerosol mass concentration and OH exposure: Experimental PAM chamber studies, *Atmos. Chem. Phys.*, 11, 1837–1852, 2011.

Shilling, J. E., Chen, Q., King, S. M., Rosenoern, T., Kroll, J. H., Worsnop, D. R., DeCarlo, P. F. Aiken, A. C., Sueper, D., Jimenez, J. L., and Martin, S. T.: Loading–dependent

elemental composition of alpha–pinene SOA particles, *Atmos. Chem. Phys.*, 9, 771–782, 2009.

Appendix

Appendix A

Role of Aldehyde Chemistry and NO$_x$ Concentrations in Secondary Organic Aerosol Formation*

**Atmospheric
Chemistry
and Physics**

Role of aldehyde chemistry and NO$_x$ concentrations in secondary organic aerosol formation

A. W. H. Chan[1], M. N. Chan[2], J. D. Surratt[1,*], P. S. Chhabra[1], C. L. Loza[1], J. D. Crounse[1], L. D. Yee[2], R. C. Flagan[1,2], P. O. Wennberg[2,3], and J. H. Seinfeld[1,2]

[1]Division of Chemistry and Chemical Engineering, California Institute of Technology, Pasadena, CA, USA
[2]Division of Engineering and Applied Science, California Institute of Technology, Pasadena, CA, USA
[3]Division of Geological and Planetary Sciences, California Institute of Technology, Pasadena, CA, USA
[*]now at: Department of Environmental Sciences and Engineering, The University of North Carolina at Chapel Hill, Chapel Hill, NC, USA

Abstract. Aldehydes are an important class of products from atmospheric oxidation of hydrocarbons. Isoprene (2-methyl-1,3-butadiene), the most abundantly emitted atmospheric non-methane hydrocarbon, produces a significant amount of secondary organic aerosol (SOA) via methacrolein (a C$_4$-unsaturated aldehyde) under urban high-NO$_x$ conditions. Previously, we have identified peroxy methacryloyl nitrate (MPAN) as the important intermediate to isoprene and methacrolein SOA in this NO$_x$ regime. Here we show that as a result of this chemistry, NO$_2$ enhances SOA formation from methacrolein and two other α,β-unsaturated aldehydes, specifically acrolein and crotonaldehyde, a NO$_x$ effect on SOA formation previously unrecognized. Oligoesters of dihydroxycarboxylic acids and hydroxynitrooxycarboxylic acids are observed to increase with increasing NO$_2$/NO ratio, and previous characterizations are confirmed by both online and offline high-resolution mass spectrometry techniques. Molecular structure also determines the amount of SOA formation, as the SOA mass yields are the highest for aldehydes that are α,β-unsaturated and contain an additional methyl group on the α-carbon. Aerosol formation from 2-methyl-3-buten-2-ol (MBO232) is insignificant, even under high-NO$_2$ conditions, as PAN (peroxy acyl nitrate, RC(O)OONO$_2$) formation is structurally unfavorable. At atmospherically relevant NO$_2$/NO ratios (3–8), the SOA yields from isoprene high-NO$_x$ photooxidation are 3 times greater than previously measured at lower NO$_2$/NO ratios. At sufficiently high NO$_2$ concentrations, in systems of α,β-unsaturated aldehydes, SOA formation from subsequent oxidation of products from acyl peroxyl radicals+NO$_2$ can exceed that from RO$_2$+HO$_2$ reactions under the same inorganic seed conditions, making RO$_2$+NO$_2$ an important channel for SOA formation.

1 Introduction

Organic matter is ubiquitous in atmospheric aerosols and accounts for a major fraction of particulate matter mass (Zhang et al., 2007a). Most particulate organic matter (POM) is secondary in origin, comprising condensable oxidation products of gas-phase volatile organic compounds (VOCs) (Hallquist et al., 2009). Despite the importance of secondary organic aerosol (SOA), its sources and formation processes are not fully understood. Global modeling studies predict that oxidation of biogenic hydrocarbons dominates the global SOA burden owing to high emissions and efficient SOA production (Chung and Seinfeld, 2002; Kanakidou et al., 2005; Henze and Seinfeld, 2006). This is supported by observations of high levels of modern (hence biogenic) carbon in ambient particulate organic matter, even in urban centers such as Nashville, TN, Tampa, FL and Atlanta, GA (Lewis et al., 2004; Lewis and Stiles, 2006; Weber et al., 2007). However, field observations have repeatedly shown that SOA formation is highly correlated with anthropogenic tracers, such as CO and acetylene (de Gouw et al., 2005, 2008).

A considerable body of laboratory chamber studies have investigated the dependence of SOA yields (mass of SOA formed per mass of hydrocarbon reacted) on NO$_x$ level, which can vary greatly between urban and remote

Correspondence to: J. H. Seinfeld
(seinfeld@caltech.edu)

areas. For photooxidation and ozonolysis of monoterpenes (Hatakeyama et al., 1991; Ng et al., 2007a; Zhang et al., 2007b; Presto et al., 2005), monocyclic (Song et al., 2005; Hurley et al., 2001; Ng et al., 2007b) and polycyclic aromatic compounds (Chan et al., 2009b), SOA yields are larger under low-NO$_x$ conditions; for sesquiterpenes, the reverse is true (Ng et al., 2007a). SOA formation from photooxidation of isoprene exhibits especially complex behavior depending on the NO$_x$ level (Kroll et al., 2006). The effect of NO$_x$ level on SOA formation has generally been attributed to the relative reaction rates of peroxy radicals (RO$_2$) with NO and HO$_2$ and the difference in volatilities of the products from the respective pathways (Kroll and Seinfeld, 2008). Under high-NO$_x$ conditions, RO$_2$+NO dominates and leads to formation of fragmentation products or organic nitrates, which are generally volatile (Presto et al., 2005). On the contrary, the RO$_2$+HO$_2$ pathway, which is competitive only when [NO]$\ll$1 ppb, produces less volatile hydroxyhydroperoxides and peroxy acids, leading to higher SOA yields (Johnson et al., 2005). RO$_2$+NO$_2$ reactions have not been considered as important for SOA formation due to the short lifetime of peroxy nitrates ($<$1 s); the notable exceptions are acyl peroxy nitrates (PANs) and pernitric acid (PNA). As a result, the so-called "high-NO$_x$" yields (corresponding to urban NO$_x$ levels) have typically been measured under high-NO conditions. For example, the overall SOA mass yield for isoprene photooxidation ranges from 0.01–0.05 under low-NO$_x$ conditions (Kroll et al., 2006) to 0.002–0.03 under high-NO$_x$ (high-NO) conditions (Kroll et al., 2005a; Dommen et al., 2006). Owing to the large emissions of isoprene (Guenther et al., 2006), isoprene has been estimated to be the single largest source of SOA globally (Henze and Seinfeld, 2006; Carlton et al., 2009).

In a recent study of the mechanism of SOA formation from isoprene, it was shown that aerosol-phase 2-methylglyceric acid (2-MG) and its oligoesters are produced from methacrolein oxidation through the peroxy methacryloyl nitrate (MPAN) channel, as the SOA from MPAN oxidation is similar in composition to that from high-NO$_x$ oxidation of isoprene and methacrolein (Surratt et al., 2010). Since MPAN is formed from the reversible reaction of methacryloyl peroxy radicals with NO$_2$, SOA formation can be highly sensitive to the NO$_2$ concentration, an effect of gas-phase aldehyde chemistry that had previously not been recognized. Given the large emissions and the substantial fraction of isoprene reacting under high-NO$_x$ conditions (a recent modeling study predicts that globally up to two-thirds of isoprene reacts under high-NO$_x$ conditions (Paulot et al., 2009)), it is essential to understand more generally how gas-phase aldehyde chemistry and both NO and NO$_2$ affect SOA yield and composition. Here we present the results of a systematic study of the effect of NO$_2$/NO ratio on SOA formation from methacrolein and two other α,β-unsaturated aldehydes, acrolein and crotonaldehyde. In addition, other structurally similar aldehydes and alcohols are studied to provide insight

Table 1. Hydrocarbons studied.

Name	Structure	OH rate constant, cm^3 molec^{-1} s^{-1}
isoprene		1×10^{-10} [a]
methacrolein		2.9×10^{-11} [a]
acrolein		2.0×10^{-11} [b]
crotonaldehyde (*cis* and *trans*)		3.5×10^{-11} [b]
2-methyl-2-butenal (2M2B)		unknown
3-methyl-2-butenal (3M2B)		6.2×10^{-11} [c]
2-pentenal		unknown
4-pentenal		unknown
2-methyl-3-buten-1-ol (MBO231)		unknown
2-methyl-3-buten-2-ol (MBO232)		3.9×10^{-11} [d]

[a] Atkinson and Arey (2003); [b] Magneron et al. (2002); [c] Tuazon et al. (2005); [d] Fantechi et al. (1998).

into the reaction mechanism and to establish the role of PAN-type compounds as important SOA intermediates.

2   Experimental section

2.1   Experimental protocols

Experiments were carried out in the Caltech dual 28-m^3 Teflon chambers. Details of the facilities have been described previously (Cocker et al., 2001; Keywood et al., 2004). Before each experiment, the chambers were flushed with dried purified air for $>$24 h ($\sim$4–6 air changes), until the particle number concentration $<$100 cm^{-3} and the volume concentration $<$0.1 μm^3 cm^{-3}. In all experiments, inorganic seed particles were injected by atomization of a 0.015 M aqueous ammonium sulfate solution. The parent hydrocarbon was then introduced into the chamber by injecting a known volume of the liquid hydrocarbon into a glass bulb, and the vapor was carried into the chamber with 5 L min^{-1} of purified air.

Table 2. Experimental conditions and results.

Date[a] (DD/MM/YY)	Compound	[HC]$_0$, ppb	OH precursor	NO$_x$ addition	[NO]$_0^b$, ppb	[NO$_2$]$_0^b$, ppb	NO$_2$/NO[c]	V_0^d, μm^3 cm^{-3}	ΔM_o^e, μg m^{-3}	SOA Yield
14/07/09	methacrolein	277	HONO	+NO	725	365	0.5	11.4	10.1	0.019
16/07/09	methacrolein	285	HONO	+NO$_2$	296	692	1.7	12.3	24.5	0.052
19/07/09	methacrolein	257	HONO	−	527	407	0.7	12.1	14.4	0.030
31/07/09[f]	methacrolein	232	HONO	+NO	653	394	0.5	11.7	13.3	0.030
12/09/09	methacrolein	255	CH$_3$ONO	+NO+NO$_2$	222	799	10.0	13.9	276.3	0.392
15/09/09	methacrolein	67	CH$_3$ONO	+NO+NO$_2$	164	549	5.8	14.8	39.9	0.211
17/09/09	methacrolein	20	CH$_3$ONO	+NO+NO$_2$	170	602	3.6	16.0	10.8	0.194
19/09/09	methacrolein	48	CH$_3$ONO	+NO+NO$_2$	167	582	4.7	13.2	28.8	0.213
21/09/09	methacrolein	32	CH$_3$ONO	+NO+NO$_2$	176	657	4.2	14.4	22.4	0.242
16/12/09	methacrolein	32	CH$_3$ONO	+NO+NO$_2$	243	444	2.7	13.9	6.8	0.079
17/12/09[g]	methacrolein	32	CH$_3$ONO	+NO+NO$_2$	233	518	2.7	16.2	6.7	0.075
08/08/09	isoprene	523	HONO	−	312	510	7.7	10.8	65.2	0.044
23/09/09	isoprene	228	CH$_3$ONO	+NO+NO$_2$	293	825	8.4	16.0	47.4	0.074
24/09/09	isoprene	94	CH$_3$ONO	+NO+NO$_2$	271	735	5.0	14.8	16.0	0.061
25/09/09	isoprene	153	CH$_3$ONO	+NO+NO$_2$	316	859	6.1	18.7	27.2	0.064
27/09/09	isoprene	44	CH$_3$ONO	+NO+NO$_2$	259	715	4.0	15.8	5.2	0.042
30/09/09	isoprene	33	CH$_3$ONO	+NO+NO$_2$	289	768	3.4	18.4	2.9	0.031
15/08/09	acrolein	676	HONO	−	214	389	2.5	13.2	21.3	0.022
16/08/09	acrolein	540	HONO	+NO	550	359	0.8	11.2	4.4	0.006
17/08/09	acrolein	611	HONO	+NO$_2$	233	630	2.0	13.2	9.9	0.015
28/09/09	acrolein	220	CH$_3$ONO	+NO+NO$_2$	313	830	5.5	19.2	16.6	0.035
18/08/09	crotonaldehyde	293	HONO	−	214	371	2.3	12.1	14.0	0.019
19/08/09	crotonaldehyde	297	HONO	+NO	600	416	1.1	12.3	9.0	0.013
20/08/09	crotonaldehyde	361	HONO	+NO$_2$	245	625	2.6	12.2	12.9	0.017
29/09/09	crotonaldehyde	74	CH$_3$ONO	+NO+NO$_2$	248	664	3.8	16.4	9.2	0.044
26/12/09	2-pentenal	174	CH$_3$ONO	+NO+NO$_2$	230	548	6.7	13.9	18.1	0.03
27/12/09	4-pentenal	191	CH$_3$ONO	+NO+NO$_2$	243	488	6.5	15.8	8.2	0.012
28/12/09	2M2B	277	CH$_3$ONO	+NO+NO$_2$	240	706	9.3	13.8	376.7	0.391
29/12/09	3M2B	207	CH$_3$ONO	+NO+NO$_2$	268	747	8.7	16.1	5.6	0.008
31/12/09	MBO231	589	CH$_3$ONO	+NO+NO$_2$	308	493	13.2	16.8	87.6	0.042
22/02/10	MBO231	329	CH$_3$ONO	+NO+NO$_2$	351	768	7.8	14.5	21.9	0.019
24/02/10	MBO231	300	HONO	+NO	642	514	1.8	14.2	<2	<0.002
25/02/10	MBO231	378	CH$_3$ONO	+NO+NO$_2$	346	793	5.5	17.5	10.7	0.008
01/01/10	MBO232	492	CH$_3$ONO	+NO+NO$_2$	251	442	11.4	14.8	<2	<0.002
23/02/10	MBO232	388	CH$_3$ONO	+NO+NO$_2$	345	809	8.4	17.1	<2	<0.002

[a] All experiments carried out at temperatures of 293–295 K and RH of 9–11%. [b] As measured by chemiluminescence NO$_x$ monitor. Note interference on NO$_2$ signal from HONO and CH$_3$ONO. [c] Estimated by photochemical modeling (see Appendix). [d] V_0: volume concentration of ammonium sulfate seed. [e] ΔM_o: mass concentration of SOA. [f] Gas-phase nitric acid added during experiment. [g] Low O$_2$ experiment.

To study the sensitivity of aerosol yields and composition to relative concentrations of NO and NO$_2$, different OH precursors were used. Use of nitrous acid (HONO) and methyl nitrite (CH$_3$ONO) as OH precursors allows for SOA yield measurements over a wide range of NO$_2$/NO ratios. For "high NO" experiments, OH radicals were generated from photolysis of HONO. We refer to these experiments as "high NO" experiments because NO concentrations are sufficiently high that RO$_2$+NO≫RO$_2$+NO$_2$, most notably for acyl peroxy radicals, even though NO$_2$ concentrations are high (>100 ppb). HONO was prepared by adding 15 mL of 1 wt% aqueous NaNO$_2$ dropwise into 30 mL of 10 wt% sulfuric acid in a glass bulb. A stream of dry air was then passed through the bulb, sending HONO into the chamber. During this process, NO and NO$_2$ formed as side products and were also introduced into the chamber. To achieve high NO$_2$

concentrations, CH$_3$ONO was employed as the OH precursor. These experiments are referred to as "high NO$_2$" experiments, as NO$_2$ concentrations are sufficiently higher than NO concentrations such that PAN formation is favored over reaction of acyl peroxy radicals with NO. CH$_3$ONO was vaporized into an evacuated 500 mL glass bulb and introduced into the chamber with an air stream of 5 L min^{-1}. The mixing ratio of CH$_3$ONO injected was estimated to be 200–400 ppb, based on the vapor pressure in the glass bulb measured using a capacitance manometer (MKS). In all experiments, varying amounts of NO and NO$_2$ were also added from gas cylinders (Scott Marrin) both to ensure high-NO$_x$ conditions and to vary the NO$_2$/NO ratio. For the C$_5$ unsaturated aldehydes and 2-methyl-3-buten-2-ol (MBO232), only high NO$_2$ experiments were conducted. Abbreviations, structures, and OH rate constants (Atkinson and Arey, 2003; Magneron et al.,

2002; Tuazon et al., 2005; Fantechi et al., 1998) of the compounds studied are listed in Table 1, and initial conditions of the experiments are summarized in Table 2.

2.2 Materials

The parent hydrocarbons studied and their stated purities are as follows: isoprene (Aldrich, 99%), methacrolein (Aldrich, 95%), acrolein (Fluka, ≥99%), crotonaldehyde (Aldrich, 98%, predominantly *trans*), trans-2-pentenal (Alfa Aesar, 96%), 4-pentenal (Alfa Aesar, 97%), trans-2-methyl-2-butenal (Aldrich, 96+%), 3-methyl-2-butenal (Sigma-Aldrich, 97%), 2-methyl-3-buten-1-ol (Aldrich, 98%), and 2-methyl-3-buten-2-ol (Aldrich, 98%). CH$_3$ONO was synthesized following the method described by Taylor et al. (1980). 9 g of NaNO$_2$ was added to a mixture of 50 mL of methanol and 25 mL of water. 25 mL of 50 wt% sulfuric acid solution was added dropwise into the solution. The CH$_3$ONO vapor was carried in a small stream of ultra high purity N$_2$ through a concentrated NaOH solution and an anhydrous CaSO$_4$ trap to remove any sulfuric acid and water, respectively. The CH$_3$ONO was then collected in a cold trap immersed in a dry ice/acetone bath ($-80\,°C$) and stored under liquid N$_2$ temperature.

2.3 Measurements

Aerosol size distribution, number and volume concentrations were measured with a differential mobility analyzer (DMA, TSI, 3081) coupled with a condensation nuclei counter (TSI, CNC-3760). The volume concentration was corrected for particle wall loss by applying size-dependent first-order loss coefficients, obtained in a separate seed-only experiment, using methods described in Keywood et al. (2004). Aerosol volume concentrations are converted to mass concentrations assuming a density of $1.4\,\mathrm{g\,cm^{-3}}$ (Kroll et al., 2005a). Concentrations of isoprene, methacrolein, methyl vinyl ketone (MVK), acrolein, and crotonaldehyde were monitored using a gas chromatograph with flame ionization detector (GC/FID, Agilent 6890N), equipped with an HP-PLOT Q column (15 m×0.53 mm ID×30 μm thickness, J&W Scientific). For 2M2B, 3M2B, 2-pentenal, 4-pentenal, MBO231 and MBO232 experiments, the GC/FID was equipped with an HP-5 column (15 m×0.53 mm ID×1.5 μm thickness, Hewlett Packard). A commercial chemiluminescence NO/NO$_x$ analyzer (Horiba, APNA 360) was used to monitor NO and NO$_x$. Both HONO and CH$_3$ONO produce interference on the NO$_2$ signal from the NO$_x$ monitor. Concentrations of NO and NO$_2$ are estimated by photochemical modeling (see Appendix). Temperature, RH, and ozone (O$_3$) were continuously monitored.

A custom-modified Varian 1200 triple-quadrupole chemical ionization mass spectrometer (CIMS) was used to continuously monitor gas-phase species over each experiment. Details of the operation of the CIMS can be found in a num-

ber of previous reports (Crounse et al., 2006; Paulot et al., 2009). The CIMS was operated in negative ion mode, in which CF$_3$O$^-$ is used as the reagent ion, and in positive ion mode of proton transfer mass spectrometry (PTR-MS). In the negative mode, the reagent ion CF$_3$O$^-$ clusters with the analyte, R, forming ions at mass-to-charge ratios (m/z) MW+85 (R·CF$_3$O$^-$), or, with more acidic species, at m/z MW+19 (HF·R$_{-H}^-$). In the positive mode, positively charged water clusters, n(H$_2$O)H$^+$, react via proton transfer with the analyte, R, to form the positively charged ion, R·n(H$_2$O)·H$^+$. In some cases, tandem mass spectrometry (MS/MS) was used to separate isobaric compounds. In brief, the parent ions selected in the first quadrupole undergo collision-induced dissociation (CID) in the second quadrupole. The parent ions of isobaric compounds can exhibit different CID patterns and yield different daughter ions. Hence, with the third quadrupole acting as a second mass filter for the daughter ions, this allows for separate measurement of these isobaric compounds (see Supplementary Material). The significance of this separation will be discussed in a later section.

Real-time particle mass spectra were collected continuously by an Aerodyne High Resolution Time-of-Flight Aerosol Mass Spectrometer (DeCarlo et al., 2006; Canagaratna et al., 2007), hereby referred to as the AMS. The AMS switched once every minute between the high resolution "W-mode" and the lower resolution, higher sensitivity "V-mode". The "V-mode" data were analyzed using a fragmentation table to separate sulfate, ammonium, and organic spectra and to time-trace specific mass-to-charge ratios. "W-mode" data were analyzed using a separate high-resolution spectra toolbox known as PIKA to determine the chemical formulas contributing to distinct m/z ratios (DeCarlo et al., 2006).

Aerosol samples were also collected on Teflon filters and analyzed by offline mass spectrometry. Detailed sample collection and extraction protocol are described in Surratt et al. (2008). Filter extraction using 5 mL of high-purity methanol (i.e., LC-MS Chromasolv Grade) was performed by 45 min of sonication. The filter extracts were then analyzed by a Waters ACQUITY ultra performance liquid chromatography (UPLC) system, coupled with a Waters LCT Premier TOF mass spectrometer equipped with an ESI source operated in the negative ($-$) mode, allowing for accurate mass measurements (i.e., determination of molecular formulas) to be obtained for each observed ion. Operation conditions and parameters for the UPLC/($-$)ESI-TOFMS measurement have been described by Surratt et al. (2008).

3 SOA formation

The importance of isoprene as an SOA source was suggested by identification of 2-methyltetrols and 2-methylglyceric acid (2-MG) in both ambient POM (Claeys et al., 2004; Edney et al., 2005; Ion et al., 2005; Kourtchev et al., 2005)
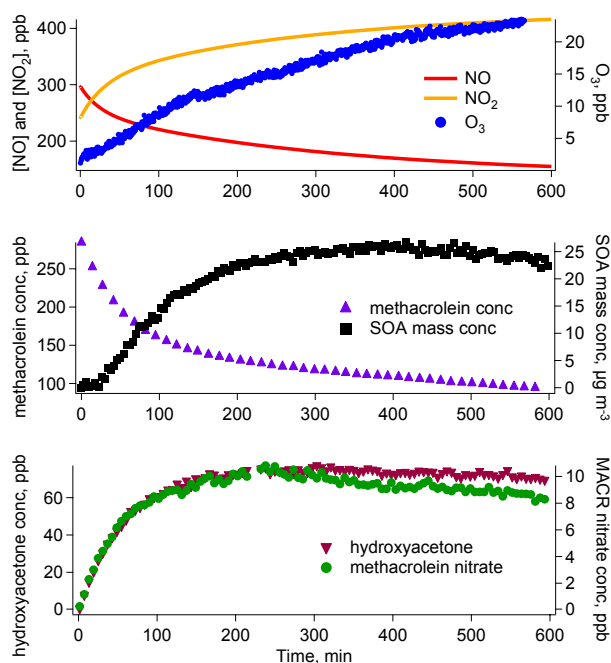
Fig. 1. Concentration profiles of gas-phase species during a typical methacrolein/high-NO experiment (16/07/09). In this experiment, additional NO$_2$ was injected prior to irradiation. Concentrations of NO and NO$_2$ shown here are calculated from a photochemical model (see Appendix).

Fig. 2. Concentration profiles of gas-phase species during a typical methacrolein/high-NO$_2$ experiment (15/09/09). Additional NO (100 ppb) and NO$_2$ (200 ppb) were injected prior to irradiation. Concentrations of NO and NO$_2$ shown here are calculated from a photochemical model (see Appendix). As a result of the higher OH concentrations from CH$_3$ONO than from HONO, more methacrolein was reacted and the concentrations of methacrolein nitrate relative to those of hydroxyacetone were lower than those in high-NO experiments, owing to a more rapid consumption by OH.

and laboratory aerosol generated from isoprene photooxidation (Edney et al., 2005; Surratt et al., 2006; Szmigielski et al., 2007; Kleindienst et al., 2009). Methacrolein, a first-generation oxidation product of isoprene, has been shown to produce SOA upon further oxidation (Kroll et al., 2006; Surratt et al., 2006) and has been identified as the precursor to aerosol-phase 2-MG and its corresponding oligoester products (Surratt et al., 2006; Szmigielski et al., 2007). A recent study shows aerosol formation from methacrolein oxidation proceeds via subsequent oxidation of MPAN (Surratt et al., 2010). Here we focus our attention on photooxidation of methacrolein under high-NO$_x$ conditions to establish the effect of relative NO and NO$_2$ concentrations on SOA yields and composition. Acrolein, crotonaldehyde, 2-methyl-2-butenal (2M2B), 3-methyl-2-butenal (3M2B), 2-pentenal, and 4-pentenal differ from methacrolein by one or two methyl groups, and studying their SOA formation provides insight into the mechanism of formation of low-volatility products. Furthermore, aerosol formation from photooxidation of 2-methyl-3-buten-2-ol (MBO232), an atmospherically important unsaturated alcohol (Harley et al., 1998), and structurally similar 2-methyl-3-buten-1-ol (MBO231) is studied to investigate the role of PAN-like compounds in SOA formation.

3.1 Methacrolein

Figures 1 and 2 show typical concentration profiles of various gas-phase species in methacrolein/HONO (high NO) and methacrolein/CH$_3$ONO (high NO$_2$) photooxidation experiments, respectively. In all experiments, NO concentrations remain above 50 ppb during SOA growth, at which conditions RO$_2$+HO$_2$ or RO$_2$+RO$_2$ reactions are not competitive with those of RO$_2$ with NO and NO$_2$. Products of these reactions, such as methacrylic acid and methacrylic peracid, are not observed by CIMS. Instead, hydroxyacetone and methacrolein nitrate, products from RO$_2$+NO reactions, are observed. During these experiments, RO$_2$ and HO$_2$ produced from methacrolein oxidation react with NO to produce NO$_2$, which photolyzes to form ozone. As a result, ozone concentrations reach a maximum of up to 126 ppb. Despite relatively high levels of ozone, reaction rates of methacrolein and peroxy methacryloyl nitrate (MPAN) with ozone are still slow compared to those with OH, as efficient photolysis of HONO or CH$_3$ONO leads to OH concentrations $>3 \times 10^6$ molec cm^{-3}, estimated from the methacrolein decay. For high-NO experiments, the initial decay of methacrolein slows down after 5 h, consistent with the HONO signal (CIMS (–) m/z 66) approaching zero. In
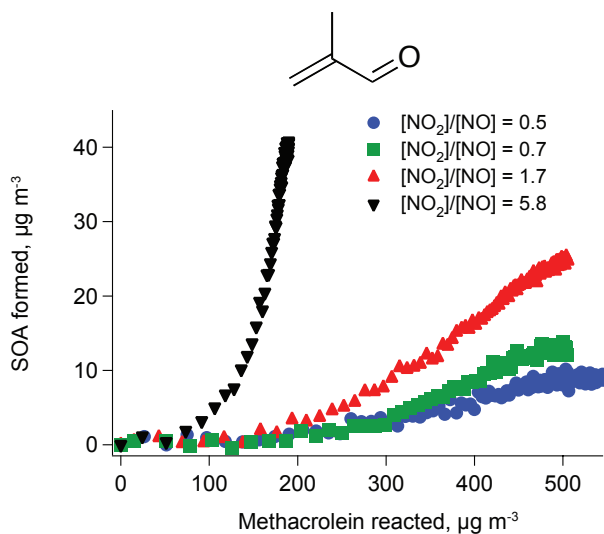
Fig. 3. Time-dependent SOA growth curves for methacrolein photooxidation. NO$_2$/NO ratios are computed from photochemical modeling (see Appendix). In the high-NO experiments (NO$_2$/NO<2) HONO was used as the OH precursor, and the NO$_2$/NO ratio was varied by adding different amounts of NO or NO$_2$. In the high-NO$_2$ experiment (black triangles), CH$_3$ONO was used as the OH precursor.

Fig. 4. Time-dependent SOA growth curves for acrolein photooxidation. Similar to methacrolein photooxidation, NO$_2$/NO ratios are computed from photochemical modeling (see Appendix). In the high-NO experiments (NO$_2$/NO< 3), HONO was used as the OH precursor, and the NO$_2$/NO ratio was varied by adding different amounts of NO or NO$_2$. In the experiment in which NO$_2$ was added (red triangles), high levels of NO$_2$ depress OH concentrations, resulting in less acrolein reacted. Concentrations of NO did not drop as rapidly as in other high-NO experiments, leading to a lower NO$_2$/NO ratio. In the high-NO$_2$ experiment (black triangles), CH$_3$ONO was used as the OH precursor.

these experiments, more than 70% of the inital methacrolein is consumed before SOA growth ceases. In the high-NO$_2$ experiments, more than 90% of the initial methacrolein is consumed before SOA growth ceases.

Mass concentrations of SOA versus the concentration of methacrolein reacted, so-called "time-dependent growth curves", are shown in Fig. 3. As reported previously, under high-NO conditions (with HONO as the OH precursor), when additional NO is added before irradiation, aerosol formation (mass yield of 0.019) from photooxidation of 277 ppb of methacrolein is suppressed (Surratt et al., 2010). In contrast, SOA yields are higher when no additional NO is added (0.030 from 257 ppb methacrolein), and the highest when 350 ppb of additional NO$_2$ (instead of NO) is injected (0.052 from 285 ppb methacrolein) (Surratt et al., 2010). In all high-NO experiments, the NO$_2$/NO ratio remains low (<2), owing to presence of NO impurity in HONO synthesis and production of NO during HONO photolysis. The observed dependence of SOA yields on NO$_2$/NO ratio is not a result of condensation of nitric acid from OH+NO$_2$, as the experiments were conducted under dry (<10% RH) conditions. In confirmation of this conclusion, addition of gas-phase nitric acid in one experiment (31/07/09) did not lead to additional aerosol growth.

In the high-NO$_2$ experiments, CH$_3$ONO was used as the OH precursor and lower NO concentrations are expected, owing to relatively pure CH$_3$ONO synthesis and no net production of NO from CH$_3$ONO photolysis (see Appendix). Higher SOA yields are observed at higher NO$_2$/NO ratios;

correspondingly, much lower concentrations of methacrolein are required to produce the same amount of SOA (see Fig. 3). Also, owing to the high concentrations of CH$_3$ONO injected, more than 90% of the initial methacrolein is consumed before CH$_3$ONO is depleted. For example, when 255 ppb of initial methacrolein is oxidized using CH$_3$ONO as OH precursor (12/09/09), the SOA yields are more than 5 times larger than when a similar amount of methacrolein is reacted using HONO as OH precursor. This rules out a larger extent of reaction as the cause of the high observed SOA yields. HO$_2$ concentrations, quantified from the pernitric acid signal on the CIMS ((−) m/z 98) and modelled NO$_2$ concentrations, do not exceed 60 ppt in all experiments. At organic loadings of 10–20 µg m^{-3}, SOA mass yields of methacrolein/high-NO$_2$ and methacrolein/high-NO photooxidation are roughly 0.19 and 0.03, respectively.

3.2 Acrolein and crotonaldehyde

Figures 4 and 5 show SOA growth curves for acrolein and crotonaldehyde photooxidation, respectively. The SOA yields of these compounds are lower than those of methacrolein, with maximum yields of roughly 0.08 at the highest loadings (>100 µg m^{-3}). These compounds exhibit a similar dependence of SOA growth on NO$_2$/NO ratio to that of methacrolein: SOA formation is suppressed with addition
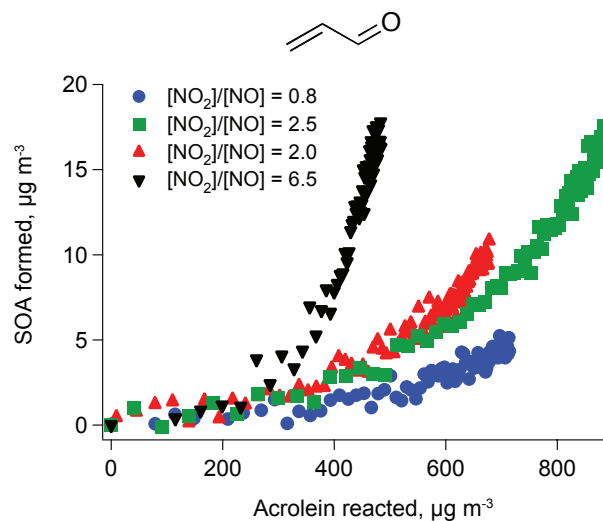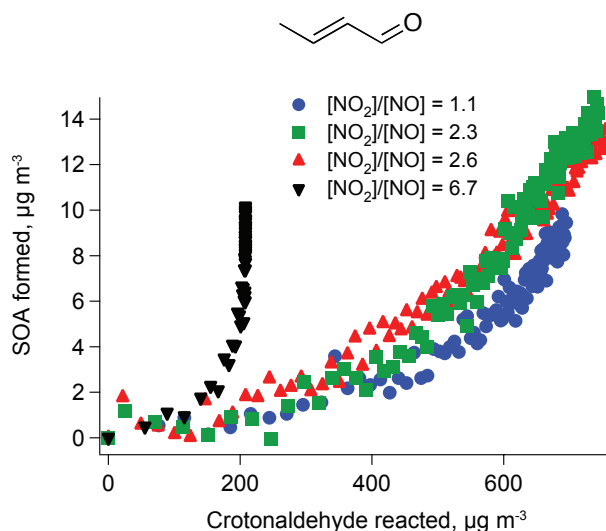
Fig. 5. Time-dependent SOA growth curves for crotonaldehyde photooxidation. Similar to methacrolein photooxidation, NO$_2$/NO ratios are computed from photochemical modeling (see Appendix). In the high-NO experiments (NO$_2$/NO<3), HONO was used as the OH precursor, and the NO$_2$/NO ratio was varied by adding different amounts of NO or NO$_2$. In the high-NO$_2$ experiment (black triangles), CH$_3$ONO was used as the OH precursor.

of NO, and enhanced with addition of NO$_2$. SOA yields are highest in the high-NO$_2$ experiments. Oxidation products analogous to those found in the methacrolein system, such as glycolaldehyde and hydroxynitrates, are observed in the gas phase at similar yields.

3.3 Other aldehydes and methylbutenols (MBO)

The growth curves for 2M2B and 3M2B photooxidation are shown in Fig. 6. Significant SOA growth is observed for 2M2B (277 ppb) photooxidation under high-NO$_2$ conditions, with mass yields exceeding 0.35. Similar to methacrolein, 2M2B contains a methyl group in the α-position. Interestingly, photooxidation of 3M2B under similar NO$_x$ conditions and hydrocarbon loadings (207 ppb), produces less SOA (mass yield <0.01). 3M2B is a structural isomer of 2M2B with the methyl group in the β-position. The trend in SOA yields between 2M2B and 3M2B is consistent with that observed for methacrolein and crotonaldehyde, their C$_4$ analogs. The SOA yields from 2-pentenal, a straight-chain α,β-unsaturated aldehyde, are higher than those from 4-pentenal, in which the olefinic bond is not adjacent to the aldehyde group (see Fig. 6).

We also carried out MBO232 and MBO231 photooxidation under high-NO$_2$ conditions. Both MBO's are structurally similar to isoprene and, upon high-NO$_x$ photooxidation, produce an aldehyde (i.e., hydroxy-methylpropanal, HMPR) analogous to methacrolein. Previous results have shown that aerosol formation from MBO232 photooxidation

under high-NO conditions is negligible, with mass yields of <0.001 (Carrasco et al., 2007; Chan et al., 2009a). Here we do not observe SOA growth even at high NO$_2$/NO ratios. Gas-phase compounds such as glycolaldehyde and HMPR are observed at molar yields of 0.6 and 0.3, respectively, consistent with those published in previous product studies (Carrasco et al., 2007; Chan et al., 2009a). On the other hand, MBO231, a structural isomer with the hydroxyl group in the 1-position, produces a significant amount of SOA (mass yields of 0.008–0.042) upon oxidation under high-NO$_2$ conditions, comparable to that of isoprene under similar conditions (see Fig. 6). Under high-NO conditions, no SOA is formed. The dependence of SOA yields from MBO231 on NO$_2$/NO ratio is therefore consistent with that observed in unsaturated aldehydes.

4 Chemical composition of SOA

4.1 Offline chemical analysis

In previous work, offline chemical analysis of SOA from photooxidation of isoprene, methacrolein, and MPAN by UPLC/(–)ESI-TOFMS has been presented (Surratt et al., 2010). The same compounds are detected in the methacrolein experiments in this work under both high-NO and high-NO$_2$ conditions, and are summarized in Table 3. Four series of oligoester products from 2-methylglyceric acid (2-MG) and C$_4$-hydroxynitrooxycarboxylic acid are identified in the SOA. The compounds in the 2-MG oligoester series differ by 102 Da, corresponding to esterification of a 2-MG monomer unit (Surratt et al., 2006). The accurate masses of the identified ions confirm their elemental compositions, and their structures are proposed based on detailed characterization by tandem MS and GC/MS analyses with prior trimethylsilylation (Szmigielski et al., 2007).

All ions detected by UPLC/(–)ESI-TOFMS in acrolein and crotonaldehyde SOA are listed in the Supplementary Material. It is noteworthy that the identities of detected aerosol-phase products are the same regardless of the OH precursor used. The ions detected in acrolein SOA differ from those found in methacrolein SOA by one methyl group for every monomer unit, and those detected in crotonaldehyde SOA have the same exact mass and elemental composition as those in methacrolein SOA. Detected [M-H]$^-$ ions in SOA from 2M2B and 2-pentenal can also be found in the Supplementary Material. No filter sample was collected for 3M2B owing to low aerosol loading. Aerosol-phase products of methacrolein, acrolein, crotonaldehyde, 2M2B and 2-pentenal are structural analogs of each other, and the structures for the deprotonated ions are proposed based on those characterized previously in isoprene and methacrolein SOA (Surratt et al., 2006; Szmigielski et al., 2007). Interestingly, SOA produced from 4-pentenal is composed of entirely different products, and hence no structures are proposed at this
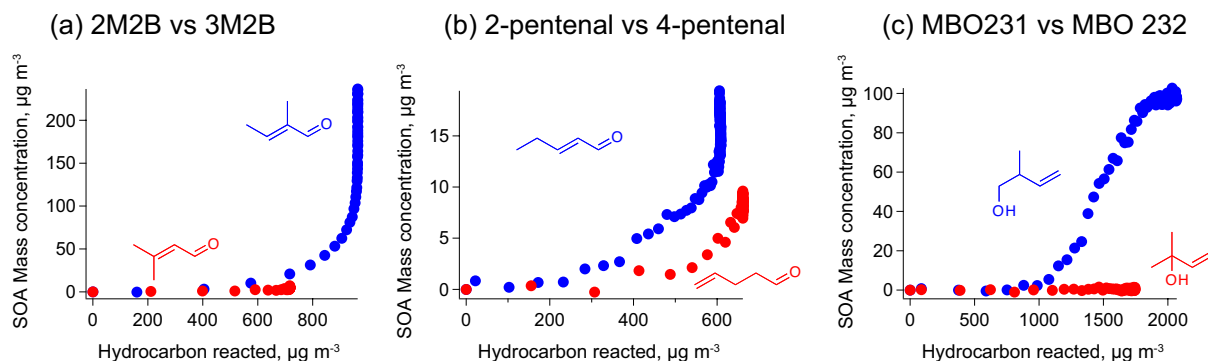
Fig. 6. Comparisons of time-dependent SOA growth from photooxidation of **(a)** 2M2B and 3M2B, **(b)** 2-pentenal and 4-pentenal, and **(c)** MBO232 and MBO 231 under high-NO$_2$ conditions. Within each plot, initial concentrations of parent hydrocarbons are comparable (see Table 2).

Table 3. SOA constituents detected by UPLC/(−)ESI-TOFMS and AMS in methacrolein experiments. All ions were detected in both high-NO and high-NO$_2$ experiments, unless otherwise noted.

	[M − H]$^{-a}$	UPLC/ESI-TOFMS Measured Mass	TOFMS Suggested Ion Formula	Error (mDa)	i-Fit	# of 2-MG Monomer Units (n)	Structure	[M − OH]$^{+b}$	AMS Suggested Ion Formula ^{c}
Oligoester Series 1		not detected				1		103	C$_4$H$_7$O$_3^+$
	221	221.0661	C$_8$H$_{13}$O$_7^-$	1.6	0.3	2		205	C$_8$H$_{13}$O$_6^+$
	323	323.0979	C$_{12}$H$_{19}$O$_{10}^-$	0.1	22.6	3		^{d}	--
	425	425.1290	C$_{16}$H$_{25}$O$_{13}^-$	-0.5	48.0	4		^{d}	--
	527 ^{e}	527.1609	C$_{20}$H$_{31}$O$_{16}^-$	-0.3	3.7	5		^{d}	--
Oligoester Series 2	266	266.0507	C$_8$H$_{12}$NO$_9^-$	-0.5	32.8	1		^{d}	--
	368	368.0831	C$_{12}$H$_{18}$NO$_{12}^-$	0.2	11.4	2		^{d}	--
	470	470.1149	C$_{16}$H$_{24}$NO$_{15}^-$	0.3	56.3	3		^{d}	--
	572	572.1510	C$_{20}$H$_{30}$NO$_{18}^-$	4.7	1.0	4		^{d}	--
Oligoester Series 3 ^{f}		not detected				1		131	C$_5$H$_7$O$_4^{+\,g}$
	249	249.0616	C$_9$H$_{13}$O$_8^-$	0.6	2.7	2		233	C$_9$H$_{13}$O$_7^+$
	351	351.0912	C$_{13}$H$_{19}$O$_{11}^-$	-1.5	46.9	3		^{d}	--
	453	453.1248	C$_{17}$H$_{25}$O$_{14}^-$	0.4	63.7	4		^{d}	--
	555 ^{e}	555.1610	C$_{21}$H$_{31}$O$_{17}^-$	4.9	3.0	5		^{d}	--
Oligoester Series 4 ^{h}		not detected				1		145	C$_6$H$_9$O$_4^+$
	263	263.0740	C$_{10}$H$_{15}$O$_8^-$	-2.7	4.7	2		247	C$_{10}$H$_{15}$O$_7^+$
	365	365.1061	C$_{14}$H$_{21}$O$_{11}^-$	-2.3	54.9	3		^{d}	--
	467	467.1434	C$_{18}$H$_{27}$O$_{14}^-$	3.3	23.7	4		^{d}	--
	569	569.1711	C$_{18}$H$_{27}$O$_{14}^-$	-0.7	20.0	5		^{d}	--
Oligoester Series 5	311	311.0333	C$_8$H$_{11}$N$_2$O$_{11}^-$	-3.0	58.9	0		^{d}	--
	413	413.0664	C$_{12}$H$_{17}$N$_2$O$_{14}^-$	-1.6	71.9	1		^{d}	--
	515 ^{e}	515.1039	C$_{16}$H$_{23}$N$_2$O$_{17}^-$	4.2	3.6	2		^{d}	--
Other Oligoesters	458 ^{e}	458.0558	C$_{12}$H$_{16}$N$_3$O$_{16}^-$	2.7	3.3	n/a		^{d}	--

^{a} Observed by UPLC/(−)ESI-TOFMS. ^{b} Observed by AMS V mode. ^{c} Suggested by AMS high-resolution W mode.
^{d} Not observed by AMS, most likely due to fragmentation of nitrate group, or below detection limit. ^{e} Detected in high-NO$_2$ experiments only. ^{f} This oligoester series involves the esterification with formic acid. ^{g} C$_6$H$_{11}$O$_3^+$ also detected. ^{h} This oligoester series involves the esterification with acetic acid.
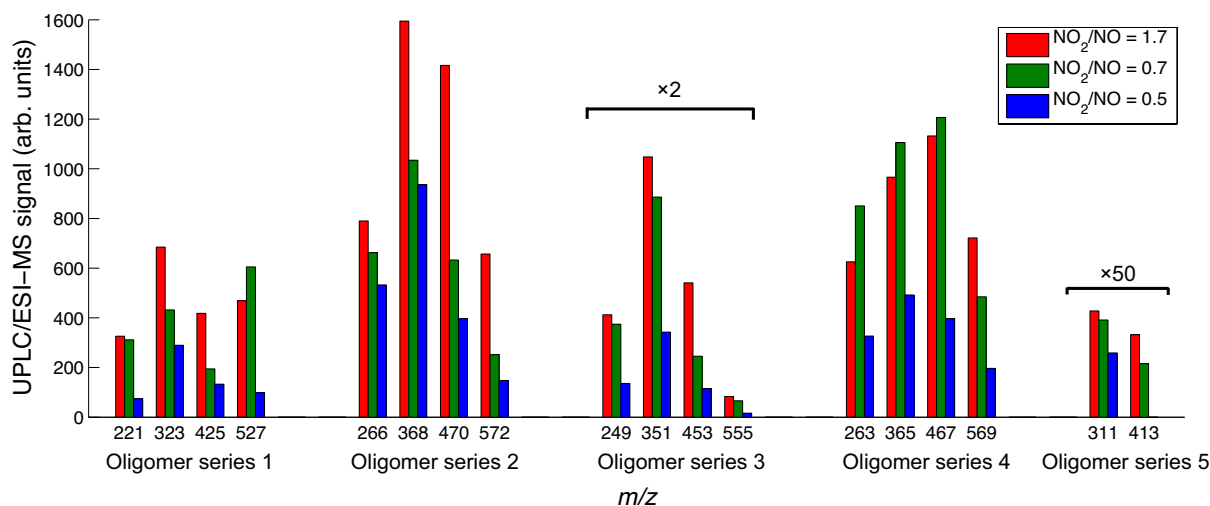
Fig. 7. Absolute peak areas (normalized by sampling volume) of all deprotonated ions detected by UPLC/(–)ESI-TOFMS in methacrolein/high-NO experiments, listed in Table 3. The positive dependence of oligoester abundance on NO$_2$/NO ratios is consistent with the observed trend in overall SOA growth.

time. The significance of this result will be discussed in a later section.

While the identities of the detected aerosol-phase compounds are independent of the OH precursor, the relative amounts vary greatly and exhibit a strong correlation with NO$_2$/NO ratio. Figure 7 shows the extracted ion signals for the oligoester products detected by UPLC/(–)ESI-TOFMS in the methacrolein high-NO experiments. The amount of identified aerosol-phase components shows the same dependence on NO$_2$/NO ratio as the total amount of SOA growth. In general, the abundance of each compound decreases when NO is added and increases when NO$_2$ is added.

4.2 Online AMS measurements

AMS V-mode organic spectra of SOA from high-NO$_2$ photooxidation of isoprene and methacrolein are shown in Fig. 8. The mass fragments above m/z 200 likely contain more than 5 carbon atoms, and display a repetitive pattern, indicative of oligomer formation. In addition, 102 Da differences between major peaks were also observed, consistent with previous AMS and LC/MS results (Surratt et al., 2006). Elemental formulas based on accurate mass measurements are determined from high-resolution W-mode data for a number of the major ion peaks observed, as shown in Fig. 9. The ions suggested by these elemental formulas differ from many of the ions detected by UPLC/(–)ESI-TOFMS by an O^{2-} group. The observed AMS ions are consistent with loss of a hydroxyl group from the molecular ion (i.e. α-cleavage of a hydroxyl group under electron impact ionization). In UPLC/(–)ESI-TOFMS, these compounds are detected in their deprotonated form (loss of H$^+$). As shown in Table 3, the oligoesters are detected by both online and offline high-resolution mass

spectrometry, and the agreement between the two techniques confirms that the oligoesters identified are indeed present in the SOA, and that the observations by offline aerosol analysis are not the result of filter sampling artifacts. AMS organic spectra of SOA from oxidation of acrolein and crotonaldehyde show similar features, and accurate mass measurements of a number of the major peaks correspond to the products analogous to those found in the methacrolein system (see Supplementary Material).

5 Effect of NO$_2$/NO ratios on SOA yield and composition

As mentioned in the Introduction, studies on the effect of NO$_x$ concentrations on SOA formation has shown that for most systems, SOA yields are inversely correlated with NO$_x$ concentrations (Hatakeyama et al., 1991; Hurley et al., 2001; Presto et al., 2005; Song et al., 2005; Zhang et al., 2007b; Ng et al., 2007a,b; Chan et al., 2009b). The "NO$_x$ effect" on SOA formation has been described as a competition of the chemistries for RO$_2$ between HO$_2$ (the high-yield pathway) and NO (the low-yield pathway), such that the ratio of HO$_2$ to NO is critical in determining the branching ratio between these two pathways (Kroll and Seinfeld, 2008; Henze et al., 2008). Aerosol yields from isoprene photooxidation are also sensitive to HO$_2$/NO ratios, with higher yields measured under HO$_2$-dominated conditions (using H$_2$O$_2$ as OH source) (Kroll et al., 2006) than under NO-dominated conditions (using HONO or NO$_x$ cycling as OH source) (Kroll et al., 2005b; Pandis et al., 1991; Dommen et al., 2006). Addition of NO also suppresses SOA growth in low-NO$_x$ experiments, indicating that the RO$_2$+NO pathway yields
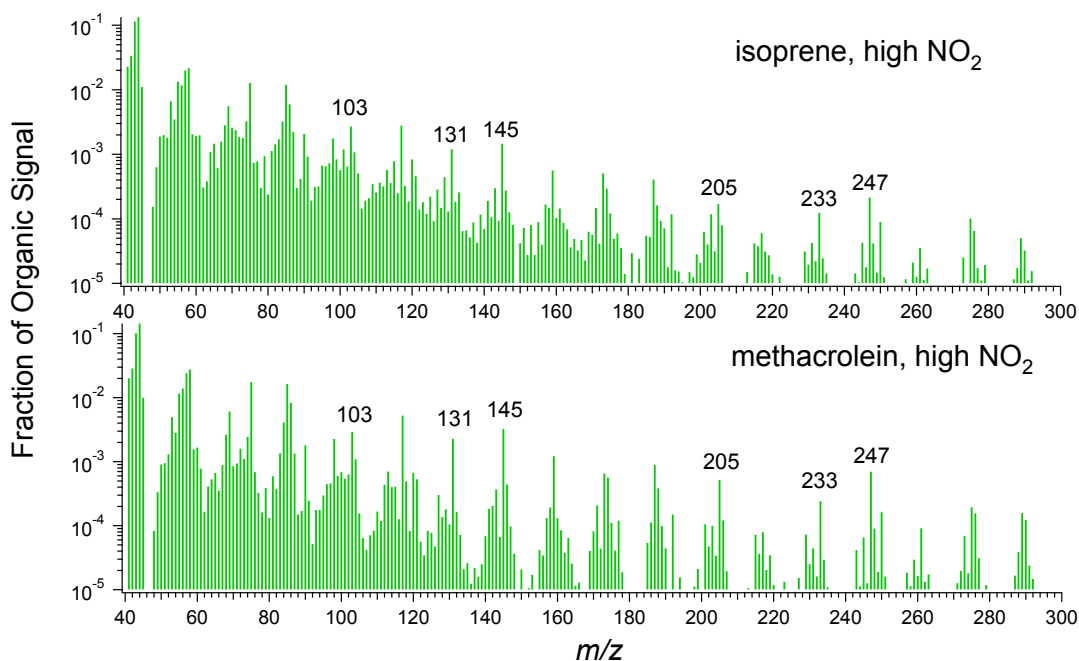
Fig. 8. AMS V-mode organic spectra of SOA from high-NO$_2$ photooxidation of isoprene and methacrolein. The labelled ion peaks differ from compounds listed in Table 3 by an O^{2-} group. The accurate masses are confirmed by W-mode high-resolution analysis, as shown in Fig. 9. Separation of 102 Da between major peaks is consistent with esterification with a 2-MG monomer.

more volatile products, and hence less SOA (Kroll et al., 2006). However, under the experimental conditions in the present study, RO$_2$+HO$_2$ reactions are not expected to be significant. Rather, the dependence of SOA yield on the NO$_2$/NO ratio is consistent with analysis of SOA composition, which is consistent with MPAN, a product of the acyl peroxy radical+NO$_2$ reaction, being the intermediate in SOA formation. Although the absolute concentrations of NO$_2$ in these experiments are a factor of 10 higher than ambient levels, we expect the OH-adduct of alkenes and aldehydes studied here to react predominantly with O$_2$ to form alkyl peroxy or acyl peroxy radicals. Compounds with nitro functional groups (R-NO$_2$), such as those found in the aromatic systems (Calvert et al., 2002), were not detected in these experiments.

Based on the proposed mechanism shown in Fig. 10, the acyl peroxy radical formed from abstraction of the aldehydic hydrogen atom of an unsaturated aldehyde react with either NO or NO$_2$. The reversible reaction of RO$_2$ with NO$_2$ forms a PAN-type compound (MPAN for methacrolein), which, in the absence of competing reactions, reaches thermal equilibrium. The irreversible reaction of RO$_2$ with NO leads to fragmentation into CO$_2$ and a vinyl radical, which subsequently forms volatile gas-phase products, such as formaldehyde and CO (Orlando et al., 1999). At [OH]= 2 × 10^6 molec cm^{-3}, the reaction of MPAN with OH has a rate comparable to that of thermal decomposition (Orlando et al., 2002), and leads to formation of aerosol products. Hence, the SOA formation potential for this system depends critically on the NO$_2$/NO

ratio. High NO$_2$/NO ratios shift the thermal equilibrium towards the unsaturated PAN, and SOA formation increases as the fraction of PAN reacting with OH radicals increases. At low NO$_2$/NO ratios, acyl peroxy radicals react predominantly with NO, leading to relatively volatile products.

Previous measurements of isoprene SOA yields under high-NO$_x$ conditions have been carried out using photolysis of HONO (Kroll et al., 2005a) or the recycling of HO$_x$ and NO$_x$ to generate OH (so-called classical photooxidation) (Pandis et al., 1991; Dommen et al., 2006). Low SOA yields were observed as NO concentrations remained high during the experiments. In fact, SOA growth occurred only after NO concentrations decreased to less than 10 ppb (Kroll et al., 2005a; Dommen et al., 2006). It was proposed that after NO has been consumed, aerosol formation commences as the RO$_2$+HO$_2$ pathway becomes competitive. However, such a mechanism is inconsistent with the major differences in composition observed between high- and low-NO$_x$ SOA products. High-NO$_x$ SOA from isoprene photooxidation is dominated by esterification products of C$_4$-carboxylic acids, whereas under low-NO$_x$ conditions, SOA is dominated by peroxides and C$_5$-tetrols (Surratt et al., 2006). It is more likely that the decrease in NO concentration (and increase in NO$_2$ concentration) leads to a transition from an RO$_2$+NO dominated regime to an RO$_2$+NO$_2$ dominated regime, resulting in significant SOA formation via the MPAN route.
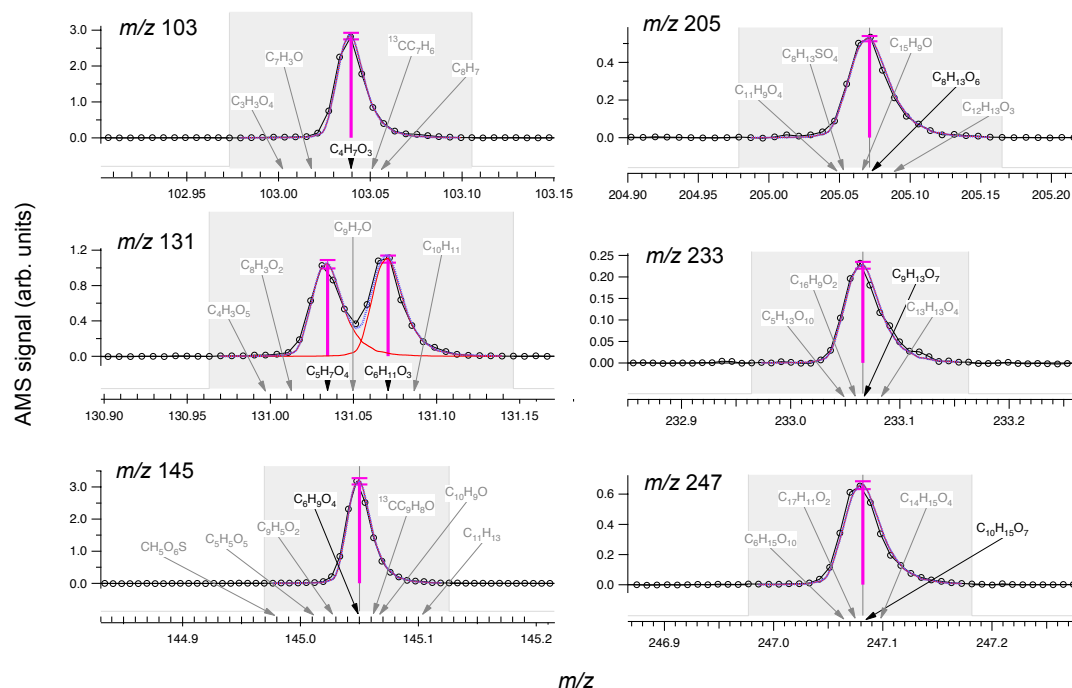
Fig. 9. High-resolution W-mode AMS peaks of a number of the major fragment ions observed in methacrolein/high-NO$_2$ experiments. Knowledge of the accurate masses allow assignments of molecular formulas, corresponding to loss of hydroxyl groups from compounds detected by offline analysis, suggesting that detection of compounds listed in Table 3 is not a result of sampling artifacts. *m/z* 131 contains two different ions, only one of which is consistent with compounds detected by offline UPLC/(–)ESI-TOFMS analysis.

At NO$_2$/NO ratios (between 3 and 8) higher than in previous studies (and more relevant to urban conditions), SOA yields from isoprene are approximately 3 times larger than previously measured. The yields even exceed those under low-NO$_x$ conditions at the same organic aerosol loadings, as shown in Fig. 11. This is, in fact, consistent with observations from Kroll et al. (2006) that at very low NO$_x$ concentrations, addition of NO actually increases SOA yield. It is likely that under very low NO concentrations, the NO$_2$/NO ratio increases rapidly, as NO is quickly converted to NO$_2$. SOA yields are therefore higher than those in the absence of NO, as RO$_2$ (from methacrolein)+NO$_2$ forms SOA more efficiently than RO$_2$ (from isoprene)+HO$_2$. However, further increasing NO decreases the NO$_2$/NO ratio. RO$_2$ (from methacrolein)+NO becomes more dominant, forms volatile products and leads to a decrease in SOA yield. It must be noted that the effect of RO$_2$ radical chemistry on SOA formation is complex and can be unique to different systems (Kroll and Seinfeld, 2008). Also, the acidity of the inorganic seed can increase SOA yields significantly: Surratt et al. (2010) shows that SOA yields from isoprene low-NO$_x$ photooxidation can be as high as 0.29. Detailed knowledge of the chemical mechanism is required to predict the effect of NO$_x$ conditions on SOA production.

6 Role of PAN in SOA formation

6.1 Unsaturated aldehydes

One can infer from the shapes of the growth curves the relative timescales of the reaction steps of SOA formation. In all high-NO$_2$ experiments, a greater extent of reaction is achieved than in high-NO experiments, and SOA formation continues after the parent hydrocarbon is completely consumed; this behavior is characterized by a vertical portion ("hook") at the end of the SOA growth curve. The presence of this vertical portion indicates that SOA formation results from further reaction of first-generation products, which is the rate-limiting step in the mechanism (see Figs. 3–5). This observation is consistent with our previous results showing that first-generation products of methacrolein, such as hydroxyacetone and MPAN, are themselves still volatile (Surratt et al., 2010). SOA is instead formed from the further OH reaction of MPAN, which has a comparable rate coefficient to that of methacrolein (Orlando et al., 2002).

Formation of dihydroxycarboxylic acids (e.g. 2-MG), hydroxynitrooxycarboxylic acids, and corresponding oligoesters appears to be important SOA formation pathways for the five α, β-unsaturated aldehydes studied here (methacrolein, acrolein, crotonaldehyde, 2M2B, 2-pentenal). All of the SOA constituents detected by offline UPLC/(–)ESI-TOFMS in these systems are structural
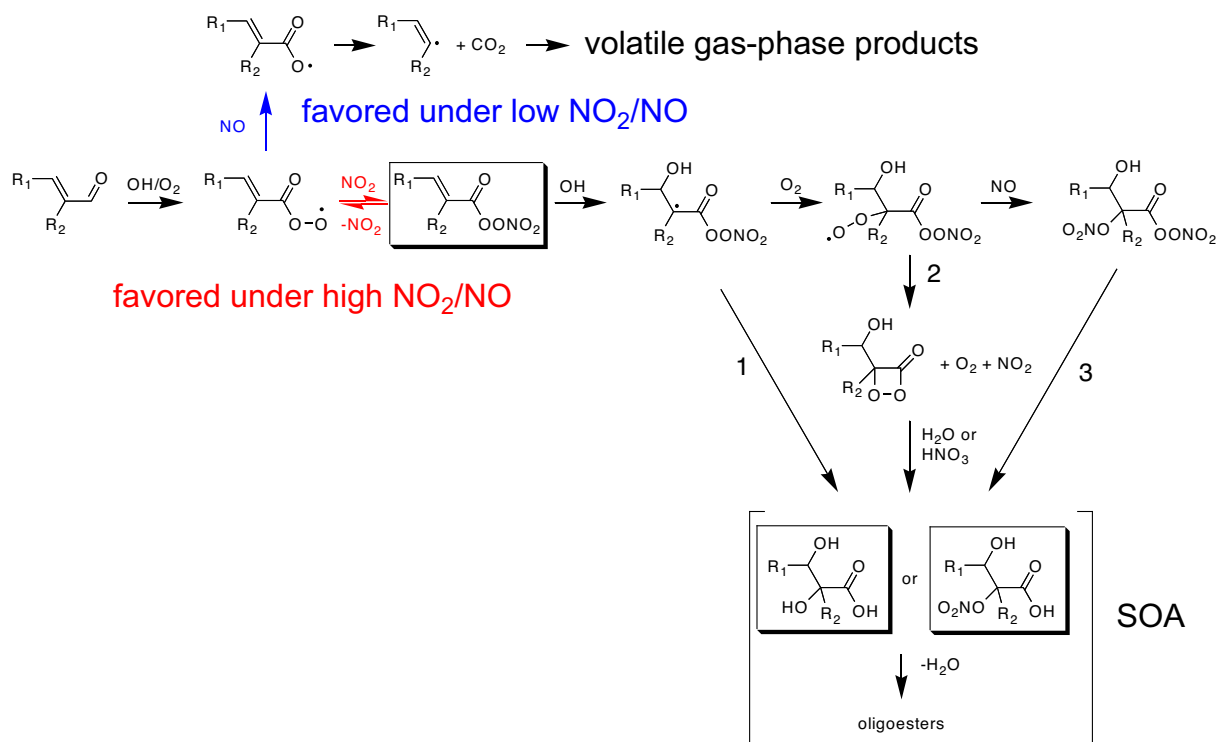
Fig. 10. Proposed mechanism to form aerosol-phase products from α,β-unsaturated aldehydes. The pathways highlighted in red are favored under high NO$_2$/NO ratios and lead to aerosol formation. The pathways highlighted in blue are favored under low NO$_2$/NO ratios and lead to fragmentation into volatile products. Aerosol formation from OH-reaction of unsaturated PANs can proceed via 3 possible routes (routes 1–3), and detailed investigation of each route is discussed in the main text.

analogs of each other, as confirmed by the online AMS operated in the high-resolution W-mode. Based on similarities in SOA growth trends and composition, we expect that the formation of SOA products proceeds via pathways similar to those elucidated in Surratt et al. (2010) (see Fig. 10). Although oxidation of these aldehydes can lead to α-dicarbonyls, such as glyoxal and methylglyoxal, which can undergo reactive uptake under humid conditions (Liggio et al., 2005; Kroll et al., 2005b; Volkamer et al., 2009), these compounds are not expected to contribute significantly to SOA formation under dry conditions. In addition, the AMS spectra for acrolein and crotonaldehyde SOA do not show peaks that are characteristic of glyoxal and its oligomers, as described in Liggio et al. (2005) and Galloway et al. (2009).

While MPAN is clearly the intermediate in SOA formation from methacrolein, the exact mechanism by which MPAN leads to such aerosol-phase products as 2-MG and hydroxynitrooxycarboxylic acids has not been established. From the oligoesters observed in the aerosol phase, it appears that the C$_4$ backbone of MPAN remains intact. Following OH addition to the double bond, the only known gas-phase pathway that would preserve the carbon backbone is formation of hydroxynitrates. (Fragmentation of the MPAN-alkoxy radical would break up the C$_4$ backbone and yield smaller products.) The nitrooxy functional groups could then be hydrolyzed to

hydroxyl groups (Sato, 2008) to form 2-MG and high-MW oligoesters (Route 3 in Fig. 10). However, gas-phase abundances of C$_4$- (for methacrolein and crotonaldehyde) or C$_5$- (for 2M2B, 3M2B and 2-pentenal) hydroxynitrate-PAN, the supposed SOA intermediate in all these systems, do not correlate with the amount of aerosol formed. Substitution of the α-carbon atom by methyl groups (from crotonaldehyde to methacrolein, or from 3M2B to 2M2B) leads to an increase in the amount of SOA formed by more than a factor of 4, but no increase in gas-phase signal of the hydroxynitrate-PAN is observed (see Fig. 12), implying that it is unlikely the SOA-forming channel.

Another possible mechanism is that in which after OH addition to the double bond in MPAN the OH-adduct undergoes intramolecular rearrangement before addition of O$_2$, leading to formation of 2-MG and oligoesters (Route 1 in Fig. 10). Such isomerization can be competitive with O$_2$ addition, as the O-O bond in the peroxy nitrate moiety is weak. In one experiment (17/12/09), the chambers were flushed with nitrogen to lower the oxygen content to 2%, thereby slowing down addition of O$_2$ by a factor of 10. Compared to another experiment with 21% O$_2$ (16/12/09), no increase in aerosol formation is observed, suggesting that SOA formation likely involves O$_2$ addition to the MPAN-OH adduct, though it is also possible that the intramolecular rearrangement reaction
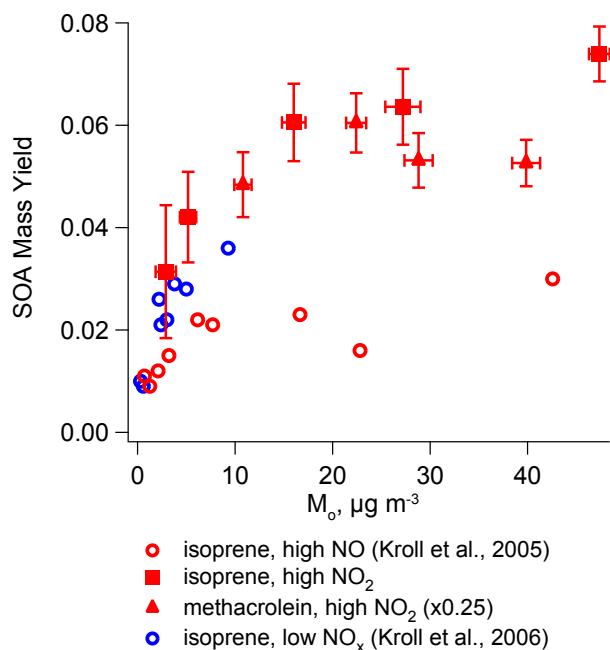
Fig. 11. SOA mass yields from isoprene photooxidation under neutral seed conditions as a function of organic loading. The solid markers indicate SOA yields measured in this study, using CH$_3$ONO as the OH precursor under high NO$_2$/NO ratios (between 3 and 8). The SOA yields for methacrolein (solid red triangles) have been multiplied by 0.25 to account for the gas-phase product yield of methacrolein from isoprene high-NO$_x$ oxidation. The SOA yields measured under high-NO$_2$/NO conditions are higher than both high-NO (open red circles) and low-NO$_x$ conditions (open blue circles) under neutral seed conditions. With an acidified seed, SOA yields can be as high as 0.29 (Surratt et al., 2010).

is sufficiently fast that O$_2$ addition is not competitive at these O$_2$ levels.

From the trends of SOA formation observed in the unsaturated aldehyde systems, it appears that the chemical environment of the carbon atom adjacent to the aldehyde group plays an important role in determining the extent of SOA formation. Low-volatility oligoesters are formed only when the α- and β-carbon atoms are unsaturated; SOA yields of 4-pentenal, for which the olefinic bond is in the 4-position, are lower than those of 2-pentenal, and the SOA products are not analogous to those found in SOA from α, β-unsaturated aldehydes (see Fig. 13). SOA formation is correlated with fraction of OH addition to the β-carbon atom, which forms a radical at the α site: SOA yields of crotonaldehyde and 2-pentenal (in which OH addition to the β-carbon is favored) exceed those of 3M2B (in which OH addition to the α-carbon is favored), even though 3M2B has an equal or higher molecular weight. This suggests that an interaction responsible for producing low-volatility species occurs between the peroxy nitrate functional group and the α-carbon (likely a radical species) that our experiments are not able to precisely re-
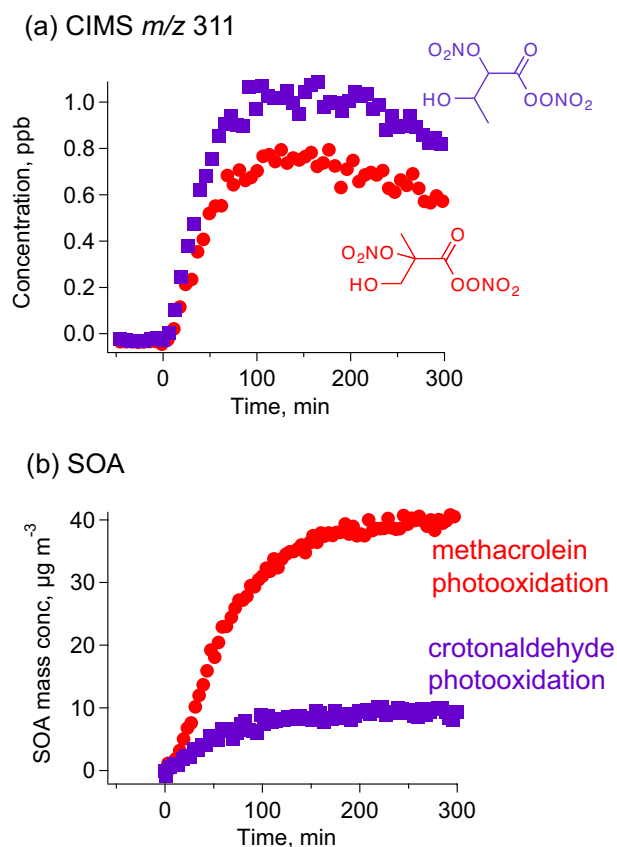
Fig. 12. Time trends of **(a)** gas-phase CIMS m/z 311 and **(b)** SOA growth during high-NO$_2$ photooxidation of methacrolein (red) and crotonaldehyde (purple). m/z 311 corresponds to the unit mass of CF$_3$O$^-$ adduct of C$_4$-hydroxynitrate-PAN. The observed gas-phase signals of C$_4$-hydroxynitrate-PAN in both experiments are within 20% of each other, but the amount of SOA formed from methacrolein photooxidation is about a factor of 4 higher. A similar difference was observed between 2M2B and 3M2B photooxidation. This suggests that C$_4$- and C$_5$-hydroxynitrate-PANs are not precursors to low-volatility aerosol-phase products.

veal. We hypothesize that the peroxy radical undergoes self cyclization to form a highly reactive dioxoketone intermediate, which subsequently reacts with H$_2$O or HNO$_3$ heterogeneously to form the low-volatility products observed in the SOA (see Fig. 10). This intermediate is likely short-lived, and further work is required to identify this species and its role in SOA formation.

One possible explanation for the higher SOA yields observed from methacrolein and 2M2B is that for these compounds SOA formation is favored by steric hindrance. With an additional methyl group on the α carbon, steric repulsion causes the methyl group to move away from the neighbouring peroxy nitrate functional group by rotation of the C-C bond. As a result, the intramolecular reaction leading to SOA formation can be enhanced, consistent with the relatively higher SOA yields. For the other α, β-unsaturated

Fig. 13. UPLC/(–)ESI-TOFMS base peak ion chromatograms (BPCs) for high-NO$_2$ photooxidation of **(a)** crotonaldehyde **(b)** 2M2B **(c)** 2-pentenal and (d) 4-pentenal. The exact 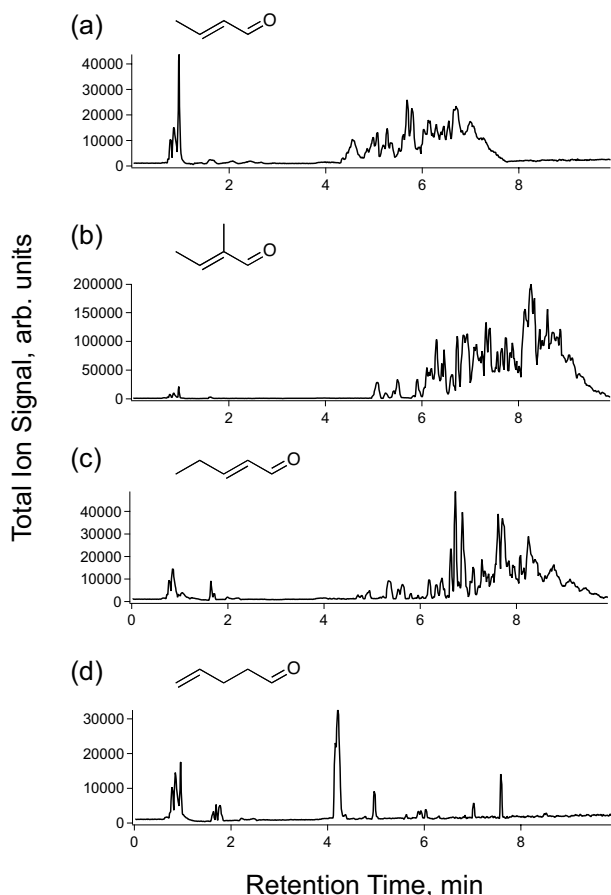masses and elemental composition of detected [M-H]$^-$ ions are listed in the Supplementary Material. Compounds detected in crotonaldehyde, 2M2B and 2-pentenal SOA are likely similar. (SOA products from C$_5$ 2M2B and 2-pentenal are less polar than those from crotonaldehyde, a C$_4$ compound, and therefore have longer retention times in reverse-phase chromatography.) The chemical composition of 4-pentenal SOA is significantly different from those all 3 other aldehydes, and no oligoester products are detected, suggesting a different SOA formation mechanism.

aldehydes, this interaction is likely not favored, as the hydrogen atom on the α carbon is in plane with the peroxy nitrate group in the most stable rotational conformer (see Fig. 14). The interaction between the peroxy nitrate group and the added functional group is reduced, corresponding to lower SOA formation. Thermodynamic calculations of the relative stabilities of the conformers are required to confirm this hypothesis.
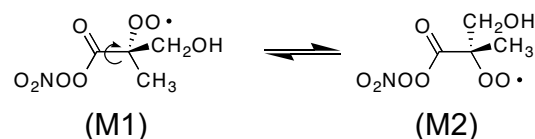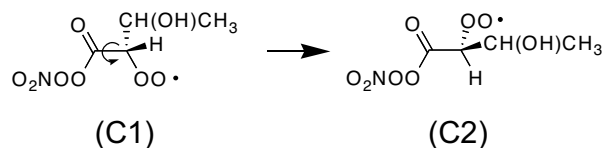

Fig. 14. Rotational conformers of hypothesized SOA intermediate in methacrolein and crotonaldehyde mechanism. For methacrolein, the methyl group on the α-carbon presents significant steric hinderance, which favors the conformer M2. This increases the interaction between the peroxy radical and the peroxy nitrate group, leading to significant SOA formation. For crotonaldehyde, the hydrogen atom presents much smaller steric hinderance, favoring the conformer C2. As a result, the peroxy radical is out of plane with the PAN group, and the reaction to form SOA can be less favorable.

6.2 Methylbutenols (MBO)

MBO232 is a biogenic hydrocarbon potentially important in forest photochemistry (Harley et al., 1998). The SOA yields of MBO232 photooxidation have been shown to be negligible, under both high- and low-NO$_x$ conditions (Carrasco et al., 2007; Chan et al., 2009a). In this study, SOA formation from MBO232 photooxidation is below detection limit, even at high NO$_2$/NO ratios (which would favor any PAN formation). This is likely linked to the lack of PAN products from MBO232 oxidation. The fate of the alkoxy radical formed from OH-initiated oxidation of MBO232 is shown in Fig. 15. Scission of the C-C bond adjacent to the tertiary carbon is favored, leading to high yields of glycolaldehyde (>0.6). Formation of 2-hydroxymethylpropanal (2-HMPR) following scission of the C-C bond adjacent to the primary carbon is not the favored route, and hence the yields of 2-HMPR are relatively low (< 0.4). Furthermore, OH oxidation of 2-HMPR proceeds by OH abstraction of the aldehydic hydrogen, but owing to the neighbouring hydroxyl group, decomposition to acetone and CO is favored over addition of O$_2$ to form an acyl peroxy radical. Carrasco et al. (2006) found no PAN formation from photooxidation of 2-HMPR, despite high NO$_2$/NO ratios.

MBO231 photooxidation produces, in contrast, substantial amounts of SOA, at mass yields of 0.008 – 0.042. In MBO231, the hydroxyl group is in the 1-position and is not adjacent to the double bond. Decomposition of the analogous alkoxy radical therefore proceeds by scission of the C-C
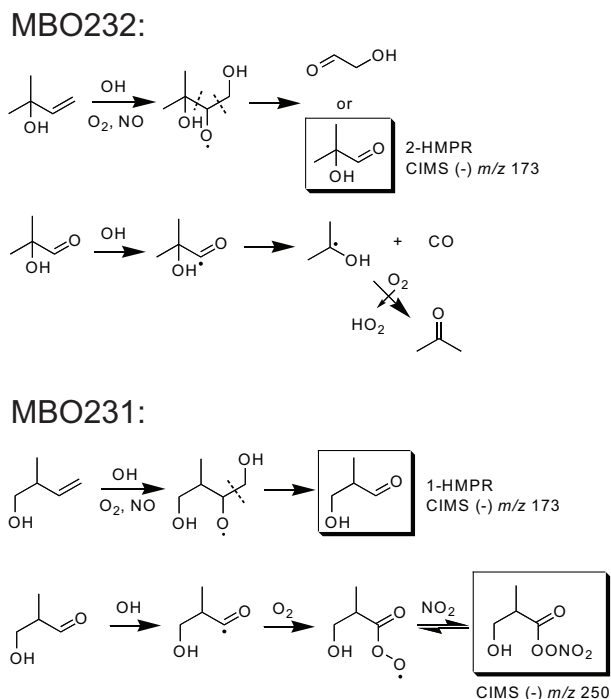
MBO232:

MBO231:

Fig. 15. Mechanism of MBO231 and MBO232 photooxidation under high-NO$_x$ conditions. The dashed lines indicate possible locations of C-C bond scission under decomposition of alkoxy radicals. For MBO232, 2-HMPR formation is relatively small, as scission of the C-C bond with the 4-carbon is not favored. In addition, the acyl radical from H-abstraction of 2-HMPR rapidly decomposes to CO and acetone. As a result, PAN formation is unlikely. For MBO231, 1-HMPR formation is favored from the decomposition of the alkoxy radical. Furthermore, OH reaction of 1-HMPR leads to an acyl peroxy radical, which reacts with NO$_2$ to form a C$_4$-hydroxy-PAN.

bond adjacent to the primary carbon, favoring the formation of 1-HMPR; observed HMPR (CIMS (–)m/z 173) concentrations in MBO231 photooxidation were twice as high as those in MBO232 photooxidation. Also, following abstraction of the aldehydic hydrogen from 1-HMPR, addition of O$_2$ to form an acyl peroxy radical is favored over decomposition to CO. Under high-NO$_2$ conditions, the acyl peroxy radical can react with NO$_2$ to form a C$_4$-hydroxy-PAN (see Fig. 15). Tandem mass spectrometry was used to distinguish gas-phase C$_4$-hydroxy-PAN from the isobaric C$_5$ dihydroxynitrate, both observed at (–)m/z 250 (see Supplementary Material for details). The C$_5$ dihydroxynitrate is a first generation oxidation product of both MBO231 and MBO232 formed from RO$_2$+NO at molar yields of 0.10–0.15 (Chan et al., 2009a). In high-NO photooxidation of MBO231 and high-NO$_2$ photooxidation of MBO232, no C$_4$-hydroxy-PAN was observed in the gas phase, corresponding to negligible aerosol formation. In high-NO$_2$ photooxidation of MBO231, C$_4$-hydroxy-PAN is a major gas-phase product, and SOA formation is significant. The identification of C$_4$-hydroxy-PAN

is further supported by the ratios of ion signals of m/z 250 to m/z 251, its ^{13}C isotopologue, which indicate that the signal at m/z 250 was dominated by a C$_4$ compound during MBO231 high-NO$_2$ photooxidation, and by a C$_5$ compound during MBO232 photooxidation. Hence, the low SOA yields from MBO232 are due to the lack of PAN formation, illustrating the potentially important role of PAN compounds as SOA intermediates.

7 Conclusions

In this work, we systematically investigate the effect of relative NO and NO$_2$ concentrations on SOA formation from aldehyde photooxidation under high-NO$_x$ conditions. A strong positive correlation of SOA yields with NO$_2$/NO ratio is observed for methacrolein (a major oxidation product of isoprene responsible for SOA formation) and two related α,β-unsaturated aldehydes, acrolein and crotonaldehyde. Oligoester products from dihydroxycarboxylic acids and hydroxynitrooxycarboxylic acids are also observed to depend on NO$_2$/NO ratio, confirming that PAN chemistry plays an important role in formation of these low-volatility products. Offline high-resolution aerosol mass spectrometry reveals that analogous oligoester products are major constituents in SOA formed from all α,β-unsaturated aldehyes studied here. By comparing SOA formation from structurally similar aldehydes, we establish that SOA formation is favored when the α-carbon is substituted by a methyl group and the olefinic bond is in the 2-position, such as in methacrolein and 2M2B. The experimental data suggest that SOA formation proceeds via an intramolecular reaction involving the peroxy nitrate functional group, following the addition of O$_2$ to the MPAN+OH adduct. No aerosol formation is observed from MBO232, an atmospherically important unsaturated alcohol, even at high NO$_2$/NO ratios, as PAN formation is structurally unfavorable.

Understanding the overall effect of NO$_x$ on SOA yields is important, as SOA yields can vary greatly depending on NO$_x$ conditions. In most photooxidation systems, addition of OH, followed by O$_2$, to an olefinic bond results in formation of a hydroxyperoxy radical. The competition between the RO$_2$+HO$_2$ pathway (which forms low-volatility hydroperoxides) and the RO$_2$+NO pathway (which forms volatile organic nitrates and fragmentation products) determines the SOA yields. In the isoprene-high-NO$_x$ system, owing to the MPAN chemistry, aerosol formation proceeds via OH abstraction of the aldehydic hydrogen from methacrolein. As a result, a competition exists between reaction of the acyl peroxy radical with NO$_2$, leading to formation of MPAN and SOA, and with NO to form volatile fragmentation products. The present work shows the importance of the RO$_2$+NO$_2$ pathway of unsaturated aldehyde photooxidation as a route leading to SOA formation. This could have important implications on SOA formation from
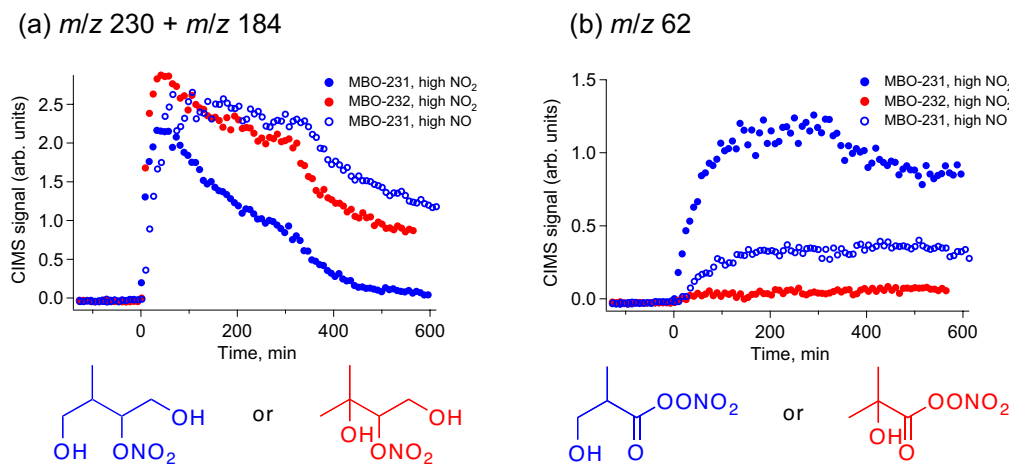
Fig. 16. Gas-phase ion signals of C_4-hydroxy-PAN and C_5-dihydroxynitrate from photooxidation of MBO231 and MBO232, as observed by negative chemical ionization-tandem mass spectrometry of m/z 250. Neutral losses of HF or CF_2O are associated with the C_5-dihydroxynitrate under CID of the parent ion m/z 250, leading to daughter ions of 230 and 184, respectively. The daughter ion m/z 62, most likely NO_3^-, is associated with the C_4-hydroxy-PAN. (See Supplementary Material for more details.) After 300 minutes of irradiation, more OH precursor was added to further react oxidation products. PAN formation was observed only from MBO231 oxidation and is positively correlated with NO_2/NO, similar to unsaturated aldehydes.

other atmospheric compounds, especially those with conjugated double bonds. For example, photooxidation of aromatic compounds (Calvert et al., 2002) can lead to α, β-unsaturated aldehydes, which can form significant amounts of low-volatility products via a PAN intermediate. At atmospherically relevant NO_2/NO ratios, SOA yields from isoprene are 0.031–0.074 at organic aerosol loadings of 3–47 µg m^{-3}; these values are 3 times higher than those previously measured under high-NO conditions. The yields exceed even those measured under low-NO_x conditions. An implication of these results is that atmospheric SOA formation from aldehydes may be significantly underestimated in current models, since an appreciable fraction of SOA is generated in areas where NO_2/NO ratios are high.
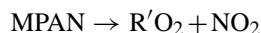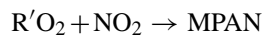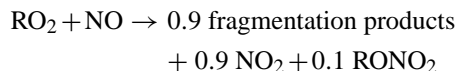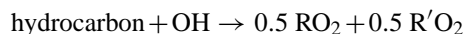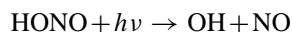
Radiocarbon (^{14}C) studies have repeatedly shown that ambient organic aerosol is dominated by biogenic carbon, suggesting that biogenic hydrocarbons are an important source of SOA. However, field measurements have shown that organic aerosol levels tend to be correlated with anthropogenic tracers such as CO and acetylene. From satellite observations one can infer that while the source of carbon in many regions is most likely biogenic, the aerosol formation from biogenic hydrocarbons is significantly enhanced by anthropogenic activities (i.e. NO_x and SO_x emissions (Goldstein et al., 2009; Carlton et al., 2010)). The present work moves in the direction of reconciling these two seemingly contradictory observations of biogenic carbon versus anthropogenic enhancement. Here we show that the SOA yields from photooxidation of isoprene under atmospherically relevant NO_2/NO ratios are significantly larger than those previously measured under lower NO_2/NO ratios. Moreover, the SOA yields un-

der these conditions are larger than those under low-NO_x conditions, suggesting that SOA formation from isoprene, the most abundantly emitted non-methane biogenic hydrocarbon, can be more efficient in urban high-NO_x plumes than in remote regions.

Appendix A

Photochemical modeling to estimate NO and NO_2 concentrations

Owing to interference with the NO_2 signal by HONO and CH_3ONO in the chemiluminescence NO_x monitor, we estimate NO and NO_2 concentrations during chamber experiments by photochemical modeling. In experiments in which HONO is the source of OH, the photolysis rate of HONO is estimated from the first-order decay of the m/z 66 signal on the CIMS, which correspond to the $HF \cdot ONO^-$ ion. The initial mixing ratio of HONO was estimated based on the decay of parent hydrocarbon and known rate constants (Atkinson and Arey, 2003; Magneron et al., 2002). Previous comparison to a GC/NO_2 analyzer allows us to determine the HONO interference on the NO_2 signal, and hence the amount of NO and NO_2 produced during HONO synthesis (Chan et al., 2009b). The initial mixing ratio of NO_2 is therefore the sum of the concentrations of NO_2 impurity from HONO synthesis (calculated by multiplying the NO_2 signal after HONO injection by a known factor) and additional NO_2 injected (the increase in NO_2 signal from direct injection). For unsaturated aldehydes, the photochemical model includes the following reactions:

$$HONO + h\nu \rightarrow OH + NO$$
$$hydrocarbon + OH \rightarrow 0.5\,RO_2 + 0.5\,R'O_2$$
$$RO_2 + NO \rightarrow 0.9\,fragmentation\,products$$
$$+\,0.9\,NO_2 + 0.1\,RONO_2$$
$$R'O_2 + NO \rightarrow fragmentation\,products + NO_2$$
$$R'O_2 + NO_2 \rightarrow MPAN$$
$$MPAN \rightarrow R'O_2 + NO_2$$

RO$_2$ denotes the peroxy radical produced by OH addition to the C=C double bond, followed by O$_2$. R'O$_2$ denotes the acyl peroxy radical produced by OH abstraction of the aldehydic hydrogen, followed by O$_2$ addition. These two channels (OH addition and abstraction) have a branching ratio of 1:1 for methacrolein (Tuazon and Atkinson, 1990). Other reactions involving O$_3$, HO$_x$, NO$_x$ are also included in the mechanism. For MBO231 and MBO232, the reactions described in Chan et al. (2009a) are used. The calculated NO$_2$/NO ratios averaged over the first 200 min of irradiation (the period during which SOA formation occurred, see Fig. 1) are listed in Table 2.

For the high-NO$_2$ experiments, CH$_3$ONO was used as the OH precursor:

$$CH_3ONO + h\nu \rightarrow CH_3O + NO$$
$$CH_3O + O_2 \rightarrow HCHO + HO_2$$
$$HO_2 + NO \rightarrow OH + NO_2$$
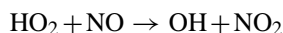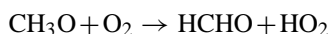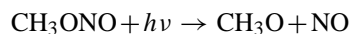
The photolysis rate of CH$_3$ONO was estimated by the first-order decay of the CH$_3$ONO signal on GC/FID. The initial mixing ratio of CH$_3$ONO was determined from the measured vapor pressure of CH$_3$ONO in the injection bulb. The modeled decay of the hydrocarbon is consistent with that observed by GC/FID. FTIR analysis shows no NO or NO$_2$ impurities are produced during CH$_3$ONO synthesis ([NO$_2$] was less than 0.6% of [CH$_3$ONO]). In the photochemical calculations, the initial NO and NO$_2$ concentrations are determined from the increase in NO and NO$_2$ signals from direct injection. The calculated NO$_2$/NO ratios averaged over the first 100 min of irradiation are listed in Table 2 (see Fig. 2).

Supplementary material related to this article is available online at: http://www.atmos-chem-phys.net/10/7169/2010/ acp-10-7169-2010-supplement.pdf.

References

Atkinson, R. and Arey, J.: Atmospheric degradation of volatile organic compounds, Chem. Rev., 103, 4605–4638, 2003.

Calvert, J. G., Atkinson, R., Becker, K. H., Kamens, R. M., Seinfeld, J. H., Wallington, T. J., and Yarwood, G.: The mechanisms of atmospheric oxidation of aromatic hydrocarbons, Oxford University Press, 2002.

Canagaratna, M. R., Jayne, J. T., Jimenez, J. L., Allan, J. D., Alfarra, M. R., Zhang, Q., Onasch, T. B., Drewnick, F., Coe, H., Middlebrook, A., Delia, A., Williams, L. R., Trimborn, A. M., Northway, M. J., DeCarlo, P. F., Kolb, C. E., Davidovits, P., and Worsnop, D. R.: Chemical and microphysical characterization of ambient aerosols with the Aerodyne aerosol mass spectrometer, Mass. Spec. Rev., 26, 185–222, 2007.

Carlton, A. G., Wiedinmyer, C., and Kroll, J. H.: A review of Secondary Organic Aerosol (SOA) formation from isoprene, Atmos. Chem. Phys., 9, 4987–5005, doi:10.5194/acp-9-4987-2009, 2009.

Carlton, A. G., Pinder, R. W., Bhave, P. V. and Pouliot, G. A.: To what extent can biogenic SOA be controlled? Environ. Sci. Technol., 44, 3376–3380, 2010.

Carrasco, N., Doussin, J. F., Picquet-Varrault, B., and Carlier, P.: Tropospheric degradation of 2-hydroxy-2-methylpropanal, a photo-oxidation product of 2-methyl-3-buten-2-ol: Kinetic and mechanistic study of its photolysis and its reaction with OH radicals, Atmos. Environ., 40, 2011–2019, 2006.

Carrasco, N., Doussin, J. F., O'Connor, M., Wenger, J. C., Picquet-Varrault, B., Durand-Jolibois, R., and Carlier, P.: Simulation chamber studies of the atmospheric oxidation of 2-methyl-3-buten-2-ol: Reaction with hydroxyl radicals and ozone under a variety of conditions, J. Atmos. Chem., 56, 33–55, 2007.

Chan, A. W. H., Galloway, M. M., Kwan, A. J., Chhabra, P. S., Keutsch, F. N., Wennberg, P. O., Flagan, R. C., and Seinfeld, J. H.: Photooxidation of 2-methyl-3-buten-2-ol (MBO) as a potential source of secondary organic aerosol, Environ. Sci. Technol., 43, 4647–4652, 2009a.

Chan, A. W. H., Kautzman, K. E., Chhabra, P. S., Surratt, J. D., Crounse, J. D., Kürten, A, Wennberg, P. O., Flagan, R. C., Seinfeld, J. H.: Secondary organic aerosol formation from photooxidation of naphthalene and alkylnaphthalenes: implications for oxidation of intermediate volatility organic compounds (IVOCs), Atmos. Chem. Phys., 9, 3049-3060, doi:10.5194/acp-9-3049-2009, 2009.

Chung, S. H. and Seinfeld, J. H.: Global distribution and climate forcing of carbonaceous aerosols, J. Geophys. Res.-Atmos., 107, doi:10.1029/2001JD001397, 2002.

Claeys, M., Graham, B., Vas, G., Wang, W., Vermeylen, R., Pashynska, V., Cafmeyer, J., Guyon, P., Andreae, M. O., Artaxo, P., and Maenhaut, W.: Formation of secondary organic aerosols through photooxidation of isoprene, Science, 303, 1173–1176, 2004.

Cocker, D. R., Flagan, R. C., and Seinfeld, J. H.: State-of-the-art chamber facility for studying atmospheric aerosol chemistry, Environ. Sci. Technol., 35, 2594–2601, 2001.

Crounse, J. D., McKinney, K. A., Kwan, A. J., and Wennberg, P. O.: Measurement of gas-phase hydroperoxides by chemical ionization mass spectrometry, Anal. Chem., 78, 6726–6732, 2006.

de Gouw, J. A., Middlebrook, A. M., Warneke, C., Goldan, P. D., Kuster, W. C., Roberts, J. M., Fehsenfeld, F. C., Worsnop, D. R., Canagaratna, M. R., Pszenny, A. A. P., Keene, W. C., Marchewka, M., Bertman, S. B., and Bates, T. S.: Budget of organic carbon in a polluted atmosphere: Results from the New England Air Quality Study in 2002, J. Geophys. Res.-Atmos., 110, D16305, doi:10.1029/2004JD005623, 2005.

de Gouw, J. A., Brock, C. A., Atlas, E. L., Bates, T. S., Fehsenfeld, F. C., Goldan, P. D., Holloway, J. S., Kuster, W. C., Lerner, B. M., Matthew, B. M., Middlebrook, A. M., Onasch, T. B., Peltier, R. E., Quinn, P. K., Senff, C. J., Stohl, A., Sullivan, A. P., Trainer, M., Warneke, C., Weber, R. J., and Williams, E. J.: Sources of particulate matter in the northeastern United States in summer: 1. Direct emissions and secondary formation of organic matter in urban plumes, J. Geophys. Res.-Atmos., 113, D08301, doi: 10.1029/2007JD009243, 2008.

DeCarlo, P. F., Kimmel, J. R., Trimborn, A., Northway, M. J., Jayne, J. T., Aiken, A. C., Gonin, M., Fuhrer, K., Horvath, T., Docherty, K. S., Worsnop, D. R., and Jimenez, J. L.: Field-deployable, high-resolution, time-of-flight aerosol mass spectrometer, Anal. Chem., 78, 8281–8289, 2006.

Dommen, J., Metzger, A., Duplissy, J., Kalberer, M., Alfarra, M. R., Gascho, A., Weingartner, E., Prevot, A. S. H., Verheggen, B., and Baltensperger, U.: Laboratory observation of oligomers in the aerosol from isoprene/NO$_x$ photooxidation, Geophys. Res. Lett., 33, L13805, doi:10.1029/2006GL026523, 2006.

Edney, E. O., Kleindienst, T. E., Jaoui, M., Lewandowski, M., Offenberg, J. H., Wang, W., and Claeys, M.: Formation of 2-methyl tetrols and 2-methylglyceric acid in secondary organic aerosol from laboratory irradiated isoprene/NO$_x$/SO$_2$/air mixtures and their detection in ambient PM2.5 samples collected in the eastern United States, Atmos. Environ., 39, 5281–5289, 2005.

Fantechi, G., Jensen, N. R., Hjorth, J., and Peeters, J.: Determination of the rate constants for the gas-phase reactions of methyl butenol with OH radicals, ozone, NO$_3$ radicals, and Cl atoms, Int. J. Chem. Kinet., 30, 589–594, 1998.

Galloway, M. M., Chhabra, P. S., Chan, A. W. H., Surratt, J. D., Flagan, R. C., Seinfeld, J. H., and Keutsch, F. N.: Glyoxal uptake on ammonium sulphate seed aerosol: reaction products and reversibility of uptake under dark and irradiated conditions, Atmos. Chem. Phys., 9, 3331–3345, doi:10.5194/ acp-9-3331-2009, 2009.

Goldstein, A. H., Koven, C. D., Heald, C. L., and Fung, I. Y.: Biogenic carbon and anthropogenic pollutants combine to form a cooling haze over the southeastern United States, Proc. Natl. Acad. Sci. USA, 106, 8835–8840, 2009.

Guenther, A., Karl, T., Harley, P., Wiedinmyer, C., Palmer, P. I., and Geron, C.: Estimates of global terrestrial isoprene emissions using MEGAN (Model of Emissions of Gases and Aerosols from Nature), Atmos. Chem. Phys., 6, 3181–3210, doi:10.5194/ acp-6-3181-2006, 2006.

Hallquist, M., Wenger, J. C., Baltensperger, U., Rudich, Y., Simpson, D., Claeys, M., Dommen, J., Donahue, N. M., George, C., Goldstein, A. H., Hamilton, J. F., Herrmann, H., Hoffmann, T., Iinuma, Y., Jang, M., Jenkin, M. E., Jimenez, J. L., Kiendler-Scharr, A., Maenhaut, W., McFiggans, G., Mentel, Th. F., Monod, A., Prvt, A. S. H., Seinfeld, J. H., Surratt, J. D., Szmigielski, R., and Wildt, J.: The formation, properties and impact of secondary organic aerosol: current and emerging issues, Atmos. Chem. Phys., 9, 5155–5236, doi:10.5194/ acp-9-5155-2009, 2009.

Harley, P., Fridd-Stroud, V., Greenberg, J., Guenther, A., and Vasconcellos, P.: Emission of 2-methyl-3-buten-2-ol by pines: A potentially large natural source of reactive carbon to the atmosphere, J. Geophys. Res.-Atmos., 103, 25479–25486, 1998.

Hatakeyama, S., Izumi, K., Fukuyama, T., Akimoto, H., and Washida, N.: Reactions of OH with alpha-pinene and beta-pinene in air – Estimate of global CO production from the atmospheric oxidation of terpenes, J. Geophys. Res.-Atmos., 96, 947–958, 1991.

Henze, D. K. and Seinfeld, J. H.: Global secondary organic aerosol from isoprene oxidation, Geophys. Res. Lett., 33, L09812, doi: 10.1029/2006GL025976, 2006.

Henze, D. K., Seinfeld, J. H., Ng, N. L., Kroll, J. H., Fu, T.-M., Jacob, D. J., and Heald, C. L.: Global modeling of secondary organic aerosol formation from aromatic hydrocarbons: high- vs. low-yield pathways, Atmos. Chem. Phys., 8, 2405–2420, doi: 10.5194/acp-8-2405-2008, 2008.

Hurley, M. D., Sokolov, O., Wallington, T. J., Takekawa, H., Karasawa, M., Klotz, B., Barnes, I., and Becker, K. H.: Organic aerosol formation during the atmospheric degradation of toluene, Environ. Sci. Technol., 35, 1358–1366, 2001.

Ion, A. C., Vermeylen, R., Kourtchev, I., Cafmeyer, J., Chi, X., Gelencsr, A., Maenhaut, W., and Claeys, M.: Polar organic compounds in rural PM$_{2.5}$ aerosols from K-puszta, Hungary, during a 2003 summer field campaign: Sources and diel variations, Atmos. Chem. Phys., 5, 1805–1814, doi:10.5194/ acp-5-1805-2005, 2005.

Johnson, D., Jenkin, M. E., Wirtz, K., and Martin-Reviejo, M.: Simulating the formation of secondary organic aerosol from the photooxidation of aromatic hydrocarbons, Environ. Chem., 2, 35–48, 2005.

Kanakidou, M., Seinfeld, J. H., Pandis, S. N., Barnes, I., Dentener, F. J., Facchini, M. C., Van Dingenen, R., Ervens, B., Nenes, A., Nielsen, C. J., Swietlicki, E., Putaud, J. P., Balkanski, Y., Fuzzi, S., Horth, J., Moortgat, G. K., Winterhalter, R., Myhre, C. E. L., Tsigaridis, K., Vignati, E., Stephanou, E. G., and Wilson, J.: Organic aerosol and global climate modelling: a review, Atmos. Chem. Phys., 5, 1053–1123, doi: 10.5194/acp-5-1053-2005, 2005.

Keywood, M. D., Varutbangkul, V., Bahreini, R., Flagan, R. C., and Seinfeld, J. H.: Secondary organic aerosol formation from the ozonolysis of cycloalkenes and related compounds, Environ. Sci. Technol., 38, 4157–4164, 2004.

Kleindienst, T. E., Lewandowski, M., Offenberg, J. H., Jaoui, M., and Edney, E. O.: The formation of secondary organic aerosol from the isoprene + OH reaction in the absence of NOx, Atmos. Chem. Phys., 9, 6541–6558, doi:10.5194/acp-9-6541-2009, 2009.

Kourtchev, I., Ruuskanen, T., Maenhaut, W., Kulmala, M., and Claeys, M.: Observation of 2-methyltetrols and related photooxidation products of isoprene in boreal forest aerosols from

Hyytiälä, Finland, Atmos. Chem. Phys., 5, 2761–2770, doi: 10.5194/acp-5-2761-2005, 2005.

Kroll, J. H. and Seinfeld, J. H.: Chemistry of secondary organic aerosol: Formation and evolution of low-volatility organics in the atmosphere, Atmos. Environ., 42, 3593–3624, 2008.

Kroll, J. H., Ng, N. L., Murphy, S. M., Flagan, R. C., and Seinfeld, J. H.: Secondary organic aerosol formation from isoprene photooxidation under high-NO$_x$ conditions, Geophys. Res. Lett., 32, L18808, doi:10.1029/2005GL023637, 2005a.

Kroll, J. H., Ng, N. L., Murphy, S. M., Varutbangkul, V., Flagan, R. C., and Seinfeld, J. H.: Chamber studies of secondary organic aerosol growth by reactive uptake of simple carbonyl compounds, J. Geophys. Res.-Atmos., 110, D23207, doi:10.1029/2005JD006004, 2005b.

Kroll, J. H., Ng, N. L., Murphy, S. M., Flagan, R. C., and Seinfeld, J. H.: Secondary organic aerosol formation from isoprene photooxidation, Environ. Sci. Technol., 40, 1869–1877, 2006.

Lewis, C. W. and Stiles, D. C.: Radiocarbon content of PM2.5 ambient aerosol in Tampa, FL, Aerosol. Sci. Tech., 40, 189–196, 2006.

Lewis, C. W., Klouda, G. A., and Ellenson, W. D.: Radiocarbon measurement of the biogenic contribution to summertime PM-2.5 ambient aerosol in Nashville, TN, Atmos. Environ., 38, 6053–6061, 2004.

Liggio, J., Li, S. M., and McLaren, R.: Heterogeneous reactions of glyoxal on particulate matter: Identification of acetals and sulfate esters, Environ. Sci. Technol., 39, 1532–1541, 2005.

Magneron, I., Thevenet, R., Mellouki, A., Le Bras, G., Moortgat, G. K., and Wirtz, K.: A study of the photolysis and OH-initiated oxidation of acrolein and trans-crotonaldehyde, J. Phys. Chem. A., 106, 2526–2537, 2002.

Ng, N. L., Chhabra, P. S., Chan, A. W. H., Surratt, J. D., Kroll, J. H., Kwan, A. J., McCabe, D. C., Wennberg, P. O., Sorooshian, A., Murphy, S. M., Dalleska, N. F., Flagan, R. C., and Seinfeld, J. H.: Effect of NO$_x$ level on secondary organic aerosol (SOA) formation from the photooxidation of terpenes, Atmos. Chem. Phys., 7, 5159–5174, doi:10.5194/acp-7-5159-2007, 2007a.

Ng, N. L., Kroll, J. H., Chan, A. W. H., Chhabra, P. S., Flagan, R. C., and Seinfeld, J. H.: Secondary organic aerosol formation from m-xylene, toluene, and benzene, Atmos. Chem. Phys., 7, 3909–3922, doi:10.5194/acp-7-3909-2007, 2007b.

Orlando, J. J., Tyndall, G. S., and Paulson, S. E.: Mechanism of the OH-initiated oxidation of methacrolein, Geophys. Res. Lett., 26, 2191–2194, 1999.

Orlando, J. J., Tyndall, G. S., Bertman, S. B., Chen, W. C., and Burkholder, J. B.: Rate coefficient for the reaction of OH with CH$_2$=C(CH$_3$)C(O)OONO$_2$ (MPAN), Atmos. Environ., 36, 1895–1900, 2002.

Pandis, S. N., Paulson, S. E., Seinfeld, J. H., and Flagan, R. C.: Aerosol formation in the photooxidation of isoprene and beta-pinene, Atmos. Environ., 25, 997–1008, 1991.

Paulot, F., Crounse, J. D., Kjaergaard, H. G., Kurten, A., St Clair, J. M., Seinfeld, J. H., and Wennberg, P. O.: Unexpected epoxide formation in the gas-phase photooxidation of isoprene, Science, 325, 730–733, 2009.

Presto, A. A., Hartz, K. E. H., and Donahue, N. M.: Secondary organic aerosol production from terpene ozonolysis. 2. Effect of NO$_x$ concentration, Environ. Sci. Technol., 39, 7046–7054, 2005.

Sato, K.: Detection of nitrooxypolyols in secondary organic aerosol formed from the photooxidation of conjugated dienes under high-NO$_x$ conditions, Atmos. Environ., 42, 6851–6861, 2008.

Song, C., Na, K. S., and Cocker, D. R.: Impact of the hydrocarbon to NO$_x$ ratio on secondary organic aerosol formation, Environ. Sci. Technol., 39, 3143–3149, 2005.

Surratt, J. D., Murphy, S. M., Kroll, J. H., Ng, N. L., Hildebrandt, L., Sorooshian, A., Szmigielski, R., Vermeylen, R., Maenhaut, W., Claeys, M., Flagan, R. C., and Seinfeld, J. H.: Chemical composition of secondary organic aerosol formed from the photooxidation of isoprene, J. Phys. Chem. A, 110, 9665–9690, 2006.

Surratt, J. D., Gomez-Gonzalez, Y., Chan, A. W. H., Vermeylen, R., Shahgholi, M., Kleindienst, T. E., Edney, E. O., Offenberg, J. H., Lewandowski, M., Jaoui, M., Maenhaut, W., Claeys, M., Flagan, R. C., and Seinfeld, J. H.: Organosulfate formation in biogenic secondary organic aerosol, J. Phys. Chem. A, 112, 8345–8378, 2008.

Surratt, J. D., Chan, A. W. H., Eddingsaas, N. C., Chan, M. N., Loza, C. L., Kwan, A. J., Hersey, S. P., Flagan, R. C., Wennberg, P. O., and Seinfeld, J. H.: Reactive intermediates revealed in secondary organic aerosol formation from isoprene, Proc. Natl. Acad. Sci. USA, 107, 6640–6645, 2010.

Szmigielski, R., Surratt, J. D., Vermeylen, R., Szmigielska, K., Kroll, J. H., Ng, N. L., Murphy, S. M., Sorooshian, A., Seinfeld, J. H., and Claeys, M.: Characterization of 2-methylglyceric acid oligomers in secondary organic aerosol formed from the photooxidation of isoprene using trimethylsilylation and gas chromatography/ion trap mass spectrometry, J. Mass. Spectrom., 42, 101–116, 2007.

Taylor, W. D., Allston, T. D., Moscato, M. J., Fazekas, G. B., Kozlowski, R., and Takacs, G. A.: Atmospheric photo-dissociation lifetimes for nitromethane, methyl nitrite, and methyl nitrate, Int. J. Chem. Kinet., 12, 231–240, 1980.

Tuazon, E. C. and Atkinson, R.: A product study of the gas-phase reaction of methacrolein with the OH radical in the presence of NO$_x$, Int. J. Chem. Kinet., 22, 591–602, 1990.

Tuazon, E. C., Aschmann, S. M., Nishino, N., Arey, J., and Atkinson, R.: Kinetics and products of the OH radical-initiated reaction of 3-methyl-2-butenal, Phys. Chem. Chem. Phys., 7, 2298–2304, 2005.

Volkamer, R., Ziemann, P. J., and Molina, M. J.: Secondary Organic Aerosol Formation from Acetylene (C$_2$H$_2$): seed effect on SOA yields due to organic photochemistry in the aerosol aqueous phase, Atmos. Chem. Phys., 9, 1907–1928, doi:10.5194/acp-9-1907-2009, 2009.

Weber, R. J., Sullivan, A. P., Peltier, R. E., Russell, A., Yan, B., Zheng, M., de Gouw, J., Warneke, C., Brock, C., Holloway, J. S., Atlas, E. L., and Edgerton, E.: A study of secondary organic aerosol formation in the anthropogenic-influenced southeastern United States, J. Geophys. Res.-Atmos., 112, D13302, doi:10.1029/2007JD008408, 2007.

Zhang, Q., Jimenez, J. L., Canagaratna, M. R., Allan, J. D., Coe, H., Ulbrich, I., Alfarra, M. R., Takami, A., Middlebrook, A. M., Sun, Y. L., Dzepina, K., Dunlea, E., Docherty, K., DeCarlo, P. F., Salcedo, D., Onasch, T., Jayne, J. T., Miyoshi, T., Shimono, A., Hatakeyama, S., Takegawa, N., Kondo, Y., Schneider, J., Drewnick, F., Borrmann, S., Weimer, S., Demerjian, K., Williams, P., Bower, K., Bahreini, R., Cottrell, L., Griffin,

R. J., Rautiainen, J., Sun, J. Y., Zhang, Y. M., and Worsnop, D. R.: Ubiquity and dominance of oxygenated species in organic aerosols in anthropogenically-influenced Northern Hemisphere midlatitudes, Geophys. Res. Lett., 34, L13801, doi:10.1029/2007GL029979, 2007a.

Zhang, Y., Huang, J. P., Henze, D. K., and Seinfeld, J. H.: Role of isoprene in secondary organic aerosol formation on a regional scale, J. Geophys. Res.-Atmos., 112, D20207, doi:10.1029/2007JD008675, 2007b.

Appendix B

Chemical Composition of Gas– and Aerosol– hase Products from the Photooxidation of Naphthalene*

Chemical Composition of Gas- and Aerosol-Phase Products from the Photooxidation of Naphthalene

K. E. Kautzman,[†] J. D. Surratt,[†] M. N. Chan,[‡] A. W. H. Chan,[†] S. P. Hersey,[‡] P. S. Chhabra,[†] N. F. Dalleska,[‡] P. O. Wennberg,[‡,§] R. C. Flagan,[†,‡] and J. H. Seinfeld*,[†,‡]

Division of Chemistry and Chemical Engineering, Division of Engineering and Applied Science, and Division of Geological and Planetary Sciences, California Institute of Technology, Pasadena, CA

Received: September 3, 2009; Revised Manuscript Received: October 15, 2009

The current work focuses on the detailed evolution of the chemical composition of both the gas- and aerosol-phase constituents produced from the OH-initiated photooxidation of naphthalene under low- and high-NO_x conditions. Under high-NO_x conditions ring-opening products are the primary gas-phase products, suggesting that the mechanism involves dissociation of alkoxy radicals (RO) formed through an $RO_2 + NO$ pathway, or a bicyclic peroxy mechanism. In contrast to the high-NO_x chemistry, ring-retaining compounds appear to dominate the low-NO_x gas-phase products owing to the $RO_2 + HO_2$ pathway. We are able to chemically characterize 53−68% of the secondary organic aerosol (SOA) mass. Atomic oxygen-to-carbon (O/C), hydrogen-to-carbon (H/C), and nitrogen-to-carbon (N/C) ratios measured in bulk samples by high-resolution electrospray ionization time-of-flight mass spectrometry (HR-ESI-TOFMS) are the same as the ratios observed with online high-resolution time-of-flight aerosol mass spectrometry (HR-ToF-AMS), suggesting that the chemical compositions and oxidation levels found in the chemically-characterized fraction of the particle phase are representative of the bulk aerosol. Oligomers, organosulfates ($R-OSO_3$), and other high-molecular-weight (MW) products are not observed in either the low- or high-NO_x SOA; however, in the presence of neutral ammonium sulfate seed aerosol, an organic sulfonic acid ($R-SO_3$), characterized as hydroxybenzene sulfonic acid, is observed in naphthalene SOA produced under both high- and low-NO_x conditions. Acidic compounds and organic peroxides are found to account for a large fraction of the chemically characterized high- and low-NO_x SOA. We propose that the major gas- and aerosol-phase products observed are generated through the formation and further reaction of 2-formylcinnamaldehyde or a bicyclic peroxy intermediate. The chemical similarity between the laboratory SOA and ambient aerosol collected from Birmingham, Alabama (AL) and Pasadena, California (CA) confirm the importance of PAH oxidation in the formation of aerosol within the urban atmosphere.

1. Introduction

A large fraction (80−90% in some locations) of atmospheric organic aerosol is secondary in origin.[1] The formation of secondary organic aerosol (SOA) results from the formation of low-vapor-pressure products in the oxidation of volatile organic compounds (VOCs), where the resultant low-vapor-pressure oxidation products partition between the gas and aerosol phases. Many VOCs, such as monoterpenes (e.g., α-pinene) and single-ringed aromatic hydrocarbons (e.g., toluene), are known to produce SOA. However, the mass of SOA observed in many locations cannot be accounted for by known precursor VOC, suggesting that many sources of SOA are not yet identified or well characterized.[2−4] Recent identification of isoprene oxidation as a significant source of SOA,[5−12] the role of NO_x in forming SOA from the oxidation of aromatics[13−15] and other hydrocarbons,[16−18] the effects of aerosol acidity and heterogeneous chemistry (e.g., oligomer[19−27] and organosulfate formation[24,28−32]), and the contribution of glyoxal to SOA formation[24,33−35] have provided significant insights into potential missing and poorly characterized sources of SOA. Additionally, Robinson et al.[36]

have shown that primary organic aerosol (POA), previously considered as nonvolatile, contains gas-phase components of intermediate volatility that themselves are sources of SOA.

Although it is traditionally assumed that small volatile aromatic organic compounds, such as toluene and benzene, are the primary precursors for anthropogenic SOA, it has recently been shown that substantial contributions to SOA formation may also come from compounds of lower volatility,[36] such as polycyclic aromatic hydrocarbons (PAHs). PAHs account for a significant portion of the semivolatile gas-phase emissions from diesel fuels,[37] with substantial emissions also being produced from gasoline engines,[38] wood burning,[39,40] and cooking sources.[41,42] Photooxidation of PAHs has been shown to produce high-MW, low-vapor-pressure, oxygenated compounds.[40,43−47] The nitro PAHs, specifically nitronaphthalenes, have been observed in ambient particulate matter[48] and are of particular importance due to their expected role as carcinogens.[49−52]

We have previously reported SOA yields, defined as the ratio of mass of SOA formed, ΔM_o, to the mass of hydrocarbon reacted, ΔHC, from the photooxidation of naphthalene, 1-methylnaphthalene (1-MN), 2-methylnaphthalene (2-MN), and 1,2-dimethylnaphthalene (1,2-DMN) as a function of organic mass loading under both high- and low-NO_x conditions.[15] Yields for high-NO_x conditions were observed between 0.19 and 0.30 for

---

* Author to whom correspondence should be addressed. Phone: (626) 395-4635, Fax: (626) 796-2591, E-mail: seinfeld@caltech.edu.
† Division of Chemistry and Chemical Engineering.
‡ Division of Engineering and Applied Science.
§ Division of Geological and Planetary Sciences.

165

914 *J. Phys. Chem. A, Vol. 114, No. 2, 2010*   Kautzman et al.

TABLE 1: Instruments Employed in Chamber Experiments[a]

instrumentation	measurement	time resolution	detection limit/range
hygrometer (capacitance probe)	temperature	online	10–50 °C
Vaisala HMP233	humidity	online	5–95%
chemiluminescent NO_x analyzer	NO, NO_2 concentrations	online	2 ppb
luminol NO_x analyzer	concentration of NO_2 separated from PAN by GC	online	5 ppb
O_3 analyzer	ozone concentration	online	2 ppb
differential mobility analyzer (DMA)	aerosol number concentration, size distribution, and volume concentration	4 min	0.2 $\mu m^3 cm^{-3}$, 15–780 nm
gas chromatography/flame ionization detector (GC/FID)	parent hydrocarbon concentration	12 min	~1 ppb[b]
chemical ionization mass spectrometry (CIMS)	gas-phase oxidation products	~9 min	~0.1 ppb[b], unit mass resolution
gas chromatography/electron ionization-time-of-flight mass spectrometry (GC/EI-TOFMS)	gas-phase oxidation products, structural indentification	semionline, off-line	0.5 ppb[b], resolution ~7000
ultra performance liquid chromatography/electrospray ionization-time-of-flight mass spectrometry(UPLC/ESI-TOFMS)	particle-phase products, structural identification	off-line	1 ng m^{-3} [b], resolution ~12 000
high performance liquid chromatography electrospray ionization-ion trap mass spectrometry (HPLC/ESI-ITMS)	particle-phase products, structural identification	off-line	1 ng m^{-3} [b], unit mass resolution
high-resolution time-of-flight aerosol mass spectrometry (HR-ToF-AMS)	particle-phase composition	online	0.03 $\mu g\ m^{-3}$, 50–600 nm
particle into liquid sampler-ion chromotography (PILS-IC)	water-soluble aerosol composition	online	~0.1 $\mu g\ m^{-3}$ [b]

[a] Instruments employed at the Caltech dual chamber environmental facility. [b] Detection limits dependent on identity of target species.

naphthalene, 0.19 and 0.39 for 1-MN, 0.26 and 0.45 for 2-MN, and constant at 0.31 for 1, 2-DMN, at aerosol mass loadings between 10 and 40 $\mu g\ m^{-3}$. Under low-NO_x conditions, yields were found to be 0.73, 0.68, and 0.58, for naphthalene, 1-MN, and 2-MN, respectively. Gas-phase products were tentatively identified, and trends involving ring-opening versus ring-retaining oxidation mechanisms were established. Calculations of SOA formation from these PAHs demonstrated that these precursors may contribute significantly to the amount of urban SOA. The suite of instruments associated with the Caltech dual indoor environmental chamber facility (Table 1), by which the data to be presented were obtained, permits a thorough analysis of the generation of SOA commencing with the oxidation of the gas-phase hydrocarbon to the formation of SOA. Here we describe the detailed evaluation of the chemical composition of both the gas- and aerosol-phase constituents produced from the photooxidation of naphthalene, the most abundant PAH in the urban atmosphere.[48]

2. Experimental Section

2.1. Chamber Experiments. All experiments were carried out in the Caltech dual 28 m^3 Teflon chambers. Details of the facilities have been described previously.[53,54] Before each experiment, the chambers were flushed with dried purified air for >24 h, until the particle number concentration was <100 cm^{-3} and the volume concentration was <0.1 $\mu m^3\ cm^{-3}$. In most experiments, ammonium sulfate seed aerosol was used to promote condensation of low volatility oxidation products. The seed aerosol was generated by atomization of a 0.06 M aqueous ammonium sulfate solution. The hydrocarbon was introduced into the chamber by flowing purified air through an FEP tube packed with solid naphthalene at 1 L min^{-1}.

For high-NO_x experiments (NO > 350 ppb initially) nitrous acid (HONO) was used as the OH precursor. HONO was prepared by adding 10 mL of 1 wt % aqueous $NaNO_2$ dropwise into 20 mL of 10 wt % sulfuric acid in a glass bulb. A stream

of dry air was then passed through the bulb, sending HONO into the chamber. During this process, NO and NO_2 formed as side products and were also introduced into the chamber. NO/NO_x was measured with a commercial chemiluminescence NO_x monitor (Horiba, APNA-360). In some experiments, NO_2 was monitored by a gas chromatograph with luminol detector (University of California, Riverside, CA) in which NO_2 and peroxyacyl nitrate (PAN) were separated by gas chromatography and detected by chemiluminescence of reaction with luminol.[55] Reaction of HONO with luminol is unlikely, and thus no interference with the NO_2 signal is expected. The NO_2 measurement from the NO_x monitor is higher due to interferences from HONO. The injection of HONO was stopped when the mixing ratio of NO_2 reached about 80 ppb in the chamber as measured by the Riverside NO_2 monitor. Additional NO was added until total NO was about 400 ppb. For all experiments, the concentrations of NO and NO_2 remained approximately constant over the course of photooxidation, and ozone (O_3) concentrations remained insignificant. For low-NO_x experiments, hydrogen peroxide (H_2O_2) was used as the OH precursor. Prior to atomization of the ammonium sulfate seed, H_2O_2 was introduced by bubbling purified air through a 50% aqueous H_2O_2 solution for 2.5 h at 5 L min^{-1} resulting in a mixing ratio of 2–8 ppm of H_2O_2.

The aerosol number concentrations, size distributions, and volume concentrations were measured by a differential mobility analyzer (DMA, TSI model 3081) coupled with a condensation nuclei counter (TSI, CNC-3760). After allowing for all concentrations to stabilize, irradiation was initiated. The temperature (T), relative humidity (RH), and concentrations of O_3, NO, and NO_x were continuously monitored. Table 2 summarizes the experimental conditions for the series of naphthalene oxidation experiments conducted.

2.2. Gas-Phase Measurements.

2.2.1. Gas Chromatography/Flame-Ionization Detection (GC/FID). The concentration of naphthalene was continuously monitored by GC/FID. Chamber air was sampled into a 10 mL

166

Photooxidation of Naphthalene

J. Phys. Chem. A, Vol. 114, No. 2, 2010 **915**

TABLE 2: Experimental Conditions from Chamber Experiments

	initial naphthalene (ppb)	oxidant precursor[a]	initial NO_2 (ppb)	initial NO (ppb)	initial O_3 (ppb)	T (°C)[b]	RH (%)[b]	initial seed volume ($\mu m^3/cm^3$)	end volume ($\mu m^3/cm^3$)
1	60	H_2O_2	0	0	6	26	6	14	143
2	25	H_2O_2	0	3	4	26	19	26	50
3	20	H_2O_2	0	2	2	24	10	11	38
4	20	H_2O_2	0	1	1	24	13	11	40
5	48	HONO	166	401	3	28	5	16	65
6	30	HONO	245	455	1	25	7	15	51
7	35	HONO	289	487	3	25	10	15	50
8	30	HONO	260	480	3	26	17	11	n.a.

[a] H_2O_2 is used for low-NO_x conditions; HONO is used for high-NO_x conditions. [b] Reported value is averaged over the course of the experiment.

injection loop and injected onto a HP5 15 m × 0.53 mm ID × 1 μm thickness column installed on a 6890N Agilent GC. The GC was temperature-programmed as follows; initial temp 60 °C, hold 1 min, ramp 35 °C min⁻¹ to 140 °C, ramp 20 °C min⁻¹ to 200 °C, hold 2 min. The GC response was calibrated by dissolving a known mass of the naphthalene in dichloromethane, and then vaporizing a known volume of that solution into a 38 L Teflon chamber.

2.2.2. Chemical Ionization Mass Spectrometry (CIMS). Monitoring of gas-phase oxidation products was carried out in real time by the use of a CIMS instrument. The details of this instrument are described elsewhere.[17,56,57] Briefly, a 2.5 standard liters per minute (slm) aliquot of air is drawn from the experimental chamber through a 1.6 m long 0.25 in. Teflon tube. 300 standard cubic centimeters per minute (sscm) of this flow is introduced into the CIMS instrument and ionized by a reagent ion. The resultant ions are filtered using a quadrupole mass spectrometer with unit mass resolution. The instrument can operate in both negative mode, using CF_3O^- as a reagent ion, and in positive proton transfer reaction (PTR)-MS mode. Negative mode is found to be more selective toward detection of polar molecules, particularly acids, whereas positive mode detects a broader range of organic compounds. Mass scans were performed covering masses 55−450 amu for negative mode, and 56−350 amu for positive mode, with a total scan time of ~9 min. Mass scans were continuously repeated over the course of each experiment.

2.2.3. Gas Chromatography/Electron Impact Time-of-Flight Mass Spectrometry (GC/EI-TOFMS). The GC/EI-TOFMS instrument (Waters, GCT Premier) is outfitted with a standard 6890N Agilent GC for introduction of volatile samples. The ion source employed here is a traditional 70 eV positive (+)EI source. The ions produced are continuously accelerated across the source to 40 eV and perpendicularly extracted into the TOF mass analyzer at a rate >25 kHz. The ions then pass through a single reflectron with an effective path length of 1.2 m. Ions are subsequently detected by a chevron stack of microchannel plates. The arrival times of the ions are recorded by a time-to-digital converter at a rate of 3.6 GHz, providing high mass accuracy (~7000). All data are acquired and analyzed using MassLynx software version 4.1.

Various components have been added to aid with sample introduction into the GC/EI-TOFMS instrument. A preconcentrator (Entech Instruments, model 7100A) is used to draw, concentrate, and focus gas-phase samples into discrete peaks on the GC column. The preconcentrator extracts air from the environmental chamber and then cryogenically traps and concentrates VOCs in the sample. We have used two different trapping methods with the preconcentrator. The first method, microscale purge and trap (MPT), is a three-stage procedure to efficiently concentrate gas samples. The initial trap, which is

filled with glass beads, is used to remove water vapor from the sample and removes bulk atmospheric gases (e.g., O_2 and N_2). The initial concentration step is then followed by trapping of VOCs with a Tenax adsorbent trap, and the sample is subsequently flushed into the cryofocusing module where the sample is focused and rapidly injected onto the GC column. The second method, cold trap dehydration (CTD), uses only the Tenax trap and cryofocusing modules. Although CTD is less effective at removing moisture from humid samples, it is the preferred method of sample concentration for water-soluble compounds such as aldehydes. This method also provides superior handling of samples with high CO_2 levels. Both the MPT and CTD methods have been found to be effective for sampling volatile and semivolatile compounds, although for the highly oxidized products of interest here, the preconcentrator is believed to be the controlling factor for the ultimate detection limit of these latter products. All modules in the preconcentrator have an upper temperature range of 200 °C. Similarly, the transfer line between the preconcentrator and GC can be heated only to a maximum of 150 °C. The upper temperature limit of the preconcentrator makes detection of low-vapor-pressure oxidized compounds challenging.

The concentrations of naphthalene (<40 ppb) employed in the chamber experiments outlined in Table 2 preclude detection of the gas-phase oxidation products by the GC/EI-TOFMS technique as implemented at Caltech. Thus, additional high-concentration experiments were carried out in a separate 3 m³ Teflon chamber to identify gas-phase products from the photooxidation of naphthalene under high- and low-NO_x conditions using the GC/EI-TOFMS instrument. The initial mixing ratio of the naphthalene in these experiments was ~40 ppm, and the concentration of HONO in high-NO_x experiments was ~10 ppm. For low-NO_x experiments initial mixing ratios of H_2O_2 were ~30−80 ppm. Two methods were used to monitor the formation of gas-phase oxidation products; first, 1000 mL samples were drawn from the 3 m³ Teflon chamber and introduced directly into the three-step preconcentrator. After preconcentration, the sample was injected onto the GC DB-5MS column (30 m × 0.25 mm ID × 0.25 μm thickness) and temperature-programmed as follows: initial temp 40 °C, hold 2 min, ramp 5 °C min⁻¹ to 300 °C. This method has limited time resolution due to the preconcentration and GC steps. In order to improve the time resolution, Tenax tube samples were collected. Air from the 3 m³ Teflon chamber was drawn through Tenax TA glass tubes (Supelco, 6 mm × 11.5 cm) at a rate of 0.455 L min⁻¹ using a critical orifice. Each tube sampled chamber air for 20 min. Subsequently, the tubes were desorbed at 300 °C into the preconcentrator and analyzed as described above. Gas-phase products were identified by NIST library searching the mass spectra,[58] and authentic standards were used when possible. No

differences were observed between the preconcentrator MPT and CTD methods.

2.3. Particle-Phase Measurements.

2.3.1. Chamber Filter Sample Collection, Extraction, and Off-Line Detailed Chemical Characterization Protocols. A detailed description of the aerosol filter sample collection and extraction protocol has been previously published.[59] Briefly, aerosol samples are collected on Teflon filters (PALL Life Sciences, 47-mm diameter, 1.0-μm pore size, teflomembrane). Filter samplers employed for aerosol filter sample collection used a front and back-up filter sampling approach, where back-up filters were collected in order to examine if aerosol breakthrough was occurring on the front filter or whether evaporation of semivolatiles from the front filter was occurring during filter sampling. In all experiments outlined in Table 2, no SOA constituents were found on the back-up filters, and as a result, all detailed chemical characterizations are reported only for the front filters. Filter sampling was initiated when the aerosol volume reached its maximum (constant) value, as determined by the DMA. Depending on the total volume concentration of aerosol in the chamber, the duration of filter sampling was 1.8−2.1 h, which resulted in 2.0−2.9 m^3 of total chamber air sampled. Teflon filter extraction protocols in high-purity methanol (LC-MS CHROMASOLV-Grade, Sigma-Aldrich) have been described previously.[59] Additional filter extractions using 5 mL of high-purity acetonitrile (LC-MS CHROMASOLV-Grade, Sigma-Aldrich) were also performed by 45 min of sonication to ensure detection of SOA constituents not soluble in methanol. No additional compounds were recovered using the less-polar acetonitrile solvent. Thus, all results from the off-line ESI-MS measurements are reported only for the methanol filter extractions. The resultant filter extracts were then analyzed by a Waters ACQUITY ultra performance liquid chromatography (UPLC) system, coupled with a Waters LCT Premier TOF mass spectrometer equipped with an ESI source, allowing for accurate mass measurements (i.e., determination of molecular formulas) to be obtained for each observed ion. Operation protocols, including column information and employed chromatographic method, for the UPLC/ESI-TOFMS technique have been described in detail previously.[59]

Selected naphthalene low- and high-NO$_x$ methanol filter extracts were also analyzed by a Thermo Finnigan Surveyor high performance liquid chromatography (HPLC) system (pump and autosampler) coupled to a Thermo Finnigan LCQ ion trap mass spectrometer (ITMS) equipped with an ESI source, allowing for tandem MS measurements (i.e., generation of product ions) to be obtained. The combination of accurate mass and tandem MS measurements significantly aided in detailed structural characterization efforts. Data were acquired and processed using Xcalibur version 1.3 software. A Waters Atlantis T3 column (3 μm particle size; 2.1 × 150 mm) was employed, which is similar to the Water ACQUITY UPLC HSS column used for the UPLC/ESI-TOFMS analysis. The mobile phases consisted of 0.1% acetic acid in water (A) and 0.1% acetic acid in methanol (B). The applied 45 min gradient elution program was as follows: the concentration of eluent B was kept at 3% for 4 min, then increased to 100% in 21 min, holding at 100% for 10 min, then decreased to 3% in 5 min, and kept at 3% for 5 min. The injection volume and flow rate were 10 μL and 0.2 mL min^{-1}, respectively. The ion trap mass analyzer was operated under the following conditions: sheath gas flow (N$_2$), 65 arbitrary units; auxiliary gas flow (N$_2$), 3 arbitrary units; source voltage, −4.5 kV; capillary voltage, −14.5 V; tube lens offset, 7 V; capillary temperature, 200 °C; and maximum ion

injection time, 200 ms. Two scan events were used during each chromatographic run; scan event 1 was the full scan mode in which data were collected from m/z 120 to 600 in the negative ionization mode and scan event 2 was the MS^2 mode in which product ions were generated from significant base peak ions observed in scan event 1. For MS^2 experiments, an isolation width of 2.5 m/z units and a normalized collision energy level of 35% were applied. The [M − H]$^-$ ion signal optimization was carried out by introducing a 1 mg mL^{-1} malic acid standard solution. Due to the on-axis ESI source that is characteristic of the LCQ ITMS instrument, a solvent delay time of 3.5 min (which diverted the column effluent from the ESI source to waste) was employed to prevent clogging by nonvolatile salts at the entrance of the capillary.

Measurements of total peroxide content from the extracted filter samples were acquired by the UV−vis iodometric spectroscopy method.[19] Filter samples used for this analysis were extracted and prepared differently from the filter samples used in the UPLC/ESI-TOFMS and HPLC/ESI-ITMS analyses.[11] Standard calibration curves were generated using a series of benzoyl peroxide solutions. The structure of the benzoyl peroxide, a peroxy group linking two benzene rings, was judged to be an excellent surrogate for the naphthalene system. Calibrations and measurements were performed on a Hewlett-Packard 8452A diode array spectrophotometer. Peroxides in the form of HOOH, ROOH, and ROOR are quantified by measuring the absorbance at 470 nm of the reaction product I$_3^-$ produced under anaerobic, dark, and acidic conditions by the following reaction scheme:

$$ROOH + 2I^- + 2H^+ \rightarrow I_2 + H_2O + ROH$$
$$ROOR + 2I^- + 2H^+ \rightarrow I_2 + 2ROH$$
$$I_2 + I^- \rightarrow I_3^-$$
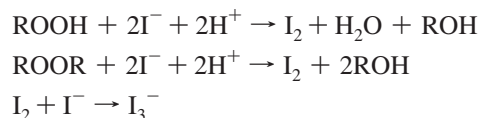
Detection of I$_3^-$ at 470 nm is 10 nm to the red from the peak of the characteristic absorbance of I$_3^-$ and has been chosen to avoid interferences with other organic compounds absorbing in this region. Extractions from three high-NO$_x$ and three low-NO$_x$ filters were performed to ensure reproducibility across experiments. No contribution of H$_2$O$_2$ to this measurement is expected due to the dry conditions employed in the present experiments, as well as owing to previous quality control experiments demonstrating that no H$_2$O$_2$ could be measured on filter samples collected from a nonirradiated chamber mixture containing only gaseous H$_2$O$_2$, VOC, and ammonium sulfate seed aerosol. These latter quality control filter samples were collected for the same duration as filter samples collected from SOA chamber experiments.

Of particular concern to the UV−vis measurements is the presence of nitronaphthalenes and nitrobenzenes in high-NO$_x$ filter samples, which in solution have a color similar to the I$_3^-$ produced from the reaction of I$^-$ with the peroxides in solution. 1000 ppm standard solutions of nitronaphthalenes (i.e., 4-nitro-1-naphthol and 2-nitro-1-naphthol), nitrobenzenes (i.e., 2-nitrophenol and 3-hydroxy-4-nitrobenzoic acid), and epoxides (i.e., α-pinene oxide, 2-methyl-2-vinyloxirane, and 2,3-epoxy-1,4-diol) were prepared and tested to confirm that no interferences were present from these compounds in the UV−vis measurement. From the analyses of the 1000 ppm standards, it was found that the nitronaphthalenes and nitrobenzenes were the only classes of compounds to absorb weakly at 470 nm, and as a result, we reanalyzed the nitronaphthalene and nitrobenzene standards at a concentration more relevant to the high-NO$_x$ SOA

samples characterized in the current study. Since the highest concentration of the nitronaphthalenes and of the nitrobenzenes was measured at ~5 ppm by the UPLC/(−)ESI-TOFMS technique (Tables 2S−4S, Supporting Information), the absorbance of a 5 ppm standard mixture of the nitronaphthalenes (i.e., 4-nitro-1-naphthol and 2-nitro-1-naphthol) and of the nitrobenzenes (i.e., 2-nitrophenol and 3-hydroxy-4-nitrobenzoic acid) was measured by the UV−vis technique. It was found that the absorbance of this standard mixture, which possessed a yellowish color characteristic of nitroaromatics in solution, was insignificant at this SOA-relevant concentration.

Non-nitro containing benzene standards (i.e., phthalic acid and *trans*-cinnamic acid) were also prepared and analyzed. These compounds did not contribute to the absorbance measurement at 470 nm, consistent with the lack of color observed in their respective standard solutions. As a result of these measurements, it was assumed that the absorbance (peroxide) measurements acquired for the high- and low-NO_x SOA samples were not affected by chemical artifacts. Finally, blank Teflon filters were also extracted and prepared in the same manner as the filter samples collected from chamber experiments; these blank filters produced no significant absorbance at 470 nm, indicating that the filter medium did not interfere with the peroxide measurements.

2.3.2. High-Resolution Time-of-Flight Aerosol Mass Spectrometry (HR-ToF-AMS).
Real-time aerosol mass spectra were obtained using an Aerodyne HR-ToF-AMS.[60] The HR-ToF-AMS was operated in both a lower resolution, higher sensitivity "V-mode", and a high-resolution "W" mode, switching between modes once every minute. The V-mode data were analyzed to extract sulfate, ammonium, and organic spectra.[61] Calculation of the SOA densities were achieved by comparing the particle mass distributions obtained using the particle ToF mode and the volume distributions obtained by the DMA in nucleation (seed-free) experiments.[62] O/C, N/C, and H/C ratios were determined from W mode data using the APES toolbox and applying the procedures outlined in Aiken et al.[63,64] The particle-phase signal of CO^+ and the organic contribution to H_xO^+ ions were estimated as described in Aiken et al.[64]

2.3.3. Particle-into-Liquid Sampler/Ion Chromatography (PILS/IC).
The PILS/IC instrument is designed to measure aerosol water-soluble ions and is based on the original design of Weber et al.[65] The current instrument has been modified to utilize syringe pumps to introduce the samples from the impactor into vials for later analysis by IC.[66] Chamber air, sampled through a 1 mm cut-size impactor, is passed through three denuders (URG and Sunset Laboratories) to remove gas-phase species. The aerosol is mixed with steam in a condensation chamber and grows by condensation of supersaturated water vapor to diameters >1 μm. Droplets grow sufficiently large to be collected by impingement on a quartz impactor, are washed to the bottom of the impactor, then collected and stored in airtight vials. Vials are analyzed off-line by IC (ICS-2000 with 25 μL sample loop, Dionex Inc.); columns used in the IC and the chromatographic methods employed have been previously described in detail by Sorooshian et al.[66] Vials were collected prior to each experiment to establish background levels of individual species, including Na^+, NH_4^+, K^+, Mg^{2+}, Ca^{2+}, SO_4^{2-}, Cl^-, NO_2^-, NO_3^-, oxalate, pyruvate, formate, and phthalate. Chromatographic peaks were identified and quantified using authentic standards; standards used in the current work are: teraphthalic acid, benzoic acid, *trans*-cinnamic acid, 5-hydroxy isophthalic acid, 1,2,4-benzene tricarboxylic acid, 4-formylcinnamic acid, 2-hydroxy isophthalic acid, 3-hydroxy benzoic

acid, 4-hydroxybenzoic acid, 3-formyl benzoic acid, 3-hydroxy-4-nitrobenzoic, 2-nitrophenol, 2-nitro-1-napthol, 4-nitro-1-napthol, and salicylic acid. Additionally, the presence of dicarboxylic acids of C_2 (oxalic), C_3 (malonic), C_4 (succinic), C_5 (glutaric), and C_6 (adipic) compounds were investigated using authentic standards.

2.4. Ambient Aerosol Samples: Filter Collection Protocols and Off-Line Chemical Analysis.
Selected archived quartz fiber filters collected from Birmingham, AL during the Southeastern Aerosol Research and Characterization (SEARCH) 2004 campaign were reanalyzed by the UPLC/(−)ESI-TOFMS technique, as described above for the naphthalene SOA chamber filters. Details of the SEARCH network, which includes descriptions of each site, aerosol filter sample collection protocols, gas- and particle-phase measurements conducted, can be found elsewhere.[67,68] Birmingham, AL (denoted as BHM in the SEARCH network) is an urban site consisting of both industrial and residential settings. Quartz fiber filter extractions and sample preparation procedures have been described previously.[69] However, solid-phase extraction (SPE) was not employed in the current study to avoid possible loss of early eluting naphthalene SOA products.

In addition to the ambient aerosol filters samples collected from Birmingham, AL, quartz fiber filters were also collected in Pasadena, CA, during June and July, 2009 using the same high-volume filter sampling approach as used by the SEARCH network. These samples are a part of the Pasadena Aerosol Characterization Observatory (PACO), an ambient sampling study located on the campus of Caltech. Selected PACO filter samples collected on June 3, June 19, and July 14, 2009, were analyzed by the UPLC/(−)ESI-TOFMS technique as described above. These filters represent 4 h integrated morning (7−11 a.m.) and 4 h integrated afternoon (3−7 p.m.) sampling periods. June 19 and July 14 were chosen for this chemical analysis due to the high total organic mass aerosol loadings as measured by a compact time-of-flight AMS instrument (maximum of 21.12 and 11.72 μg m^{-3}, respectively, assuming a collection efficiency of 0.5), O_3 mixing ratios (71 and 56 ppb, respectively), and daytime temperature (29 and 34 °C, respectively). June 3 was chosen as a relatively clean day for comparison with June 19 and July 14, and had a maximum total organic mass aerosol loading of 5.66 μg m^{-3} (assuming a collection efficiency of 0.5), O_3 mixing ratio of 19 ppb, and daytime temperature of 20 °C. Further results and details from the PACO 2009 campaign will be presented in a forthcoming publication. Here, the chemical characterization data obtained from the ambient filters were compared to that of the naphthalene SOA chamber experiments to identify potential ambient SOA tracer compounds that can be used in source apportionment studies.

2.5. Chemicals.
Most of the reagents used in this study were purchased from Sigma Aldrich and their stated purities are listed in Table 1S (Supporting Information). Additionally, 2-formylcinnamaldehyde was synthesized by ozonolysis of naphthalene using the technique of Larson et al.,[70] but was not purified. Identification of both *E*- and *Z*- isomers was confirmed by NMR measurements.

3. Results

3.1. High-NO_x Conditions.

3.1.1. Chemical Characterization of High-NO_x Gas-Phase Oxidation Products.
Table 3 lists the gas-phase products detected by the CIMS instrument in positive and negative ion modes and structures identified by the GC/EI-TOFMS technique. These data are compared to aerosol measurements made by the UPLC/ESI-TOFMS technique, thus establishing the connection between the gas and particle phases. When the CIMS is operated

Kautzman et al.

TABLE 3: Summary of Chemically Characterized Gas- and Particle-Phase Products Produced from the Photooxidation of Naphthalene
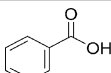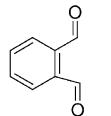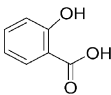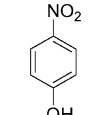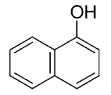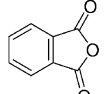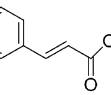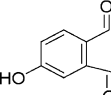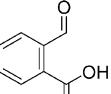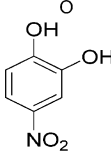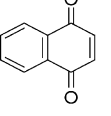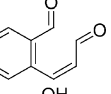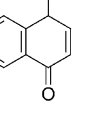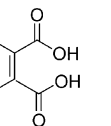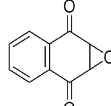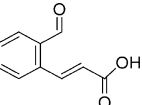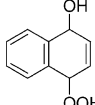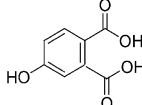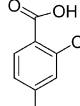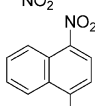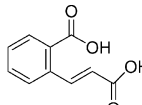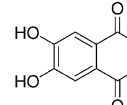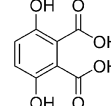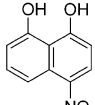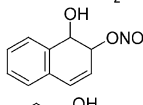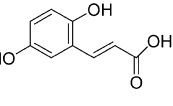
MW	Gas-phase measurements					Particle-phase measurements				proposed structure[e]
	CIMS detection[a]			GC/EI-TOFMS		UPLC/ESI-TOFMS				
	[M + H]+	[M + F]-	[M + CF₃O]-	accurate mass	error (mDa)	accurate mass[b]	avg.error (mDa)	% SOA HNO$_x$[c]	% SOA LNO$_x$[d]	
122	B	B		122.0368	-0.4	121.0301 121.0293 121.0267	0.3	1.57	2.12	
134	B			134.0390	2.4	135.0444	-0.2	n.q.	n.q	
138		B	B			137.0253 137.0228 137.0255 137.0222	-0.05	1.64	3.63	
139						138.0225 138.0179 138.0198	1.0	1.13	0	
144	B	B	B			143.0531 143.0536	3.7	n.q.	n.q.	
148	B	B	B							
148						147.0432 147.0473 147.0480	1.6	0.25	0.57	
150						151.0401	0.6	n.q	n.q	
50	B	B	B			149.0231 149.0241 149.0239 149.0248	-0.1	1.24	2.8	
155						154.013	2.5	0.94	0	
158	B			158.0387	1.9	159.0453	0.7	n.q	n.q	
160	B		B	160.0524	0.40					
160						161.0578	-2.5	n.q	n.q	
164						165.0539 165.0545 165.0525	-1.6	n.d.	n.q.	
166	B					165.0181 165.0148	2.3	2.71	4.01	

170

Photooxidation of Naphthalene

J. Phys. Chem. A, Vol. 114, No. 2, 2010 **919**

TABLE 3: Continued

MW	Gas-phase measurements					Particle-phase measurements				proposed structure[e]
	CIMS detection[a]			GC/EI-TOFMS		UPLC/ESI-TOFMS				
	[M + H]+	[M + F]-	[M + CF3O]-	accurate mass	error (mDa)	accurate mass[b]	avg.error (mDa)	% SOA HNOx[c]	% SOA LNOx[d]	
173				173.0495 173.0477	1.7 1.3					
174	B	B	B	174.0328	1.1					
176	B	B	B			175.0377 175.0375 175.0395 175.0403	0.8	1.46	0.53	
178	B		B			179.069	-1.8	n.q	n.q.	
180						179.0325 179.0327 179.0341 179.0320	0.6	2.53	4.56	no tentatitve structure proposed
182						181.0128 181.0146 181.0128	0.3	3.3	9.8	
183						182.0096 182.0072	0.5	0.52	0	
189	H	H		189.0417	-0.9	188.0336 188.0367 188.0310 188.0341 188.0326 188.0357	0.9	0.4	0	
192	B					191.0364 191.0381 191.0345 191.0375	0.0	2.05	1.28	
192						193.0511	1.0	n.q	n.q	
198						197.0108	2.2	n.q	3.5	
205			H			204.0295 204.0281 204.0286	1.0	0.39	0	
207						206.0477 206.0469	2.0	0.07	0	
208	B					207.03020 207.02891 207.02930 207.03070 207.02830	-0.6	2.18	4.54	

[a] CIMS does not permit structural identification. All proposed structures are derived from either GC/TOFMS, UPLC/TOFMS, or previously identified structures found in the literature. H denotes products observed only under high-NOx conditions. B denotes products observed under both NOx conditions. [b] Accurate masses are determined by [M − H]− or [M + H]+ mode. Reported masses are thus 1 H+ from the true mass. [c] High-NOx case (HNOx). [d] Low-NOx case (LNOx). [e] For simplicty only one isomer is shown. Number of observed isomers can be determined by the number of entries in the accurate mass column.
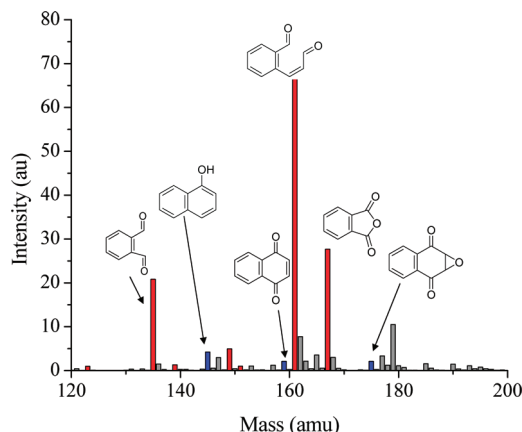
Figure 1. (+)CIMS mass spectrum taken at 70% reacted naphthalene under high-NO$_x$ conditions. Red data indicate ring-opening products. Ring-retaining products are indicated in blue.
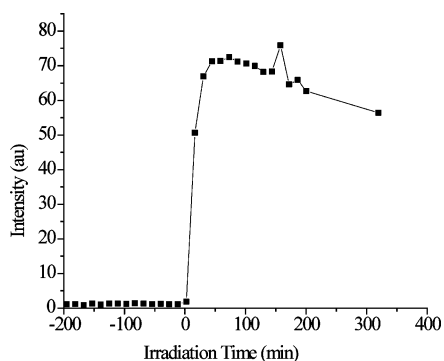

Figure 2. Time trace of 2-formylcinnamaldehyde obtained by the (+)CIMS technique.

in positive mode, compounds with proton affinities higher than that of water extract a proton and are subsequently detected by quadrupole MS; this mode is used for detecting a wide variety of organic compounds. The masses seen in positive mode will generally be detected as [M + H]$^+$ ions and are denoted in the CIMS [M + H]$^+$ column shown in Table 3. The negative mode of operation is highly selective toward acidic and polar molecules. The analyte clusters with CF$_3$O$^-$ forming an [M + CF$_3$O]$^-$ cluster ion, or subsequently loses CF$_2$O to form the [M + F]$^-$ ion. Generally, identification of an [M + F]$^-$ ion corresponds with detecting carboxylic acids, while [M + CF$_3$O]$^-$ ions may also include hydroxy carbonyls. Owing to the unit-mass resolution of the CIMS technique, structural assignments are based on the results from the GC/EI-TOFMS and from previous results on the photooxidation of naphthalene. Products identified, along with suggested structures and accurate mass measurements obtained by the GC/EI-TOFMS technique are presented in Table 3.

The (+)CIMS mass spectrum from a typical high-NO$_x$ experiment is shown in Figure 1. 2-Formylcinnamaldehyde (at *m/z* 161), phthaldialdehyde (at *m/z* 135), and phthalic anhydride (at *m/z* 167) represent the largest peaks. We refer to these compounds as "ring-opening" products and indicate their presence in Figure 1 by the red mass spectral peaks. These observed compounds are consistent with those of other studies that report products of naphthalene and will be discussed subsequently. Closed-ring or "ring-retaining" compounds, such as isomeric naphthols (at *m/z* 145), 1,4-naphthoquinone (at *m/z* 159), 2,3-epoxy-1,4-naphthoquinone (at *m/z* 175), and isomeric nitronaphthols (at *m/z* 190), are also tentatively identified, as indicated by blue mass spectral peaks in Figure 1.

In the CIMS positive mode, the most abundant gas-phase product identified is a compound detected at *m/z* 161 (Figure 1). This compound is also observed in the GC/EI-TOFMS data and is positively identified as 2-formylcinnamaldehyde based on a mass spectral comparison with a synthesized standard (as shown in Figure 2S, Supporting Information). The present amounts of this compound are significantly less than found in other studies[71,72] due to losses in the preconcentrator. The time trace for 2-formylcinnamaldehyde under typical high-NO$_x$ conditions in Figure 2 indicates that 2-formylcinnamaldehyde grows rapidly once oxidation is initiated, then decays relatively slowly. From the (−)CIMS measurements, we learn that, after about 2 h of irradiation, all the HONO is consumed; naphthalene concentrations stabilize and generation of 2-formylcinnamaldehyde ends. 2-formylcinnamaldehyde then decays at a rate of 0.06 h^{-1} due to photolysis. After 6 h of irradiation, ∼70% of the initially formed 2-formylcinnamaldehyde remains.

Results from the GC/EI-TOFMS technique demonstrate the presence of both the 1- and 2-nitronaphthalene isomers in the gas phase. 1-Nitronaphthalene has been positively identified using an authentic reference standard (Sigma-Aldrich, 99%) in conjunction with NIST library matching. 2-Nitronaphthalene is identified based on NIST library matching, accurate mass measurements, and comparison of the mass spectrum with the 1-nitronaphthalene isomer. Nitronaphthols are also identified based on NIST library matching. The 4-nitro-1-naphthol authentic standard was run for comparison, but did not match the retention time of the assigned peak. We expect that this is another structural isomer of 4-nitro-1-naphthol, most likely either 1-nitro-2-naphthol or 2-nitro-1-naphthol, both of which have been identified in previous studies.[72,73] Naphthoquinone and 2,3-epoxy-1,4-naphthoquinone are also observed. In addition to these ring-retaining compounds, benzoic acid and phthaldialdehyde are also observed by the GC/EI-TOFMS technique. Chromatograms for selected photooxidation products observed by the GC/EI-TOFMS method are shown in Figure 1S (Supporting Information).

The two methods of sample collection described in Section 2.2.3 yield similar results. Directly introducing the sample into the preconcentrator yielded greater intensities for the nitronaphthalene products; however, the gas-phase product of MW 160 (2-formylcinnamaldehyde) was detected with reduced efficiency using this method. Although the second Tenax tube method detected the gas-phase product of MW 160 with greater efficiency, phthaldialdehyde was not detected. Detection of all other oxidation products was comparable using these two sampling techniques.

3.1.2. Chemical Characterization of High-NO$_x$ SOA. The chemical composition of naphthalene SOA was probed with the battery of techniques described earlier. HR-ToF-AMS particle-phase data were acquired under a wide range of initial naphthalene mixing ratios. The naphthalene mixing ratios for which aerosol measurements from other instruments were acquired are 20−30 ppb. Hydrocarbon mixing ratios, along with the calculated density and observed aerosol atomic O/C, N/C, and H/C ratios are presented in Table 4. Errors in accuracy associated with AMS compositional ratios are reported as ±30%, ±22%, and ±10% of the measured O/C, N/C, and H/C ratios, respectively, in accordance with findings from Aiken et al.[64] Densities of 1.48 g cm^{-3} were found for high-NO$_x$ SOA.

Under high-NO$_x$ conditions, ∼53% of the overall SOA mass is chemically characterized by off-line chemical analyses of aerosol filter samples using both the UPLC/(−)ESI-TOFMS and total peroxide content measurement techniques. An UPLC/

TABLE 4: Summary of Experimental Conditions and Results from the HR-ToF-AMS Instrument

[naphthalene] (ppb)	NO$_x$	seed vol (μm^3/cm^3)	end vol (μm^3/cm^3)	density (g/cm^3)	SOA mass (μg/m^3)	O/C ratio	N/C ratio	H/C ratio
5	low	10.64	18.48	1.55	12.15	0.61 ± 0.18	0	0.97 ± 0.1
20	low	10.48	41.48	1.55	48.06	0.72 ± 0.22	0	0.88 ± 0.09
60	low	13	143	1.55	201.5	0.6 ± 0.18	0	0.82 ± 0.08
5	high	12.25	16.23	1.48	6.18	0.55 ± 0.17	0.01 ± 0.02	1.03 ± 0.1
25	high	12.82	39.18	1.48	40.87	0.55 ± 0.17	0.01 ± 0.02	0.90 ± 0.1
30	high	0	26.3	1.48	40.76	0.45 ± 0.15	0.01 ± 0.02	0.90 ± 0.1
40	high	14.67	63.11	1.48	75.08	0.51 ± 0.15	0.01 ± 0.01	0.81 ± 0.08

(−)ESI-TOFMS base peak ion chromatogram (BPC) obtained for a typical high-NO$_x$ naphthalene SOA experiment is shown in Figure 3. Peaks found under both the high- and low-NO$_x$ conditions are denoted in black, while those SOA constituents found only in the high-NO$_x$ case are denoted in green. Due to the use of (NH$_4$)SO$_4$ seed aerosol, bisulfate (detected as *m/z* 97) was found to elute first from the reverse-phase C18 column. A complete listing of the high-NO$_x$ SOA constituents identified and quantified by the UPLC/(−)ESI-TOFMS technique is provided in Tables 2S−4S (Supporting Information). As shown in Tables 2S−4S (Supporting Information) and Table 3, ∼24−28% of the high-NO$_x$ naphthalene SOA is chemically characterized at the molecular level by the UPLC/(−)ESI-TOFMS technique. These chemical characterizations are further supported by the tandem MS measurements provided by the HPLC/(−)ESI-ITMS technique; major product ions produced for each of the major characterized high-NO$_x$ SOA constituents are also listed in Tables 2S−4S (Supporting Information). All SOA constituents were quantified by calibration with either an authentic or surrogate standard. Dominant contributions to the high-NO$_x$ SOA mass come from phthalic acid and hydroxy benzoic acids. Standard deviations for each UPLC/(−)ESI-TOFMS identified product were calculated across experiments (experiments 2−5 in Table 2). The fraction of SOA mass assigned to each product has a standard deviation of less than 3%, and the average standard deviation for the entire product range was ∼2%, indicating the high level of reproducibility of these experiments.

As shown by the time trace in Figure 4, analysis by the PILS/IC technique confirms that phthalic acid is a significant component of the high-NO$_x$ SOA (Retention Time (RT) = 13.88 min), increasing from 0 to 5.23 μg m^{-3} over the course of the experiment (Experiment 7 in Table 2). Figure 5 shows the ion chromatograms for a high-NO$_x$ chamber sample on the bottom panel. The top panel shows a chromatogram from a 2 ppm standard of phthalic acid. The chromatographic peak with RT of 15.27 min also shows trends of increasing concentration with photochemical age and is not present in background vials, suggesting that this peak corresponds to a SOA constituent; however, this compound could not be identified using available standards. No other water-soluble SOA constituents are observed by the PILS/IC technique, indicating that small organic acids do not account for the unidentified fraction of the SOA mass. This is in contrast to data from the photooxidation of single-ringed aromatic compounds, such as benzene, toluene, and *m*-xylene, for which small organic acids comprise a substantial portion of the overall SOA mass (unpublished data). Small organic acids have also been observed in SOA generated from the photooxidation of 1,3,5-trimethylbenzene.[74]

On the basis of results from the UPLC/(−)ESI-TOFMS method, N-containing compounds account for ∼3% of the total high-NO$_x$ SOA mass formed. Most of the N-containing compounds were quantified using calibration curves generated by either 2-nitro-1-naphthol or 4-nitro-1-naphthol standards. Using 4-nitro-1-naphthol in the quantification of these products yields concentrations that are an order of magnitude reduced from calibrations utilizing the 2-nitro-1-naphthol isomer. Final quantitative results reported here are determined by use of the more conservative mass concentrations. Quantification of these chemically characterized SOA constituents yields an N/C ratio of 0.04. This ratio should be considered as a lower limit for the N/C ratio, because some of the N-containing compounds that are
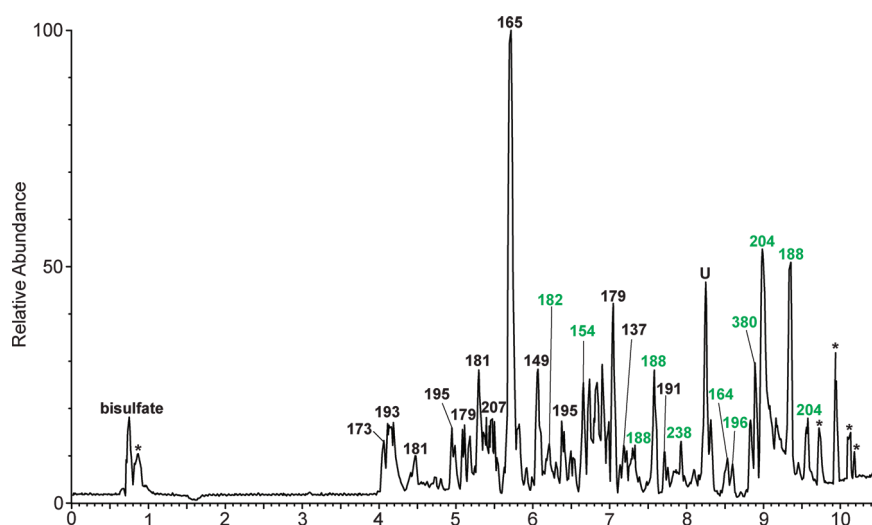
Figure 3. UPLC/(−)ESI-TOFMS base peak ion chromatogram (BPC) of a representative naphthalene high-NO$_x$ SOA sample (Experiment 6). Chromatographic peaks designated with black [M − H]$^-$ ions are also observed in the naphthalene low-NO$_x$ SOA samples. Chromatographic peaks designated with green [M − H]$^-$ ions are only observed in the naphthalene high-NO$_x$ SOA samples. Chromatographic peaks designated with an asterisk, *, were also observed on a blank filter, and they are not considered high-NO$_x$ SOA constituents. Major chromatographic peaks that remain uncharacterized in this study are designated as: U.

922 *J. Phys. Chem. A, Vol. 114, No. 2, 2010*

Kautzman et al.
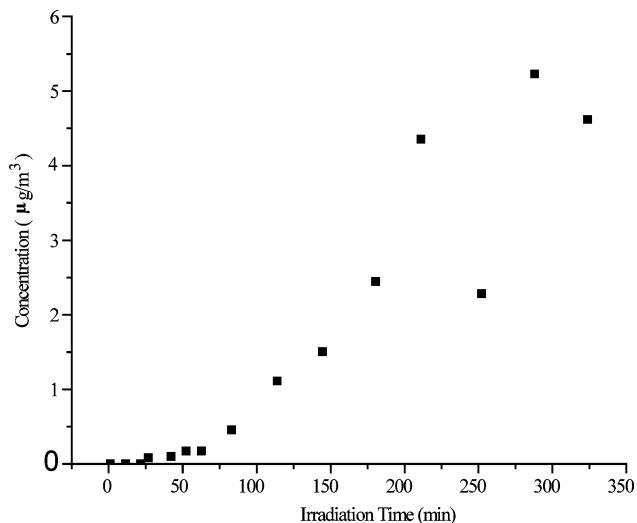
Figure 4. Time trace of phthalic acid acquired from Experiment 6 using the PILS/IC technique.

likely formed are not directly detectable by the UPLC/(−)ESI-TOFMS technique unless the molecule also contains a functional group with an acidic proton that can be abstracted. For example, the UPLC/(−)ESI-TOFMS method detects six isomers of nitronaphthol, as shown in Table 3; however, the 1- and 2-nitronaphthalene compounds identified in the gas phase by the GC/EI-TOFMS technique are not detected, even though the nitronaphthalenes are reported to exist primarily in the particle phase.[46] Given that the 1- and 2-nitronaphthalene isomers are reported to account for 0.3−7%[43,45,72] of the gas-phase yield, and may partition into the particle phase,[46] the detection of these nonacidic nitronaphthalenes in the aerosol phase would likely increase the N/C ratio. We also expect that the formation of PANs, for example from phthaldialdehyde, may play a significant role in SOA formation in the atmosphere. However, owing to the large NO to NO_2 ratio employed in these experiments, and to the difficulty in detecting nonacidic N-containing compounds, PANs are not observed in either the gas- or aerosol-phase.

Bulk HR-ToF-AMS measurements yield measurements of N-containing compounds producing N/C ratios ranging from 0.01−0.044. We place upper and lower bounds on the N/C ratio using calculations with and without the addition of compounds that possess NO^+ and NO_2^+ mass spectral peaks, respectively. Under high-NO_x conditions, OH and NO_2 can react to form nitric acid. Nitric acid can then react with ammonium from the ammonium sulfate seed to produce inorganic nitrates. This process should be of minimal importance for the experiments performed here owing to the dry experimental conditions; however, for the lower-limit calculations, we exclude compounds that have contributions from NO^+ and NO_2^+ mass spectral peaks from the N/C calculation to prevent biasing the chemical composition calculations with the formation of these inorganic nitrates. These lower-limit calculations include only the measurement of organic nitrate (NO_3) functional groups, yielding an atomic N/C ratio of 0.01. Only one organic nitrate is identified by the UPLC/(−)ESI-TOFMS method, supporting the minimal contribution from this class of compounds. However, inclusion of "NO family" ions with mass spectral peaks corresponding to NO^+ and NO_2^+ is necessary to account for the NO_2 groups observed in compounds such as nitronaphthalene, but may introduce artifacts from inorganic nitrates. Inclusion of the NO and NO_2 groups increases the atomic N/C ratio to 0.044, thus providing an upper bound of the N/C ratio. Inclusion of these compounds into the composition calculations also shifts the O/C ratios from 0.51 ± 0.17 (Table 4) to 0.57 ± 0.17. Again, the upper-bound of 0.044 ± 0.01 for the N/C is in good agreement with the lower bound of 0.036 obtained from the UPLC/(−)ESI-TOFMS data as discussed above.

In general, the procedures for compositional analysis determined from high-resolution AMS data are still relatively new, and further studies of the technique are necessary to fully understand the data acquired using this complex instrument. For example, calibrations of compositional ratios performed here are based on AMS data from Aiken et al.,[63] which likely possess a different molecular composition than that of the current experiments. To achieve more accurate ratios, the ionization efficiency of each oxidation product by atomizing standards into

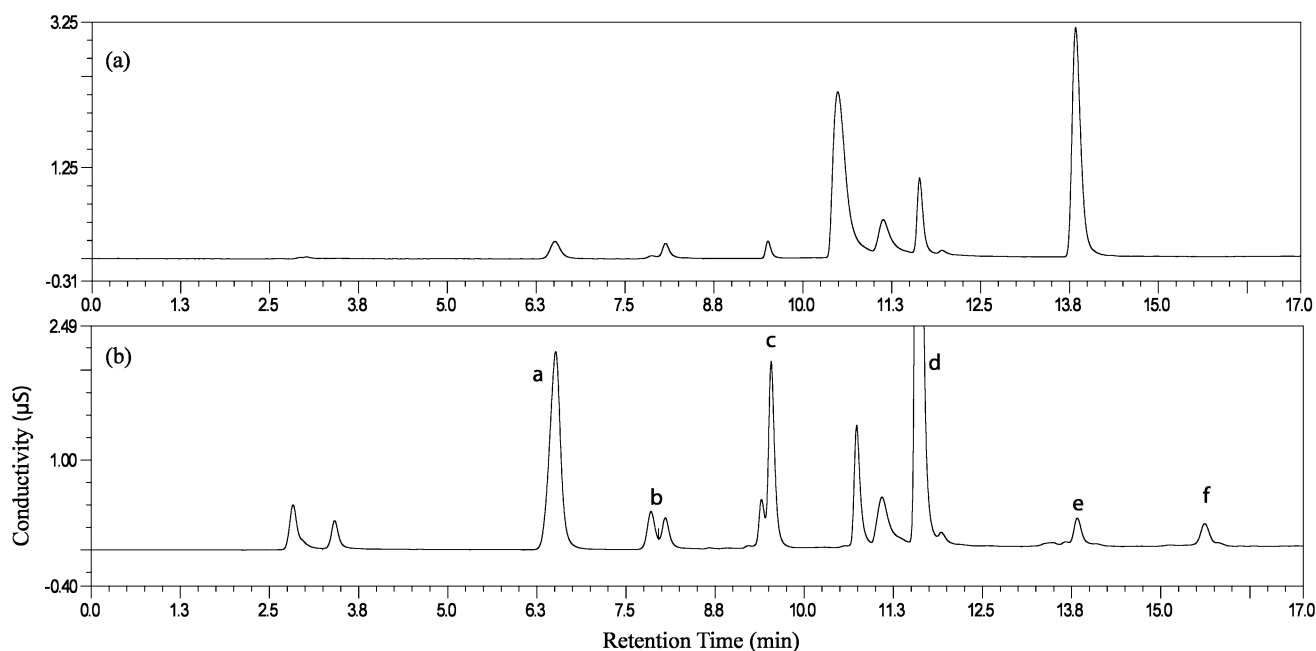**Figure 5.** Chromatograms obtained by the PILS/IC technique. The top panel shows a 2 ppm standard of phthalic acid. The bottom panel shows a representative chromatogram of a PILS sample collected under high-NO_x conditions in the presence of ammonium sulfate seed (Experiment 7). Peak assignments are: a-chloride, b-nitrite, c-nitrate, d-sulfate, e-phthalic acid, f-unidentified peak (see text).

the AMS instrument need to be investigated or alternatively, a much larger database of structures would need to be assembled. More work needs to be performed to fully characterize the appropriateness of the compositional ratios acquired by this technique, particularly for the N-containing compounds which have received less attention.

The high-NO$_x$ naphthalene SOA chemically characterized through the filter sampling methods exhibits an average atomic O/C ratio of 0.48. This ratio is largely consistent with the measurements from the HR-ToF-AMS technique, from which an overall O/C ratio of 0.51 ± 0.17 is detected. Atomic H/C ratios of 0.83 calculated from the filter data are also in agreement with the HR-ToF-AMS value of 0.9 ± 0.10, and as stated above, the N/C ratios are also in relative agreement. The implications of the agreement of the O/C, H/C, and N/C ratios between these two analytical techniques is that the 53% of the total SOA mass that has been chemically characterized is an excellent representation of the chemical composition and oxidation level of the entire high-NO$_x$ naphthalene SOA.

The total peroxide measurement based on the iodometric spectroscopic method indicates that under high-NO$_x$ conditions ~28% of the total SOA mass can be attributed to organic peroxides (i.e., ROOH and/or ROOR). Contributions of organic peroxides are calculated by determining the molar concentration of peroxides in the solution. The measured concentration of peroxides obtained by absorption at 470 nm is converted to μg m^{-3} using the known solution volume, molar-weighted average mass, and the volume of chamber air sampled. The molar-weighted average MW is determined by multiplying the MW of each product by the product mole fraction and summing over the individual products. For the high-NO$_x$ system, we have taken a molar-weighted average mass of the chemically characterized SOA constituents listed in Tables 2S−4S (Supporting Information) and assumed this to be the average MW of the unknown organic peroxide structures. The assumption that this average MW would be representative for the unknown organic peroxides is supported by the similar O/C, N/C, and H/C ratios found using both the chemically characterized filter data and the total aerosol HR-ToF-AMS measurements. For the high-NO$_x$ case, the molar-weighted average mass is determined to be 172 amu. As will be discussed subsequently, we believe this is a conservative estimate of the average peroxide mass. If the actual average mass of the peroxides is indeed higher than the assumed mass of 172 amu, then the contribution from peroxides to the total SOA mass would increase. It should be noted that the iodometric spectroscopic method provides no detailed chemical characterization of the quantified organic peroxide content.

3.2. Low-NO$_x$ Conditions.

3.2.1. Chemical Characterization of Low-NO$_x$ Gas-Phase Oxidation Products.

A representative (+)CIMS mass spectrum obtained for naphthalene photooxidation under low-NO$_x$ conditions is shown in Figure 6. This mass spectrum was taken at the same fraction of naphthalene reacted as that for the high-NO$_x$ experiment previously shown in Figure 2, and thus the extents of reaction are similar. Whereas the tentatively identified products are the same as those observed under high-NO$_x$ conditions, the relative intensities of the identified compounds are substantially different. In the low-NO$_x$ case, the intensities of the ring-retaining products (e.g., naphthol, naphthoquinone, and epoxyquinone), as denoted by blue mass spectral peaks in Figure 6, are all significantly greater than those found under high-NO$_x$ conditions. Nevertheless, the m/z 161 signal continues to dominate the overall (+)CIMS mass spectrum. When compared with data from both the high-NO$_x$ experiments and
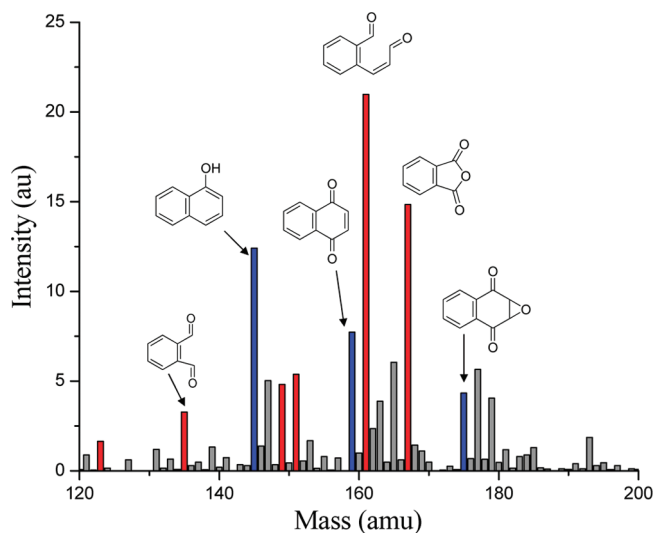

Figure 6. (+)CIMS mass spectrum taken at 70% reacted naphthalene under low-NO$_x$ conditions. Red data indicate ring-opening products. Ring-retaining products are indicated in blue.

from injection of the synthesized standard, it is found that the GC retention times, mass spectra, and exact masses (i.e., chemical formulas) obtained using the GC/EI-TOFMS technique match, thus confirming that the compound observed at m/z 161 in the (+)CIMS mass spectrum under low-NO$_x$ conditions is 2-formylcinnamaldehyde.

3.2.2. Chemical Characterization of Low-NO$_x$ SOA.

An UPLC/(−)ESI-TOFMS BPC obtained for a typical low-NO$_x$ naphthalene SOA experiment is shown in Figure 7. Detailed comparison of this chromatogram and the high-NO$_x$ BPC (Figure 3) demonstrates that the aerosol compositions are quite similar. All of the chromatographic peaks are also observed in the naphthalene high-NO$_x$ SOA samples. No N-containing SOA constituents are observed under low-NO$_x$ conditions due to the lack of NO and NO$_2$ addition reactions. Under low-NO$_x$ conditions, we have been able to chemically characterize ~68% of the SOA mass, as compared to the ~53% identified in the high-NO$_x$ regime. The increase in speciation is the result of a substantial enhancement in the concentration of the acidic species under low-NO$_x$ conditions, with consistent peroxide contributions under both NO$_x$ conditions. As shown in Table 3 and in Supporting Information, the fractions of total SOA mass attributed to phthalic acid and hydroxy phthalic acid, for example, increase by factors of 2 and 3, respectively. Similar increases are observed for benzoic acid, hydroxy benzoic acid, cinnamic acid, and dihydroxy cinnamic acid. The ring-retaining compounds are present in low-NO$_x$ SOA samples, but we cannot remark on their relative abundance compared to the high-NO$_x$ case, owing to the fact that standards are often not available, and these components were not quantified. Detection efficiencies for these nonacidic ring-retaining compounds are lower than those of the acidic ring-opening compounds. Hydroxy cinnamic acid (see Table 3, MW 164) was the only additional compound identified specific to the low-NO$_x$ regime. The atomic O/C compositional ratio from filter sampling methods is 0.50, and the H/C ratio is 0.82. O/C and H/C ratios determined from the HR-ToF-AMS technique are 0.64 ± 0.19 and 0.89 ± 0.1, respectively.

The total organic peroxide contribution was determined in the same manner as that carried out for the high-NO$_x$ experiments as detailed in Section 3.1.2. The molar-weighted average mass was determined to be slightly higher than that of the high-
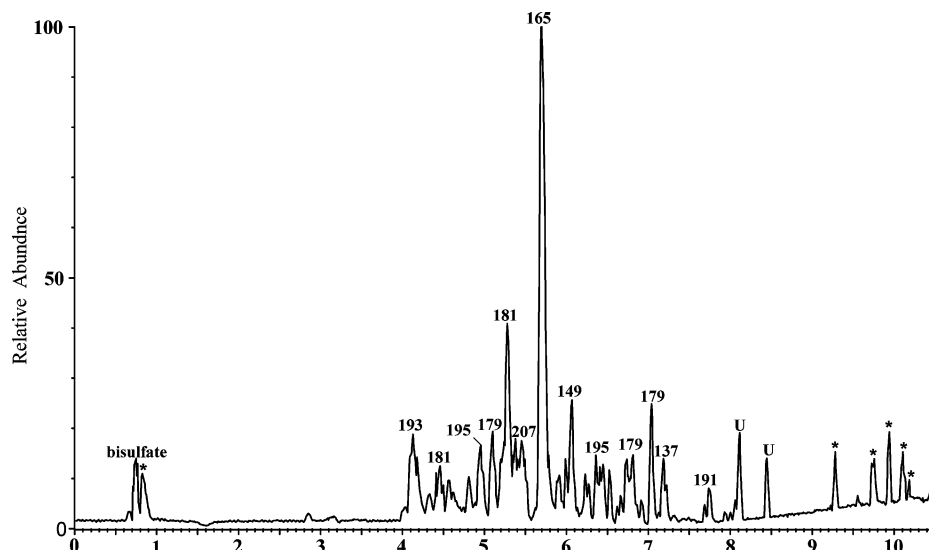
Figure 7. UPLC/(−)ESI-TOFMS base peak ion chromatogram (BPC) of a representative naphthalene low-NO$_x$ SOA sample (Experiment 3). All major chromatographic peaks are marked with their corresponding [M − H]$^-$ base peak ions. Chromatographic peaks designated with an asterisk, *, were also observed on a blank filter, and they are not considered high-NO$_x$ SOA constituents. Major chromatographic peaks that remain uncharacterized in this study are designated as: U.

NO$_x$ SOA at 174 amu due to the increased contribution from larger acids, for example, hydroxy phthalic acid (MW 182 and observed by the UPLC/(−)ESI-TOFMS technique at m/z 181). The total peroxide contribution under low-NO$_x$ conditions is calculated to be ~26.2% of the total SOA mass. This is similar to the 28% contribution found in the high-NO$_x$ case. As in the high-NO$_x$ case, we believe this to be a lower limit of the total peroxide contribution to the SOA mass.

4. Discussion

4.1. High-NO$_x$ Conditions.

4.1.1. High-NO$_x$ Gas-Phase Chemistry. The gas-phase mechanism of naphthalene photooxidation has been the subject of considerable study. Our present findings can be viewed within the context of this prior work. We concentrate first on the high-NO$_x$ case, an atmospherically interesting situation owing to the coemissions with other anthropogenic sources and the relatively short lifetime of naphthalene in the urban atmosphere.[43,75−78] Proposed formation mechanisms of the major high-NO$_x$ naphthalene gas-phase products are provided in Scheme 1. The gas-phase photooxidation products detected are boxed, and the MWs of the identified products are highlighted in red. The mechanism presented here does not incorporate all of the chemically characterized products; a complete list of identified products can be found in Tables 2S−4S (Supporting Information). The majority of the gas-phase mechanism has been previously established.[43,45,47,72,79,80] Qu et al.[81] have performed theoretical calculations exploring the OH oxidation of naphthalene in the presence of O$_2$ and NO$_x$, and have detailed much of the gas-phase reaction dynamics. As determined by Wang et al.,[47] 68% of the OH addition occurs at the C$_1$ position to form the hydroxycyclohexadienyl radical. The 1-hydroxycyclohexadienyl radical lies 10 kcal mol^{-1} lower in energy than the 2-isomer.[81] The preference for addition at the 1-site is supported by the fact that 2-nitronaphthalene is ~2 times more abundant than the 1-nitronaphthalene isomer.[80] The addition, the 1-site also determines the formation of the epoxide, although 2-formyl-cinnamaldehyde could be formed from either the 1- or 2-hydroxycyclohexadienyl radical.

The OH-naphthalene adduct reacts with either NO$_2$ or O$_2$. GC/FID data combined with GC/MS-negative ion chemical

ionization (NCI) data from other chamber studies[80] suggest that the NO$_2$ and O$_2$ reactions with the OH-naphthalene adduct may be of equal importance for NO$_2$ mixing ratios in the range of 60 ppb. The NO$_2$ mixing ratio used in the present high-NO$_x$ experiments is ~80 ppb, so these pathways should be of roughly equal importance in the present experiments. A detailed description of the importance of the NO/NO$_2$ in these experiments is previously discussed in Section 3.2.1.

The N-containing compounds (i.e., nitronaphthalenes and nitronaphthols) formed through the NO$_2$ reaction pathway are of particular interest due to their mutagenic properties.[50,51] In extensive studies of the nitronaphthalene isomers, along with other nitroarene compounds, Arey and co-workers[43,48,73,80,82] have found that both 1- and 2-nitronaphthalene isomers form during daytime conditions by OH reaction of naphthalene, but actually concentrations of these compounds reach a maximum at night due to N$_2$O$_5$ chemistry.[48] The major loss process for 1- and 2-nitronaphthalene under atmospheric conditions is photolysis, with photolytic lifetimes on the order of 2 h.[73] Photolysis is approximately an order of magnitude more important than OH reaction, for which the reaction rate coefficients are 5.4×10^{-12} cm^3 molecule^{-1} s^{-1} and 5.6×10^{-12} cm^3 molecule^{-1} s^{-1} for the 1- and 2-nitro isomers, respectively. Arey et al.[73] also suggest that 1-nitronaphthalene is the precursor to the 1,4-naphthoquinone product, which is formed through a photolysis pathway, denoted in Scheme 1 by an open arrow. These OH rates are consistent with the work of Bunce et al.[45] for which lifetimes of 20−34 h against OH reaction for the 1-nitronaphthalene and 2-nitronaphthalene isomers, respectively, were calculated using the same OH concentration, but neglecting the photolysis pathway.

Formation of ring-opening compounds is consistent with decomposition of the alkoxy (RO) radicals formed from the RO$_2$ + NO pathway,[72] which leads to 2-formylcinnamaldehyde (MW 160) and observed by the (+)CIMS technique at m/z 161, the precursor to the majority of the ring-opening products found in Scheme 2. 2-formylcinnamaldehyde is detected as both *E*- and *Z*- isomers and is the major gas-phase product observed under high-NO$_x$ conditions.[45,71,72] Sasaki et al.[72] suggested a combined yield for the cinnamaldehyde *E*- and *Z*- isomers of 35%. Although two further compounds with MW 160 are identified,

J. Phys. Chem. A, Vol. 114, No. 2, 2010 **925**

SCHEME 1: Proposed High-NO$_x$ Mechanism for the Formation of Ring-Retaining Products and 2-Formylcinnamaldehyde (MW 160)^a
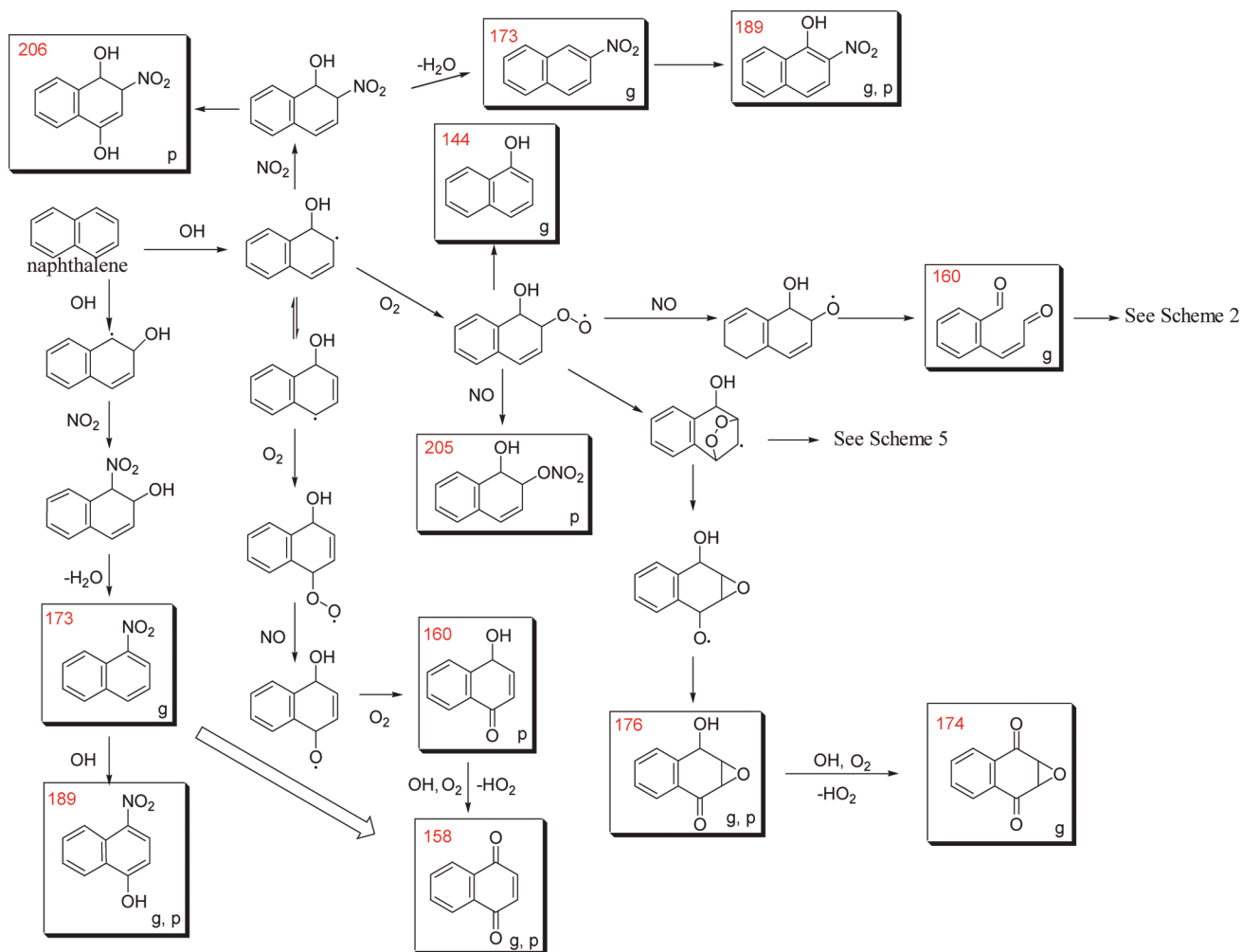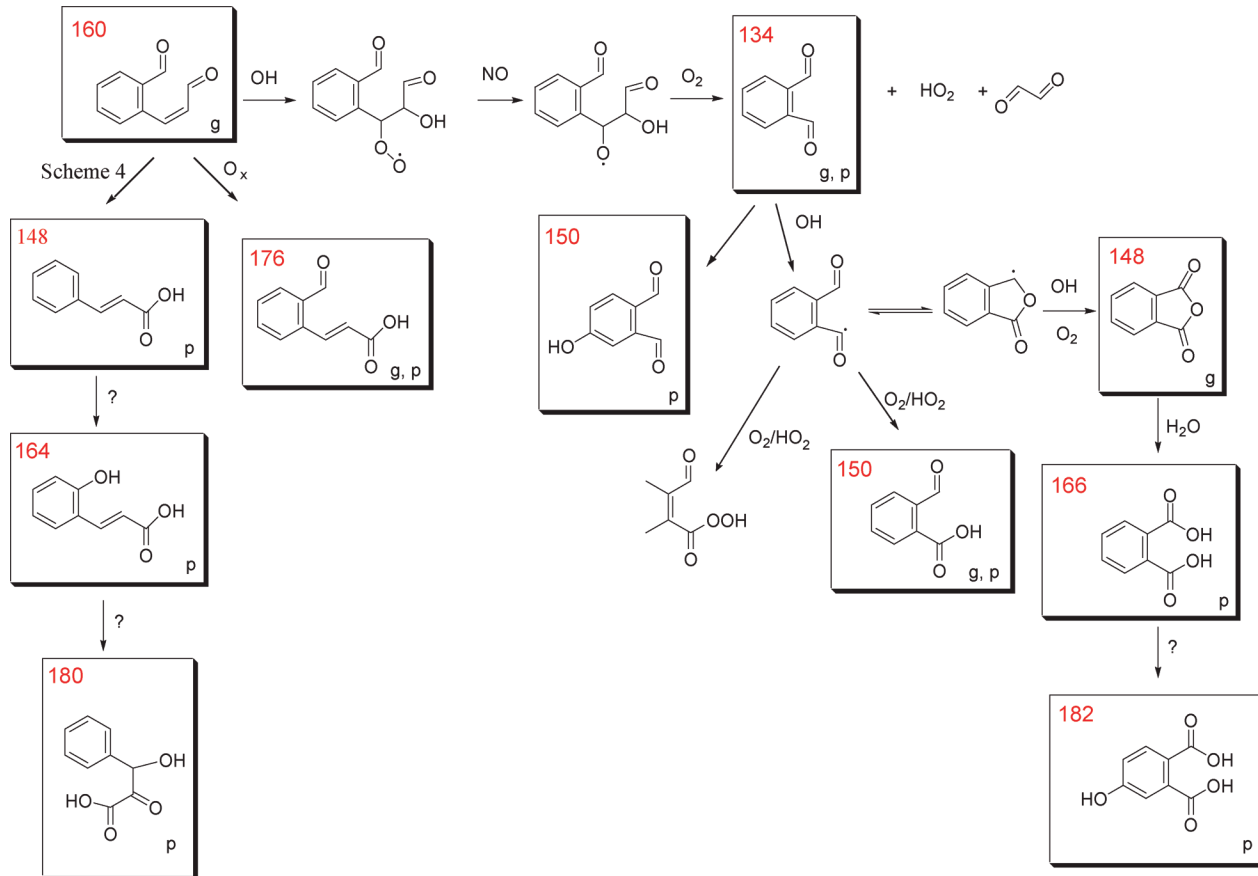

^{a} Observed products are boxed. MWs are shown in red, and the phase of the observed product (gas, g, or particle, p) is denoted in the lower right corner.

based on peak intensity, the authors suggest that the *E*- and *Z*-2-formylcinnamaldehyde structures account for ~92% of the products with MW 160. The remaining two compounds with MW 160 have yet to be identified, although data suggest that one of these compounds is an aldehyde isomer, whereas the other compound most likely contains a carbonyl group. The latter structure may be the hydroxy carbonyl identified as MW 160 shown in Scheme 1. We note that dihydroxynaphthalene compounds would also be consistent with this mass.

An alternate route to the formation of 2-formylcinnamaldehyde proposed by Qu et al.[81] involves a hydride shift from the alcohol group on the naphthol peroxy intermediate to form a hydroperoxy intermediate. Subsequent loss of OH and breaking of the C_1-C_2 bond yields the 2-formylcinnamaldehyde. The authors calculate that this reaction is exothermic by 24.88 kcal mol^{-1}. The two mechanisms for the formation of 2-formylcinnamaldehyde are shown in Scheme 3. The first mechanism would result in the formation of NO$_2$ and HO$_2$, whereas the second mechanism would result in the formation of OH. It is not possible to confirm one mechanism over the other from our data, and both mechanisms remain as plausible routes to the formation of the major 2-formylcinnamaldehyde oxidation product. 2-Formylcinnamaldehyde undergoes further reaction as shown in Scheme 2 to form ring-opening products, including phthalic anhydride, phthalic acid, and phthaldialdehyde.

In addition to the pathway for ring-opening products through the 2-formylcinnamaldehyde product, the bicyclic peroxy radical may play a crucial role in the formation of not only ring-opened products, but the formation of peroxide and epoxide compounds as well. This alternate pathway will be discussed in Section 4.1.2. An alternate pathway to the formation of ring-opening products is supported by the decay time for 2-formlycinnamaldehyde. As shown in Figure 2, 70% of the 2-formylcinnamaldehyde remains at the completion of the experiment. Given that, under high-NO$_x$ conditions, the SOA mass yield for naphthalene is ~30%,[15] and 2-formylcinnamaldehyde is suggested as the major gas-phase product (30–60%),[72,83] one would expect to see a greater decay in 2-formylcinnamaldehyde in order to produce the observed aerosol yields. This is suggestive that another route to the ring-opening products may play a role in the formation of high-NO$_x$ SOA.

Previous studies present evidence that photolysis plays a significant role in the loss processes for the 2-formylcinnamaldehyde isomers, competing with the various reaction pathways. Wang et al.[47] have detailed the various loss processes for 2-formylcinnamaldehyde and report a ratio of OH reaction to photolysis of 1.8 under blacklamp photolysis conditions with corrections for wall-loss. A further study by Nishino et al.[71] reexamined the competing pathways of 2-formylcinnamaldehyde OH-reaction versus photolysis. Nishino et al. suggest a yield

Kautzman et al.

SCHEME 2: Proposed Mechanism for the Formation of Ring-Opening Products from the Further Reaction of 2-Formylcinnamaldehyde[a]

[a] Observed products are boxed. MWs are shown in red, and the phase of the observed product (gas, g, or particle, p,) is denoted in the lower right corner.

SCHEME 3: Suggested Mechanism for the Formation of 2-Formylcinnamaldehyde[a]
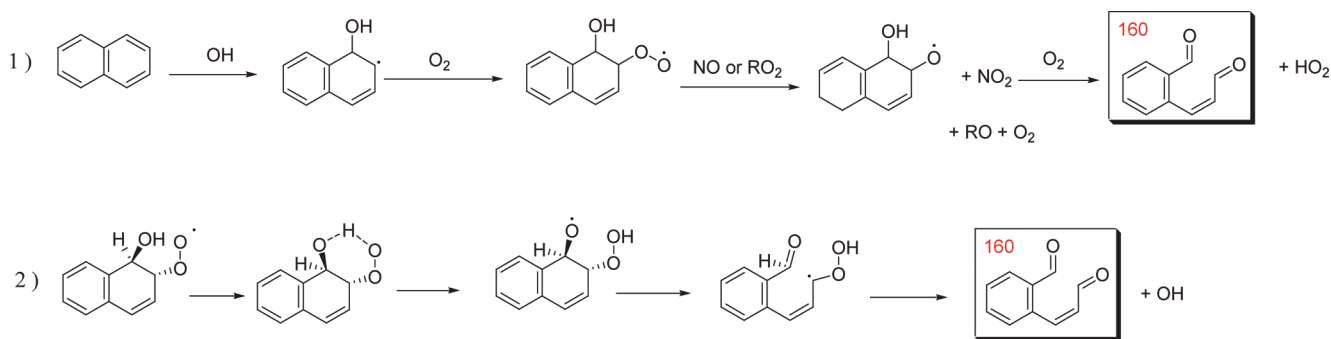
[a] Mechanism 2 from ref 81 begins with the formation of the peroxide assuming the same initial steps as demonstrated in mechanism 1.

of 58−61% for the combined *E*- and *Z*- isomers of 2-formyl-cinnamaldehyde with the OH-reaction and photolysis decay pathways being of equal importance under experimental conditions.

In addition to the aforementioned products we have identified a range of C_7 and C_9 compounds (benzoic acid, etc) in low abundance. While some of these compounds have been previously observed,[45] a mechanism leading to them has not yet been proposed. We suggest two possible mechanisms as minor routes. Photolytic loss of the formyl group from 2-formlycinnamaldehyde followed by a hydride shift to the benzene ring and further oxidation by O_2 and HO_2 seems to be a plausible mechanism for forming compounds in this class.

Alternatively, as shown in Scheme 4, C_7 and C_9 compounds could be formed through O_2 addition to the radical formed on the formyl group by H-abstraction by OH radical to form a RO_2 radical that subsequently reacts with NO to form an alkoxy radical. Loss of a CO_2 moiety followed by a hydride shift and oxidation of the radical carbonyl to form an acid would generate the observed product with MW 148 denoted in Scheme 2. Similarly, the corresponding peroxyacid would likely be formed in conjunction with the acid (MW 148) during the O_2 addition, and may go on to further react in the aerosol phase.

4.1.2. High-NO_x SOA Chemistry. Two previous studies have addressed the chemical composition of SOA formed from the photooxidation of naphthalene.[46,84] We present here detailed quantitative analysis on the chemical composition and potential reaction pathways relevant to naphthalene high-NO_x SOA formation. The compounds identified from the UPLC/(−)ESI-TOFMS analysis of filter samples yield atomic O/C, N/C, and

SCHEME 4: Possible Mechanism for the Formation of C7 and C9 Compounds
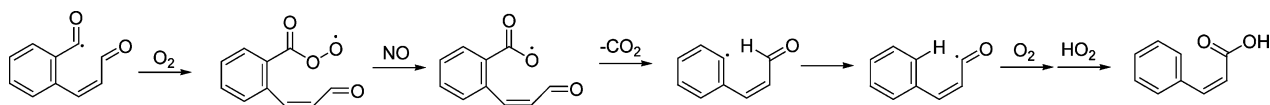
SCHEME 5: Proposed Reaction Mechanisms for Bicyclic Peroxide Structure
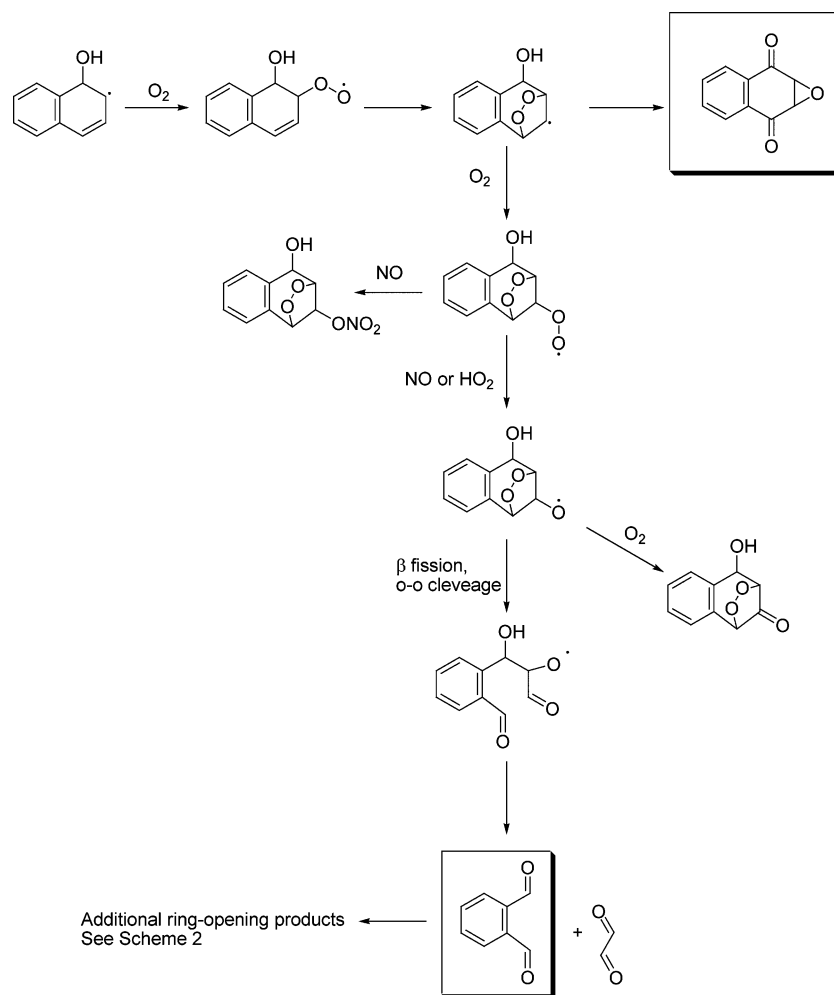
H/C ratios that are in agreement with bulk measurements from HR-ToF-AMS samples. This indicates that the chemical nature of the characterized SOA constituents is a good representation of the bulk aerosol formed from the photooxidation of naphthalene under high-NO$_x$ conditions. The chemical mechanisms shown in Schemes 1 and 2 demonstrate how the gas-phase oxidation products are likely to evolve by further oxidation to form the components identified in the aerosol phase. The "g" and "p" superscripts associated with each product denote the phase of the component. A minor fraction of the SOA mass is attributed to the N-containing compounds such as nitronaphthols. The chemically characterized portion of the aerosol, which we assume to be representative of the bulk aerosol based on detailed composition measurements, is primarily composed of single-ring (ring-opening) acids (e.g., formylcinnamic acid and further oxidized compounds from phthalic acid).

We have performed calculations determining the average number of carbonyls/molecule for the SOA in order to compare with previous FTIR measurements. Dekermenjian et al.[84] reported an average of 3.2 carbonyl/molecule based on the assumption that the average molecule possesses a 10 carbon backbone. As shown in Table 3, many of the compounds with

significant yield possess C8 structures, thus calling into question the appropriateness of assuming a 10-carbon backbone. In order to determine the average number of carbonyls/molecule we have counted the number of carbonyl groups on each identified product, and weighted this number by mole fraction, to establish that the average structure possesses ~1.25 carbonyls/molecule. We believe the average we report here is an accurate representation of the degree of molecular oxidation, as it is based on identified structures for which the bulk composition is known. In comparison, the chemical composition determined by FTIR will be strongly dependent on the length of the carbon backbone, the accuracy of the composition calibrations, and the form of the carbonyl group (e.g., acidic, aldehydic, or ketone).[85]

Organic peroxides are found to contribute ~28% of the total high-NO$_x$ SOA mass. We propose that a mechanism for the formation of these compounds may occur through the formation of a bicyclic peroxy radical as shown in Scheme 5. Analogous reaction pathways have been examined in single-ringed aromatic hydrocarbons (SAH). For toluene, benzene, and *m*-xylene it was proposed that isomerization of the primary RO$_2$ radical to form the bridged bicyclic structure is faster than the competing reaction with NO$_2$, and a reaction with NO to form the RO
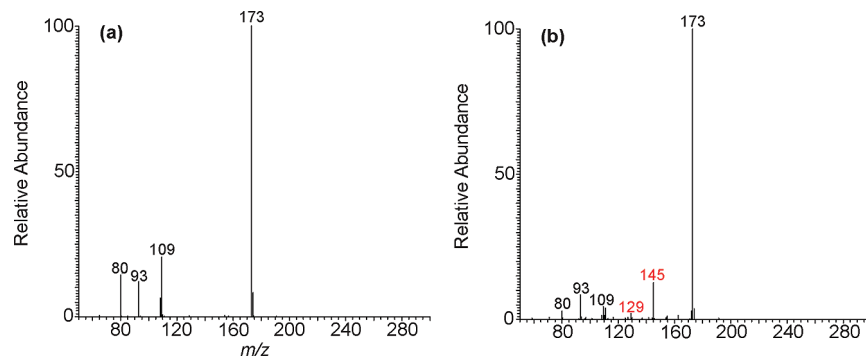
Figure 8. (−)ESI-ITMS MS^2 of *m/z* 173 collected via direct infusion analysis from (a) a 20 ppm 4-hydroxybenzene sulfonic acid standard and from (b) a naphthalene high-NO$_x$ SOA sample (Experiment 6). Due to the generation of these MS^2 via direct infusion, isobaric *m/z* 173 ions were analyzed simultaneously from the high-NO$_x$ SOA sample. As a result, red ions highlighted in (b) are not due to the hydroxybenzene sulfonic acid. Product ions observed at *m/z* 93 and 109 are due to neutral losses of SO$_2$ and SO$_3$, respectively, which are neutral losses characteristic of aromatic sulfonates. The product ion observed at *m/z* 80 is due to the production of SO$_3^-$, which is also a characteristic ion of aromatic sulfonates. The hydroxybenzene sulfonic acids lack the presence of a *m/z* 97 ion (i.e., HSO$_4^-$) in their MS^2 spectra, which is a characteristic product ion of organosulfate functional groups (−ROSO$_3$).

radical may only occur after O$_2$ addition.[86] The simplest bicyclic structure from naphthalene, which has molar mass of 192 amu, is shown below in Scheme 5. Thus, structures related to the bicyclic RO$_2$ radical would yield masses of 192 or higher, and the contributions from peroxides based on the average yield-weighted calculations detailed in Section 3.1.2 would be underestimated. If one uses the single-ringed aromatic compounds as exemplary of the PAH products, then a reasonable mechanism for both peroxides and ring-opening products can be determined as shown in Scheme 5. The initial naphthalene−OH adduct can either undergo hydrogen abstraction through reaction with O$_2$ to form naphthol or can react with O$_2$ to form the RO$_2$ radical. For benzene, master equation calculations suggest that formation of the phenolic compound accounts for 55−65% of the reaction mechanism, and the formation of the bicyclic peroxy radical is the other major pathway.[87] Resonance fluorescence studies for several aromatic species have also shown that the OH-aromatic adduct reacts preferentially with O$_2$ over both NO$_2$ and NO to form either the alcohol or the bicyclic peroxide structure, and reaction with NO can only occur after the initial addition of O$_2$.[86] Reactions of the aromatic-peroxy adduct with NO to form the alkoxy radical are found to be of minor importance for the SAH.[86,88] The bicyclic peroxy radical that forms from the aromatic−OH reaction with O$_2$ can isomerize to yield an epoxide; however, this route has been suggested based on master equation calculations[87] for benzene, and based on ab initio calculations[86] for toluene, to be of minor importance in the atmosphere, although the epoxide formed from this type of mechanism has been detected in the experiments reported here. For benzene, the pathway to the bicyclic RO$_2$ structure has a 10 kcal mol^{-1} barrier and is exothermic by ∼69 kcal mol^{-1}. Comparatively, the barrier to epoxide formation is 74 kcal mol^{-1} and the reaction is exothermic by 59 kcal mol^{-1}.[87] Once the bicyclic RO$_2$ radical forms, the radical termination steps can lead to a carbonyl, an organic nitrate, or an RO radical, with the latter undergoing β-fission followed by cleavage of the bridge O−O bond to form ring-opening products. For the SAH, the primary fate of the bicyclic radical is isomerization to form the epoxide or reaction with O$_2$ to lead to ring-opening products. We include the route through reaction of the alkoxy radical with O$_2$ to form the carbonyl merely for completeness, but this should be a very minor channel.

Both the mechanism through the bicyclic structure (Scheme 5) and the mechanism shown for the formation of phthaldialedhyde in Scheme 2 are supported by the observed concur-

rent growth of glyoxal.[47] However, reaction through the bicyclic mechanism generates phthaldialdehyde and glyoxal as first generation products, while further reaction through 2-formyl-cinnamaldehyde (Scheme 2) leads to second-generation glyoxal and phthaldialdehyde. The bicyclic structure to form ring-opened products has been extensively studied for the single-ringed aromatics,[89] but to the best of our knowledge, has only been suggested in the pathway to epoxide formation for the PAH compounds. Given that about 70% of the 2-formylcinnamaldehyde was found to remain at the completion of the chamber experiments, formation of the ring-opening products through an alternate pathway may be of significance. Further mechanistic studies on the reaction pathways of bicyclic structures related to PAHs could yield important insights into the further gas-phase reactions of this class of compounds.

In addition to the ring-opening and ring-retaining structures previously outlined, an organic sulfonic acid (R-SO$_3$), which was characterized as hydroxylbenzene sulfonic acid using an authentic standard, is observed here in naphthalene SOA produced under both high- and low-NO$_x$ conditions in the presence of neutral ammonium sulfate seed aerosol. Comparisons of these mass spectra are displayed in Figure 8. Product ions observed at *m/z* 93 and 109 are due to neutral losses of SO$_2$ and SO$_3$, respectively. These neutral losses are characteristic of aromatic sulfonates.[90] The product ion observed at *m/z* 80 is due to the production of SO$_3^-$, which is also a characteristic ion of aromatic sulfonates.[91,92] The hydroxylbenzene sulfonic acids lack the presence of a *m/z* 97 ion (i.e., HSO$_4^-$) in their MS^2 spectra, which is a characteristic product ion of organosulfate functional groups (−ROSO$_3$).[29,32,59] The absence of this peak clearly suggests that the product identified cannot be an organosulfate. In combination with the accurate mass measurements and similar retention times, the comparison of these MS^2 spectra further supports the identification of hydroxylbenzene sulfonic acids in naphthalene low- and high-NO$_x$ SOA formed in the presence of ammonium sulfate seed. The formation of this product requires reaction with the ammonium sulfate seed, as the seed is the only source of sulfur in the system; however, the mechanism by which an organic sulfonic acid would be produced remains unclear. Methyl sulfonate has been reported in marine layer aerosol due to the oxidation of dimethyl sulfide.[93−95] The presence of sulfonate compounds known as of linear alkylbenzene sulfonates (LAS) has been observed in river and seawater[96] as well. LAS compounds, which are used as surfactants in the manufacturing of cleaning products,[97] are

Photooxidation of Naphthalene

J. Phys. Chem. A, Vol. 114, No. 2, 2010 **929**

SCHEME 6: Proposed Low-NO$_x$ Mechanism for the Formation of Ring-Retaining Products and 2-Formylcinnamaldehyde (MW 160) under Low-NO$_x$ Conditions^a
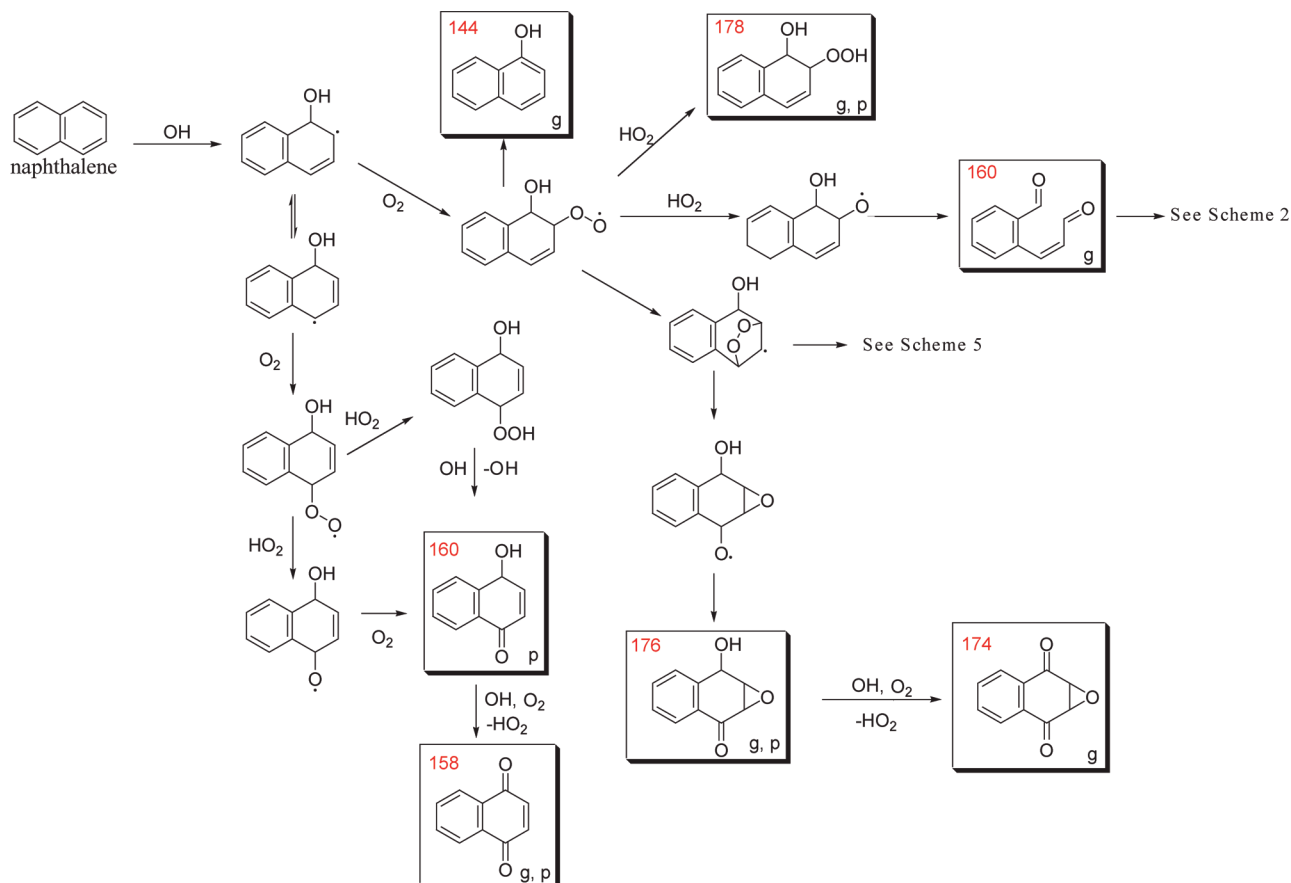
^{a} Observed products are boxed. MWs are shown in red, and the phase of the observed product (gas, g, or particle, p) is denoted in the lower right corner.

found in these aquatic systems due to incomplete removal from wastewaters. Most recently, Altieri et al.[98] have observed the presence of LAS directly in precipitation samples. The presence of sulfonates in the environment due to pollution sources does not yield insights into the generation of these compounds in our chamber studies. Nevertheless, the photooxidation of PAHs (e.g., naphthalene) in the presence of sulfur-containing aerosols might yield an additional source of sulfonates found in the environment.

4.2. Low-NO$_x$ Conditions.

4.2.1. Low-NO$_x$ Gas-Phase Chemistry. Although the major gas-phase products observed under low-NO$_x$ conditions are similar to those under high-NO$_x$ conditions, the intensities of the resultant compounds differ dramatically. Scheme 6 shows the proposed mechanism for the formation of the identified products under low-NO$_x$ conditions. Under low-NO$_x$ conditions, the ring-opening products can be formed mechanistically through RO$_2$ + RO$_2$ or RO$_2$ + HO$_2$ pathways. Given the high concentrations of HO$_2$ prevalent in these chamber studies, the RO$_2$ + RO$_2$ route is calculated to be of minor importance compared to RO$_2$ + HO$_2$ reactions. A simple kinetic simulation similar to those performed for SAH,[13] indicates that in order for RO$_2$ + RO$_2$ mechanisms to be competitive with RO$_2$ + HO$_2$ reactions, RO$_2$ + RO$_2$ rate constants would need to be at least a factor of 10 larger than RO$_2$ + HO$_2$ rate constants based on relative concentrations of RO$_2$ and HO$_2$ found in the chamber. From the master chemical mechanism (MCM) version 3.1 it is found that $k_{(RO_2+HO_2)}$ are generally on the order of 2.0×10^{-11} cm^3 molecule^{-1} s^{-1}, whereas $k_{(RO_2+RO_2)}$ are no more than $1.0 \times$

10^{-12} cm^3 molecule^{-1} s^{-1}, indicating that RO$_2$ + HO$_2$ pathways should dominate over RO$_2$ + RO$_2$ reactions under our experimental conditions.

We also acknowledge that a different pathway for the 1,4-naphthoquinone product under low-NO$_x$ conditions may be possible. In their study of the OH-initiated photooxidation of naphthalene, Qu et al.[81] predict that the quinone is formed by addition of HO$_2$ to 1-naphthol followed by reaction with O$_2$ to form the 1,4-carbonyl peroxy naphthalene intermediate. Two subsequent reactions with HO$_2$ yield 1,4-naphthoquinone and OH radical. The overall reaction is exothermic by −58.49 kcal/mol. This type of HO$_2$ mechanism has not been well established, and reaction rates have not been reported, thus determining the atmospheric importance of such a mechanism is not possible, although it is energetically plausible.

4.2.2. Low-NO$_x$ SOA Composition Chemistry. Under low-NO$_x$ conditions ∼68% of the SOA mass has been identified, of which 26.2% is associated with organic peroxide compounds, and the remaining 42% is chemically characterized at the molecular level in Table 3 (and Tables 5S−7S) with dominant contributions coming from acids. Under low-NO$_x$ conditions a significant enhancement in the formation of acids is observed. As shown in Table 3, the contribution of hydroxyphthalic acid to the overall SOA mass increases from 3% in high-NO$_x$ condition to 9% for the low-NO$_x$ case. The increase in the concentration of acidic species is expected in the low-NO$_x$ case as RO$_2$ + HO$_2$ chemistry dominates over the formation of alkoxy radicals in the absence of NO. However, the formation of alkoxy radicals through an RO$_2$ + HO$_2$ route still leads to
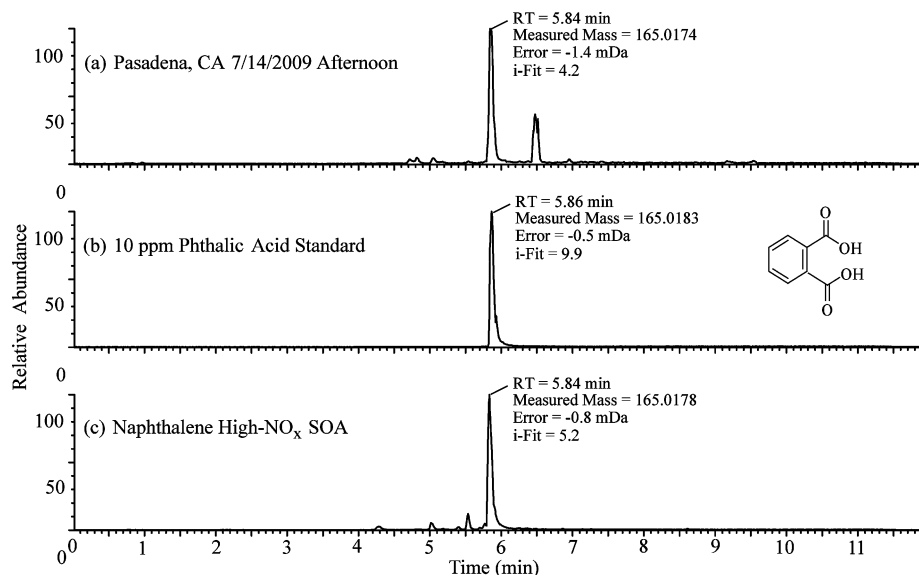
Kautzman et al.

Figure 9. UPLC/(−)ESI-TOFMS EICs of *m/z* 165 from (a) ambient samples collected in Pasadena, CA, (b) a 10 ppm phthalic acid standard, and (c) naphthalene high-NO$_x$ experiments (Experiment 6).

the presence of ring-opening species, as does the bicyclic mechanism shown in Scheme 5. The 28% of SOA mass attributed to organic peroxides, along with the enhancement of acidic species, indicates the importance of RO$_2$ + HO$_2$ reactions. The further reaction of bicyclic RO$_2$ radicals may contribute significantly to the generation of ring-opening products, the epoxide, and organic peroxide species. O/C ratios from the filter sampling method are slightly higher than in the high-NO$_x$ data (0.50 vs 0.48, respectively), as is expected given the enhancement of acidic species. AMS data shows that the O/C ratios and H/C ratios are also slightly higher in the low-NO$_x$ experiments, though still within error bars when compared to the high-NO$_x$ experiments. These higher compositional ratios obtained from the AMS technique appear to not only be an effect of increasing acid concentration, but also of aging. Owing to the lower OH concentration achieved in the low-NO$_x$ experiments, longer reaction times are required to reach a constant aerosol volume, thus more oxidation may occur in the aerosol, though the observed affect is small.

4.3. Atmospheric Significance of Naphthalene SOA: Identification of Potential Ambient SOA Tracers in Urban Atmospheres. Urban aerosol filter samples collected in Birmingham, AL and in Pasadena, CA, were examined for the presence of naphthalene SOA constituents chemically characterized in the present study (Table 3). The UPLC/(−)ESI-TOFMS data obtained from the urban aerosol samples are compared to the laboratory-generated high-NO$_x$ naphthalene SOA. Upon detailed comparison of the UPLC/(−)ESI-TOFMS BPCs obtained from both the laboratory-generated and ambient organic aerosol samples, it becomes evident that several of naphthalene high-NO$_x$ SOA constituents characterized in the present study are observed in the urban aerosol samples. Figure 9 shows the UPLC/(−)ESI-TOFMS extracted ion chromatograms (EICs) of *m/z* 165 obtained from an urban aerosol sample collected from Pasadena, CA, a 10 ppm phthalic acid authentic standard, and a typical naphthalene high-NO$_x$ photooxidation experiment, respectively. The comparison of these 3 EICs suggests that phthalic acid may be a potential ambient naphthalene SOA tracer
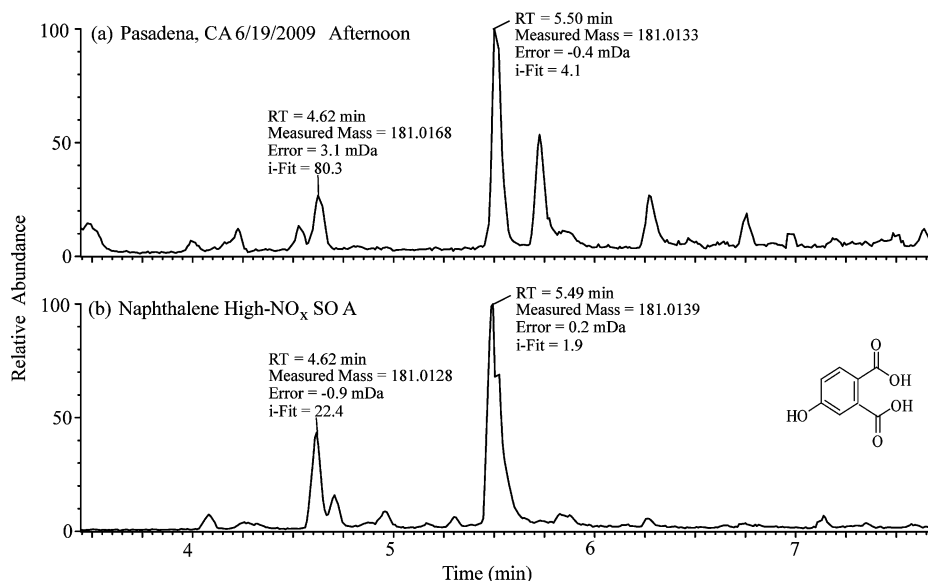

Figure 10. UPLC/(−)ESI-TOFMS EICs of *m/z* 181 from (a) ambient samples collected in Pasadena, CA and (b) naphthalene high-NO$_x$ experiments (Experiment 6).

182

Photooxidation of Naphthalene

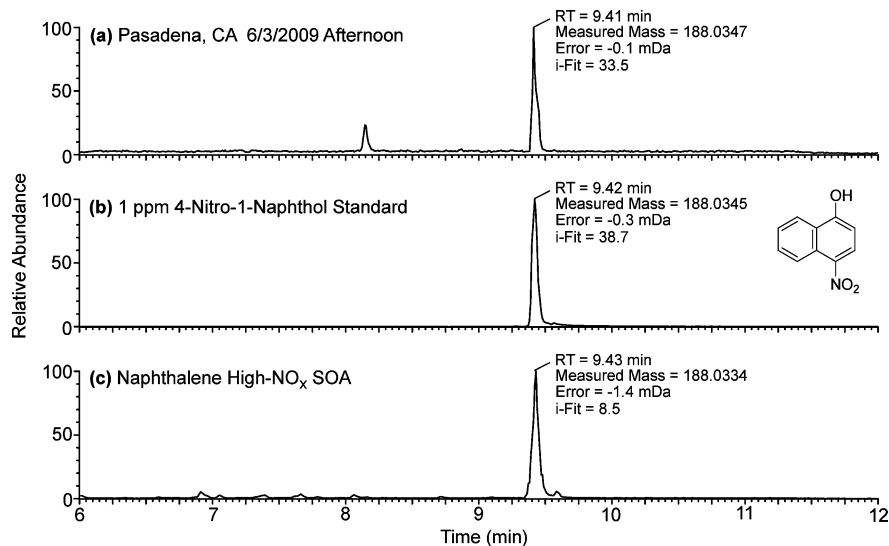*J. Phys. Chem. A, Vol. 114, No. 2, 2010* **931**

Figure 11. UPLC/(−)ESI-TOFMS EICs of m/z 188 from (a) ambient samples collected in Pasadena, CA, (b) a 1 ppm standard of 4-nitro-1-naphthol, and (c) naphthalene high-NO$_x$ experiments (Experiment 6).

that could be used in a SOA source apportionment methods.[99,100] Additionally, Figure 3S (Supporting Information) shows the UPLC/(−)ESI-TOFMS EICs of m/z 165 obtained for a typical naphthalene high-NO$_x$ SOA sample, a 10 ppm phthalic acid standard, and an urban aerosol sample collected from Birmingham, AL. The use of phthalic acid as a potential tracer compound for naphthalene photooxidation is tempting due to the large quantities ($\sim$14 ng m^{-3}) found in the ambient aerosol sample collected from Birmingham, AL. In comparison, 2-methyltetrols, which are ambient tracer compounds for isoprene SOA, have been measured between 200 pg m^{-3} and 365 ng m^{-3} during the summer in aerosol samples collected from many forested locations.[101] Since isoprene is the most abundant nonmethane hydrocarbon emitted into the atmosphere annually, the mass concentrations of phthalic acid found in urban aerosol samples analyzed in the present study are of some significance. In fact, phthalic acid and other dicarboxylic acids have been previously proposed as tracers.[102,103] However, because phthalic acid/anhydride is known to be formed from a wide variety of sources including sewage sludge[104,105] and plastic processing,[106] its use as a tracer is of questionable value.

Figure 10 shows the UPLC/(−)ESI-TOFMS EICs of m/z 181 obtained in a typical naphthalene high-NO$_x$ SOA sample and in an urban aerosol sample collected from Pasadena, CA. The chromatographic peaks eluting at 5.45 min have the same elemental compositions (i.e., molecular formulas) as determined by the accurate mass measurements. This strongly indicates that the hydroxy phthalic acid product characterized in Table 3 can be used as an ambient tracer compound for naphthalene SOA; however, it cannot be ruled out that, as with phthalic acid, other sources may contribute to the formation of hydroxy phthalic acid in ambient aerosol. As a result, we cannot suggest that hydroxy phthalic acid be used solely as an ambient tracer compound for naphthalene SOA.

Another naphthalene high-NO$_x$ SOA constituent found in the urban aerosol samples is 4-nitro-1-naphthol (MW 189). Figure 11 shows the UPLC/(−)ESI-TOFMS EICs of m/z 188 obtained for an urban aerosol sample collected from Pasadena, CA, a 1 ppm 4-nitro-1-naphthol authentic standard, and a typical naphthalene high-NO$_x$ SOA sample. The comparison of these EICs clearly demonstrates the presence of this naphthalene high-NO$_x$ SOA compound in ambient aerosol. Additionally, Figure 4S
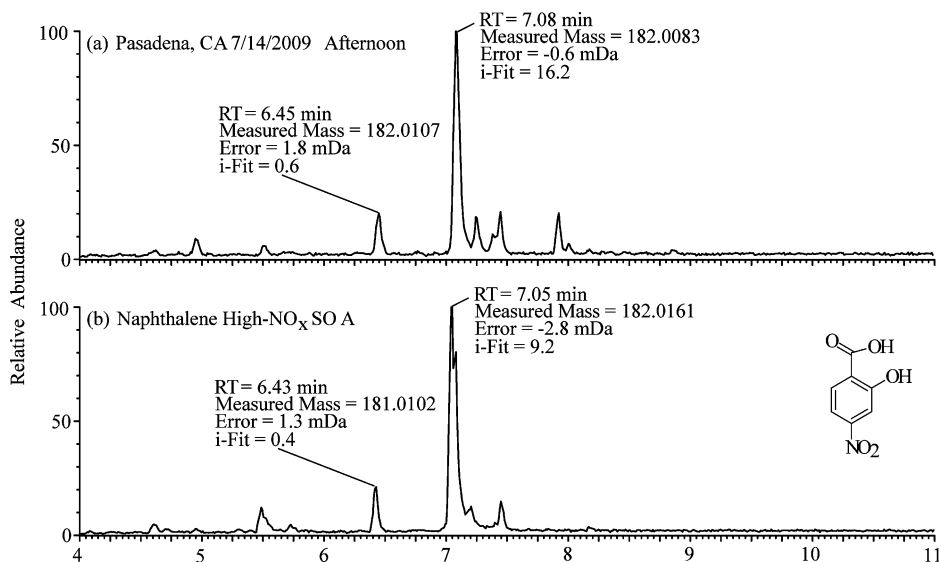

Figure 12. UPLC/(−)ESI-TOFMS EICs of m/z 182 from (a) ambient samples collected in Pasadena, CA and (b) naphthalene high-NO$_x$ experiments (Experiment 6).

(Supporting Information) shows the UPLC/(−)ESI-TOFMS EICs of *m/z* 188 obtained for a typical naphthalene high-NO$_x$ SOA sample, a 1 ppm 4-nitro-1-naphthol authentic standard, and an urban aerosol sample collected from Birmingham, AL, respectively. Concentrations of 4-nitro-1-naphthol from the Birmingham, AL site were found to be 1.6 ng m^{-3}, and the concentration of 4-nitro-1-naphthol collected from Pasadena, CA during summertime polluted conditions was 228 pg m^{-3}. This compound could prove to be an excellent ambient tracer for anthropogenic PAH chemistry. Apparent from the chamber studies, and Birmingham, AL and Pasadena, CA ambient aerosol samples, this compound, found at concentrations comparable to those of other common tracers (i.e., 2-methyltetrol), appears not to have been reported from alternate biogenic or anthropogenic sources. The added concern of N-containing naphthalene compounds, such as the 4-nitro-1-naphthol found in these ambient aerosol samples, as possible carcinogens makes these compounds of particular interest.

Comparison of the UPLC/(−)ESI-TOFMS EICs of *m/z* 182 found in Figure 12 demonstrate that the hydroxy nitrobenzoic acid with MW 183 characterized in the naphthalene high-NO$_x$ SOA (Table 3) is also present in aerosol samples collected from Pasadena, CA. We note that this single-ring aromatic SOA constituent may also form in the atmosphere due to the photooxidation of SAHs (e.g., toluene). However, we have verified that naphthalene is a valid precursor to the presence of this compound in SOA. Since other SAHs and PAHs likely contribute to the formation of this compound in urban aerosol, it is likely not reasonable to use this compound solely as a naphthalene SOA tracer.

As a result of our detailed comparison of the laboratory-generated naphthalene high-NO$_x$ SOA and the urban aerosol samples, we recommend that 4-nitro-1-naphthol might serve as a suitable ambient tracer for naphthalene SOA. It is worth mentioning that other compounds not highlighted here in this discussion were also observed in both the laboratory-generated and ambient aerosol, but these were concluded to be unsuitable ambient tracer compounds for naphthalene SOA; these include the following [M − H]$^-$ ions identified in Table 3: *m/z* 137,149,154, 179, 193, and 209.

5. Conclusions

We report extensive studies on the gas- and particle-phase constituents produced from the OH-initiated photooxidation of naphthalene under both high- and low-NO$_x$ conditions. These studies provide significant insights into the chemical mechanisms that lead to SOA formation. For the high-NO$_x$ case, 53% of the SOA mass is chemically identified, of which organic peroxides constitute 28%. The comparison of O/C and H/C ratios between the off-line molecularly characterized analyses are in agreement with measurements from online bulk measurements suggesting that the chemically characterized portion of the aerosol is representative of bulk aerosol components. Additionally, hydroxybenzene sulfonic acid is observed in the aerosol phase for both the low- and high-NO$_x$ cases, although a mechanism for the generation of this product is not established. Under low-NO$_x$ conditions, ~68% of the SOA mass has been chemically identified, of which 26.2% is associated with organic peroxides. A significant enhancement in the formation of acids is observed relative to the high-NO$_x$ case.

Naphthalene high-NO$_x$ SOA constituents characterized in the present study are compared with urban aerosol samples collected from Birmingham, AL and Pasadena, CA, confirming the presence of SOA from naphthalene photooxidation in the urban

atmosphere. In particular, phthalic acid, hydroxy phthalic acid, 4-nitro-1-naphthol and hydroxy nitrobenzoic acid are observed in both the laboratory-generated high-NO$_x$ SOA and the urban organic aerosols. Of these compounds, 4-nitro-1-naphthol appears to be a valid ambient organic tracer for naphthalene high-NO$_x$ SOA.

Note Added in Proof. We proposed the formation of ring-opening products by a bicyclic peroxy intermediate in the text and in Scheme 5. After this work was submitted the following paper came to our attention: Nishino, N.; Arey, J.; Atkinson R. *Environ. Sci. Technol.* **2009**, in press. Nishino et al. also suggest the formation of phthaldialdehyde and glyoxal by the route in Scheme 5.

Supporting Information Available: Table 1S lists the chemicals employed in this study along with their purities. Tables 2S−7S display identification, quantification and (−)ESI-ITMS MS^2 information for experiments 2−8. EICs for selected photooxidation products observed using the GC/EI-TOFMS technique are shown in Figure 1S. Figure 2S compares mass spectra for 2-formylcinnamladehyde (MW 160) from injection of the standard and from chamber studies. Figures 3S and 4S compare ambient data collected in Birmingham, AL and samples collected in Pasadena, CA, with authentic standards. This material is available free of charge via the Internet at http://pubs.acs.org.

References and Notes

(1) Kroll, J. H.; Seinfeld, J. H. *Atmos. Environ.* **2008**, *42*.
(2) Volkamer, R.; Jimenez, J. L.; Martini, F. S.; Dzepina, K.; Zhang, Q.; Salcedo, D.; Molina, L. T.; Worsnop, D. R.; Molina, M. J. *Geophys. Res. Lett.* **2006**, *33*, 4.
(3) Heald, C. L.; Jacob, D. J.; Park, R. J.; Russell, L. M.; Huebert, B. J.; Seinfeld, J. H.; Liao, H.; Weber, R. J. *Geophys. Res. Lett.* **2005**, *32*, 4.
(4) de Gouw, J. A.; Middlebrook, A. M.; Warneke, C.; Goldan, P. D.; Kuster, W. C.; Roberts, J. M.; Fehsenfeld, F. C.; Worsnop, D. R.; Canagaratna, M. R.; Pszenny, A. A. P.; Keene, W. C.; Marchewka, M.; Bertman, S. B.; Bates, T. S. *J. Geophys. Res.* **2005**, *110*.
(5) Claeys, M.; Graham, B.; Vas, G.; Wang, W.; Vermeylen, R.; Pashynska, V.; Cafmeyer, J.; Guyon, P.; Andreae, M. O.; Artaxo, P.; Maenhaut, W. *Science* **2004**, *303*, 1173.

Photooxidation of Naphthalene

J. Phys. Chem. A, Vol. 114, No. 2, 2010 **933**

(6) Claeys, M.; Wang, W.; Ion, A. C.; Kourtchev, I.; Gelencsér, A.; Maenhaut, W. *Atmos. Environ.* **2004**, *38*, 4093.

(7) Dommen, J.; Metzger, A.; Duplissy, J.; Kalberer, M.; Alfarra, M. R.; Gascho, A.; Weingartner, E.; Prévôt, A. S. H.; Verheggen, B.; Baltensperger, U. *Geophys. Res. Lett.* **2006**, *33*.

(8) Edney, E. O.; Kleindienst, T. E.; Jaoui, M.; Lewandowski, M.; Offenberg, J. H.; Wang, W.; Claeys, M. *Atmos. Environ.* **2005**, *39*, 5281.

(9) Kroll, J. H.; Ng, N. L.; Murphy, S. M.; Flagan, R. C.; Seinfeld, J. H. *Geophys. Res. Lett.* **2005**, *32*, L18808.

(10) Kroll, J. H.; Ng, N. L.; Murphy, S. M.; Flagan, R. C.; Seinfeld, J. H. *Environ. Sci. Technol.* **2006**, *40*, 1869.

(11) Surratt, J. D.; Murphy, S. M.; Kroll, J. H.; Ng, N. L.; Hildebrandt, L.; Sorooshian, A.; Szmigielski, R.; Vermeylen, R.; Maenhaut, W.; Claeys, M.; Flagan, R. C.; Seinfeld, J. H. *J. Phys. Chem. A* **2006**, *110*, 9665.

(12) Szmigielski, R.; Surratt, J. D.; Vermeylen, R.; Szmigielska, K.; Kroll, J. H.; Ng, N. L.; Murphy, S. M.; Sorooshian, A.; Seinfeld, J. H.; Claeys, M. *J. Mass Spectrom.* **2007**, *42*, 101.

(13) Ng, N. L.; Kroll, J. H.; Chan, A. W. H.; Chhabra, P. S. *Atmos. Chem. Phys.* **2007**, *7*.

(14) Song, C.; Na, K. S.; Cocker, D. R. *Environ. Sci. Technol.* **2005**, *39*, 3143.

(15) Chan, A. W. H.; Kautzman, K. E.; Chhabra, P. S.; Surratt, J. D.; Chan, M. N.; Crounse, J. D.; Kürten, A.; Wennberg, P. O.; Flagan, R. C.; Seinfeld, J. H. *Atmos. Chem. Phys.* **2009**, *9*, 3049.

(16) Hatakeyama, S.; Izumi, K.; Fukuyama, T.; Akimoto, H.; Washida, N. *J. Geophys. Res.* **1991**, *96*, 947.

(17) Ng, N. L.; Chhabra, P. S.; Chan, A. W. H.; Surratt, J. D.; Kroll, J. H.; Kwan, A. J.; McCabe, D. C.; Wennberg, P. O.; Sorooshian, A.; Murphy, S. M.; Dalleska, N. F.; Flagan, R. C.; Seinfeld, J. H. *Atmos. Chem. Phys.* **2007**, *7*, 3909.

(18) Presto, A. A.; Huff Hartz, K. E.; Donahue, N. M. *Environ. Sci. Technol.* **2005**, *39*.

(19) Docherty, K. S.; Wu, W.; Lim, Y. B.; Ziemann, P. J. *Environ. Sci. Technol.* **2005**, *39*, 4049.

(20) Gao, S.; Keywood, M.; Ng, N. L.; Surratt, J.; Varutbangkul, V.; Bahreini, R.; Flagan, R. C.; Seinfeld, J. H. *J. Phys. Chem. A* **2004**, *108*, 10147.

(21) Iinuma, Y.; Böge, O.; Gnauk, T.; Herrmann, H. *Atmos. Environ.* **2004**, *38*, 761.

(22) Jang, M. S.; Czoschke, N. M.; Lee, S.; Kamens, R. M. *Science* **2002**, *298*, 814.

(23) Kalberer, M.; Paulsen, D.; Sax, M.; Steinbacher, M.; Dommen, J.; Prevot, A. S. H.; Fisseha, R.; Weingartner, E.; Frankevich, V.; Zenobi, R.; Baltensperger, U. *Science* **2004**, *303*, 1659.

(24) Liggio, J.; Li, S. M.; McLaren, R. *J. Geophys. Res.* **2005**, *110*.

(25) Liggio, J.; Li, S. M.; McLaren, R. *Environ. Sci. Technol.* **2005**, *39*, 1532.

(26) Tobias, H. J.; Ziemann, P. J. *Environ. Sci. Technol.* **2000**, *34*, 2105.

(27) Tolocka, M. P.; Jang, M.; Ginter, J. M.; Cox, F. J.; Kamens, R. M.; Johnston, M. V. *Environ. Sci. Technol.* **2004**, *38*, 1428.

(28) Gómez-González, Y.; Surratt, J. D.; Cuyckens, F.; Szmigielski, R.; Vermeylen, R.; Jaoui, M.; Lewandowski, M.; Offenberg, J. H.; Kleindienst, T. E.; Edney, E. O.; Blockhuys, F.; Van Alsenoy, C.; Maenhaut, W.; Claeys, M. *J. Mass Spectrom* **2008**, *43*, 371.

(29) Iinuma, Y.; Müller, C.; Berndt, T.; Böge, O.; Claeys, M.; Herrmann, H. *Environ. Sci. Technol.* **2007**, *41*, 6678.

(30) Iinuma, Y.; Müller, C.; Böge, O.; Gnauk, T.; Herrmann, H. *Atmos. Environ.* **2007**, *41*, 5571.

(31) Surratt, J. D.; Gómez-González, Y.; Chan, A. W. H.; Vermeylen, R.; Shahgholi, M.; Kleindienst, T. E.; Edney, E. O.; Offenberg, J. H.; Lewandowski, M.; Jaoui, M.; Maenhaut, W.; Claeys, M.; Flagan, R. C.; Seinfeld, J. H. *J. Phys. Chem. A* **2008**, *112*, 8345.

(32) Surratt, J. D.; Kroll, J. H.; Kleindienst, T. E.; Edney, E. O.; Claeys, M.; Sorooshian, A.; Ng, N. L.; Offenberg, J. H.; Lewandowski, M.; Jaoui, M.; Flagan, R. C.; Seinfeld, J. H. *Environ. Sci. Technol.* **2007**, *41*, 517.

(33) Galloway, M. M.; Chhabra, P. S.; Chan, A. W. H.; Surratt, J. D.; Flagan, R. C.; Seinfeld, J. H.; Keutsch, F. N. *Atmos. Chem. Phys.* **2009**, *9*, 3331.

(34) Kroll, J. H.; Ng, N. L.; Murphy, S. M.; Varutbangkul, V.; Flagan, R. C.; Seinfeld, J. H. *J. Geophys. Res.* **2005**, *110*, 10.

(35) Volkamer, R.; Martini, F. S.; Molina, L. T.; Salcedo, D.; Jimenez, J. L.; Molina, M. J. *Geophys. Res. Lett.* **2007**, *34*.

(36) Robinson, A. L.; Donahue, N. M.; Shrivastava, M. K.; Weitkamp, E. A.; Sage, A. M.; Grieshop, A. P.; Lane, T. E.; Pierce, J. R.; Pandis, S. N. *Science* **2007**, *315*, 1259.

(37) Schauer, J. J.; Kleeman, M. J.; Cass, G. R.; Simoneit, B. R. T. *Environ. Sci. Technol.* **1999**, *33*, 1578.

(38) Schauer, J. J.; Kleeman, M. J.; Cass, G. R.; Simoneit, B. R. T. *Environ. Sci. Technol.* **2002**, *36*, 1169.

(39) Ravindra, K.; Sokhi, R.; Van Grieken, R. *Atmos. Environ.* **2008**, *42*, 2895.

(40) Schauer, J. J.; Kleeman, M. J.; Cass, G. R.; Simoneit, B. R. T. *Environ. Sci. Technol.* **2001**, *35*, 1716.

(41) Schauer, J. J.; Kleeman, M. J.; Cass, G. R.; Simoneit, B. R. T. *Environ. Sci. Technol.* **1999**, *33*, 1566.

(42) Schauer, J. J.; Kleeman, M. J.; Cass, G. R.; Simoneit, B. R. T. *Environ. Sci. Technol.* **2002**, *36*, 567.

(43) Atkinson, R.; Arey, J. *Polycycl. Aromatic Compd.* **2007**, *27*, 15.

(44) Atkinson, R.; Aschmann, S. M.; Arey, J.; Carter, W. P. L. *Int. J. Chem. Kinetics* **1989**, *21*, 801.

(45) Bunce, N. J.; Liu, L.; Zhu, J.; Lane, D. A. *Environ. Sci. Technol.* **1997**, *31*, 2252.

(46) Mihele, C. M.; Wiebe, H. A.; Lane, D. A. *Polycycl. Aromatic Compd.* **2002**, *22*, 729.

(47) Wang, L.; Atkinson, R.; Arey, J. *Environ. Sci. Technol.* **2007**, *41*, 2803.

(48) Arey, J.; Atkinson, R.; Zielinska, B.; McElroy, P. A. *Environ. Sci. Technol.* **1989**, *23*, 321.

(49) Gupta, P.; Harger, W. P.; Arey, J. *Atmos. Environ.* **1996**, *30*, 3157.

(50) Helmig, D.; Arey, J.; Harger, W. P.; Atkinson, R.; Lopezcancio, J. *Environ. Sci. Technol.* **1992**, *26*, 622.

(51) Helmig, D.; Lopezcancio, J.; Arey, J.; Harger, W. P.; Atkinson, R. *Environ. Sci. Technol.* **1992**, *26*, 2207.

(52) Grosovsky, A. J.; Sasaki, J. C.; Arey, J.; Eastmond, D. A.; Parks, K. K.; Atkinson, R. *Res. Rep. Health Eff. Inst.* **1999**, i.

(53) Cocker, D. R.; Flagan, R. C.; Seinfeld, J. H. *Environ. Sci. Technol.* **2001**, *35*, 2594.

(54) Keywood, M. D.; Varutbangkul, V.; Bahreini, R.; Flagan, R. C.; Seinfeld, J. H. *Environ. Sci. Technol.* **2004**, *38*, 4157.

(55) Burkhardt, M. R.; Maniga, N. I.; Stedman, D. H.; Paur, R. *J. Anal. Chem.* **1988**, *60*, 816.

(56) Paulot, F.; Crounse, J. D.; Kjaergaard, H. G.; Kroll, J. H.; Seinfeld, J. H.; Wennberg, P. O. *Atmos. Chem. Phys.* **2009**, *9*, 1479.

(57) Crounse, J. D.; McKinney, K. A.; Kwan, A. J.; Wennberg, P. O. *Anal. Chem.* **2006**, *78*, 6726.

(58) Stein, S. M. Y.; Tchekhovski, D.; Mallard, G.; Mikaia, A.; Zaikin, V.; Zhu, J.; Clifton, C.; Sparkman, D. *The NIST Mass Spectral Search Program for the NIST/EPA/NIH Mass Spectral Library*, 2005 ed.; 2005.

(59) Surratt, J. D.; Gómez-González, Y.; Chan, A. W. H.; Vermeylen, R.; Shahgholi, M.; Kleindienst, T. E.; Edney, E. O.; Offenberg, J. H.; Lewandowski, M.; Jaoui, M.; Maenhaut, W.; Claeys, M.; Flagan, R. C.; Seinfeld, J. H. *J. Phys. Chem. A* **2008**, *112*, 8345.

(60) DeCarlo, P. F.; Kimmel, J. R.; Trimborn, A.; Northway, M. J.; Jayne, J. T.; Aiken, A. C.; Gonin, M.; Fuhrer, K.; Horvath, T.; Docherty, K. S.; Worsnop, D. R.; Jimenez, J. L. *Anal. Chem.* **2006**, *78*, 8281.

(61) Allan, J. D.; Delia, A. E.; Coe, H.; Bower, K. N.; Alfarra, M. R.; Jimenez, J. L.; Middlebrook, A. M.; Drewnick, F.; Onasch, T. B.; Canagaratna, M. R.; Jayne, J. T.; Worsnop, D. R. *J. Aerosol Sci.* **2004**, *35*, 909.

(62) Bahreini, R.; Keywood, M. D.; Ng, N. L.; Varutbangkul, V.; Gao, S.; Flagan, R. C.; Seinfeld, J. H.; Worsnop, D. R.; Jimenez, J. L. *Environ. Sci. Technol.* **2005**, *39*, 5674.

(63) Aiken, A. C.; DeCarlo, P. F.; Jimenez, J. L. *Anal. Chem.* **2007**, *79*, 8350.

(64) Aiken, A. C.; Decarlo, P. F.; Kroll, J. H.; Worsnop, D. R.; Huffman, J. A.; Docherty, K. S.; Ulbrich, I. M.; Mohr, C.; Kimmel, J. R.; Sueper, D.; Sun, Y.; Zhang, Q.; Trimborn, A.; Northway, M.; Ziemann, P. J.; Canagaratna, M. R.; Onasch, T. B.; Alfarra, M. R.; Prevot, A. S. H.; Dommen, J.; Duplissy, J.; Metzger, A.; Baltensperger, U.; Jimenez, J. L. *Environ. Sci. Technol.* **2008**, *42*, 4478.

(65) Weber, R. J.; Orsini, D.; Daun, Y.; Lee, Y. N.; Klotz, P. J.; Brechtel, F. *Aerosol Sci. Technol.* **2001**, *35*, 718.

(66) Sorooshian, A.; Brechtel, F. J.; Ma, Y. L.; Weber, R. J.; Corless, A.; Flagan, R. C.; Seinfeld, J. H. *Aerosol Sci. Technol.* **2006**, *40*, 396.

(67) Edgerton, E. S.; Hartsell, B. E.; Saylor, R. D.; Jansen, J. J.; Hansen, D. A.; Hidy, G. M. *J. Air Waste Manage. Assoc.* **2005**, *55*, 1527.

(68) Hansen, D. A.; Edgerton, E. S.; Hartsell, B. E.; Jansen, J. J.; Kandasamy, N.; Hidy, G. M.; Blanchard, C. L. *J. Air Waste Manage. Assoc.* **2003**, *53*, 1460.

(69) Gao, S.; Surratt, J. D.; Knipping, E. M.; Edgerton, E. S.; Shahgholi, M.; Seinfeld, J. H. *J. Geophys. Res.* **2006**, *111*, D14314.

(70) Larson, R. A.; Garrison, W. J.; Marley, K. A. *Tetrahedron Lett.* **1986**, *27*, 3987.

(71) Nishino, N.; Arey, J.; Atkinson, R. *Environ. Sci. Technol.* **2009**.

(72) Sasaki, J.; Aschmann, S. M.; Kwok, E. S. C.; Atkinson, R.; Arey, J. *Environ. Sci. Technol.* **1997**, *31*, 3173.

(73) Atkinson, R.; Aschmann, S. M.; Arey, J.; Zielinska, B.; Schuetzle, D. *Atmos. Environ.* **1989**, *23*, 2679.

(74) Fisseha, R.; Dommen, J.; Sax, M.; Paulsen, D.; Kalberer, M.; Maurer, R.; Hofler, F.; Weingartner, E.; Baltensperger, U. *Anal. Chem.* **2004**, *76*, 6535.

(75) Lu, R.; Wu, J.; Turco, R. P.; Winer, A. M.; Atkinson, R.; Arey, J.; Paulson, S. E.; Lurmann, F. W.; Miguel, A. H.; Eiguren-Fernandez, A. *Atmos. Environ.* **2005**, *39*, 489.

Kautzman et al.

(76) Fraser, M. P.; Cass, G. R.; Simoneit, B. R. T. *Environ. Sci. Technol.* **1998**, *32*, 2051.

(77) Marr, L. C.; Kirchstetter, T. W.; Harley, R. A.; Miguel, A. H.; Hering, S. V.; Hammond, S. K. *Environ. Sci. Technol.* **1999**, *33*, 3091.

(78) Bunce, N. J. D., H. G. *Can. J. Chem.* **1992**, *70*, 1966.

(79) Lane, D. A.; Fielder, S. S.; Townsend, S. J.; Bunce, N. J.; Zhu, J.; Liu, L.; Wiens, B.; Pond, P. *Polycycl. Aromatic Compd.* **1996**, *9*, 53.

(80) Nishino, N.; Atkinson, R.; Arey, J. *Environ. Sci. Technol.* **2008**, *42*, 9203.

(81) Qu, X. H.; Zhang, Q. Z.; Wang, W. X. *Chem. Phys. Lett.* **2006**, *429*, 77.

(82) Atkinson, R.; Arey, J. *Polycycl. Aromatic Compd.* **2007**, *27*, 15.

(83) Nishino, N. A. J.; Atkinson, R. *Environ. Sci. Technol.* 2009.

(84) Dekermenjian, M.; Allen, D. T.; Atkinson, R.; Arey, J. *Aerosol Sci. Technol.* **1999**, *30*, 273.

(85) Palen, E. J.; Allen, D. T.; Pandis, S. N.; Paulson, S. E.; Seinfeld, J. H.; Flagan, R. C. *Atmos. Environ., Part A* **1992**, *26*, 1239.

(86) Koch, R.; Knispel, R.; Elend, M.; Siese, M.; Zetzsch, C. *Atmos. Chem. Phys.* **2007**, *7*, 2057.

(87) Glowacki, D. R.; Wang, L. M.; Pilling, M. J. *J. Phys. Chem. A* **2009**, *113*, 5385.

(88) Suh, I.; Zhang, R. Y.; Molina, L. T.; Molina, M. J. *J. Am. Chem. Soc.* **2003**, *125*, 12655.

(89) Calvert, J. G.; Atkinson, R.; Becker, K. H.; Kamens, R. M.; Seinfeld, J. H.; Wallington, T. J.; Yarwood, G. *The Mechanisms of Atmospheric Oxidation of Aromatic Hydrocarbons*; Oxford University Press, Inc.: New York, 2002.

(90) Reemtsma, T. *J. Chromatogr. A* **2003**, *1000*, 477.

(91) Rodil, R.; Quintana, J. B.; Lopez-Mahia, P.; Muniategui-Lorenzo, S.; Prada-Rodriguez, D. *Anal. Chem.* **2008**, *80*, 1307.

(92) Frömel, T.; Peschka, M.; Fichtner, N.; Hierse, W.; Ignatiev, N. V.; Bauer, K. H.; Knepper, T. P. *Rapid Commun. Mass Spectrom.* **2008**, *22*, 3957.

(93) Barnes, I.; Hjorth, J.; Mihalopoulos, N. *Chem. Rev.* **2006**, *106*, 940.

(94) Johnson, M. T.; Bell, T. G. *Environ. Chem.* **2008**, *5*, 259.

(95) Tang, M. J.; Zhu, T. *Sci. China Ser. B-Chem.* **2009**, *52*, 93.

(96) Lara-Martin, P. A.; Gomez-Parra, A.; Gonzalez-Mazo, E. *Environ. Pollut.* **2008**, *156*, 36.

(97) Lara-Martin, P. A.; Gomez-Parra, A.; Gonzalez-Mazo, E. *J. Chromatogr. A* **2006**, *1137*, 188.

(98) Altieri, K. E.; Turpin, B. J.; Seitzinger, S. P. *Atmos. Chem. Phys.* **2009**, *9*, 2533.

(99) Kleindienst, T. E.; Jaoui, M.; Lewandowski, M.; Offenberg, J. H.; Lewis, C. W.; Bhave, P. V.; Edney, E. O. *Atmos. Environ.* **2007**, *41*, 8288.

(100) Offenberg, J. H.; Lewis, C. W.; Lewandowski, M.; Jaoui, M.; Kleindienst, T. E.; Edney, E. O. *Environ. Sci. Technol.* **2007**, *41*, 3972.

(101) Hallquist, M.; Wenger, J. C.; Baltensperger, U.; Rudich, Y.; Simpson, D.; Claeys, M.; Dommen, J.; Donahue, N. M.; George, C.; Goldstein, A. H.; Hamilton, J. F.; Herrmann, H.; Hoffmann, T.; Iinuma, Y.; Jang, M.; Jenkin, M. E.; Jimenez, J. L.; Kiendler-Scharr, A.; Maenhaut, W.; McFiggans, G.; Mentel, T. F.; Monod, A.; Prevot, A. S. H.; Seinfeld, J. H.; Surratt, J. D.; Szmigielski, R.; Wildt, J. *Atmos. Chem. Phys.* **2009**, *9*, 5155.

(102) Schuetzle, D.; Cronn, D.; Crittenden, A. L.; Charlson, R. J. *Environ. Sci. Technol.* **1975**, *9*, 838.

(103) Chebbi, A.; Carlier, P. *Atmos. Environ.* **1996**, *30*, 4233.

(104) Mougin, C.; Dappozze, F.; Brault, A.; Malosse, C.; Schmidt, J. E.; Amellal-Nassr, N.; Patureau, D. *Environ. Chem. Lett.* **2006**, *4*, 201.

(105) Thiruvenkatachari, R.; Kwon, T. O.; Moon, I. S. *J. Environ. Sci. Health, Part A* **2006**, *41*, 1685.

(106) Butte, W.; Hostrup, O.; Walker, G. *Gefahrstoffe Reinhaltung Der Luft* **2008**, *68*, 79.